IMPERIAL COLLEGE OF SCIENCE, TECHNOLOGY AND MEDICINE

University of London

STRUCTURAL DYNAMIC ANALYSIS AND TESTING OF COUPLED STRUCTURES

by

Wenjie Liu

A thesis submitted to the University of London
for the Degree of Doctor of Philosophy and
for the Diploma of Imperial College

Department of Mechanical Engineering
Imperial College of Science, Technology and Medicine
London SW7

October, 2000

ABSTRACT

Engineering structures normally exist in the form of assemblies of several components or substructures, and the modelling, prediction and optimisation of the assembled structures are presently achieving far from the required accuracy and reliability, and from that which is attained for the individual components. This is the essential problem addressed by this research.

The difficulties in achieving the required accuracy are almost certainly due to the variety and complexity of joint types and to the lack of an accurate estimation of the interactions between substructures. This thesis provides two approaches for joint parameter identification, a least-squares method based and a neural network based one. Their mathematical backgrounds are thoroughly presented and their validity is examined by numerical case studies.

The coupling analysis method has the equal importance to the joint parameter identification. Two branches of coupling methods, CMS and FRF-based, are systematically investigated. Two new methods, one in each branch, are developed to take joint effects into account in the analysis. Numerical studies show that these methods are accurate and efficient. The significance of modal incompleteness and measurement noise to the coupling analysis is also estimated.

Two relevant issues in joint modelling and substructure coupling are also discussed in this thesis. They are (i) non-linearity considerations in joint modelling and substructure coupling and (ii) impact of rotational DOF information. The former reviews the progress of nonlinear joint modelling as well as the analysis methods dealing with nonlinear coupling problem, indicating that the nonlinear behaviour of fastening joints is not significant. The latter demonstrates the importance of the RDOF-related information in both joint modelling and FRF coupling analysis.

ACKNOWLEDGEMENTS

I am deeply indebted to Professor D J Ewins for his supervision throughout this research work. It is his initiatives and instructions that enabled me to achieve developments in this area. I am also grateful to the other members of the staff who helped me a lot during these years, Dr. Imregun, Mr. Robb, Mrs. Savage and Mr. Woodward.

I wish to express my appreciation to my colleagues in the Dynamics Section of Imperial College for their friendly cooperation and useful discussions.

I would to express my gratitude to Bosch GmbH and CVCP. It would have been impossible for me to study here without the financial support from them.

Special thanks to my parents for all their love, encouragement and understanding.

Finally, I wish to thank my wife and son for their love and sacrifice. They shared my happiness and disappointments.

NOMENCLATURE

Matrices and vectors

$\mathbf{C}$	viscous damping matrix of structure
$\mathbf{C}$	viscous damping matrix of joint
$\mathbf{D}$	structural damping matrix of joint
$\mathbf{E}$	error matrix
$\mathbf{F}$	force vector of assembled structure
$\mathbf{H}$	receptance matrix
$\mathbf{I}$	identity matrix
$\mathbf{K}$	stiffness matrix of assembled structure
$\mathbf{K}$	stiffness matrix of joint
$\mathbf{M}$	mass matrix of assembled structure
$\mathbf{M}$	mass matrix of joint
$\mathbf{R}$	residual matrix
$\mathbf{T}$	transformation matrix
$\mathbf{Z}$	joint impedance matrix
$\mathbf{c}$	viscous damping matrix of substructure
$\mathbf{c}$	viscous damping vector of joint
$\mathbf{d}$	structural damping vector of joint
$\mathbf{f}$	force vector of substructure
$\mathbf{f}$	force vector of joint
$\mathbf{k}$	stiffness matrix of substructure
$\mathbf{k}$	stiffness vector of joint
$\mathbf{m}$	mass matrix of substructure
$\mathbf{m}$	mass vector of joint
$\mathbf{n}$	noise sequence, a vector
$\mathbf{p}$	normal coordinates

$\mathbf{q}$	generalised coordinates
$\mathbf{x}$	physical coordinates
$\boldsymbol{\omega}^2$	eigen-value matrix, diagonal
$\boldsymbol{\Phi}$	mass normalised eigen-vector matrix
$\boldsymbol{\varphi}$	mass normalised eigen-vector
$\boldsymbol{\Psi}$	eigen-vector matrix
$\boldsymbol{\Gamma}$	residual attachment mode matrix

Scalars

A	cross section area
E	Young's modulus
$h(t)$	response function of unit pulse
$H(\omega)$	the simulated noise-free FRF
$\tilde{H}(\omega)$	the simulated noise-contaminated FRF
I	bending section modulus
L	number of internal DOFs
l	length of a beam element
n	number of DOFs
n_c	number of coupling DOFs of an assembly of substructures
n_f	number of frequency points
ω^2	eigen-value
β	proportional coefficient of damping matrix
σ	singular value or standard deviation of added noise
γ	percentage of noise

Symbols

A	substructure A
B	substructure B
C	coupling coordinate of assembled structure, subscript
$\overline{C}$	coupling coordinate on substructure A of assembled structure, subscript
$\widetilde{C}$	coupling coordinate on substructure B of assembled structure, subscript
I	internal coordinates of assembled structure, subscript
c	coupling coordinate of a set of substructures, subscript
$\overline{c}$	coupling coordinate on substructure A in a set of substructures, subscript
$\widetilde{c}$	coupling coordinate on substructure B in a set of substructures, subscript
h	subscript, high frequency range
i	internal coordinates of a set of substructures, subscript
l	subscript, low frequency range
$\Re$	real set

Abbreviations

CMS	component mode synthesis
CMSJ	CMS with joint considered and residual attachment mode compensation
DOF	degree of freedom
FE	finite element
FRAC	frequency response assurance criteria
FRF	frequency response function
GJDM	general joint description method
K-J	Klosterman-Jetmundsen method
LSM	least-squares method
PCA	principal element analysis
RBF	radial basis function
RDOF	rotational degree of freedom
TDOF	translational degree of freedom

Table of Contents

CHAPTER 1

GENERAL INTRODUCTION

1.1. INTRODUCTION TO THE PROBLEM

Structural dynamics analysis is required more and more by industry to make accurate predictions of the response of structures under a variety of circumstances. With regard to increasing international competition, this requirement is becoming urgent because successful predictions will lead to more elegant and efficient designs, more durable and comfortable products as well as to lower energy consumption related to dynamics.

The modelling and dynamic response prediction techniques for individual structural components have been well developed and a number of sophisticated and powerful software packages are in practical use. However, most engineering structures exist in the form of assemblies of several components or substructures, and the modelling, response prediction and optimisation of the assembled structures′ dynamics are presently far from attaining the required

accuracy and reliability, and from that which is obtained for the individual components. This is the essential problem addressed in this thesis.

The difficulties encountered in achieving the required accuracy of dynamic response predictions are almost certainly due to the variety and complexity of joint types and behaviour as well as to the lack of an accurate description of the interactions between substructures. However, general methods which are able to model various types of joints have not been reported and the prediction methods for substructure coupling with joints included have not been systematically developed. Fundamental research on these two aspects is urgently demanded and further progress on developing powerful applicable software is needed by industry. It is intended that new methods are developed whereby we can not only understand the characteristics of the joints and the mechanisms of coupling, but also learn to utilise the dynamic properties of joints in coupling analysis so as to modify and to optimise the dynamic response of our structures.

1.2. BRIEF REVIEW OF STATE-OF-THE-ART

Engineering structures are often fabricated from components by using a variety of connections, such as bolted, riveted, welded and bonded joints *etc*. In the past three decades, the importance of joint modelling or descriptions of joint dynamic properties has become more and more significant. Modelling methods which have been reported are basically classified into two categories: linear joint models and nonlinear joint models. The linear joint models are mostly used in modelling tightly fastened joints in engineering structures and are the main concern of this thesis. The nonlinear joint models normally exhibit friction-related non-linearities.

Experimental investigations on adhesive bonded joints were carried out in 1972 by Thornley and Lees [ThLe72]. Static and dynamic experiments showed the stiffness and damping properties of the joints by measuring loads as well as displacements. The stiffness was found to be dependent on the type of machined surface and the quality of surface roughness. In general, the smaller the

roughness value of the surface the higher the stiffness. The stiffness was basically linear and became softening after the interface pressure exceeded a certain value. A small increase in damping was achieved when using the epoxy resin adhesives compared with that obtained with dry friction. Normal loads were applied without any significant sliding of the joint faces. Thornley and Lees' work revealed that the joint bonded by adhesives has improved stiffness and damping characteristics.

A simple analytical joint model, comprising a spring and a parallel dashpot connecting each co-ordinate direction of two substructures, was first proposed by Yoshima [Yosh77] for describing welded and bolted joints. The stiffness of the springs and damping coefficients of the dampers used in the model were the equivalent stiffness and damping coefficients of the joints. They were identified iteratively by comparing the resonance frequencies and damping ratios of the first two modes. This method was later applied to a dynamic analysis of a vertical lathe [Yosh79]. The joint model proposed by Yoshima is simple and reliable in his case studies, but his algorithm for the identification is not effective.

Wang and Liou used the same model, a group of parallel stiffnesses and dashpots, to represent bolted joints and developed a direct identification method [WaLi90][WaLi91]. The parameters of these connections, stiffness and damping coefficients, were identified by employing a least-squares method with the input of FRFs of the substructures as well as their assembly. This algorithm is more general and effective compared with Yoshima's [Yosh77]. Witek applied the same model and similar algorithm to identify dynamic parameters of vibro-isolation pads in machines [Wite97].

A more general joint model which is expressed by stiffness and damping coefficient matrices was proposed by Wang and Sas [WaSa90]. The essential algorithm for identifying the joint parameters is to transform the assembled system into several single DOF systems using selected eigen-vectors. These eigen-vectors should be sensitive to the identified parameters. It is obvious that

this method relies on the availability and accuracy of the mode shapes of the assembled structure. It is not very promising for practical applications.

To extract joint parameters without interference from complicated dynamic characteristics of substructures, a method based on rigid-body dynamics and frequency response function measurement was developed by Becker *et al*. [BeWB99]. Joints are isolated by connecting rigid bodies instead of elastic substructures. It is easy to obtain the stiffness matrix of the joint by means of this method but the application of this technique is quite limited.

In the area of finite element model updating, joint modelling is of interest because of the existence of unknowns in joints. Mottershead and Friswell *et al* [MoFr94] used an eigen-value sensitivity analysis based method to update the finite element models of structures which consist of adhesive, welded and bolted joints. The updating parameters were chosen according to the characteristics of different types of joint. For instance, in the study of two adhesive joints between plates, stiffness parameters of the elements in the adhesive area were selected as updating parameters. In the study of bolted joints between two beams with welded flanges, the updating parameters were mass and stiffness for the bolts and the offset dimensions of the beam elements in both beam and flanges. This eigenvalue sensitivity based method was also applied to the welded joints in a tubular H-frame [HoGu99]. It can be seen that with this technique the updating parameters may not be unique to achieve the same goal in the updating procedure and in most problems parametric uncertainty exists in both the joints and the substructures simultaneously.

Similar to the work reported in [MoFr94], nodal offset dimensions were taken as updating geometric parameters to update a structure with welded joints in [AhMF96]. A generic element model approach, which decomposes the stiffness matrices of an element or a group of elements into local modes and generates a family of acceptable stiffness matrices, was applied to update the joints. The Generic model approach was regarded as a more general method and yielded a better result compared with the updated model using offset parameters.

A general impedance joint model was proposed by Ren and Beards [ReBe95]. This is basically a generalised method developed from [WaLi90]. Compared with Wang and Liou′s joint model, Ren′s method deals with a more general type of joint. The impedance matrix of the joint is constructed using mass, stiffness, viscous and/or structural damping matrices. FRFs measured from substructures and their assembly are required for input data and a least-squares method is employed for solving the joint parameters. The drawback of this method is that the coefficient matrix of the linear equations about joint parameters is often ill-conditioned and sensitive to noise in input FRFs.

A hybrid method, combining a finite element model with the modal testing technique, was proposed by Yuan and Wu [YuWu85]. The finite element model of an assembled structure is given with unknown joint parameters. Experimental modal analysis provides eigenvalues and eigenvectors of the system, which are applied to the finite element model to form such a hybrid equation of motion. The unknowns in this equation are then calculated. A similar idea was also reported by Park and Kim [PaKi95], who applied an optimisation method to solve joint parameters and devising a cost function as the difference between experimental and analytical results.

Nonlinear joint modelling has not been studied as thoroughly as that based on linear models because of the difficulty in understanding the mechanisms and the necessity in practical applications. A few papers published by Gaul *et al* on bolted joint modelling [Gaul83][GaNW94][LeGa95] basically represent the current situation. These papers will be introduced in Chapter 6 in detail.

Substructure coupling analysis has essentially two techniques: (i) component modal synthesis (CMS) and (ii) the impedance coupling or frequency response function (FRF) coupling methods. The CSM was first developed by Craig and Bampton [CrBa68] and has been in use for over three decades with little development was achieved so far [Crai00]. An attempt to introduce joints into the synthesis procedure was tried by Urgueira in 1989 [Urgu89] and by Lou in 1993 [LoGh93]. Lou introduced a concept of residual attachment mode to

compensate for the error caused by mode truncation encountered in [Urgu89] and also devised quite a useful method.

The FRF coupling method reported by Jetmundsen *et al* [JeBi88] has an inherent advantage of being able to use measured FRFs directly. There are therefore no errors introduced by modal analysis but the noise contained in the measured FRFs is usually the trade-off. A development of this method made by Ferreira [Ferr98] introduces parallel scalar nonlinear springs between the substructures and it can be applied to relatively simple cases.

To sum up, linear joint modelling, which includes mathematical expressions for joints (spring and dashpot, impedance matrix *etc*.) and algorithms for solving the parameters in these expressions, has not been fully developed. The currently developed methods still have flaws either in the way that the mathematical expressions for the joints are too specific or the algorithms to solve the parameters are not efficient and robust. On the other hand, the classical CMS methods do not have the joints involved [CrBa68] [CrCh77] and the recent development of CMS with joints [LoGh93] needs to be validated. The FRF coupling methods have similar problems as CMS and lack for a general description for joints. Therefore, a general joint description and a robust algorithm for joint parameter identification are needed and the coupling analysis methods, both CMS and FRF coupling, should be developed systematically with a general type of joint included.

1.3. PROPOSED DEVELOPMENTS

The major purpose of this research is to develop methods which enable the construction of mathematical models of assembled structures in order to predict the required response levels to a required accuracy by giving the necessary input data of damping and excitation levels.

The proposed developments of the research reported in this thesis are

- development of a least-squares based method to model joints on the basis of a linear assumption and thereby to identify the joint parameters;
- development of a neural networks based method to identify parameters of joints, utilising parametric families of finite element models and PCA techniques to extract feature vectors as training sets;
- development of conventional CMS and FRF coupling methods to analyse coupled structures with joints involved and providing fundamental theories, algorithms and examples for verification;
- understanding of the mechanics and extent of nonlinear effects in real joints;
- clarification of the impact of rotational degrees of freedom to both joint parameter identification and coupling analysis.

1.4. SUMMARY OF THE THESIS

Two major issues are addressed in this thesis: joint parameter identification and substructure coupling analysis. These two parts of the work determine the basic profile of the necessary theory for solving the problem of interest. Logically, these two aspects are independent in development and application but they deal with related problems in structural dynamics, namely, the response prediction of coupled structures. Classifying these two parts of work mathematically, we regard coupling analysis as a direct problem and parameter identification as an inverse problem. This thesis presents the methodologies for both aspects systematically by building up fundamental mathematical principles and validating these principles by numerical simulations. Two controversial topics, the nonlinear effects and the impact of rotational degrees of freedom (RDOF), are separately discussed in terms of their importance to the major issues. The new methods developed in this thesis are validated by numerical studies and it is expected to apply them to more complicated cases and to practical structures in industry.

In Chapter 2, a least-squares method (LSM) based procedure to identify joint parameters using measured frequency response functions (FRFs) is presented. This procedure deals with general linear joint models and identifies joint mass,

stiffness and damping coefficient matrices. Since the numerical problems existed in the final linear equation for the solution of joint parameters, two different algorithms are developed and the robustness is examined by numerical investigations.

In Chapter 3, neural networks are used to identify appropriate equivalent joint parameters. The application of neural networks to joint parameter identification is a new development to the subject. This method is proposed due to the consideration that neural networks have a good reputation in mapping nonlinear relationships between input and output. After a network is properly trained, it possesses very good generality and tolerance to input noise. Two relevant techniques used to prepare training sets for the networks, the parametric families of finite element models and principal element analysis, are also introduced in this chapter.

Chapter 4 addresses the classical component modal synthesis (CMS) method with developments for adding joint between the assembled components. This basically is a computation-based method; e.g. component modal properties are obtained from its finite element model. An inherent problem, the out-of-range modes residual effects on the analysis results is discussed and a residual attachment mode method is introduced to accommodate the problem.

Chapter 5 introduces the general joint description method (GJDM), which is newly developed in this area and extends the conventional existing FRF coupling analysis procedure to a more sophisticated level by including joints between the substructures. The principle of the method, an algorithm to implement the method and case studies to verify the method are provided.

Two relevant issues in joint modelling and substructure coupling are also systematically discussed in this thesis. They are in Chapter 6, non-linearity considerations in joint modelling and substructure coupling, and in Chapter 7, the impact of rotational degrees of freedom (RDOFs) information in the analysis. The former chapter reviews over 40 publications which represent the progress of research on friction modelling and nonlinear properties of structural

joints. The importance of nonlinear joint modelling is then discussed according to the review and some experiences in experiment. A strategy to deal with non-linearity in FRF coupling analysis is also discussed. The latter chapter indicates the consequence of the absence of the RDOF-related information in both LSM based joint parameter identification and FRF coupling analysis. The RDOF-related FRFs play an important role in both of the applications.

Major conclusions drawn from the research are summarised in Chapter 8, the last chapter. Detailed mathematical derivations arising from different parts of the research are left to Appendix A through E.

CHAPTER 2

LINEAR JOINT MODELLING – LEAST SQUARES METHOD

2.1. INTRODUCTION AND OBJECTIVES

Joint modelling plays a critical role in practical coupled structure analysis. Standard coupling methods are based on the assumption that substructures are coupled with perfect joints, *i.e.* rigid connections in spatial coordinates. This assumption can be far from the truth in some of the real-world situations where structures are coupled with bolts, rivets, glue or welds. On the other hand, the study of joint modelling or joint parameter identification has been developed independently in the areas of FE model updating and vibration control. It is expected that the combination of standard coupling methods and joint modelling methods will produce more practical and more accurate solutions for the analysis of coupled structures.

Studies on joint modelling have been carrying out since it was realised that the determination of joint parameters is critical to the analysis of assembled structures, in both static and dynamic respects. A review of the studies on linear joint modelling has been made in the first chapter of this thesis. Of the methods reviewed the direct method for joint parameter identification developed by Wang and Liou [WaLi90] [WaLi91] has the advantage of being simple and free of factitious error by using the measured FRFs. The interface displacement vectors of the coupling substructures are related to the interface force vector by a transfer function. It is this transfer function that describes joint properties in a diagonal impedance matrix, *i.e.* it corresponds to the point-wise connections as shown in Fig.2.1. This joint model has two drawbacks: the specific form of transfer function and the requirement of measurement at coupling DOFs of the assembled structure. These two disadvantages confine the application of this method.

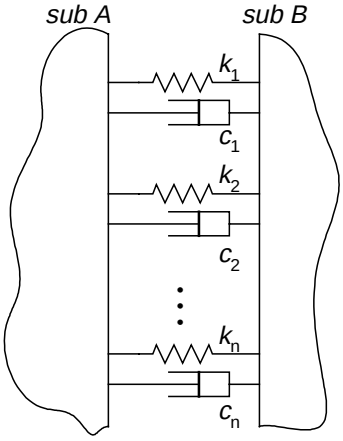

Fig. 2.1 A linear joint model

The linear joint model presented by Ren [Ren92] is more general. The transfer function which relates the interface displacement vectors of substructures to the interface force vector is a symmetric impedance matrix. This joint impedance matrix, $\mathbf{Z}$, consists of all possible physical parameters of the joints such as $\mathbf{K}$, $\mathbf{M}$, $\mathbf{C}$ and $\mathbf{D}$. There are also more choices for the measurement DOFs in Ren's method. If the coupling DOFs in the assembled structure are not accessible, the FRFs measured at other DOFs can be employed instead. Apart from these two

advantages, the conditions of equilibrium and compatibility are the same in both methods. A problem of Ren's method is that the coefficient matrix is often being ill-conditioned and the solutions obtained using least-squares method are then sensitive to the noise in measured FRFs.

In this chapter, a general method for the identification of linear joint parameters using measured FRFs is presented based on Wang's and Ren's methods. The development of this general method and the improvement of its constituent algorithms are reported.

The objectives of the work in this chapter are:

- deriving the mathematical expressions of the identification method;
- providing numerical simulations to validate the developed method;
- investigating the robustness of the method, which includes noise simulation in FRFs and error propagation analysis in the procedure of solution;
- refining the method by suggesting a proper usage.

2.2. THEORETICAL BACKGROUND

2.2.1. Definition of Joint

A set of substructures, substructure A and B, which have not been assembled, are shown in Fig. 2.2, where the joint is considered as a collection of the connections between substructure A and B. The coupled system is shown in Fig. 2.3.

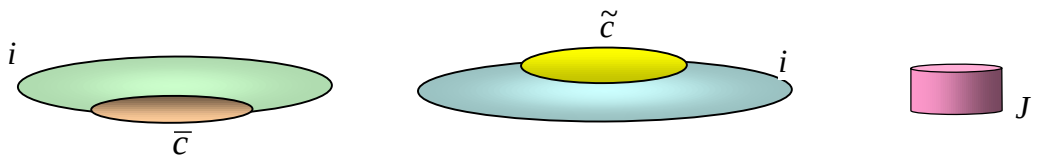

Fig. 2.2 Collected substructures and joint

To distinguish the status of expressions before and after coupling, we use lower case letters to denote the uncoupled system and use upper case letters for the coupled system. In the uncoupled substructures, the DOFs related with the connections are called "coupling DOFs" and are denoted by the subscript *c*, and those DOFs not related with the connections are called "internal DOFs" and are denoted by the subscript *i*.

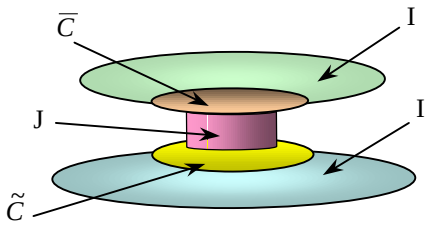

Fig. 2.3 The coupled system

In the coupled system, the coupling DOFs are denoted by *C* and the internal DOFs are denoted by *I*.

The joint has no internal DOFs. All its DOFs are coupling DOFs connecting substructure A and substructure B.

2.2.2. Conditions of Compatibility and Equilibrium

The conditions of compatibility and equilibrium must be satisfied at the coupling coordinates in the coupled structure. Therefore, the condition of equilibrium should be expressed as

$$\mathbf{F}_C = \mathbf{f}_c + \mathbf{f} \tag{2.1}$$

The force vector of the assembled structure equals the vector summation of the force vector of substructures and joint. Partitioning these force vectors according to substructure A (subscripts with –) and substructure B (subscripts with ~), we have

$$\begin{Bmatrix} \mathbf{F}_{\bar{C}} \\ \mathbf{F}_{\tilde{C}} \end{Bmatrix} = \begin{Bmatrix} \mathbf{f}_{\bar{c}} \\ \mathbf{f}_{\tilde{c}} \end{Bmatrix} + \begin{Bmatrix} \bar{\mathbf{f}} \\ \tilde{\mathbf{f}} \end{Bmatrix} \tag{2.2}$$

The condition of compatibility is

$$\mathbf{X}_C = \mathbf{x}_c = \mathbf{x} \tag{2.3}$$

which means that at the coupling DOFs the displacement vector of the assembled structure is equal to the displacement vector of the substructures and the displacement vector of the joint. Similar to equation (2.2), the partitioned form of the condition of compatibility is then

$$\begin{Bmatrix} \mathbf{X}_{\bar{C}} \\ \mathbf{X}_{\tilde{C}} \end{Bmatrix} = \begin{Bmatrix} \mathbf{x}_{\bar{c}} \\ \mathbf{x}_{\tilde{c}} \end{Bmatrix} = \begin{Bmatrix} \bar{\mathbf{x}} \\ \tilde{\mathbf{x}} \end{Bmatrix} \tag{2.4}$$

2.2.3. Essential Equations

Considering the coupled system, the relationship between the displacements and the forces is built up via the system receptance matrix:

$$\begin{Bmatrix} \mathbf{X}_I \\ \mathbf{X}_C \end{Bmatrix} = \begin{bmatrix} \mathbf{H}_{II} & \mathbf{H}_{IC} \\ \mathbf{H}_{CI} & \mathbf{H}_{CC} \end{bmatrix} \begin{Bmatrix} \mathbf{F}_I \\ \mathbf{F}_C \end{Bmatrix} \tag{2.5}$$

For any of the substructures, the relationship between the displacements and the forces is then:

$$\begin{Bmatrix} \mathbf{x}_i \\ \mathbf{x}_c \end{Bmatrix} = \begin{bmatrix} \mathbf{H}_{ii} & \mathbf{H}_{ic} \\ \mathbf{H}_{ci} & \mathbf{H}_{cc} \end{bmatrix} \begin{Bmatrix} \mathbf{f}_i \\ \mathbf{f}_c \end{Bmatrix} \tag{2.6}$$

Also, the joint is described as:

$$\mathbf{Z}\mathbf{x} = \mathbf{f} \tag{2.7}$$

Forces and displacements of the internal coordinates keep no change before and after coupling. Hence,

$$\mathbf{F}_I \equiv \mathbf{f}_i \tag{2.8}$$

$$\mathbf{X}_I \equiv \mathbf{x}_i \tag{2.9}$$

Substituting equations (2.1), (2.3), (2.6) and (2.8) into (2.7), we obtain

$$\mathbf{f}_c = \left[\mathbf{I} + \mathbf{Z}\mathbf{H}_{cc}\right]^{-1}\left(\mathbf{F}_C - \mathbf{Z}\mathbf{H}_{ci}\mathbf{F}_I\right) \tag{2.10}$$

Substituting equations (2.3), (2.9) and (2.10) into (2.6), leads to

$$\begin{Bmatrix} \mathbf{X}_I \\ \mathbf{X}_C \end{Bmatrix} = \begin{bmatrix} \mathbf{H}_{ii} - \mathbf{H}_{ic}\left(\mathbf{I} + \mathbf{Z}\mathbf{H}_{cc}\right)^{-1}\mathbf{Z}\mathbf{H}_{ci} & \mathbf{H}_{ic}\left(\mathbf{I} + \mathbf{Z}\mathbf{H}_{cc}\right)^{-1} \\ \mathbf{H}_{ci} - \mathbf{H}_{cc}\left(\mathbf{I} + \mathbf{Z}\mathbf{H}_{cc}\right)^{-1}\mathbf{Z}\mathbf{H}_{ci} & \mathbf{H}_{cc}\left(\mathbf{I} + \mathbf{Z}\mathbf{H}_{cc}\right)^{-1} \end{bmatrix} \begin{Bmatrix} \mathbf{F}_I \\ \mathbf{F}_C \end{Bmatrix} \tag{2.11}$$

Comparing equation (2.11) with equation (2.5), the sub-matrices of the receptance matrix of the coupled system can be obtained in terms of frequency response sub-matrices of the substructures and the impedance matrix of joint as follows:

$$\begin{aligned}
\mathbf{H}_{II} &= \mathbf{H}_{ii} - \mathbf{H}_{ic}\left(\mathbf{I} + \mathbf{Z}\mathbf{H}_{cc}\right)^{-1}\mathbf{Z}\mathbf{H}_{ci} \\
\mathbf{H}_{CI} &= \mathbf{H}_{ci} - \mathbf{H}_{cc}\left(\mathbf{I} + \mathbf{Z}\mathbf{H}_{cc}\right)^{-1}\mathbf{Z}\mathbf{H}_{ci} \\
\mathbf{H}_{IC} &= \mathbf{H}_{ic}\left(\mathbf{I} + \mathbf{Z}\mathbf{H}_{cc}\right)^{-1} \\
\mathbf{H}_{CC} &= \mathbf{H}_{cc}\left(\mathbf{I} + \mathbf{Z}\mathbf{H}_{cc}\right)^{-1}
\end{aligned} \tag{2.12}$$

Substituting the third equation in (2.12) into the first one, and substituting the fourth equation in (2.12) into the second one then rearranging the first and the second equations, we have

$$\begin{aligned}
\mathbf{H}_{IC}\,\mathbf{Z}\,\mathbf{H}_{ci} &= \mathbf{H}_{ii} - \mathbf{H}_{II} \\
\mathbf{H}_{CC}\,\mathbf{Z}\,\mathbf{H}_{ci} &= \mathbf{H}_{ci} - \mathbf{H}_{CI}
\end{aligned} \tag{2.13}$$

Also, rearranging the third and the fourth equations in (2.12), we have

$$\begin{aligned}
\mathbf{H}_{IC}\,\mathbf{Z}\,\mathbf{H}_{cc} &= \mathbf{H}_{ic} - \mathbf{H}_{IC} \\
\mathbf{H}_{CC}\,\mathbf{Z}\,\mathbf{H}_{cc} &= \mathbf{H}_{cc} - \mathbf{H}_{CC}
\end{aligned} \tag{2.14}$$

Equations (2.13) and (2.14) are the basic formulae which can be used to identify the joint impedance matrix, $\mathbf{Z}$.

2.2.4. Discussion on the Applicability

The two formulae in equation (2.13) and the other two in (2.14) provide alternative ways to use FRF data for the identification of joint parameters. When FRFs at the coupling DOFs of the assembled structure**,** $\mathbf{H}_{CC}$**,** are difficult to measure because of accessibility, the FRF matrix $\mathbf{H}_{IC}$ can be measured instead and the first formulae in (2.13) and (2.14) shall be used in the identification. From this point of view, the first equations in (2.13) and (2.14) are recommended rather than the second ones.

Furthermore, in order to avoid the problem of measurement accessibility, a method which does not need FRFs related to the coupling DOFs of the coupled

system at all, can be derived from the expression for $\mathbf{H}_{II}$, one of the frequency response function sub-matrices of the coupled system in (2.12). Since

$$\mathbf{I} + \mathbf{Z}\mathbf{H}_{cc} = \mathbf{Z}\left(\mathbf{Z}^{-1} + \mathbf{H}_{cc}\right) \tag{2.15}$$

$$\left(\mathbf{I} + \mathbf{Z}\mathbf{H}_{cc}\right)^{-1} = \left(\mathbf{Z}^{-1} + \mathbf{H}_{cc}\right)^{-1}\mathbf{Z}^{-1} \tag{2.16}$$

in which $\mathbf{Z}$ has to be non-singular, we have

$$\mathbf{H}_{II} = \mathbf{H}_{ii} - \mathbf{H}_{ic}\left(\mathbf{Z}^{-1} + \mathbf{H}_{cc}\right)^{-1}\mathbf{H}_{ci} \tag{2.17}$$

$$\mathbf{Z}^{-1} = \mathbf{H}_{ci}\left(\mathbf{H}_{ii} - \mathbf{H}_{II}\right)^{-1}\mathbf{H}_{ic} - \mathbf{H}_{cc} \tag{2.18}$$

The trade-off of this method is that one more inversion is introduced, which reduces the efficiency and accuracy of the solution and makes the method sensitive to measurement errors and to other factors that affect the condition of the FRF matrix.

Once the impedance matrix $\mathbf{Z}$ is obtained, the physical parameters of joint can be calculated according to the definition of impedance matrix:

$$\mathbf{Z}(\omega) = \mathbf{K} - \omega^2\mathbf{M} + i\left(\omega\,\mathbf{C} + \mathbf{D}\right) \tag{2.19}$$

where $\mathbf{K}$, $\mathbf{M}$, $\mathbf{C}$ and $\mathbf{D}$ are the joint matrices of stiffness, mass, viscous damping and structural damping coefficients.

2.3. ALGORITHM FOR SOLVING JOINT PARAMETERS

The implementation of the methods for joint parameter identification mentioned in the preceding section of theoretical background are discussed here. Two algorithms are proposed for computation of the required parameters, $\mathbf{M}$, $\mathbf{K}$, $\mathbf{C}$ and $\mathbf{D}$. First, the general version of the basic equations (2.13) and (2.14) are derived.

2.3.1. Derivation of the Linear Equations for Joint Parameter Identification

According to equations (2.13) and (2.14), the expressions for the impedance matrix, $\mathbf{Z}$, have the generalised form of

$$\mathbf{H}^{a}_{L\times n_c}\mathbf{Z}_{n_c\times n_c}\mathbf{H}^{b}_{n_c\times L}=\mathbf{H}^{c}_{L\times L} \tag{2.20}$$

For instance, if the first equation in (2.13) is employed, we have

$$\begin{aligned}\mathbf{H}^{a}&=\mathbf{H}_{IC}\\ \mathbf{H}^{b}&=\mathbf{H}_{ci}\\ \mathbf{H}^{c}&=\mathbf{H}_{ii}-\mathbf{H}_{II}\end{aligned} \tag{2.21}$$

One of the elements of equation (2.20) has the expression of

$$\sum_{q=1}^{n_c}\sum_{p=1}^{n_c}H^{a}_{kp}\mathsf{Z}_{pq}H^{b}_{ql}=H^{c}_{kl}\ \text{ where }\ k=1,2,\ldots,L\ \text{ and }\ l=1,2,\ldots,L \tag{2.22}$$

Rewriting equation (2.20) in the form of a standard set of linear equations as

$$\tilde{\mathbf{A}}\mathbf{v}=\mathbf{b} \tag{2.23}$$

we have the relationship among the elements of the matrices in equation (2.20) and the matrix and vectors in (2.23) as follows

$$\tilde{A}_{pq}=H^{a}_{ki}H^{b}_{jl} \tag{2.24}$$

$$v_q=\mathsf{Z}_{ij} \tag{2.25}$$

$$b_p=H^{c}_{kl} \tag{2.26}$$

The relationships among the subscripts are:

$$p = (k-1)L + l \qquad q = (i-1)n_c + j \tag{2.27}$$

and the variation ranges of these subscripts are:

$$k = 1,2,\ldots,L \quad i = 1,2,\ldots,n_c \quad j = 1,2,\ldots,n_c \quad l = 1,2,\ldots,L \tag{2.28}$$

These expressions, from equation (2.24) to (2.28), can be verified by examining one of the elements in vector **b** of (2.23):

$$b_p = \sum_{q=1}^{n_c^2} \tilde{A}_{pq} v_q \tag{2.29}$$

Substituting equations (2.24) and (2.25) into (2.29), splitting summation variable q to i and j and noticing that when q varies from *1* to n_c^2, i and j both vary from *1* to n_c, therefore,

$$b_p = \sum_{i=1}^{n_c} \sum_{j=1}^{n_c} \left(H_{ki}^a H_{jl}^b \right) Z_{ij} \tag{2.30}$$

Equation (2.30) is exactly the same as equation (2.22).

In fact, matrix $\tilde{\mathbf{A}}$ is the *Kronecker production* of matrix $\mathbf{H}^a$ and matrix $\mathbf{H}^b$,

$$\tilde{\mathbf{A}} = \mathbf{H}^a \otimes \mathbf{H}^b \tag{2.31}$$

and it is square if the first equation in (2.13) or the second equation in (2.14) is imposed.

When the dynamic stiffness of the joint structure is expressed as

$$\mathbf{Z}(\omega)_{n_c \times n_c} = \mathbf{K} - \omega^2 \mathbf{M} + (i\omega \mathbf{C} + \mathbf{D}) \tag{2.32}$$

its vector form should be

$$\mathbf{z}(\omega)_{n_c^2 \times 1} = \mathbf{k} - \omega^2 \mathbf{m} + i(\omega \mathbf{c} + \mathbf{d}) = \mathbf{T}(\omega)\mathbf{x} \tag{2.33}$$

where the transformation matrix, $\mathbf{T}(\omega)$, has the form

$$\mathbf{T}(\omega)_{n_c^2 \times 4n_c^2} = \begin{bmatrix} \mathbf{I} & -\omega^2 \mathbf{I} & i\omega \mathbf{I} & i\,\mathbf{I} \end{bmatrix} \tag{2.34}$$

and the unknown joint parameter vector is

$$\mathbf{x}_{4n_c^2\times 1} = \begin{Bmatrix} \mathbf{k} \\ \mathbf{m} \\ \mathbf{c} \\ \mathbf{d} \end{Bmatrix} \tag{2.35}$$

Substituting (2.33) into (2.23) leads to

$$\tilde{\mathbf{A}}(\omega)\mathbf{T}(\omega)\mathbf{x} = \mathbf{b}(\omega) \tag{2.36}$$

Let

$$\mathbf{A}(\omega)_{KL\times 4n_c^2} = \tilde{\mathbf{A}}(\omega)\mathbf{T}(\omega) \tag{2.37}$$

then (2.36) becomes

$$\mathbf{A}(\omega)\mathbf{x} = \mathbf{b}(\omega) \tag{2.38}$$

This is the set of simultaneous linear equations describing the unknown joint parameters. The algorithms to solve (2.38) will be presented next.

2.3.2. Non-partitioned Algorithm

The matrix $\mathbf{A}(\omega)$ and the vector $\mathbf{b}(\omega)$ in (2.38) are generally complex as

$$\begin{aligned} \mathbf{A}(\omega) &= \mathrm{Re}\,\mathbf{A}(\omega) + i\,\mathrm{Im}\,\mathbf{A}(\omega) \\ \mathbf{b}(\omega) &= \mathrm{Re}\,\mathbf{b}(\omega) + i\,\mathrm{Im}\,\mathbf{b}(\omega) \end{aligned} \tag{2.39}$$

Equation (2.39) can be rearranged as follows:

$$\overline{\mathbf{A}}(\omega)\mathbf{x} = \overline{\mathbf{b}}(\omega) \tag{2.40}$$

where

$$\overline{\mathbf{A}}(\omega) = \begin{bmatrix} \mathrm{Re}\,\mathbf{A}(\omega) \\ \mathrm{Im}\,\mathbf{A}(\omega) \end{bmatrix};\ \overline{\mathbf{b}}(\omega) = \begin{Bmatrix} \mathrm{Re}\,\mathbf{b}(\omega) \\ \mathrm{Im}\,\mathbf{b}(\omega) \end{Bmatrix} \tag{2.41}$$

If the number of frequency points involved is n_f, then

$$\overline{\mathbf{A}}(\omega) = \begin{bmatrix} \mathrm{Re}\,\mathbf{A}(\omega_1) \\ \mathrm{Im}\,\mathbf{A}(\omega_1) \\ \vdots \\ \mathrm{Re}\,\mathbf{A}(\omega_{n_f}) \\ \mathrm{Im}\,\mathbf{A}(\omega_{n_f}) \end{bmatrix}_{2n_fL^2\times 3n_c^2} \quad \text{and} \quad \overline{\mathbf{b}}(\omega) = \begin{bmatrix} \mathrm{Re}\,\mathbf{b}(\omega_1) \\ \mathrm{Im}\,\mathbf{b}(\omega_1) \\ \vdots \\ \mathrm{Re}\,\mathbf{b}(\omega_{n_f}) \\ \mathrm{Im}\,\mathbf{b}(\omega_{n_f}) \end{bmatrix}_{2n_fL^2\times 1} \tag{2.42}$$

Equation (2.40) also has its separated form as

$$\overline{\mathbf{A}}_R(\omega)\mathbf{x} = \overline{\mathbf{b}}_R(\omega) \tag{2.43}$$

$$\overline{\mathbf{A}}_I(\omega)\mathbf{x} = \overline{\mathbf{b}}_I(\omega) \tag{2.44}$$

where

$$\overline{\mathbf{A}}_R(\omega) = \begin{bmatrix} \mathrm{Re}\,\mathbf{A}(\omega_1) \\ \mathrm{Re}\,\mathbf{A}(\omega_2) \\ \vdots \\ \mathrm{Re}\,\mathbf{A}(\omega_{n_f}) \end{bmatrix}_{n_f L^2 \times 3n_c^2}, \quad \overline{\mathbf{b}}_R(\omega) = \begin{bmatrix} \mathrm{Re}\,\mathbf{b}(\omega_1) \\ \mathrm{Re}\,\mathbf{b}(\omega_2) \\ \vdots \\ \mathrm{Re}\,\mathbf{b}(\omega_{n_f}) \end{bmatrix}_{n_f L^2 \times 1} \tag{2.45}$$

and

$$\overline{\mathbf{A}}_I(\omega) = \begin{bmatrix} \mathrm{Im}\,\mathbf{A}(\omega_1) \\ \mathrm{Im}\,\mathbf{A}(\omega_2) \\ \vdots \\ \mathrm{Im}\,\mathbf{A}(\omega_{n_f}) \end{bmatrix}_{n_f L^2 \times 3n_c^2}, \quad \overline{\mathbf{b}}_I(\omega) = \begin{bmatrix} \mathrm{Im}\,\mathbf{b}(\omega_1) \\ \mathrm{Im}\,\mathbf{b}(\omega_2) \\ \vdots \\ \mathrm{Im}\,\mathbf{b}(\omega_{n_f}) \end{bmatrix}_{n_f L^2 \times 1} \tag{2.46}$$

The non-partitioning algorithm (NPA) solves equation (2.40), or its separated form (2.43) or (2.44), for all frequency points concerned using a least squares method (LSM) to find a real vector $\mathbf{x}$ which minimises the euclidean length of $\overline{\mathbf{A}}(\omega)\mathbf{x} - \overline{\mathbf{b}}(\omega)$.

For the convenience of description, we let $m = 2n_f L^2$ and $n = 3n_c^2$ so that $\overline{\mathbf{A}}$ is a matrix of $m \times n$. Suppose that $\overline{\mathbf{A}}$ is a matrix of rank *k*, the singular value decomposition of $\overline{\mathbf{A}}$ is expressed as:

$$\overline{\mathbf{A}} = \mathbf{U}\mathbf{S}\mathbf{V}^T \tag{2.47}$$

where $\mathbf{U}$ is an $m \times m$ matrix and $\mathbf{V}$ is an $n \times n$ orthogonal matrix, $\mathbf{S}$ is an $m \times n$ matrix of the form

$$\mathbf{S} = \begin{bmatrix} \mathbf{S}_{11} & \mathbf{0} \\ \mathbf{0} & \mathbf{0} \end{bmatrix} \tag{2.48}$$

where $\mathbf{S}_{11}$ is a diagnal matrix which has *k* non-zero singular values.

Define the vector, $\mathbf{g}$, as:

$$\mathbf{U}^T\overline{\mathbf{b}} = \mathbf{g} = \begin{Bmatrix} \mathbf{g}_1 \\ \mathbf{g}_2 \end{Bmatrix} \begin{matrix} \}k \\ \}\, m-k \end{matrix} \tag{2.49}$$

and introduce the new variable, $\mathbf{y}$:

$$\mathbf{V}^T\mathbf{x} = \mathbf{y} = \begin{Bmatrix} \mathbf{y}_1 \\ \mathbf{y}_2 \end{Bmatrix} \begin{matrix} \}k \\ \}\, n-k \end{matrix} \tag{2.50}$$

Now, define $\tilde{\mathbf{y}}_1$ to be the unique solution of

$$\mathbf{S}_{11}\mathbf{y}_1 = \mathbf{g}_1 \tag{2.51}$$

Then all solutions to the problem of minimising $\left\|\overline{\mathbf{A}}\mathbf{x} - \overline{\mathbf{b}}\right\|$ are of the form

$$\hat{\mathbf{x}} = \mathbf{V}\begin{Bmatrix} \tilde{\mathbf{y}}_1 \\ \mathbf{y}_2 \end{Bmatrix} \tag{2.52}$$

where $\mathbf{y}_2$ is arbitrary.

Any such $\hat{\mathbf{x}}$ gives rise to the same residual vector, **r,** satisfying

$$\mathbf{r} = \overline{\mathbf{b}} - \overline{\mathbf{A}}\hat{\mathbf{x}} = \mathbf{U}\begin{Bmatrix} \mathbf{0} \\ \mathbf{g}_2 \end{Bmatrix} \tag{2.53}$$

The norm of **r** satisfies

$$\left\|\mathbf{r}\right\| = \left\|\overline{\mathbf{b}} - \overline{\mathbf{A}}\hat{\mathbf{x}}\right\| = \left\|\mathbf{g}_2\right\| \tag{2.54}$$

The unique solution of minimum length is

$$\tilde{\tilde{\mathbf{x}}} = \mathbf{V}\begin{Bmatrix} \tilde{\mathbf{y}}_1 \\ \mathbf{0} \end{Bmatrix} \tag{2.55}$$

Notice that the solution of minimum length, the set of all solutions, and the minimum values, for the problem of minimising $\left\|\overline{\mathbf{A}}\mathbf{x} - \overline{\mathbf{b}}\right\|$, are all unique; they do not depend on the particular orthogonal decomposition.

In the cases of full rank, where $k = n$, the unique solution is simply as

$$\hat{\mathbf{x}} = \mathbf{V}\,\tilde{\mathbf{y}}_1 \tag{2.56}$$

2.3.3. Partitioned Algorithm

The partitioning algorithm (PA) partitions the equations according to two different frequency points, ω_i and ω_j. Let

$$\mathbf{A}(\omega) = \begin{bmatrix} \tilde{\mathbf{A}}(\omega_i) & \vdots & -\omega_i^2\tilde{\mathbf{A}}(\omega_i) & \vdots & i\omega_i\tilde{\mathbf{A}}(\omega_i) \\ \cdots & \cdots & \cdots & \cdots & \cdots \\ \tilde{\mathbf{A}}(\omega_j) & \vdots & -\omega_j^2\tilde{\mathbf{A}}(\omega_j) & \vdots & i\omega_j\tilde{\mathbf{A}}(\omega_j) \end{bmatrix} \tag{2.57}$$

$$\mathbf{x} = \begin{Bmatrix} \mathbf{k} \\ \cdots \\ \mathbf{m} \\ \cdots \\ \mathbf{c} \end{Bmatrix} \text{ and } \mathbf{b}(\omega) = \begin{Bmatrix} \mathbf{b}(\omega_i) \\ \cdots \\ \mathbf{b}(\omega_j) \end{Bmatrix} \tag{2.58}$$

where $\omega_i < \omega_j$. Equation (2.38) can be partitioned into

$$\tilde{\mathbf{A}}(\omega_i)\mathbf{k} - \omega_i^2\tilde{\mathbf{A}}(\omega_i)\mathbf{m} + i\omega_i\tilde{\mathbf{A}}(\omega_i)\mathbf{c} = \mathbf{b}(\omega_i) \tag{2.59}$$

$$\tilde{\mathbf{A}}(\omega_j)\mathbf{k} - \omega_j^2\tilde{\mathbf{A}}(\omega_j)\mathbf{m} + i\omega_j\tilde{\mathbf{A}}(\omega_j)\mathbf{c} = \mathbf{b}(\omega_j) \tag{2.60}$$

Pre-multiplying (2.59) with $\tilde{\mathbf{A}}(\omega_i)^+$ and pre-multiplying (2.60) with $\tilde{\mathbf{A}}(\omega_j)^+$, we have

$$\mathbf{k} - \omega_i^2\,\mathbf{m} + i\omega_i\,\mathbf{c} = \tilde{\mathbf{A}}(\omega_i)^+\mathbf{b}(\omega_i) \tag{2.61}$$

$$\mathbf{k} - \omega_j^2\,\mathbf{m} + i\omega_j\,\mathbf{c} = \tilde{\mathbf{A}}(\omega_j)^+\mathbf{b}(\omega_j) \tag{2.62}$$

Let

$$\mathbf{d}(\omega_i) = \tilde{\mathbf{A}}(\omega_i)^+\mathbf{b}(\omega_i) \tag{2.63}$$

$$\mathbf{d}(\omega_j) = \tilde{\mathbf{A}}(\omega_j)^+\mathbf{b}(\omega_j) \tag{2.64}$$

and remember that the vectors $\mathbf{d}(\omega_i)$ and $\mathbf{d}(\omega_j)$ are complex, so that we have

$$\mathbf{k} - \omega_i^2\mathbf{m} = \mathrm{Re}\,\mathbf{d}(\omega_i) \tag{2.65}$$

$$\mathbf{k} - \omega_j^2 \mathbf{m} = \mathrm{Re}\,\mathbf{d}(\omega_j) \tag{2.66}$$

$$\omega_i \mathbf{c} = \mathrm{Im}\,\mathbf{d}(\omega_i) \tag{2.67}$$

$$\omega_j \mathbf{c} = \mathrm{Im}\,\mathbf{d}(\omega_j) \tag{2.68}$$

The joint parameter vectors are then solved from (2.65) to (2.68):

$$\mathbf{k} = \frac{1}{\omega_j^2 - \omega_i^2}\left(\omega_j^2\,\mathrm{Re}\,\mathbf{d}(\omega_i) - \omega_i^2\,\mathrm{Re}\,\mathbf{d}(\omega_j)\right) \tag{2.69}$$

$$\mathbf{m} = \frac{1}{\omega_j^2 - \omega_i^2}\left(\mathrm{Re}\,\mathbf{d}(\omega_i) - \mathrm{Re}\,\mathbf{d}(\omega_j)\right) \tag{2.70}$$

$$\mathbf{c} = \frac{1}{\omega_i}\mathrm{Im}\,\mathbf{d}(\omega_i) = \frac{1}{\omega_j}\mathrm{Im}\,\mathbf{d}(\omega_j) \tag{2.71}$$

The kernel of the estimation is the computation of the pseudo-inverse of the coefficient matrix, $\tilde{\mathbf{A}}$. It is an $L^2 \times n_c^2$ complex matrix at each frequency, where L stands for the number of measured internal DOFs and n_c stands for the number of coupling DOFs.

The SVD is used in calculating the pseudo-inverse of matrix $\tilde{\mathbf{A}}$, which is required in the partition algorithm (PA). The SVD of matrix $\tilde{\mathbf{A}}$ is

$$\tilde{\mathbf{A}}_{m\times n} = \mathbf{U}_{m\times m}\begin{bmatrix}\mathbf{S}_{n\times n}\\ \mathbf{0}_{(m-n)\times n}\end{bmatrix}_{m\times n}\mathbf{V}^T_{n\times n} \tag{2.72}$$

Set the tolerance of singular value truncation, *tol*:

$$tol = \max(m,n)\cdot\max(\boldsymbol{\sigma})\cdot\varepsilon \tag{2.73}$$

where ε is the machine accuracy (floating point relative accuracy) and $\boldsymbol{\sigma}$ is the singular value vector. For double-precision representation of real numbers, *i.e.* each real number is represented by 16 digits only, $\varepsilon = 2.2204 \times 10^{-16}$. Let r be the number of singular values which are larger than *tol*, then

$$\tilde{\mathbf{A}}^{+}_{n\times m} = \mathbf{V}_{n\times r}\mathbf{S}^{-1}_{r\times r}\mathbf{U}^T_{r\times m} \tag{2.74}$$

2.4. ROBUSTNESS INVESTIGATION OF THE IDENTIFICATION APPROACHES

The linear joint parameter identification method proposed in this chapter offers two algorithms, the partitioning algorithm (PA) and the non-partitioning algorithm (NPA). The robustness of each is to be investigated in this section via numerical simulations and perturbation analysis. An algorithm is robust if it is tolerant of the perturbations in the input data such as rounding errors and measurement noise. In other words, the solution is convergent and to a feasible answer.

2.4.1. Numerical Simulation 1: A Crossbeam Structure

A cross-beam structure shown in Fig. 2.4 is used as an example to illustrate the application of the proposed method. Each substructure is discretised into 10 beam elements. To simplify the simulation, each node of the structure is constrained such that only 2 DOFs are active: one is the translation DOF, z, and the other is rotation DOF, θ_y for substructure A or θ_x for substructure B. In other words, substructures A and B are both planar beams. The joint between the substructures is modelled as a beam element as well. Two internal DOFs are selected from substructure B and the other two from substructure A, *i.e.* $L = 4$.

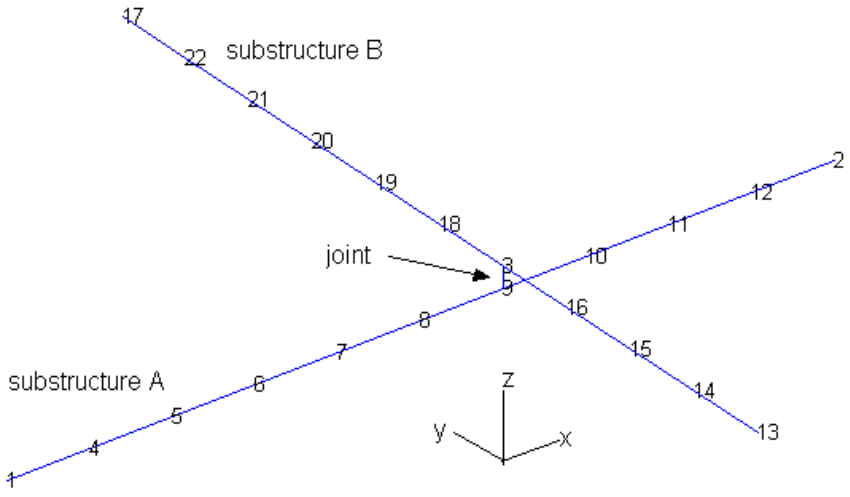

Fig. 2.4 A cross-beam structure

The identified result is represented by an element of the joint stiffness matrix, k_{11}, the axial stiffness of the joint element. The exact value of k_{11} is

$$k_{11} = \frac{EA}{l} = 3.51858 \times 10^9 \text{ N/m}$$

Both the partitioned algorithm (PA) and the non-partitioned algorithm (NPA) are used to identify the joint parameters. The FRFs used in the identification were generated from 1 to 2,000Hz with a frequency increment 1Hz.

The identified results from the PA method with noise-free input FRFs are shown in Fig. 2.5. Since each solution uses two frequency data points only, there are 1,000 solutions available between 1Hz and 2,000Hz. The condition numbers of matrix $\tilde{\mathbf{A}}$ for each solution are also checked. These identification solutions are accurate, which means that the partitioning algorithm works very well in this case. How it works with noise contaminated FRFs will be shown in numerical simulation 2.

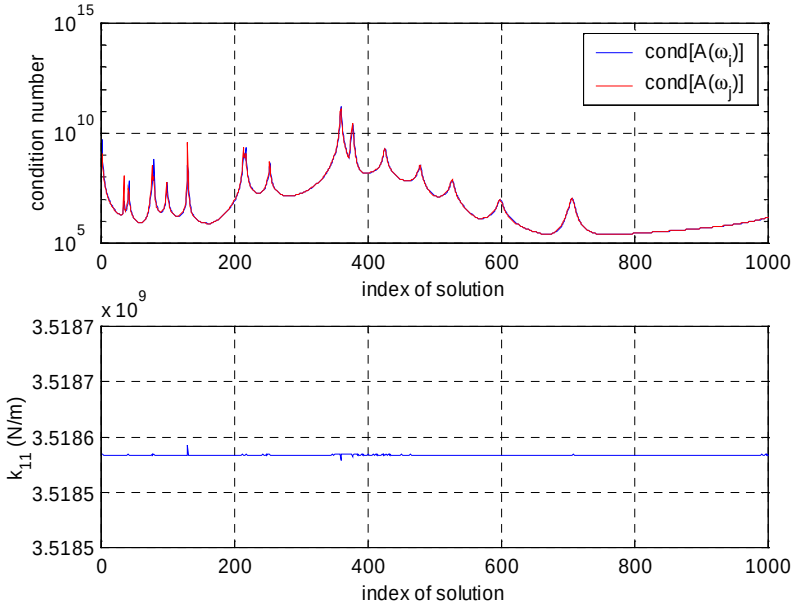

Fig. 2.5 Identified result for the joint in the cross-beam structure - PA solutions

In contrast, the non-partition algorithm (NPA) does not work well in this case. If all 2,000 frequency data points are used in the identification, The matrix $\overline{\mathbf{A}}$ thus formed in (2.42) is rank-deficient and the solution is therefore unreliable.

Considering that the minimum number of frequency points used to form a set of determined equations for the non-partitioning algorithm is 3, we use this minimum number of frequency data, moving the frequencies from low to high values, to produce 666 solutions in the range 1 – 2,000Hz. These identification solutions are shown in Fig. 2.6. Of all the 666 solutions only the first three are close to the design value. They are 3.51859×10^{9}, 3.51855×10^{9} and 3.51852×10^{9} N/m. The first three corresponding $\overline{\mathbf{A}}$ matrices are of full rank but all the rest of the $\overline{\mathbf{A}}$ matrices are rank deficient. The first three solutions cover the frequency range 1 – 9Hz only. Increasing the number of frequency points included gradually in the low frequency range for each NPA solution, we have accurate results until the frequency range covers from 1Hz up to 17Hz. When the 18th and/or higher frequency points are taken into account, matrix $\overline{\mathbf{A}}$ then becomes rank deficient and the results are not correct any more.

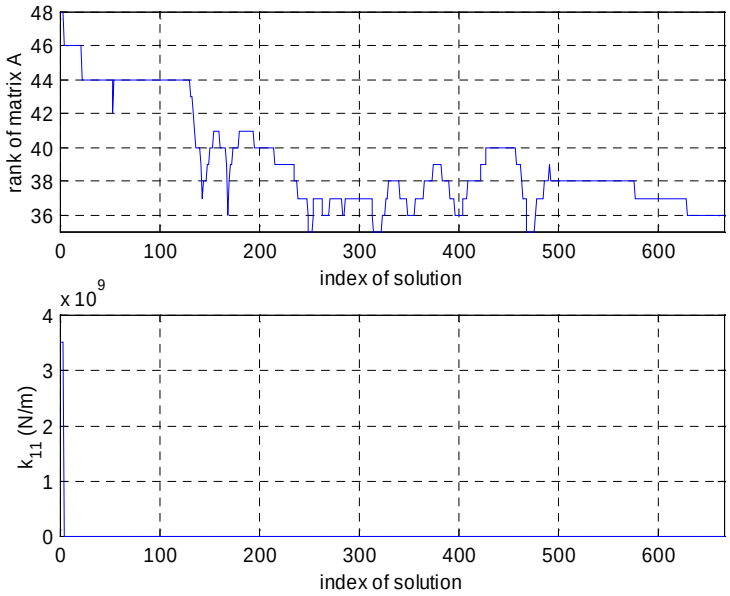

Fig. 2.6 Result for the joint in the cross-beam structure - NPA solutions

This simulation reveals that the partitioning algorithm (PA) improves the condition of the linear equations in a least-squares solution and results in accurate and stable solutions. These solutions are independent of frequency. In addition, the partitioning algorithm is much more efficient than the non-partitioning algorithm because the matrix on which pseudo-inverse is applied is much smaller than that used in non-partitioning algorithm.

2.4.2. Numerical Simulation 2: Two Beams Coupled in Line via a Joint

This second numerical example is firstly designed to validate the proposed method and algorithms, and it is then used for the algorithm robustness investigation – checking how sensitive the algorithms are to data round-off and to noise contamination. First of all, the procedure of the application of the proposed identification approaches is demonstrated.

The structure shown in Fig. 2.7 is a free-free uniform beam. The beam is evenly discretised into 6 elements and each node has two degrees of freedom, y and θ. The 4^{th} element, between nodes 4 and 5, is regarded as the joint. The segment to the left-hand side of the joint is substructure A and the part to the right-hand side of the joint is substructure B.

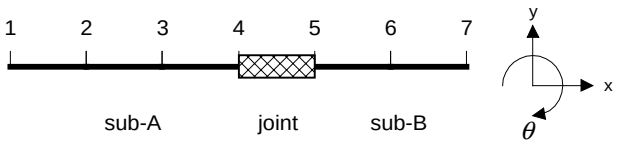

Fig. 2.7 Two-beam substructures coupled via a joint

One of the joint parameters, the lateral stiffness of the joint element, k_{11}, is chosen to represent the identified result. Its design value is

$$\mathsf{k}_{11} = \frac{12EI}{l^3} = 4.320 \times 10^3 \text{ (N/m)}.$$

The y direction translations at nodes 1, 2, 6 and 7 are selected as the internal DOFs. The matrix $\tilde{\mathbf{A}}(\omega_i)$ defined in (2.31) is then 16×16 ($L = n_c = 4$). The required data of frequency response functions are generated by mode superposition using the eigen-solution of the substructures and the assembled finite element model. The frequency range of the generated FRFs is 0 – 1000Hz with an increment of 1Hz. In the simulations for this section, there is no damping in the structure and therefore equation (2.44) is not used.

SOLUTION 1: NPA WITH FRF DATA FROM 0 TO 1,000 HZ

If all the FRF data in the frequency range 1 – 1000Hz are used in one prediction, the answer is accurate. The size of matrix $\overline{\mathbf{A}}$ in (2.40) is $2n_f L^2 \times 3n_c^2 = 32{,}000 \times 48$. If equation (2.43) is used instead of (2.40), the dimension of matrix $\overline{\mathbf{A}}_R$ is $n_f L^2 \times 3n_c^2 = 16{,}000 \times 48$. The equation, either (2.40) or (2.43), formed in this way is heavily over-determined. In other words, there are too many (redundant) equations involved. If only the first 150 frequencies are used in the prediction, the size of $\overline{\mathbf{A}}_R$ is $2{,}400 \times 48$ and the answer is already accurate with $\mathsf{k}_{11} = 4.3200 \times 10^3$. The condition number of matrix $\overline{\mathbf{A}}_R$ is 1.7342×10^9 and its rank is 48.

However, it is not the situation that any segment of frequency data produces the same result. For instance, the solution obtained from data in the frequency range 151 – 1,000Hz is far from accurate. The reason is that the matrix $\overline{\mathbf{A}}$ formed in this frequency range is rank-deficient.

Ten sets of different frequency range data were selected and the results obtained using these data are shown in Table 2.1. The frequency ranges investigated are shown in Fig. 2.8. It is seen from the table that the data in low frequency range play a very important role. The condition number κ of matrix $\overline{\mathbf{A}}_R$ decreases with the increase of data involved in the low frequency range. The data sets which exclude the data below 35Hz make the $\overline{\mathbf{A}}_R$ matrix rank deficient. In addition, the higher the starting frequency, the severer the deficient. The phenomenon presented here may not be a general principle, but it at least poses a question as to over what frequncy range the data should be used in order to guarantee a full rank matrix $\overline{\mathbf{A}}_R$ and a lower condition number?

Table 2.1

index	*freq. range*	k_{11}	κ	*rank*
1	(1,1000)	4.3200×10^3	2.3633×10^9	48
2	(26,1000)	4.3200×10^3	9.0268×10^{10}	48
3	(31,1000)	4.3200×10^3	9.7442×10^{10}	48

4	(34,1000)	4.3200×10^{3}	1.3243×10^{11}	48
5	(35,1000)	2.0423×10^{3}	1.6415×10^{11}	47
6	(36,1000)	2.2511×10^{3}	2.0135×10^{11}	47
7	(41,1000)	2.6414×10^{3}	3.8126×10^{11}	47
8	(51,1000)	5.5141×10^{2}	7.5019×10^{11}	46
9	(101,1000)	4.3367×10^{2}	7.1626×10^{12}	40
10	(151,1000)	2.3307×10^{2}	2.3975×10^{13}	38

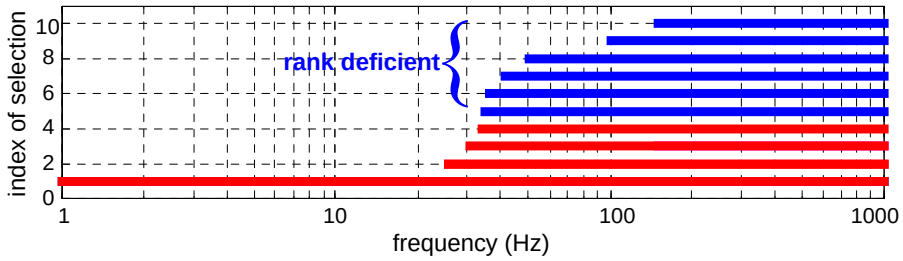

Fig. 2.8 frequency ranges investigated

SOLUTION 2: NPA WITH 3 FREQUENCIES FOR EACH SOLUTION

If three frequencies are used for each solution, the matrix $\overline{\mathbf{A}}_R$ is square,

$$n_f L^2 \times 3n_c^2 = 48\times 48$$

and the set of equations is determined according to (2.43). Selecting three adjacent frequencies each time and moving the selection from low to high frequency, we form 333 $\overline{\mathbf{A}}_R$ matrices and obtain the same number of solutions. The ranks of these

$\overline{\mathbf{A}}_R$ matrices and their corresponding solutions of k_{11} are shown in Fig. 2.9. It is

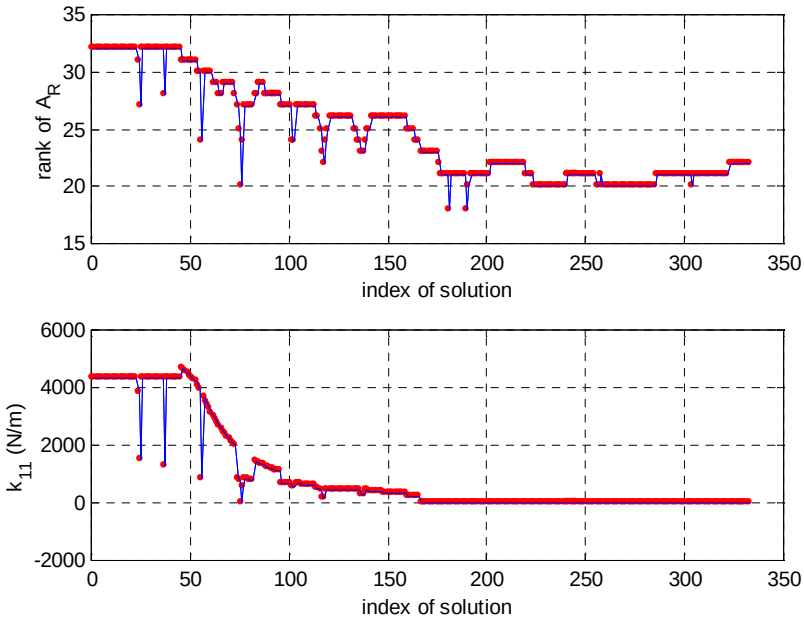

Fig. 2.9 NPA with 3 frequencies for each solution

seen that the correct answers are given within the first 50 solutions. By monitoring $rank(\overline{\mathbf{A}}_R)$ it is clear that it is the rank deficiency of matrix $\overline{\mathbf{A}}_R$ that results in the incorrect answers.

The three-frequency-points moving solution provides an indicator of selecting an appropriate frequency range for the NPA method. Fig. 2.10 shows that data in the frequency range covered by the first 50 solutions, 1 – 150Hz, are applicable for NPA as has been validated in solution 1.

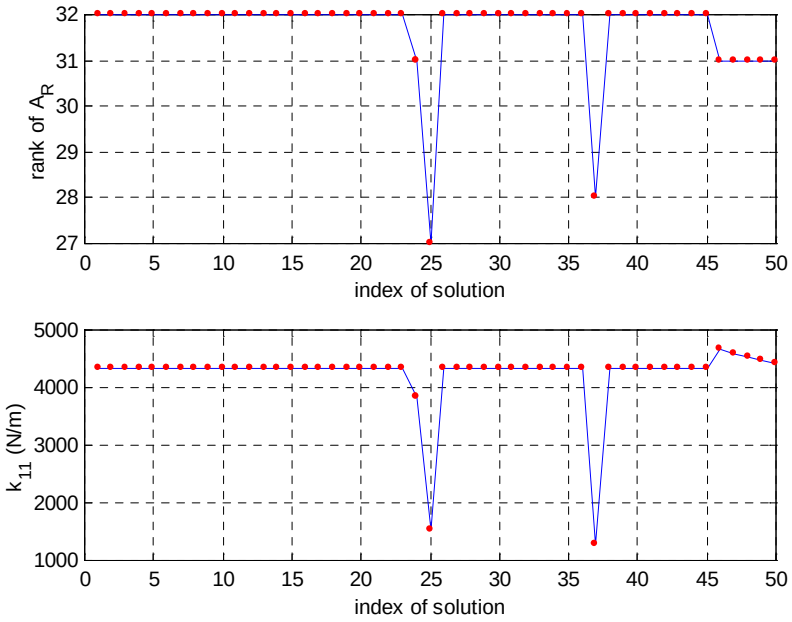

Fig. 2.10 The first 50 solutions

SOLUTION 3: PA THROUGH ALL THE FREQUENCY RANGE

The direct use of partition algorithm (PA) in the frequency range of 1 – 1,000Hz, moving from low frequency to high frequency has 500 solutions. They are shown in Fig. 2.11 with the corresponding condition numbers of matrices $\tilde{\mathbf{A}}(\omega_i)$ and $\tilde{\mathbf{A}}(\omega_j)$.

Matrices $\tilde{\mathbf{A}}(\omega_i)$ and $\tilde{\mathbf{A}}(\omega_j)$ are full-rank in the frequency range of 1 – 1,000Hz for $i = 1,2,\ldots,500$ and $j = 1,2,\ldots,500$. The identified result k_{11} shown in Fig. 2.11 is therefore much better than the result in Fig. 2.9. The first 250 solutions are identically accurate and the errors of the identification in higher frequency range, above 500Hz, are caused by the high condition number of the matrices $\tilde{\mathbf{A}}(\omega_i)$ and $\tilde{\mathbf{A}}(\omega_j)$ at specific narrow frequency bands.

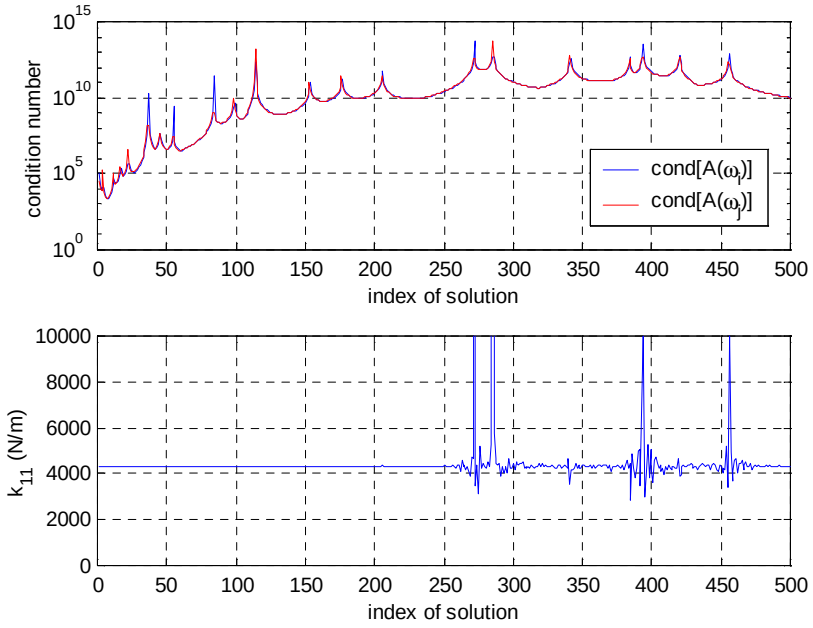

Fig. 2.11 A solution of PA

Compared with matrix $\overline{\mathbf{A}}_R$ in solution 2, matrix $\tilde{\mathbf{A}}$ in PA has no the problem of rank deficiency and also has a much smaller dimension:

$$L^2 \times n_c^2 = 16 \times 16$$

Hence, the time spent in the identification using PA is much less than that using NPA and NPA with three frequencies for each solution. The time spent on each algorithm is listed in Table 2.2.

Table 2.2

Algorithms	NPA(1,1000)	NPA 3-p moving	PA moving
time (*sec.*)	118.91	129.71	34.77

2.4.3. Improvement of the Condition of Matrix $\overline{\mathbf{A}}$

The case study in section 2.4.2 suggests that the high condition number of the matrix $\overline{\mathbf{A}}$ is the reason for the erroneous results. When the PA method was used there, the minimum number of internal DOFs was chosen to make the problem exactly determined. If more internal DOFs are included to form a series of over-determined equations, the condition number of the new $\tilde{\mathbf{A}}$ matrix might be lower. On the other hand, the FE simulation in section 2.4.2 is free of damping. If damping is introduced into the FRF generation, the condition number of $\tilde{\mathbf{A}}$

might be decreased as well. The accuracy of the identified results should be improved if the condition number of the coefficient matrix $\overline{\mathbf{A}}$ becomes smaller.

THE EFFECT OF THE NUMBER OF INTERNAL DOFS

The same structure as used in numerical simulation 2 is studied further in this section. When one more internal DOF is added, say, the *y* direction translations at nodes 1, 2, 3, 6 and 7 are selected as internal DOFs, we have $L = 5 > n_c = 4$ and dimension of matrix $\tilde{\mathbf{A}}$ becomes 25×16 rather than 16×16.

The identified result shown in Fig. 2.12 is substantially improved when compared with the previous result shown in Fig. 2.11 – the largest error here is 0.04% at 910Hz which is at the 4^{th} resonant frequency of substructure B.

Comparing the two plots of the condition number of matrix $\tilde{\mathbf{A}}$ in Fig. 2.11 and 2.12, we notice that the condition of matrix $\tilde{\mathbf{A}}$ has been significantly improved – the condition numbers have been decreased by up to 10^4 times.

This numerical experiment shows the importance of the selection of internal DOFs in joint parameter identification. At this stage, a couple of new questions arise: how many internal DOFs should be used to achieve an acceptable result? and which internal DOFs should be chosen? To answer these questions, several further numerical experiments are carried out.

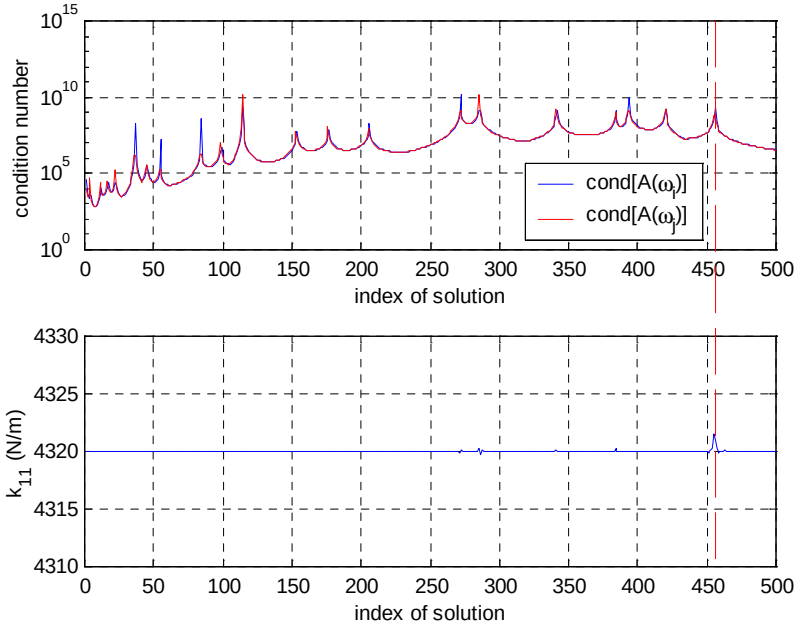

Fig. 2.12 Result of using 5 translation internal DOFs

When 5 rotational DOFs were used at nodes 1, 2, 3, 6 and 7, the identified result is as shown in Fig. 2.13. The largest error is 0.54% at 544Hz, and the corresponding condition number is higher than that found in Fig. 2.12.

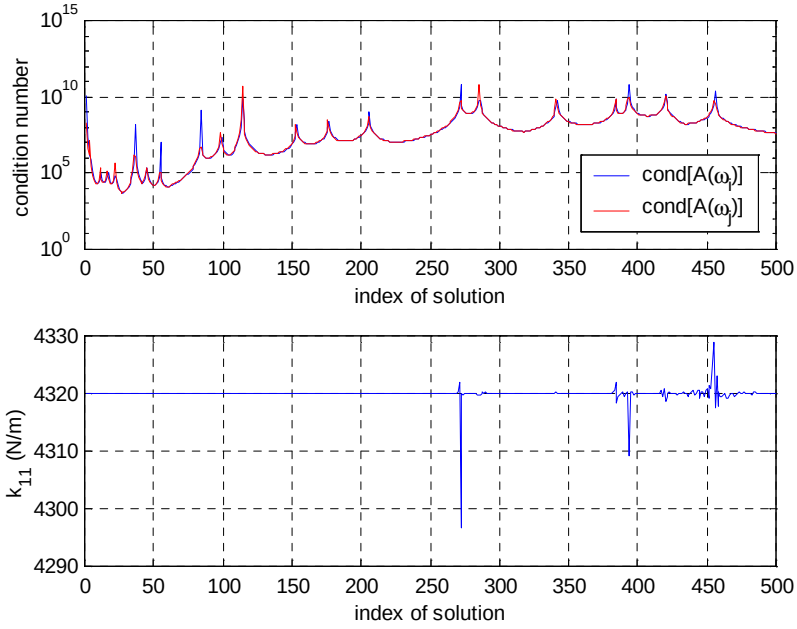

Fig. 2.13 Result of using 5 rotation internal DOFs

When all ten possible internal DOFs are used, the identified result is shown in Fig. 2.14. The dimension of matrix $\tilde{\mathbf{A}}$ is then 100×16. This result is not as good as the result in Fig. 2.12. The largest error in this case is 0.08% at frequency 840Hz.

It seems that there is a best or an optimal choice of the internal DOFs but it is difficult to extrapolate. It is not exactly the case of "the more, the better". From the above simulations, the specific selection of 5 translation DOFs as internal DOFs gives the best results.

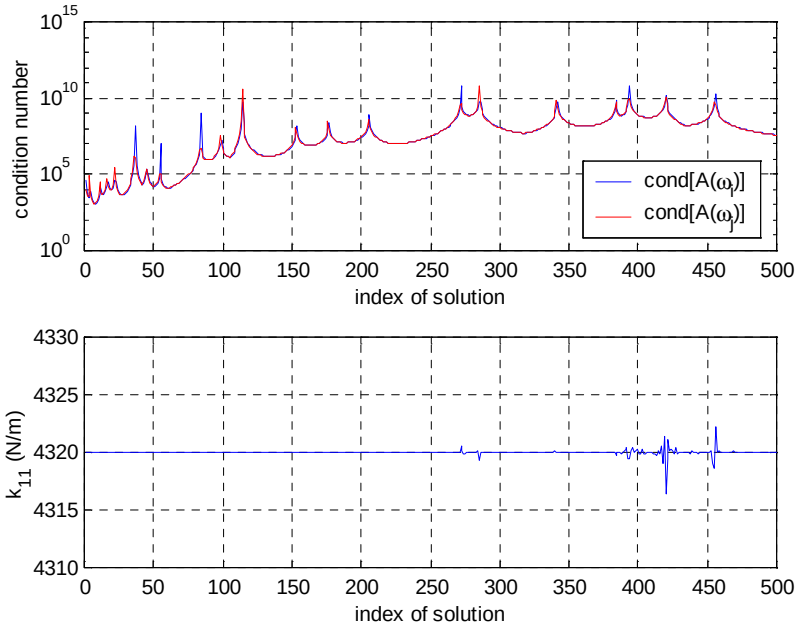

Fig. 2.14 Result of using 10 internal DOFs

THE EFFECT OF DAMPING

It is clear that introducing damping will decrease the amplitudes of the FRFs and hence tend to reduce the condition number of matrix $\tilde{\mathbf{A}}$. In the simulations of the damping effect, proportional damping is introduced to both substructures and their assembly according to the principles mentioned in Appendix C.

Let $\alpha = 0$ and $\beta = 4\times10^{-6}$ in equation (C.1). When 4 translation DOFs are used as internal DOFs, the same condition as in section 2.4.2, solution 3, the

identified result is as shown in Fig. 2.15. When 5 translation DOFs are used as internal DOFs, the identified result is shown in Fig. 2.16.

Comparing Fig. 2.15 with Fig. 2.11 – the 4 internal DOFs case and Fig. 2.16 with Fig. 2.12 – the 5 internal DOFs case, we find that the condition numbers decrease up to 10^2 by introducing the damping and the identified result is significantly improved.

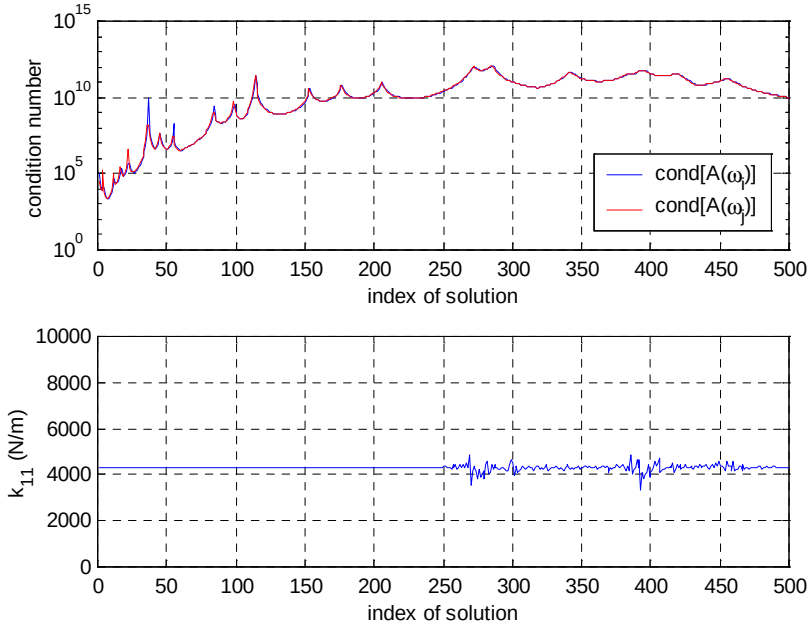

Fig. 2.15 Four translation internal DOFs with damping

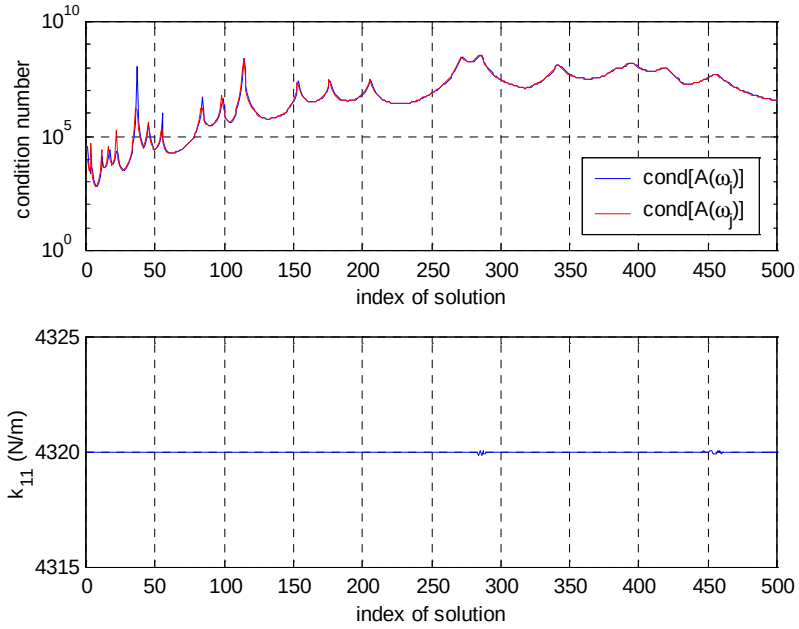

Fig. 2.16 Five translation internal DOFs with damping

2.4.4. Tests with Noise Contaminated Data and Error Analysis

In this section, simulated random noise is added to the generated FRFs to test the robustness of the algorithms. The analysis of noise simulation is given in Appendix D including the definition of noise levels and the theory background of noise simulations.

Considering the structure shown in Fig. 2.7, we apply following two available techniques to decrease the condition number of matrix $\tilde{\mathbf{A}}$: (i) selecting 5 translation DOFs as the internal DOFs; (ii) adding proportional damping ($\alpha = 0, \beta = 4\times10^{-6}$) to the data from the substructures and their assembly. When three different levels of noise are added to all the input FRFs, the identified results obtained using PA are shown in Fig. 2.17.

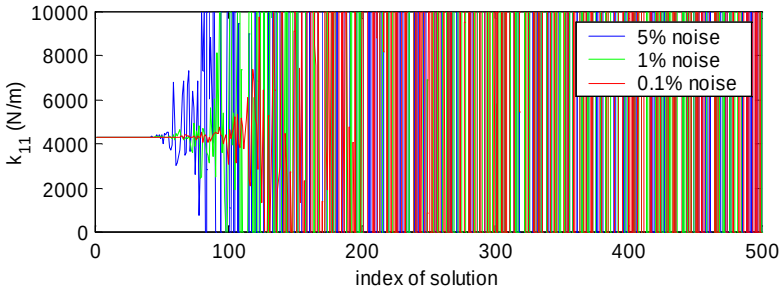

Fig. 2.17 Results from noisy data – 5 internal DOFs

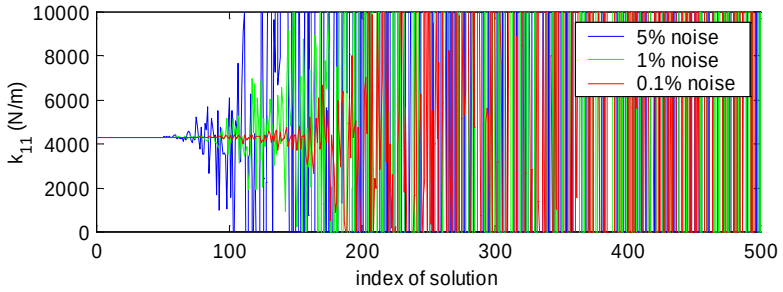

Fig. 2.18 Results of noisy data – 10 internal DOFs

Keeping all conditions the same as for Fig. 2.17 except for an increase in the number of internal DOFs to 10, the identified results are shown in Fig. 2.18. It is seen here again that the 10 internal DOFs case yields better results, *i.e.* it is more tolerant of noise.

From a general point of view, the identified results shown in Fig. 2.17 and Fig. 2.18 are not satisfactory. The errors are analysed next using the perturbation theory mentioned in Appendix B. The norms of the error matrix $\mathbf{E}$, the inverse of matrix $\tilde{\mathbf{A}}$, the residual matrix $\mathbf{R}$ and the condition number of matrix $\tilde{\mathbf{A}}$ are plotted in Fig. 2.19 to Fig. 2.22. Each matrix is shown for both 5 translation internal DOF case and 10 internal DOF case for the purpose of comparison.

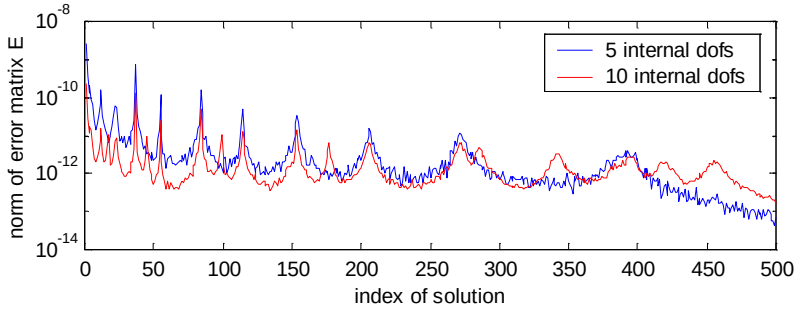

Fig. 2.19 Norm of error matrix $\mathbf{E}$

The norm of error matrix $\mathbf{E}$ represents the level of the uncertainty of matrix $\mathbf{A}$. When 3% noise is introduced into each FRF used in the identification, $\|\mathbf{E}\| < 10^{-9}$ for the 5 translation internal DOF case and $\|\mathbf{E}\| < 10^{-10}$ for the 10 internal DOF case.

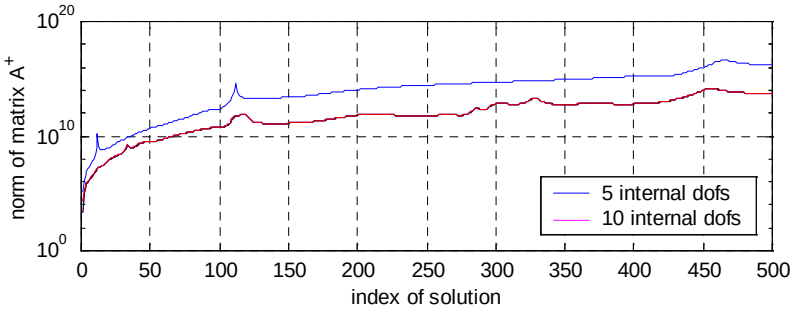

Fig. 2.20 Norm of the pseudo-inverse of matrix $\tilde{\mathbf{A}}$

The norm of the pseudo-inverse of matrix $\mathbf{A}$, $\|\mathbf{A}^+\|$, is shown in Fig. 2.20. The values of $\|\mathbf{A}^+(\omega_i)\|$, $\|\mathbf{A}^+(\omega_j)\|$, $\|\tilde{\mathbf{A}}^+(\omega_i)\|$ and $\|\tilde{\mathbf{A}}^+(\omega_j)\|$ have no significant differnce for both 5 and 10 internal DOFs cases since the noise level is low.

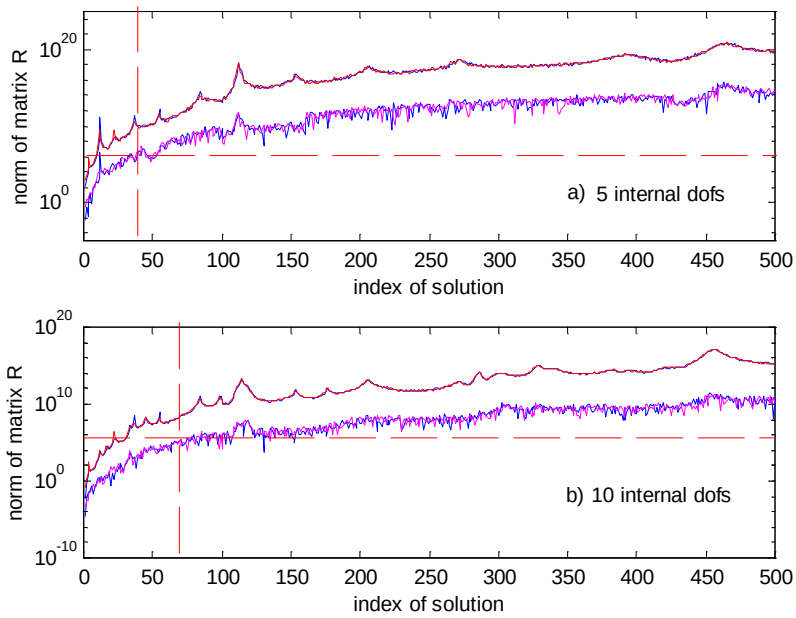

Fig. 2.21 norm of the residual matrix $\mathbf{R}$

The norm of the residual matrix $\mathbf{R}$, which is defined by equation (B.2) in Appendix B, is calculated from its definition and shown as the two lower curves in Fig. 2.21 a) and b). The upper curves are the estimated bounds by equation (B.3), (B.8), (B.9) and (B.10). The difference between these two figures is obvious. The largest difference between the $\mathbf{R}$ norm in Fig. 2.21 a) and the $\mathbf{R}$ norm in Fig. 2.21 b) is up to 10^5 times. Observing the residual matrix norms together with the identified results shown in Fig. 2.17 and Fig. 2.18, we find that they are closely related. In Fig. 2.17 and Fig. 2.18, the unsteady solutons start at 40th and 70th solutions for 5% noise level. The same solution indices in Fig. 2.21 a) and b) correspond to the same residual matrix norm value, $\|\mathbf{R}\|$, which is around 10^6. When the $\|\mathbf{R}\|$ value increases with the increase of the frequency, larger $\|\mathbf{R}\|$ values which happen beyond these frequencies cause the errornous results.

In fact, for a certain noise level, the $\|\mathbf{R}\|$ value relies on $\|\tilde{\mathbf{A}}^{+}\|$. The tendency of $\|\tilde{\mathbf{A}}^{+}\|$ to vary with frequency shown in Fig. 2.20 are the same as their respective

$\|\mathbf{R}\|$ values. At the solutions where $\|\mathbf{R}\| = 10^6$, $\|\tilde{\mathbf{A}}^+\| \approx 10^{10}$. Therefore, $\|\tilde{\mathbf{A}}^+\|$ can be used as a indicator to show which solutions are accepatable. Since

$$\|\tilde{\mathbf{A}}\| = \max(\sigma_i) \tag{2.75}$$

where σ_i $(i = 1,2,...,\min(m,n))$ is the singular value of matrix $\tilde{\mathbf{A}} \in \Re^{mn}$, therefore,

$$\|\tilde{\mathbf{A}}^+\| = 1/\min(\sigma_i) \tag{2.76}$$

That is to say, the minimum singular value of matrix $\tilde{\mathbf{A}} \in \Re^{mn}$ is a good indicator for the possible accuracy of the solution.

Finally, the condition number of matrix $\tilde{\mathbf{A}}$ is shown in Fig. 2.22. It is hard to distinguish them from their amplitudes and they cannot be used directly to tell how the matrix $\tilde{\mathbf{A}}$ affects the accuracy of the solution.

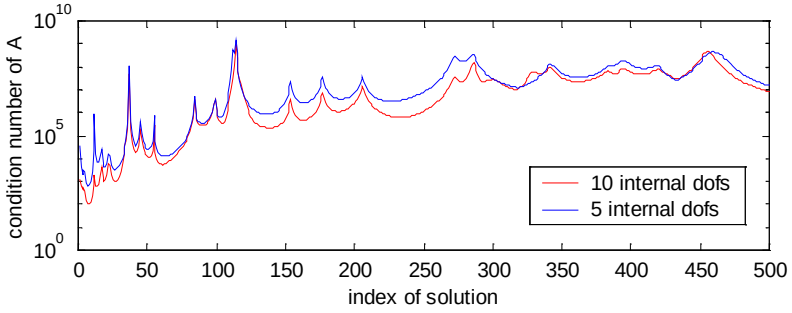

Fig. 2.22 Condition number of matrix $\tilde{\mathbf{A}}$

In addition, NPA provides accurate results under all listed noise levels. As it has been mentioned in section 2.4.2, the FRF data between 1 and 34Hz play a very important role. The 5% noise level does not affect the rank of the $\overline{\mathbf{A}}$ matrix and the condition number κ of matrix $\overline{\mathbf{A}}$ in the 5% noise case is 3.4180×10^8, which is even smaller than the condition number in the noise free case, $\kappa = 2.3633 \times 10^9$ in Table 2.1.

2.5. CRITERION OF SELECTING INTERNAL DOFS: THEOREM OF TRANSMISSIBILITY

In principle, the selection of internal DOFs is arbitrary. The only condition which should be borne in mind is that the number of internal DOFs should at least be equal to the number of unknown joint parameters. However, an improper selection of internal DOFs in some structures may yield a rank-deficient matrix, $\tilde{\mathbf{A}}(\omega)$. This phenomenon was explained by revealing the physical meaning behind it and this explanation is expressed to the *theorem of transmissibility* and given in Appendix A. This theorem gives a criterion to select internal DOFs.

The problem encountered in the simulation is demonstrated in a coupled structure shown in Fig.2.23: two parallel beams coupled via two joints.

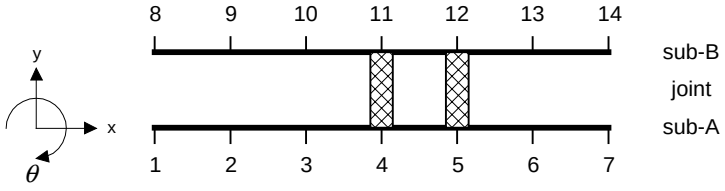

Fig.2.23 Two parallel beams coupled via joint

If each node has one degree of freedom, which is in the y direction, and nodes 1, 6, 9 and 13 are chosen to be internal DOFs, the identification procedure yields an accurate result. However, if one of the internal DOFs, translation y at node 6, is moved to node 3, the identified result is completely wrong for all three algorithms.

Checking the rank of matrix $\tilde{\mathbf{A}}(\omega)$ at each frequency in the latter case, we notice that they are all rank-deficient. Looking into the construction of matrix $\tilde{\mathbf{A}}(\omega)$ at each frequency, we find that the rank deficiency is caused by linearly dependent rows in one of the frequency response function matrices, ${}_{A}\mathbf{H}_{ic}(\omega)$.

$$ {}_A\mathbf{H}_{ic}(\omega)=\begin{bmatrix} {}_AH_{41}(\omega) & {}_AH_{51}(\omega) \\ {}_AH_{43}(\omega) & {}_AH_{53}(\omega) \end{bmatrix} \tag{2.77} $$

and the linear dependence among the elements of matrix ${}_A\mathbf{H}_{ic}(\omega)$ is then defined by a *transmissibility function*

$$ T(\omega)=\frac{{}_AH_{41}(\omega)}{{}_AH_{43}(\omega)}=\frac{{}_AH_{51}(\omega)}{{}_AH_{53}(\omega)} \tag{2.78} $$

Individual elements of matrix ${}_A\mathbf{H}_{ic}$ and the transmissibility function $T(\omega)$ are shown in Fig.2.24. It is seen that curve $T_1(\omega)$ is completely overlaid by curve $T_2(\omega)$. That means $T_1(\omega)=T_2(\omega)=T(\omega)$.

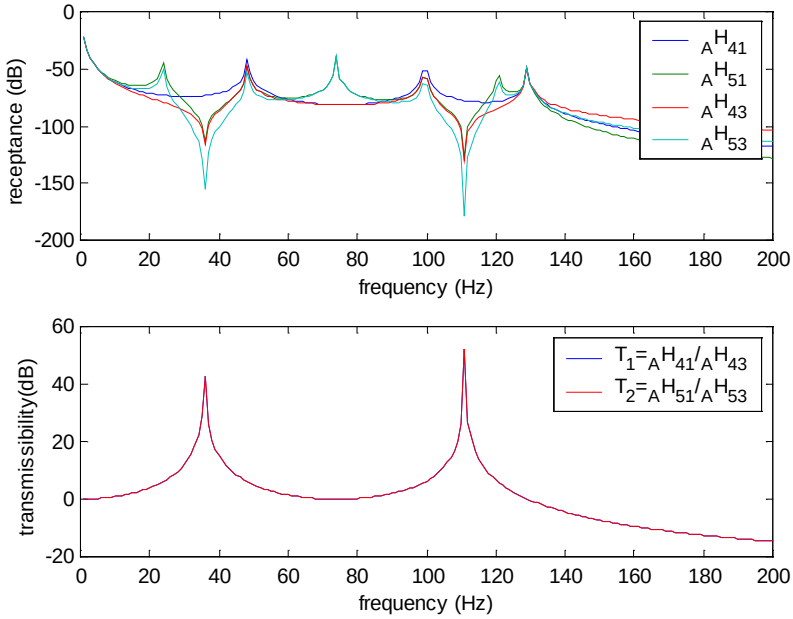

Fig.2.24 Matrix ${}_A\mathbf{H}_{ic}$ and $T(\omega)$ function

Since there is only one DOF at each node, substructure A is in fact equivalent to a 7 DOF mass-spring system as shown in Fig.2.25.

Numerical experiments show that when co-ordinate numbers 4 and 5 are "measured", the FRFs as the elements of matrix ${}_A\mathbf{H}_{ic}$ obtained by giving two excitations either at any two co-ordinates of 1, 2 and 3 or at co-ordinates 6 and 7

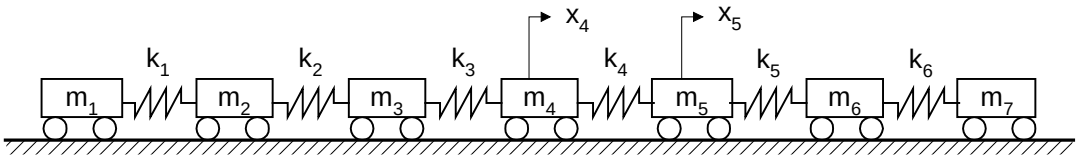

Fig.2.25 A 7-DOF mass-spring system

satisfy the relationship of (A.17) in Appendix A. It seems that the transmissibility property of matrix ${}_A\mathbf{H}_{ic}$ is not a coincidence with the selection of structural parameters. There should be a physical principle that reigns the FRFs in matrix ${}_A\mathbf{H}_{ic}$ to satisfy the transmissibility function. Appendix A presents the principle named as the *theorem of transmissibility* and provides a complete proof.

2.6. CONCLUSION

An identification method for general linear joint models between substructures has been developed in this chapter. Taking FRFs from both or all substructures and their assembly as input data, this method yields mass, stiffness as well as damping parameters of the required joint impedance matrix.

Two algorithms are proposed to solve the group of linear equations derived for this task: the partitioning algorithm (PA) and the non-partition algorithm (NPA). The PA is superior to the NPA and should be applied as the first choice. Compared with the NPA, the PA not only significantly decreases the number of equations involved in a solution but also improves the condition of the coefficient matrix in the linear equations. Therefore, it is an efficient and accurate algorithm.

Numerical simulations show that a proper selection of internal degrees of freedom and including damping in the simulated FRFs are two effective means to improve the condition of the linear equations and they results in a convergent and accurate solution. The theorem of transmissibility provides a guideline for applying this identification method to some chain-like structures. As a general

rule, the greater the number of internal DOFs used, the better the identified result will be.

The robustness investigation of the proposed algorithms has also been carried out. With the noise contaminated FRFs in the studied case, both algorithms can produce an acceptable answer. However, in the second case study, the coefficient matrix of the PA has a high condition number in some frequency ranges, and when the input FRFs are noisy, the perturbations in the coefficient matrix are magnified in the procedure of solution and results in an incorrect answer.

In general, the method gives good performance in the numerical simulations and it is promising that it works well with the experimental data if the frequency response functions supplied are consistent and the measurement noise is properly controlled.

CHAPTER 3

LINEAR JOINT MODELLING – NEURAL NETWORK METHOD

3.1. GENERAL IDEAS

The least-squares method for joint parameter identification mentioned in the previous chapter is mathematically precise and theoretically applicable. Clearly, this sort of conventional deductive method is physically meaningful but it has the drawback of being inflexible and having a low tolerance to input errors (noise contamination, non-linearity or other distortions which prevents the input data from completely satisfying the assumptions). Therefore, great care must be taken in using the least-squares based method to deal with practical engineering problems of this type. The variability and complexity of real structural joints demonds some more flexible and adaptive methods to describe and to analyse their properties. A method using neural networks to identify the joint parameters

is explored in this chapter and is found to be a promising and a more advanced method compared with the least-squares based approaches.

Neural networks have been used in mechanical engineering problems since the early 1990s. The main research areas of the application are control [NaPa90], identification [MaCh93] and damage detection [WuGh92]. The numerical simulation of identifying non-linear damping using neural networks is a good example to demonstrate the ability of generalisation of this method [LiEw95]. The use of neural networks in finite element model updating [AtIn96] [Levi98] has also shown that a multilayer preceptron (MLP) or a radial-basis function (RBF) network can provide a good mapping between frequency domain data and the physical parameters of the system being studied. In fact, a well-trained neural network has the ability to approximate any function to an arbitrary accuracy [Lesh93]. The general ideas and procedures of using neural networks to identify the joint parameters are:

- obtaining the training set from FE analysis, *i.e.* estimating sets of possible values of joint parameters and calculating the system′s corresponding frequency response using an FE package;
- constructing and training a network by feeding the network with the training sets obtained from the FE analysis so that the network can learn from them;
- testing the network by providing a typical input to see if the output is correct;
- feeding the network with practical/experimental data to obtain the identified joint parameters form the network′s output.

3.2. BRIEF REVIEW OF NEURAL NETWORKS

Neural networks have been widely applied in many fields since the 1980s. The applications are expanding because neural networks are good at solving problems, not just in engineering, science and mathematics, but also in medicine, business, finance and literature [HaDB96].

A neural network can be considered as a non-linear mapping between a set of inputs and a set of outputs, in which repeated input-output measurements are used to develop the proper mapping. Multilayer perceptrons (MLPs) and radial-basis function (RBF) networks are non-linear layered feed-forward networks and are both universal approximators. The comparison of these two types of network shows that there always exists an RBF network capable of accurately mimicking a specified MLP, and vice versa. However, these two networks differ from each other in several important respects [Hayk95], and provide alternative ways to application.

3.2.1. Multi-layer Perceptrons

A multilayer perceptron (MLP) is a multilayer feed-forward network. It has an input layer, an output layer and one or more hidden layers. The presence of the hidden units (neurons) allows the network to represent and to compute more complicated associations between patterns. The input signal propagates through the network in a forward direction, on a layer-by-layer basis, from the input layer to the output layer. The pattern of connectivity and the number of processing units in each layer may vary with some constraints. No communication is permitted between the processing units within a layer, but the processing units in each layer may send their output to the processing units in higher layers, as shown in Fig. 3.1.

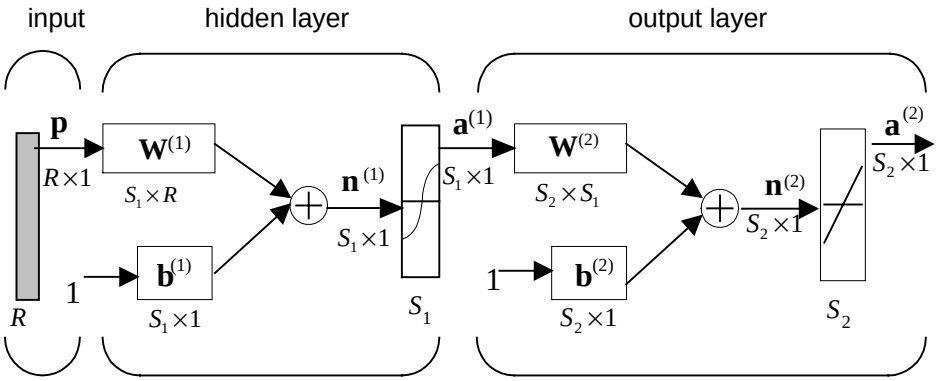

Fig. 3.1 A multilayer perceptron

Associated with each connection is a numerical value which is the strength or the weight of that connection. An element of matrix **W** either in the hidden

layer or the output layer, w_{ij}, is the strength of connection between units i and j. The connection strengths are developed during training of the neural network. There are several different training algorithms for feedforward networks. All of these algorithms use the gradient of the performance function, which is defined as the mean sum of squares of the network errors, to determine how to adjust the weights to optimise performance. The gradient is determined using a technique called back-propagation. This term refers to the manner in which the gradient is computed for non-linear multi-layer networks [HaDB96].

At the beginning of the training process, the connection strengths can be assigned random values. As the training set is presented during the training, application of the 'rule of learning' modifies the connection strengths in an iterative process. At the successful completion of the training, when the iterative process has converged, the collection of connection strength captures and stores the knowledge and the information present in the training set used in its training. Such a trained neural network is ready to be used. When presented an input pattern, a feed-forward network computation results in an output pattern which is the result of the generalisation and synthesis of what it has learned and stored in its connection strengths.

An MLP trained by the back-propagation algorithms proceeds in three steps. At first, the units in the input layer receive their activation in the form of an input pattern and this initiates the feedforward process. Secondly, the processing units in the hidden layer receive outputs from the input units and perform the following computations:

- compute their net input $n_j^{(1)}$

$$n_j^{(1)} = \sum_{k=1}^{R} w_{jk}^{(1)} p_k + b_j^{(1)} \tag{3.1}$$

where p_k = output from units impinging on unit j and R = number of units impinging on unit j;

- compute their activation values from the net input values

$$a_j^{(1)} = F_j(n_j^{(1)}) \tag{3.2}$$

F_j is usually a sigmoid function like

$$a_j^{(1)} = \frac{1}{1+e^{-n_j^{(1)}}} \tag{3.3}$$

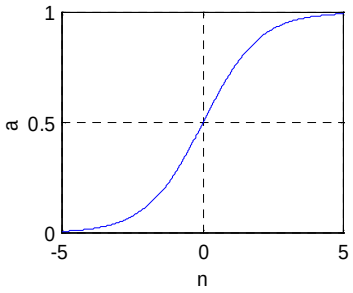

Fig. 3.2 A sigmoid transfer function

- compute their outputs from their activation values

$$n_j^{(2)} = \sum_{k=1}^{S_1} w_{jk}^{(2)} a_k^{(1)} + b_j^{(2)} \text{ and } a_j^{(2)} = n_j^{(2)} \tag{3.4}$$

- the output values are sent to other processing units along the outgoing connections.

Finally, this process continues until that the processing units in the output layer compute their activation values. These activation values are the output of the neural computations.

3.2.2. Radial Basis Function Networks

The architecture of a RBF network is shown in Fig. 3.3. There is one hidden layer (radial basis layer) and one output layer (linear layer). When the input vector, $\mathbf{p}$, is presented to the network its distance to the input weight matrix, $\mathbf{W}^{(1)}$, is measured and each neuron in the hidden layer will output a number between 0 and 1 according to the proximity of the input vector to the neuron′s weight. This output, $\mathbf{a}^{(1)}$, is weighted then by the connections between the hidden and output layers to yield the network output, $\mathbf{a}^{(2)}$. Neurons with weights far from the input vector will have an output close to zero. This small output will have only a small effect on the output neurons. In contrast, neurons

with weights close to the input vector $\mathbf{p}$ will output values close to one, and will influence the final output, $\mathbf{a}^{(2)}$.

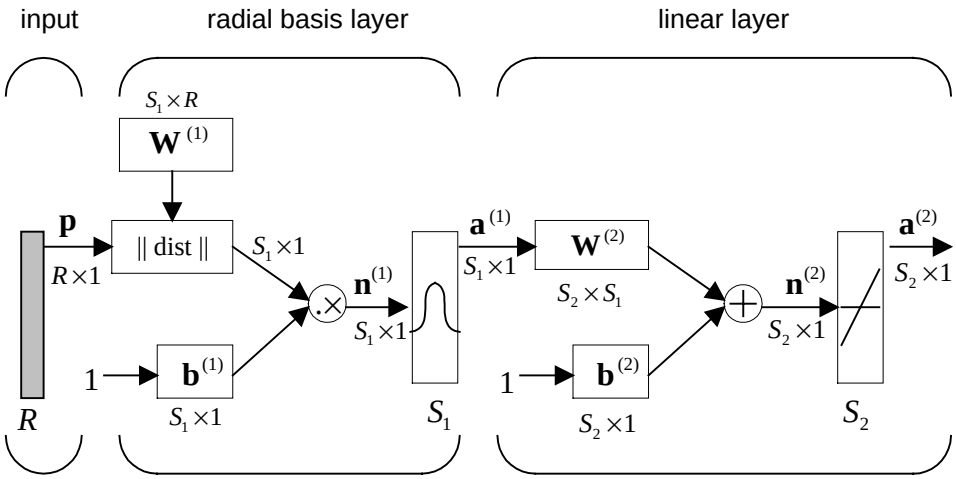

Fig. 3.3 RBF network structure

Radial basis functions are special types of linear models defined by the relationship

$$a_i^{(2)} = \sum_{j=1}^{S_1} w_{ij}^{(2)} a_j^{(1)} + b_i^{(2)} \tag{3.5}$$

in which

$$a_j^{(1)} = F(n_j^{(1)}) \text{ and } n_j^{(1)} = z_j b_j^{(1)} \tag{3.6}$$

where the argument z_j is a distance measure between vectors $\mathbf{w}_j^{(1)}$ and $\mathbf{p}$

$$z_j = \frac{1}{2}(\mathbf{p} - \mathbf{w}_j^{(1)})^T \mathbf{Q}(\mathbf{p} - \mathbf{w}_j^{(1)}) \tag{3.7}$$

Here, $\mathbf{Q}$ is a matrix defining the metric, and F is the radial basis function. The vectors $\mathbf{w}_j^{(1)}$, which belong to the input space, are called *input weights*. For the network to be a linear function of the free parameters, $w_{ij}^{(2)}$, the number of hidden layers, their positions and the metric all have to be constants.

Common choices for F are Gaussian function of the form

$$F(n) = e^{-n^2} \tag{3.8}$$

and the Cauchy function of the form

$$F(n) = \frac{1}{1+n^2} \tag{3.9}$$

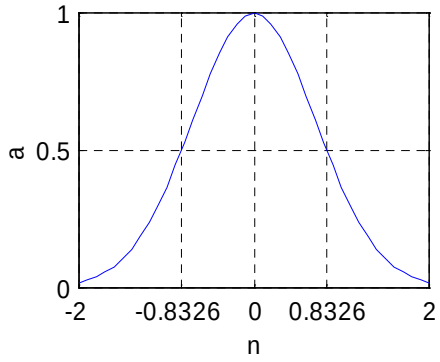

Fig. 3.4 A Gaussian radial basis function

3.2.3. Comparison of MLP and RBF Networks

Multilayer perceptrons and radial-basis function networks are examples of non-linear layered feedforward networks. However, these two networks differ from each other in several important respects as outlined below.

- An RBF network generally has a single hidden layer, whereas an MLP may have one or more hidden layers.
- The computation nodes (neurons) of an MLP, located in a hidden or output layer, share a common neuron model. On the other hand, the computation nodes in the hidden layer of an RBF network are quite different and serve a different purpose from those in the output layer of the network.
- The hidden layer of an RBF network is non-linear, whereas the output layer is linear. On the other hand, the hidden and output layers of an MLP used as a classifier are usually all non-linear, however, when the MLP is used to solve non-linear regression problems, a linear layer for the output is usually the preferred choice.

- RBF networks differ from the perceptrons also in that they are capable of implementing arbitrary non-linear transformations of the input space.
- RBF networks may require more neurons than standard MLPs but often they can be designed in a fraction of the time it takes to train MLPs. They work best when many training vectors are available.

In the cases we studied, both MLP and RBF networks are used and their performances are compared.

3.3. DISCUSSION ON PARAMETER SELECTION

As mentioned in the first section of this chapter, the purpose of using neural networks here is to present an experimental FRF to the trained network in order to obtain an estimate of the physical joint parameters. The performance of a neural network depends largely on the selection of the training set, which is generated according to different joint parameter values.

A good training set should satisfy the following conditions:

- selected parameters should be able to represent the physical properties of the joints. For a linear joint model, these can be stiffness of joint elements: stretching and compressing, torsion, bending *etc*.;
- values of these parameters should be carefully chosen to include the real values in their range, *i.e*. the minimum and maximum expected values of the joint parameters need to be defined to train the network; and
- either FRF data or modal parameters which are used as input to the network should be sensitive to changes in the joint parameters.

To identify the joint parameters of a dynamic structure it is first necessary to obtain experimental data from the physical model. The experimental data are usually provided in the form of FRFs and a set of modal data can be extracted from these FRFs using modal analysis techniques. There has been a disagreement on the issue of whether the FRF data or the modal data should be

used to describe the dynamic properties of a system when neural networks are employed as a tool in doing FE model updating [AtIn96] [Levi98].

Frequency response function (FRF) data were used by Atalla and Inman [AtIn96] because these data are directly measured from structures, and there are no approximations or assumptions introduced during modal analysis. In general, however, the measured FRF data contain too many data points to use realistically with neural networks. As the dimension of the input vector to the neural net increases, the number of training data vectors required for adequate network generalisation also increases, often exponentially. The FRFs may contain tens of thousands of data points and adequate network generalization is clearly unlikely in these circumstances. It is necessary to reduce the number of data points to manageable proportions. There is no clear boundary given at which the number of data points becomes manageable. Data reduction could be achieved by simply discarding many of the FRF data points. On the other hand, an alternative method of data reduction is to work in the modal domain, using modal analysis of the FRFs to derive the mode shapes and natural frequencies of the structure [Levi98]. The number of data points is typically reduced by several orders of magnitude by modal analysis.

In this chapter, the advantages of using FRF data as input to the network are kept and the drawback of having too many frequency points is overcome by the application of principal component analysis (PCA), which is briefly introduced in section 3.5. By applying PCA, the dimension of the FRF data is decreased considerably and neural networks trained by the sets of PCA results and target values are not sensitive to the noise presented in the normal measured FRFs. Numerical simulations are given in section 3.6.

3.4. Generation of Training Sets: A Parametric Family of FE Models

The generation of training sets needs a family of the FE model in question to be analysed in order to obtain the FRF data corresponding to different values of the joint parameters. It is obviously too costly and awkward to analyse the full finite

element model each time when only a few joint parameters of the structure are changed. To be more efficient in doing this task, a method based on using a constant basis of Ritz vectors to create parametric families of reduced models was proposed and validated by analysing the FE model of a 3-bay truss structure [Balm95a] [Balm95b].

The governing equations of a viscously damped finite element model can be expressed in the form

$$\begin{aligned} [\mathbf{M}s^2 + \mathbf{C}s + \mathbf{K}]\mathbf{q} &= \mathbf{bu} \\ \mathbf{x} &= \mathbf{cq} \end{aligned} \tag{3.10}$$

where **b** and **c** are input and output shape matrices respectively.

The system properties are described using the DOFs, **q**, by mass, **M**, damping, **C**, and stiffness, **K**, properties. All output, **x,** of the continuous structure can be expressed as linear combination of the DOFs, $\mathbf{q}$. Similarly, all inputs, **u**, exciting the system, are described in the coordinate system, $\mathbf{q}$, by forces which depend linearly on $\mathbf{u}$.

A training set required to train neural networks is equivalent to the solutions of a family of models, which is defined here as a group of models of the general form (3.9) where the matrices composing the dynamic stiffness depend on a number of design parameters α:

$$\mathbf{Z}(\alpha, s) = s^2\mathbf{M}(\alpha) + s\mathbf{C}(\alpha) + \mathbf{K}(\alpha) \tag{3.11}$$

Material density and modulus, beam section properties, plate thickness, frequency dependent damping, node location *etc*. are typical α parameters. It is often desirable to use a model description in terms of other parameters β, which depend non-linearly on the α, to describe the evolution from the initial model as a linear combination of modification matrices $\Delta\mathbf{Z}$ with coefficient β

$$\mathbf{Z}(\alpha, s) = \mathbf{Z}(\alpha_0, s) + \sum_j \beta(\alpha)\Delta\mathbf{Z}_j(s) \tag{3.12}$$

with each $\Delta\mathbf{Z}_j$ having constant mass, damping and stiffness properties.

Displacement-based reduction approaches make the assumption that there exists a reduced subspace spanned by the columns of a rectangular matrix **T** and described by reduced DOFs, $\mathbf{q}_R$. For all effectively found states, **q**, of the full-order model there exists a close approximation in the reduced subspace described by the coordinates, $\mathbf{q}_R$:

$$\mathbf{q} \approx \mathbf{T}\mathbf{q}_R \tag{3.13}$$

The approximation (3.13) of the full order model DOFs, **q,** by a linear combination of reduced model DOFs, $\mathbf{q}_R$, leads to the creation of a model of size n_R rather than n. This reduction, when applied to families of models of the form (3.11) and (3.13), leads to

$$\begin{aligned} \mathbf{T}^T\mathbf{Z}(\alpha, s)\mathbf{T}\mathbf{q}_R &= \mathbf{T}^T\mathbf{b}\mathbf{u} \\ \mathbf{y} &= \mathbf{c}\mathbf{T}\mathbf{q}_R \end{aligned} \tag{3.14}$$

For any model in a considered family, the reduced model (3.14) can give estimates of all the solutions that can be predicted with the full order model.

In fact, the variations of joint parameters do not affect all the DOFs of the full order model. A reduction matrix (Ritz vectors), **T**, can be obtained using Guyan's static model of the form

$$\begin{bmatrix} \mathbf{K}_{mm} & \mathbf{K}_{ms} \\ \mathbf{K}_{sm} & \mathbf{K}_{ss} \end{bmatrix} \begin{Bmatrix} \mathbf{q}_m \\ \mathbf{q}_s \end{Bmatrix} = \begin{bmatrix} \mathbf{I} \\ \mathbf{0} \end{bmatrix} \mathbf{b}\mathbf{u} \tag{3.15}$$

where $\mathbf{q}_m$ is the DOF related to the changed parameters and $\mathbf{q}_s$ is rest of the DOFs in $\mathbf{q}$. From (3.13) we can then have

$$\mathbf{T} = \begin{bmatrix} \mathbf{I} \\ -\mathbf{K}_{ss}^{-1}\mathbf{K}_{sm} \end{bmatrix} \tag{3.16}$$

3.5. PRINCIPAL COMPONENT ANALYSIS TECHNIQUE

Principal Component Analysis (PCA) represents a statistical technique for analysing the covariance structure of multivariate statistical observations. The principal components are the most important linear features of the random observation vector. Through PCA many variables can be represented by fewer components, so PCA can be considered either as a feature extraction or as a data compression technique and is indisputably very important in applications of signal or image coding, processing, and analysis.

PCA is a statistical technique under the general title of factor analysis. The purpose of PCA is to identify the dependence structure behind a multivariate stochastic observation in order to obtain a compact description of it. When there is nonzero correlation between the observed variables the dimension, *n*, of the data space, (*i.e.* the number of the observed variables) does not represent the number of independent variables, *m*, which is really needed to describe the data. We may suppose *m* to be the number representing the degrees of freedom of a physical system. The stronger the correlation between the observed variables, the smaller the number of independent variables that can adequately describe them.

The *n* observed variables are thus represented as functions of *m* latent variables called factors, where $m < n$ and often $m << n$. The factor variables are also called *features* of the multivariate random signal, and the vector they form is a member of *the feature space*.

3.5.1. Definition

Consider a random vector $\mathbf{x} = \{x_1, \ldots, x_n\}^T$ with mean $E[\mathbf{x}] = 0$ and covariance matrix, $\mathbf{R}_x = E[\mathbf{x}\mathbf{x}^T] \in \Re^{n \times n}$. The feature vector, $\mathbf{y}$, is an orthogonal, linear transformation of the data

$$\mathbf{y} = \mathbf{W}\mathbf{x} \tag{3.17}$$

where the columns of $\mathbf{W}$ form an orthonormal basis of a subspace $\Im$, namely, $\mathbf{W}\mathbf{W}^T = \mathbf{I}$ and $\Im = span(\mathbf{W})$. The projection of $\mathbf{x}$ onto $\Im$ is the reconstruction of $\mathbf{x}$ from $\mathbf{y}$ as

$$\hat{\mathbf{x}} = \mathbf{W}^T\mathbf{y} = \mathbf{W}^T\mathbf{W}\mathbf{x} \tag{3.18}$$

Minimise the mean square error between the observation and the reconstruction

$$J = E[\|\mathbf{x} - \hat{\mathbf{x}}\|^2] \tag{3.19}$$

to obtain the optimised $\mathbf{W}$.

The procedure can be summarised as follows:

Let the eigenvalues $\lambda_1, \lambda_2, \ldots, \lambda_n$ of $\mathbf{R}_x$ be arranged in decreasing order, and let the corresponding normalised eigenvectors be $\mathbf{e}_1, \mathbf{e}_2, \ldots, \mathbf{e}_n$. Then the minimiser of the mean square reconstruction error, J, under the constraint $\mathbf{W}\mathbf{W}^T = \mathbf{I}$, has the form

$$\mathbf{W}_{opt} = \mathbf{T}[\pm\mathbf{e}_1 \cdots \pm\mathbf{e}_m]^T \tag{3.20}$$

where $\mathbf{T}$ is any square orthogonal matrix.

The minimal reconstruction error is

$$\min J = \sum_{i=m+1}^{n} \lambda_i \tag{3.21}$$

The normal eigenvectors of $\mathbf{R}_x$ corresponding to its largest eigenvalues, *i.e.*, the row of $\mathbf{W}_{opt}$, are called *principal eigenvectors*. The features, $y_1, y_2, \ldots, y_m$, elements of the random vector $\mathbf{y}$, are called the *principal components* of $\mathbf{x}$. They are statistically not correlated:

$$E[y_i y_j] = \mathbf{e}_i^T\mathbf{R}_x\mathbf{e}_j = 0 \tag{3.22}$$

their variances are equal to the eigenvalues of $\mathbf{R}_x$:

$$E[y_i^2] = \mathbf{e}_i^T\mathbf{R}_x\mathbf{e}_i = \lambda_i \tag{3.23}$$

and are arranged in order of decreasing variance

$$E[y_1^2] \geq E[y_2^2] \geq \cdots \geq E[y_m^2] \tag{3.24}$$

The first principal component, y_1, is a linear combination of the observed variables

$$y_1 = w_{11}x_1 + \cdots + w_{1n}x_n = \mathbf{w}_1^T\mathbf{x} \tag{3.25}$$

such that its variance

$$E[y_1^2] = \mathbf{w}_1^T E[\mathbf{x}\mathbf{x}^T]\mathbf{w}_1 = \mathbf{w}_1^T\mathbf{R}_x\mathbf{w}_1 \tag{3.26}$$

is maximum under the constraint that the coefficient vector is normalised $\|\mathbf{w}_1\| = 1$. According to the Rayleigh-Ritz theorem $\mathbf{w}_1 = \mathbf{e}_1$ and the maximum eigenvalue λ_1 is equal to the variance of the first component.

The second principal component $y_2 = \mathbf{w}_2^T\mathbf{x}$ maximise the variance of y_2 under the constraint $\|\mathbf{w}_2\| = 1$ and $\mathbf{w}_2 \perp \mathbf{e}_1$. In general, for $\mathbf{w} = \mathbf{e}_p$, $p > 1$, the variance is maximised under the constraint that $\mathbf{w}$ is orthogonal to all prior eigenvectors $\mathbf{e}_1, \mathbf{e}_2, \ldots, \mathbf{e}_{p-1}$.

3.5.2. PCA and SVD

The covariance matrix $\mathbf{R}_x = E[\mathbf{x}\mathbf{x}^T] \in \Re^{n\times n}$ can be estimated by

$$\mathbf{R}_x \approx \frac{1}{N}\sum_{k=1}^{N}\mathbf{x}_k\mathbf{x}_k^T = \frac{1}{N}\mathbf{X}\mathbf{X}^T \tag{3.27}$$

where $\mathbf{X} = [\mathbf{x}_1 \quad \mathbf{x}_2 \quad \cdots \quad \mathbf{x}_N]$. The matrix $\mathbf{X}_{n\times N}$ can be decomposed by SVD to

$$\mathbf{X} = \mathbf{U}\mathbf{S}\mathbf{V}^T \tag{3.28}$$

where $\mathbf{U} \in \Re^{n\times n}$ and $\mathbf{V} \in \Re^{N\times N}$ are orthonormal matrices, $\mathbf{S} \in \Re^{n\times N}$ is a diagonal matrix. If the matrices on the right hand side of equation (3.28) are partitioned as

$$\mathbf{X} = \begin{bmatrix} \boldsymbol{\Phi} & \vdots & {}^{\perp}\boldsymbol{\Phi} \end{bmatrix} \begin{bmatrix} \mathbf{D} & \vdots & \mathbf{0} \\ \cdots & \vdots & \cdots \\ \mathbf{0} & \vdots & \mathbf{0} \end{bmatrix} \begin{bmatrix} \boldsymbol{\Psi} \\ \cdots \\ {}^{\perp}\boldsymbol{\Psi} \end{bmatrix} \tag{3.29}$$

where $\mathbf{D}$ is the diagonal matrix of nonzero singular values

$$\mathbf{D} = diag[\sigma_1, \sigma_2, \cdots, \sigma_p] \qquad \sigma_1 > \sigma_2 > \cdots > \sigma_p > 0 \tag{3.30}$$

$\boldsymbol{\Phi}$ and $\boldsymbol{\Psi}$ are the matrices of left and right singular vectors, respectively, corresponding to the nonzero singular values; ${}^{\perp}\boldsymbol{\Phi}$ and ${}^{\perp}\boldsymbol{\Psi}$ span the orthogonal complements of the respective subspaces spanned by $\boldsymbol{\Phi}$ and $\boldsymbol{\Psi}$, we have

$$\mathbf{X} = \boldsymbol{\Phi}\mathbf{D}\boldsymbol{\Psi} \tag{3.31}$$

The columns (rows) of $\boldsymbol{\Phi}$ ($\boldsymbol{\Psi}$) are called the left (right) principal vectors of $\mathbf{X}$ and are pairwise orthonormal, *i.e.*,

$$\boldsymbol{\Phi}^T\boldsymbol{\Phi} = \boldsymbol{\Psi}\boldsymbol{\Psi}^T = \mathbf{I}_p \tag{3.32}$$

where $\mathbf{I}_p$ is the *p*-dimensional identity matrix. From (3.31) and (3.32), we have

$$\mathbf{X}\mathbf{X}^T\boldsymbol{\Phi} = \boldsymbol{\Phi}\mathbf{D}^2 \tag{3.33}$$

It implies that the vectors $\boldsymbol{\varphi}_i$ are eigenvectors of the matrix $\mathbf{X}\mathbf{X}^T$ as

$$\mathbf{X}\mathbf{X}^T\boldsymbol{\varphi}_i = \sigma_i^2\boldsymbol{\varphi}_i \qquad i = 1,2,\cdots, p \tag{3.34}$$

Comparing (3.34) with (3.27), we obtain the relation between eigenvalues of the covariance matrix $\mathbf{R}_x$ and the singular values in (3.30) as

$$\lambda_i = \frac{1}{N}\sigma_i^2 \qquad i = 1,2,\cdots, p \tag{3.35}$$

The transformation matrix is then

$$\mathbf{W}_{opt} = \boldsymbol{\Phi}^T \tag{3.36}$$

3.6. CASE STUDIES ON NUMERICAL SIMULATIONS

Two numerical simulations are given in this section. The main issues addressed in these simulations are the validity of the proposed method, the selection of

frequency points, the determination of the network's parameters and the comparison with the previously presented results in chapter 2 using the LS approach. The identification procedure is summarised in the flow chart in Fig. 3.5.

There are two phases in the identification procedure: phase one is network training, connected by solid arrows, and phase two is parameter identifying, connected by hollow arrows. These two phases are implemented in sequence.

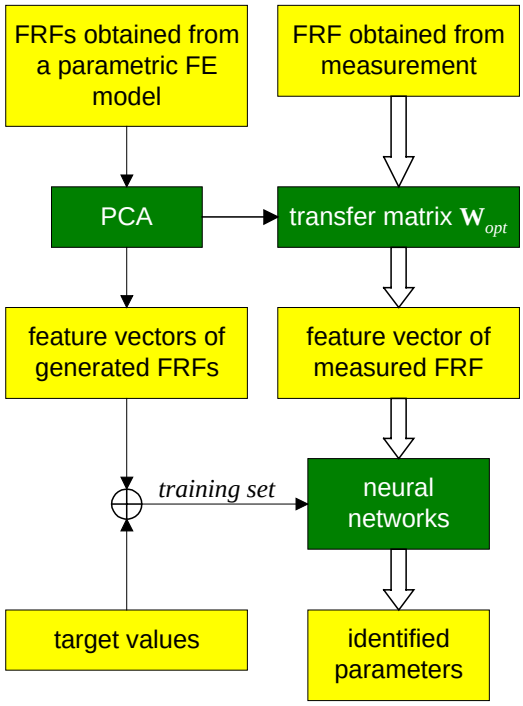

Fig. 3.5 Flowchart of the identification procedure

3.6.1. Simulation 1

In this simulation, the structure illustrated as in Fig. 3.6 is similar to the case in Fig.2.7, two beam substructures coupled via a joint, in which the joint is also a beam element.

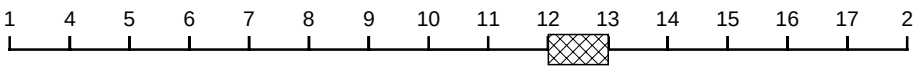

Fig. 3.6 Two beam substructures coupled via a joint

It is supposed that both substructures are precisely known and the parameters of the joint are uncertain but the knowledge about the uncertainty, *i.e*. the ranges of the variations of these parameters, is available. In this case, the joint parameters are its Young's modulus E and its mass density ρ. The uncertainty of these two parameters is denoted by factors α and β so the true values of these parameters are expressed as

$$E = \alpha E_0 \text{ and } \rho = \beta \rho_0 \tag{3.37}$$

where E_0 and ρ_0 are the initial guesses of the joint parameters, which are determined according to the current knowledge to the structure. If the factor $\alpha \in [0.5\ 1.5]$ takes the values of $\alpha = 0.5,\ 0.7,\ 0.9,\ 1.1,\ 1.3,\ 1.5$ in sequence and factor $\beta \in [0.5\ 1.5]$ takes the values of $\beta = 0.5,\ 1.0,\ 1.5$, there are 18 combinations of these two factors and the corresponding 18 point FRFs at the *y* direction of node 12 obtained by the technique of parametric families are shown in Fig.3.7. A fewer number of β values are used because the change in joint mass has a smaller effect to the structural dynamic properties compared with the change in joint stiffness. Therefore, the accuracy of β in the identification is not as important as that of α.

With a frequency resolution of 0.5 Hz, these 18 FRFs can be put into a matrix: $\mathbf{H}_{n\times N}$, in which *n* is the number of frequency points, $n = 1600$, and *N* is the number of FRFs, $N = 18$. If the FRFs are evenly divided into four segments in the frequency range and each segment is used in one identification, then we will have $n = 400$ and $N = 18$ as the dimension of matrix $\mathbf{H}$ in each frequency segment. Fig.3.8 shows the second segment of the FRFs in frequency range 200 – 400Hz. It is seen from Fig.3.7 that the variation of FRF (resonance and anti-resonance frequency shifts) corresponding to different joint parameters changes from one frequency segment to another. For instance, the variation in frequency range 200 – 400Hz is larger than that in the range of 0 – 200Hz. Therefore, it is of interest to investigate the effect of using FRFs in different frequency ranges.

A virtual FRF measurement, which is generated with $\alpha = 0.8$, $\beta = 0.7$ and in noise-free, is used as a test set and is highlighted in Fig.3.7 and 3.8.

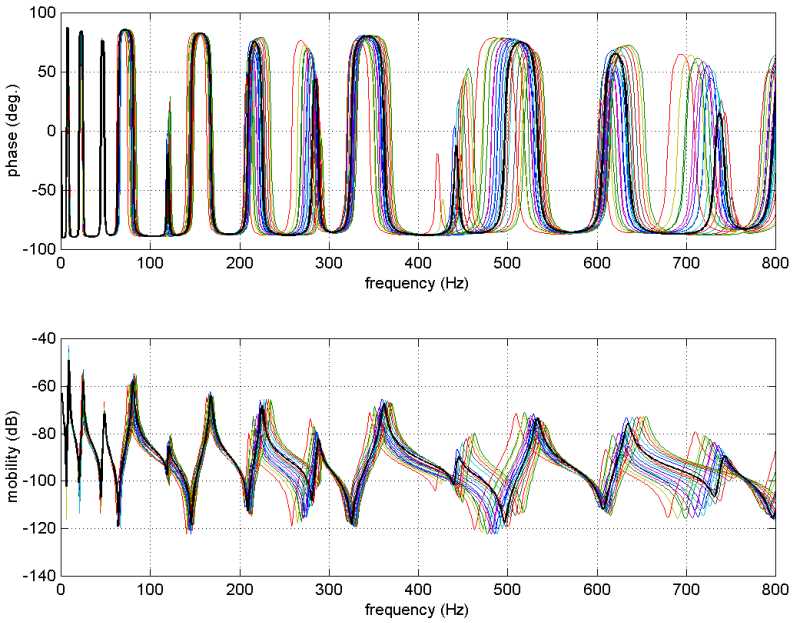

Fig.3.7 Generated FRFs overlaid with the measured FRF

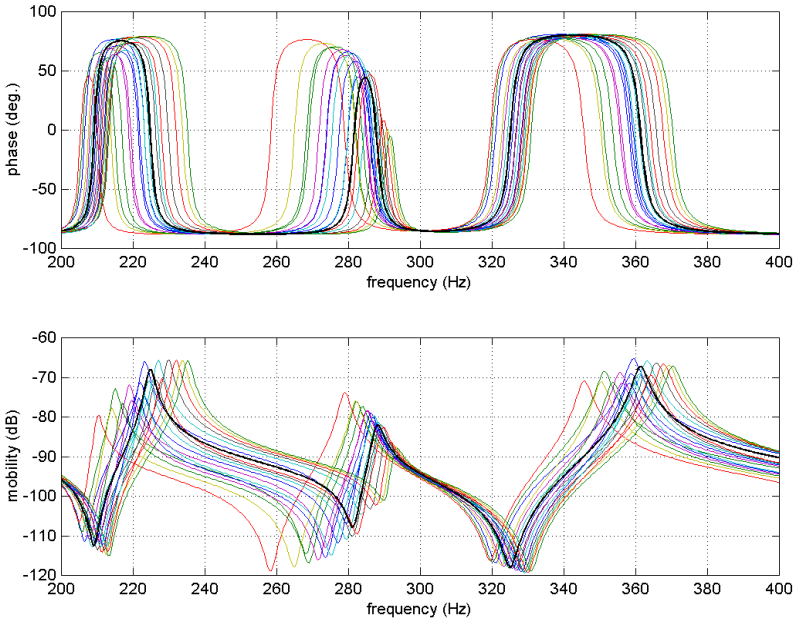

Fig.3.8 FRF segments used for training the network

The application of the PCA technique to the matrix $\mathbf{H}_{n\times N}$ produces a set of feature vectors of the FRFs, $\mathbf{y}_i$, $i=1,2,\ldots,N$, which is also named as *vectors of principal elements*. Each feature vector has only 17 elements, many fewer than the number of frequency points in its corresponding FRF. The training set for a neural network is therefore constructed of these feature vectors and their corresponding target values of α and β.

A 2-layer perceptron was built with 10 neurons in the hidden layer and 2 neurons in the output layer. The network was trained using back-propagation algorithm and the number of epochs was set to be 70. The trained network was then fed with the virtual test data. Six sets of the 'test' data were generated with different levels of noise. The noise levels were indexed as: level 1 = 0%, level 2 = 1%, level 3 = 5%, level 4 = 10%, level 5 = 15% and level 6 = 20%. One of the noise-contaminated FRF is shown in Fig.3.9 and the identification errors are shown in Fig.3.10.

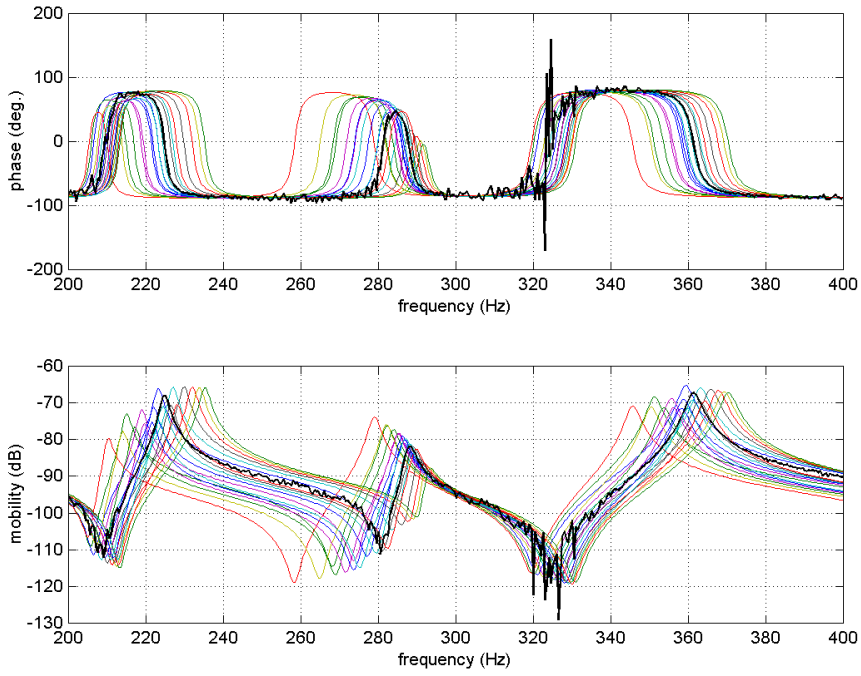

Fig.3.9 Measured FRF is contaminated by 15% noise

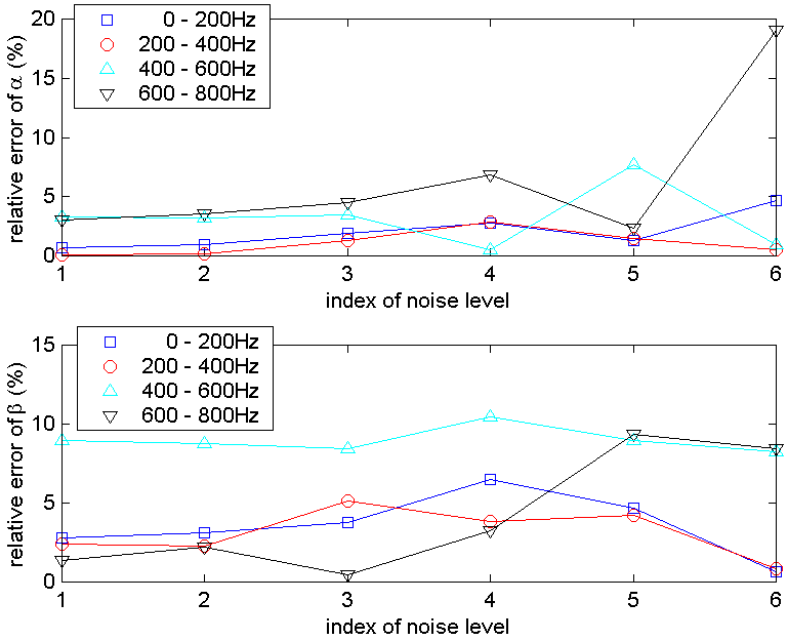

Fig.3.10 Identification errors of the MLP

An RBF network was also trained using the same sets of training data. It creates 16 neurons in its radial basis layer and reaches the convergence faster than the MLP. The identification errors are shown in Fig.3.11.

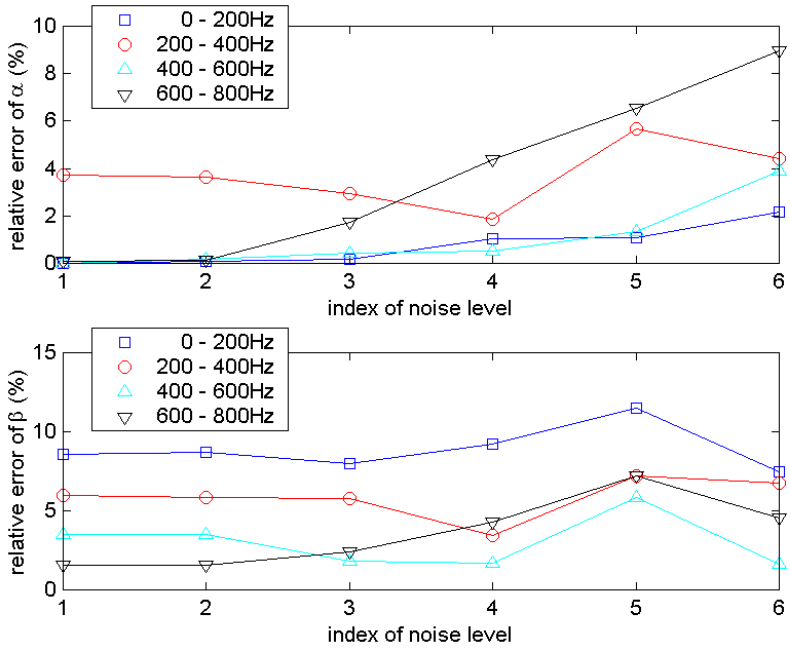

Fig.3.11 Identified errors of the RBF network

In general, both networks have a good tolerance to measurement noise, but the RBF network gave a better performance. The accuracy of the identifications

largely depends on the precision of the results obtained from the noise-free FRF data. The effects of using different frequency segments are also illustrated in Fig.3.10 and 3.11. For example, in Fig.3.11, frequency segments 0 – 200Hz and 400 – 600Hz yield accurate results with noise-free FRFs and perform well even with highly polluted FRF data. Frequency segment 600 – 800Hz gives a larger error because of the smaller dynamic range and the largest resonance frequency shift. As predicted, the error on β is much larger than the error on α. The result should be improved if more training sets are provided.

3.6.2. Simulation 2

The model of structure used for the second simulation is shown in Fig.3.12. The joint situated between the two beams is again a short beam element. In contrast to simulation 1, the structure's dynamic behaviour is not very sensitive to the change of the joint parameters. According to (3.37), setting a series of α and β values as the same as in simulation 1, we obtain a set of FRFs using the technique of parametric families and the FRFs are shown in Fig.3.13. Again, those are point FRFs at coordinate 3-*z*, with frequency resolution 1.0Hz.

If the FRFs are evenly split into two segments in the frequency range 0 to 1500 Hz, then two $\mathbf{H}_{n\times N}$ matrices are formed where $n = 750$ and $N = 18$. The 'measured' FRFs were then generated with $\alpha = 1.0$, $\beta = 1.2$.

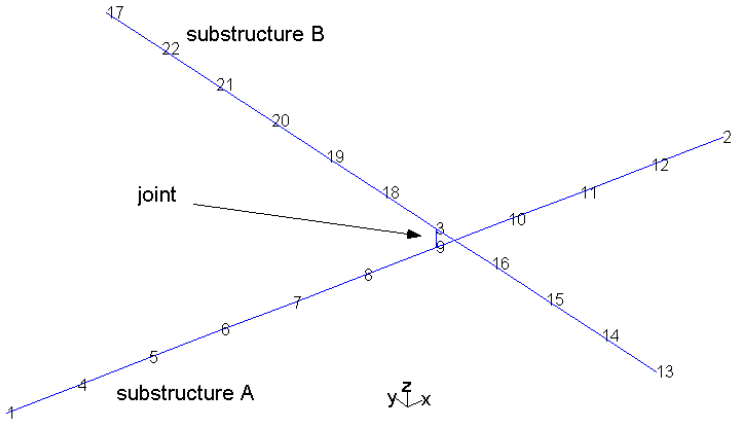

Fig.3.12 A cross-beam structure

To simulate the measurement FRFs, different levels of noise as specified in simulation 1 were added into the 'synthesised' FRF. Following the same procedure as discussed in the first simulation, we obtained the identified errors from the two sets of FRFs in different frequency segments. They are shown in Fig.3.16 and 3.17.

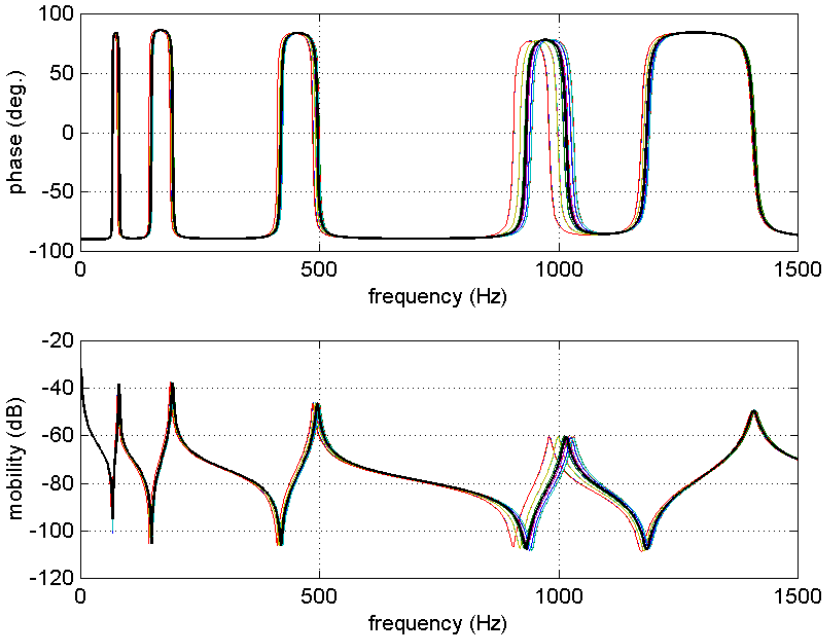

Fig.3.13 Generated FRFs overlaid with the measured FRF

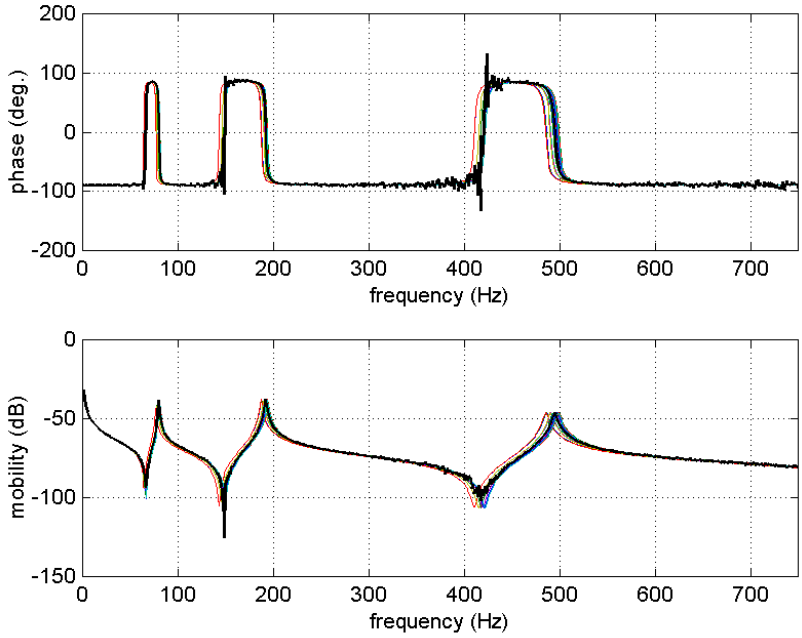

Fig.3.14 Frequency segment 1, measured FRF with 20 % noise

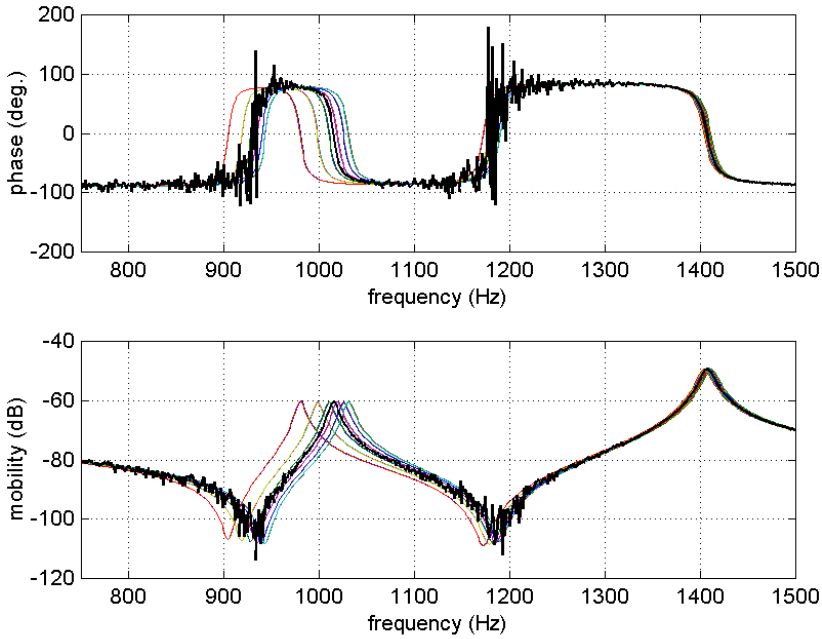

Fig.3.15 Frequency segment 2, measured FRF with 20 % noise

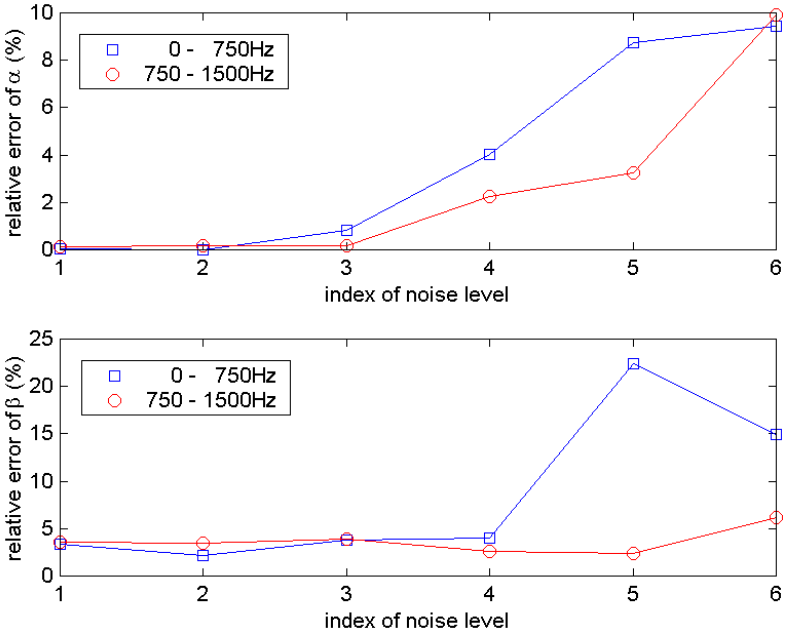

Fig.3.16 Identification errors of the MLP

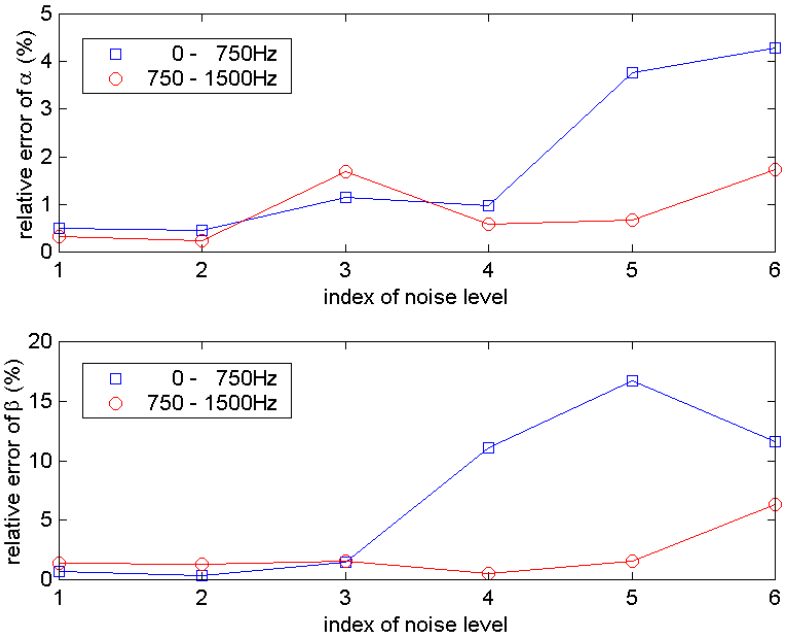

Fig.3.17 Identification errors of the RBF network

In this simulation, a 2-layer perceptron was built with the same number of neurons, 16, in the hidden layer as that used in the RBF network, and the MLP network was trained 100 epochs using backpropagation algorithm. Comparing Fig.3.16 with Fig.3.17, we can still see a better performance presented by the RBF network.

This simulation demonstrates that with a small sensitivity to joint parameters, the proposed neural network method can still perform well. It is confirmed again that this method is robust and stable even with the noisy experimental data.

3.7. CONCLUSION

A new method of identifying joint parameters using neural networks is developed in this chapter. The basic techniques involved are parametric families of finite element models, principal component analysis and neural networks. The technique of parametric families of FE models and principal component analysis are mainly used to generate training sets for neural networks to learn. The MLP and RBF neural networks then play a role of identifier. By feeding the trained neural network a feature vector extracted from a measured FRF, it yields parameters of the joint.

Creating families of FE models and PCA are implemented here because the former is efficient in obtaining dynamic properties of the system with joint parameter changing and the later is effective in compressing FRF data or extracting feature vectors from the FRFs. A large amount of redundant FRF data are excluded by applying PCA, and the training sets are then made concise without losing the necessary information.

The advantages of the developed method are:

- much fewer measured data are required compared with the LSM-based method presented in Chapter 2. The measurement is carried out on the assembled structure. No measurements are needed from the substructures. The measurement DOFs on the assembly are not necessarily to be on the interface between the substructures. In principle, any DOF at which a variation of joint parameters is reflected can be a measurement DOF. The reduction of measurement points also decreases the errors caused by inconsistency of measured FRFs and by measurement noise *etc*.;

- it is not sensitive to noise on the FRF input data. In other words, the developed method is robust. This advantage is important since measured FRFs are more or less always contaminated by noise;
- it can be extended for use in finite element model updating. Instead of using only the measured FRFs, this method is a type of hybrid method, using both the analytical model as well as measured data. The concept is to find a group of joint parameters which make the system behave with the same dynamic characteristics as those shown in the measured FRFs. If we consider the joint parameters as the parameters to be updated in an assembled structure, as the uncertainty of these parameters is obvious, the process of joint parameter identification is exactly a case of finite element model updating. Therefore, the proposed method can be regarded as a updating/modification method as well dealing with assembled structures.

The advantages given above suggest that it is promising to apply this method to practical structures. The application and further investigation will be subject of future work.

CHAPTER 4

VIBRATION ANALYSIS OF COUPLED STRUCTURES - CMS METHODS

4.1. INTRODUCTION

Component mode synthesis (CMS) techniques have been developed and used extensively in the dynamic analysis of structures for over three decades. The original idea, proposed in [CrBa68], was to idealise a structural system as an assembly of discrete structural components or substructures, thereby obtaining sets of matrix equations which predict the modal properties of the assembly. With the development of the finite element method and more and more powerful computers, the fundamental idea was then implemented and applied in practice. The motivation and expectations of CMS method were clearly described by Hintz [Hint75]. These descriptions were then widely referred by the followers.

The successful design of structures requires analysis for dynamic displacement and stress responses when the structure is placed in its operating environment. A vital part of this effort is the modal analysis of structural finite element models. In the classical approach, it is usual to determine normal modes and auxiliary static analysis directly from the finite element model. Complete structural systems have become very complex and major components are often produced by different organisations. As a result, it is often difficult to assemble an entire finite element model in a timely manner. In addition, many finite element models may contain so many degrees of freedom that they cannot be handled directly on the computers in use. For these reasons, it is desirable to develop methods for analysing substructures of a finite element model. Such analysis has come to be known as *Component Modal Synthesis* (CMS) in dynamics and *Substructure Analysis* in statics. It is desirable that component mode techniques for dynamic analysis of structures have the following characteristics [Hint75]:

- *Computational efficiency*: With the advent of powerful computers, finite element static analyses structural problem with 100,000 DOFs or more have become almost routine. However, problems with only 50,000 DOF can still challenge the finite element dynamic analyses of structural problems, especially when natural frequencies and mode shapes must be computed [FaGe92]. While it is required that the component mode representation should contain a minimum number of independent degrees of freedom or modes for each component.
- *Interchangeability*: The component mode set should be independent of the inertial and stiffness properties of adjacent components. Such a component mode set may be used interchangeably in different structural systems with compatible interfaces.
- *Boundary flexibility*: The method should permit optional interface degrees of freedom in a component mode set that may be used or discarded at the stage of synthesis. Such a mode set need not be redefined for each potential interface or potential combination of interfaces.

- *Synthesis flexibility*: A synthesis technique should not be constrained to a particular type of component mode set. Synthesis techniques should be amenable to accepting different types of component mode sets (i.e., fixed interface, free interface or inertia loading, etc.)

There are several different CMS formulations and they can be grouped into three different categories: fixed-interface, free-interface or hybrid methods. This classification is based on whether the modes are obtained with the coupling co-ordinates fixed, free or a combination of these two.

The principle of the CMS technique is that the substructures are projected from the physical space onto the mode subspace spanned by a selected set of a few lower mode shapes and other supplementary modes. As a result, the governing equations of the structure can be reduced. Hence, modal analysis at the substructure level is the basic computational effort in CMS methods. However, it has not been notified that the contribution of connections between the substructures to the modal properties of the assembly.

The objective of the study presented in this chapter is to develop such a modal synthesis method in which the free interface substructures are not directly coupled to each other as customarily done through their nodal interfaces. Instead, there are particular media that connect these substructures, which are independent of the modal analysis of the substructures. These connections are termed joints. In principle, the behaviour of joints can be linear or non-linear. The method presented here is for linear joints only. Its application to non-linear joints is not included in this study since it is beyond the scope of this thesis.

Several concepts are described below before the introduction of the method. They are *normal modes*, *constraint modes*, *rigid body modes*, *attachment modes* and *inertia relief attachment modes*.

NORMAL MODES

Substructure normal modes are defined as the solutions of an eigen-value problem

$$\left(\mathbf{k} - \omega_r^2 \mathbf{m}\right)\boldsymbol{\varphi}_r = \mathbf{0} \tag{4.1}$$

It is assumed that the modes are normalised with respect to mass matrix, $\mathbf{m}$, such that

$$\boldsymbol{\Phi}_n^T \mathbf{m} \boldsymbol{\Phi}_n = \mathbf{I}_n, \quad \boldsymbol{\Phi}_n^T \mathbf{k} \boldsymbol{\Phi}_n = \boldsymbol{\Lambda}_n \equiv diag\left(\omega_r^2\right) \tag{4.2}$$

where $\boldsymbol{\Phi}_n$ is a matrix whose columns are the substructure modes. The complete normal mode set is hereafter denoted by a subscript *n* as $\boldsymbol{\Phi}_n$, and the normal mode set which is usually truncated to a set of normal modes is denoted by substript *k* as $\boldsymbol{\Phi}_k$, for kept modes.

CONSTRAINT MODES

Let the physical coordinates, $\mathbf{x}$, be partitioned into a set *C* relative to which constraint modes are to be defined, and let *V* be the complement of *C*. A constraint mode is defined by statically imposing a unit displacement on one physical coordinate in the *C* set and zero displacement on the remaining coordinates of the *C* set. Thus, the set of constraint modes is defined by the equation

$$\begin{bmatrix} \mathbf{k}_{vv} & \mathbf{k}_{vc} \\ \mathbf{k}_{cv} & \mathbf{k}_{cc} \end{bmatrix} \begin{bmatrix} \boldsymbol{\Psi}_{vc} \\ \mathbf{I}_{cc} \end{bmatrix} = \begin{bmatrix} \mathbf{0}_{vc} \\ \mathbf{R}_{cc} \end{bmatrix} \tag{4.3}$$

where $\mathbf{R}_{cc}$ is the set of "reactions" at the *C* coordinates. From the top row of the partition

$$\boldsymbol{\Psi}_{vc} = -\mathbf{k}_{vv}^{-1} \mathbf{k}_{vc} \tag{4.4}$$

The constraint mode matrix is thus

$$\boldsymbol{\Psi}_c \equiv \begin{bmatrix} \boldsymbol{\Psi}_{vc} \\ \mathbf{I}_{cc} \end{bmatrix} = \begin{bmatrix} \mathbf{k}_{vv}^{-1} \mathbf{k}_{vc} \\ \mathbf{I}_{cc} \end{bmatrix} \tag{4.5}$$

RIGID-BODY MODES

Although rigid-body modes may be obtained in the process of solving the eigen-problem for component normal modes, they are also a special case of constraint modes. If a component has r rigid-body degrees of freedom, then an R set of coordinates may be used to restrain the component against rigid-body motion. The rigid-body modes corresponding to the R set are obtained by altering subscript c to r in (4.5) and noting that there is no reaction at the statically determinate constraint set R, that is, $\mathbf{R}_{rr} = \mathbf{0}$. Thus, if V is the complement of R, rigid-body modes are defined by

$$\boldsymbol{\Psi}_r \equiv \begin{bmatrix} \boldsymbol{\Psi}_{vr} \\ \mathbf{I}_{rr} \end{bmatrix} = \begin{bmatrix} \mathbf{k}_{vv}^{-1}\mathbf{k}_{vr} \\ \mathbf{I}_{rr} \end{bmatrix} \tag{4.6}$$

ATTACHMENT MODES

Let the physical co-ordinates of a component be divided into three sets: R, A and V, where R is a statically determinate constraint set which provides restraint against rigid-body motion. An attachment mode is defined as the static deflection of the component which results when a unit force is exerted on one co-ordinate of the A set, while the remaining co-ordinates in A are force-free. Then the attachment modes relative to constraint set R are defined by

$$\left[\begin{array}{cc:c} \mathbf{k}_{vv} & \mathbf{k}_{va} & \mathbf{k}_{vr} \\ \mathbf{k}_{av} & \mathbf{k}_{aa} & \mathbf{k}_{ar} \\ \hdashline \mathbf{k}_{rv} & \mathbf{k}_{ra} & \mathbf{k}_{rr} \end{array}\right] \left[\begin{array}{c} \boldsymbol{\Psi}_{va} \\ \boldsymbol{\Psi}_{aa} \\ \hdashline \mathbf{0}_{ra} \end{array}\right] = \left[\begin{array}{c} \mathbf{0}_{va} \\ \mathbf{I}_{aa} \\ \hdashline \mathbf{R}_{ra} \end{array}\right] \tag{4.7}$$

The attachment modes are essentially columns of a flexibility matrix, $\mathbf{g}$. Thus,

$$\boldsymbol{\Psi}_a = \begin{bmatrix} \boldsymbol{\Psi}_{va} \\ \boldsymbol{\Psi}_{aa} \\ \mathbf{0}_{ra} \end{bmatrix} = \begin{bmatrix} \mathbf{g}_{va} \\ \mathbf{g}_{aa} \\ \mathbf{0}_{ra} \end{bmatrix} \tag{4.8}$$

where $\mathbf{g}_{va}$ and $\mathbf{g}_{aa}$ are from the inverse of the upper-left partition of $\mathbf{k}$ in (4.7).

INERTIA RELIEF ATTACHMENT MODES

An alternative manner of defining attachment modes for a substructure with rigid-body freedoms leads to the so-called *inertia relief modes*. Inertia relief

modes are obtained by applying to an unrestrained substructure an equilibrated load system, $\mathbf{f}_e$, which consists of the originally-specified force vector, $\mathbf{f}$, equilibrated by the rigid body d'Alembert force vector, $\mathbf{m}\ddot{\mathbf{x}}_r$, where $\mathbf{x}_r$ is the rigid-body motion due to $\mathbf{f}$. Let the rigid-body modes, $\boldsymbol{\Psi}_r$, be orthonormalised so that

$$\boldsymbol{\Psi}_r^T \mathbf{m} \boldsymbol{\Psi}_r = \mathbf{I}_r \tag{4.9}$$

Then

$$\mathbf{f}_e = \mathbf{f} - \mathbf{m}\ddot{\mathbf{x}}_r = \mathbf{P}\mathbf{f} \tag{4.10}$$

where

$$\mathbf{P} = \mathbf{I} - \mathbf{m}\boldsymbol{\Psi}_r \boldsymbol{\Psi}_r^T \tag{4.11}$$

Matrix $\mathbf{P}$ designates the *inertia-relief loading matrix* and is simply an identity matrix when there are no rigid-body modes.

The derivation of (4.10) comes from the normal equation of motion of the substructure

$$\boldsymbol{\Psi}_r^T \mathbf{m} \boldsymbol{\Psi}_r \ddot{\mathbf{q}}_r + \boldsymbol{\Psi}_r^T \mathbf{k} \boldsymbol{\Psi}_r \mathbf{q}_r = \boldsymbol{\Psi}_r^T \mathbf{f} \tag{4.12}$$

Because $\mathbf{k}\mathbf{x}_r = \mathbf{0}$, the corresponding acceleration is obtained

$$\ddot{\mathbf{x}}_r = \boldsymbol{\Psi}_r \left(\boldsymbol{\Psi}_r^T \mathbf{m} \boldsymbol{\Psi}_r \right)^{-1} \boldsymbol{\Psi}_r^T \mathbf{f} \tag{4.13}$$

Therefore

$$\ddot{\mathbf{x}}_r = \boldsymbol{\Psi}_r \boldsymbol{\Psi}_r^T \mathbf{f} \tag{4.14}$$

Thus, the imposed forces due to *uniform acceleration* in the rigid-body DOFs can be expressed as

$$\mathbf{f}_r = \mathbf{m}\boldsymbol{\Psi}_r \boldsymbol{\Psi}_r^T \mathbf{f} \tag{4.15}$$

A special flexibility matrix of the unrestrained system is defined as:

$$\mathbf{G} = \begin{bmatrix} \tilde{\mathbf{k}}^{-1}_{(N-r)\times(N-r)} & \mathbf{0}_{(N-r)\times r} \\ \mathbf{0}_{r\times(N-r)} & \mathbf{0}_{r\times r} \end{bmatrix}_{N\times N} \tag{4.16}$$

where the singular stiffness system matrix, $\mathbf{k}$, has been constrained at r DOFs to remove rigid-body motion and $\tilde{\mathbf{k}}^{-1}$ is its corresponding flexibility matrix. The flexibility matrix, $\mathbf{G}$, is therefore expanded with zeros at r DOFs to all N DOFs of the FE model. Hence, the singularity of $\mathbf{k}$ and $\mathbf{G}$ is the same and both matrices are of rank $(N-r)$.

Upon applying the equilibrated forces onto the static flexibility matrix $\mathbf{G}$ the corresponding deflection of the constraint component is

$$\hat{\boldsymbol{\Psi}} = \mathbf{G}\mathbf{f}_e \tag{4.17}$$

Since it is of interest to find elastic attachment modes $\boldsymbol{\Psi}_a$ and elastic modes are orthogonal to all r rigid-body modes, i.e.

$$\boldsymbol{\Psi}_r^T \mathbf{m} \boldsymbol{\Psi}_a = \mathbf{0} \tag{4.18}$$

and the contribution of the constraint component of r rigid-body modes can be removed from $\hat{\boldsymbol{\Psi}}$ by:

$$\boldsymbol{\Psi}_a = \hat{\boldsymbol{\Psi}} - \boldsymbol{\Psi}_r \mathbf{q}_r \tag{4.19}$$

then the attachment modes are found by pre-multiplying equation (4.19) with $\boldsymbol{\Psi}_r^T \mathbf{m}$ and solving for the generalised co-ordinates, $\mathbf{q}_r$, of the rigid-body modes from

$$\boldsymbol{\Psi}_r^T \mathbf{m} \boldsymbol{\Psi}_a = \boldsymbol{\Psi}_r^T \mathbf{m} \hat{\boldsymbol{\Psi}} - \boldsymbol{\Psi}_r^T \mathbf{m} \boldsymbol{\Psi}_r \mathbf{q}_r \tag{4.20}$$

which resolves simply to

$$\mathbf{q}_r = \left(\boldsymbol{\Psi}_r^T \mathbf{m} \boldsymbol{\Psi}_r\right)^{-1} \boldsymbol{\Psi}_r^T \mathbf{m} \hat{\boldsymbol{\Psi}} \tag{4.21}$$

Substituting equation (4.21) into equation (4.19) leads therefore to

$$\boldsymbol{\Psi}_a = \left(\mathbf{I} - \boldsymbol{\Psi}_r \left(\boldsymbol{\Psi}_r^T \mathbf{m} \boldsymbol{\Psi}_r\right)^{-1} \boldsymbol{\Psi}_r^T \mathbf{m}\right) \hat{\boldsymbol{\Psi}} \tag{4.22}$$

$$\boldsymbol{\Psi}_a = \left(\mathbf{I} - \boldsymbol{\Psi}_r \boldsymbol{\Psi}_r^T \mathbf{m}\right) \hat{\boldsymbol{\Psi}} \tag{4.23}$$

which are the flexible attachment modes as a linear combination of the columns of the constraint deflections.

Close inspection of equations (4.10), (4.11) and (4.17), however, reveals that equation (4.23) is also:

$$\boldsymbol{\Psi}_a = \mathbf{P}^T \hat{\boldsymbol{\Psi}} \tag{4.24}$$

$$\boldsymbol{\Psi}_a = \mathbf{P}^T \mathbf{G}\mathbf{f}_e \tag{4.25}$$

$$\boldsymbol{\Psi}_a = \mathbf{P}^T \mathbf{G}\mathbf{P}\mathbf{f} \tag{4.26}$$

or

$$\boldsymbol{\Psi}_a = \mathbf{G}^e \mathbf{f} \tag{4.27}$$

where $\mathbf{G}^e$ is referred to as the *elastic flexibility matrix*. Therefore, in order to gain access to the flexibility matrix, $\mathbf{G}$, artificial boundary conditions have been imposed on the stiffness matrix $\mathbf{k}$ and these have, in effect, been eliminated with the transformation (or projection) matrix, $\mathbf{P}$, leading to $\mathbf{G}^e$.

When the force vector, $\mathbf{f}$, is expanded to a matrix and it has unit entries at the junction DOFs and zeros elsewhere as specified in the definition of attachment mode, $\boldsymbol{\Psi}_a$ defined in (4.26) is named *Inertia Relief Attachment Modes*.

4.2. REVIEW OF THE ESSENTIAL PRINCIPLES

The general principle of a method for reducing the size of an eigen-value problem

$$(-\omega^2 \mathbf{m} + \mathbf{k})\mathbf{x} = \mathbf{0} \tag{4.28}$$

consists of building a subspace $\mathbf{T}$ in such a way that the solution of (4.28) can be written in the form

$$\mathbf{x} = \mathbf{T}\mathbf{q} \tag{4.29}$$

where $\mathbf{x}$ is the physical coordinates, $\mathbf{q}$ is the substructure generalised coordinates and $\mathbf{T}$ is generally a matrix of preselected substructure modes of

the following types: rigid-body modes, normal modes of free vibration, constraint modes, and attachment modes.

If we go back to the origin variational form of Lagrange equation from which (4.28) is derived

$$\delta(\frac{1}{2}\mathbf{x}^T\mathbf{k}\mathbf{x} - \frac{1}{2}\omega^2\mathbf{x}^T\mathbf{m}\mathbf{x}) = \mathbf{0} \tag{4.30}$$

we can deduce the reduced problem in the form

$$\delta(\frac{1}{2}\mathbf{q}^T\bar{\mathbf{k}}\mathbf{q} - \frac{1}{2}\omega^2\mathbf{q}^T\bar{\mathbf{m}}\mathbf{q}) = \mathbf{0} \tag{4.31}$$

That is to say

$$(-\omega^2\bar{\mathbf{m}} + \bar{\mathbf{k}})\mathbf{q} = \mathbf{0} \tag{4.32}$$

with the reduced stiffness and mass matrices

$$\bar{\mathbf{k}} = \mathbf{T}^T\mathbf{k}\mathbf{T} \text{ and } \bar{\mathbf{m}} = \mathbf{T}^T\mathbf{m}\mathbf{T} \tag{4.33}$$

Various substructuring methods differ from each other by the determination of the reduction matrix, $\mathbf{T}$. Three of the methods, which are based on the free-interface concept, will be reviewed in this section and a more general expression – a unified form of these methods – will be given. It is beneficial to understand the connections in theory and also useful to integrate these methods into one code for practical applications.

4.2.1. CMS without Residual Compensation

This is Craig-Bampton method [CrBa68]. The normal modes of each substructure can be obtained from the solution of the following eigen-value problem

$$(-\omega^2\mathbf{m} + \mathbf{k})\mathbf{x} = \mathbf{0} \tag{4.34}$$

Defining the uncoupled system as a collection of two subsystems, A and B, without connecting to each other, we denote the number of DOFs as $n = n_A + n_B$ and the number of modes of the uncoupled system as

$m = m_A + m_B$. The equation of motion of the uncoupled system in normal co-ordinate is then

$$[\mathbf{I}]\begin{Bmatrix} {}_A\ddot{\mathbf{p}} \\ \cdots \\ {}_B\ddot{\mathbf{p}} \end{Bmatrix}_{m\times 1} + \begin{bmatrix} {}_A\boldsymbol{\omega}^2 & \vdots & \mathbf{0} \\ \cdots & \vdots & \cdots \\ \mathbf{0} & \vdots & {}_B\boldsymbol{\omega}^2 \end{bmatrix}_{m\times m} \begin{Bmatrix} {}_A\mathbf{p} \\ \cdots \\ {}_B\mathbf{p} \end{Bmatrix} = \begin{bmatrix} {}_A\boldsymbol{\Phi}^T & \vdots & \mathbf{0} \\ \cdots & \vdots & \cdots \\ \mathbf{0} & \vdots & {}_B\boldsymbol{\Phi}^T \end{bmatrix}_{m\times n} \begin{Bmatrix} {}_A\mathbf{f} \\ \cdots \\ {}_B\mathbf{f} \end{Bmatrix}_{n\times 1} \tag{4.35}$$

Corresponding to the compatibility equation for the interface displacements

$${}_A\mathbf{x}^c = {}_B\mathbf{x}^c \tag{4.36}$$

we have

$$\begin{bmatrix} {}_A\boldsymbol{\Phi}^c & \vdots & -{}_B\boldsymbol{\Phi}^c \end{bmatrix}_{n_c\times m} \begin{Bmatrix} {}_A\mathbf{p} \\ \cdots \\ {}_B\mathbf{p} \end{Bmatrix}_{m\times 1} = \mathbf{S}\mathbf{p} = \mathbf{0} \tag{4.37}$$

The matrix $\mathbf{S}$ may be partitioned as

$$\begin{bmatrix} \mathbf{S}_d & \vdots & \mathbf{S}_i \end{bmatrix} \begin{Bmatrix} \mathbf{p}_d \\ \cdots \\ \mathbf{p}_i \end{Bmatrix} = \mathbf{0} \tag{4.38}$$

where $\mathbf{S}_d \in \Re^{n_c\times n_c}$ is a non-singular square matrix and $\mathbf{S}_i \in \Re^{n_c\times(m-n_c)}$ is the remaining part of $\mathbf{S}$. This requires that the total number of modes for both components ($m = m_A + m_B$) be greater than the number of connection co-ordinates n_c, $m > n_c$. Making use of this partition we have,

$$\mathbf{p}_d = -\mathbf{S}_d^{-1}\mathbf{S}_i\mathbf{p}_i \tag{4.39}$$

Then, the following transformation matrix can be constructed as

$$\begin{Bmatrix} {}_A\mathbf{p} \\ \cdots \\ {}_B\mathbf{p} \end{Bmatrix} = \begin{Bmatrix} \mathbf{p}_d \\ \cdots \\ \mathbf{p}_i \end{Bmatrix} = \begin{bmatrix} -\mathbf{S}_d^{-1}\mathbf{S}_i \\ \cdots \\ \mathbf{I} \end{bmatrix} \mathbf{p}_i \tag{4.40}$$

$$\begin{Bmatrix} {}_A\mathbf{p} \\ \cdots \\ {}_B\mathbf{p} \end{Bmatrix} = \mathbf{T}\mathbf{q} \tag{4.41}$$

To generate the matrix $\mathbf{T} \in \Re^{m\times(m-n_c)}$, a set of m_i independent vectors $\mathbf{S}_i$ must be obtained from matrix $\mathbf{S}$, while a set of m_d dependent vectors $\mathbf{S}_d$ is retained.

Substituting (4.41) into equation (4.35) and pre-multiplying by $\mathbf{T}^T$ yields,

$$\overline{\mathbf{m}}\ddot{\mathbf{q}} + \overline{\mathbf{k}}\mathbf{q} = \overline{\mathbf{f}} \tag{4.42}$$

where

$$\overline{\mathbf{m}} = \mathbf{T}^T\mathbf{T} \tag{4.43}$$

$$\overline{\mathbf{k}} = \mathbf{T}^T \begin{bmatrix} {}_A\boldsymbol{\omega}^2 & \vdots & \mathbf{0} \\ \cdots & \vdots & \cdots \\ \mathbf{0} & \vdots & {}_B\boldsymbol{\omega}^2 \end{bmatrix} \mathbf{T} \tag{4.44}$$

$$\overline{\mathbf{f}} = \mathbf{T}^T \begin{bmatrix} {}_A\boldsymbol{\Phi}^{cT} \\ \cdots \\ -{}_B\boldsymbol{\Phi}^{cT} \end{bmatrix} \mathbf{f}^c \tag{4.45}$$

according to the equilibrium condition:

$${}_A\mathbf{f}^c = -{}_B\mathbf{f}^c = \mathbf{f}^c \tag{4.46}$$

The right-hand-side of equation (4.42) vanishes, since no external forces are acting on the coupled system. Thus, the solution of this equation gives the $(m-n_c)$ natural frequencies $\boldsymbol{\omega}^2$ and mode shapes $\overline{\boldsymbol{\Phi}}$ for the overall system, but referred to the $\mathbf{q}$ co-ordinates. The mode shapes are then transformed to the original co-ordinates, $\mathbf{x}$, according to

$$\boldsymbol{\Phi} = \begin{bmatrix} {}_A\boldsymbol{\Phi} & \vdots & \mathbf{0} \\ \cdots & \vdots & \cdots \\ \mathbf{0} & \vdots & {}_B\boldsymbol{\Phi} \end{bmatrix} \mathbf{T}\overline{\boldsymbol{\Phi}} \tag{4.47}$$

The common coordinates of substructure A and substructure B should be deleted afterwards from $\boldsymbol{\Phi}$.

4.2.2. Residual Compensation – First and Second Order Approximations

The first free-free CMS formulation including residual compensation was proposed by MacNeal in 1971 [MacN71]. It contains a first-order approximation to the residual terms and is also called the static residual compensation method.

The mode-shape matrix of each sub-system is partitioned according to lower and higher modes. The lower modes include all rigid-body modes and all low-frequency elastic modes. The higher modes are the unknown out-of-range ones, which are generally truncated due to the need to limit the measured/analysis frequency range.

For any of the substructures, we have

$$\begin{bmatrix} \boldsymbol{\omega}_l^2 - \omega^2\mathbf{I} & \vdots & \mathbf{0} \\ \cdots & \vdots & \cdots \\ \mathbf{0} & \vdots & \boldsymbol{\omega}_h^2 - \omega^2\mathbf{I} \end{bmatrix} \begin{Bmatrix} \mathbf{p}_l \\ \cdots \\ \mathbf{p}_h \end{Bmatrix} = \begin{bmatrix} \boldsymbol{\Phi}_l^T \\ \cdots \\ \boldsymbol{\Phi}_h^T \end{bmatrix} \mathbf{f} \tag{4.48}$$

The normal equation related to the high-order modes is then

$$\left(\boldsymbol{\omega}_h^2 - \omega^2\mathbf{I}\right)\mathbf{p}_h = \boldsymbol{\Phi}_h^T\mathbf{f} \tag{4.49}$$

In the case when

$$\omega_h^2 > \omega^2 \tag{4.50}$$

we have

$$\left(\boldsymbol{\omega}_h^2 - \omega^2\mathbf{I}\right)^{-1} = \left(\boldsymbol{\omega}_h^2\right)^{-1} + \omega^2\left(\boldsymbol{\omega}_h^2\right)^{-2} + \omega^4\left(\boldsymbol{\omega}_h^2\right)^{-3} + \quad \cdots\cdots \tag{4.51}$$

If only the first term on the right hand side of equation (4.51) is taken into acount, we have the first order approximation of the normal coordinates

$$\mathbf{p}_h = (\boldsymbol{\omega}_h^2)^{-1}\boldsymbol{\Phi}_h^T\mathbf{f} \tag{4.52}$$

If the first two terms are taken into acount, we then have

$$\mathbf{p}_h = \left((\boldsymbol{\omega}_h^2)^{-1} + \omega^2(\boldsymbol{\omega}_h^2)^{-2}\right)\boldsymbol{\Phi}_h^T\mathbf{f} \tag{4.53}$$

Substituting (4.52) and (4.53) back into the physical coordinates, we have

$$\mathbf{x} = \mathbf{\Phi}_l \mathbf{p}_l + \mathbf{R}\mathbf{f} \tag{4.54}$$

and

$$\mathbf{x} = \mathbf{\Phi}_l \mathbf{p}_l + \mathbf{R}\mathbf{f} + \omega^2 \overline{\mathbf{R}}\mathbf{f} \tag{4.55}$$

where

$$\mathbf{R} = \mathbf{\Phi}_h (\boldsymbol{\omega}_h^2)^{-1} \mathbf{\Phi}_h^T \tag{4.56}$$

$$\overline{\mathbf{R}} = \mathbf{\Phi}_h (\boldsymbol{\omega}_h^2)^{-2} \mathbf{\Phi}_h^T \tag{4.57}$$

and also

$$\overline{\mathbf{R}} = \mathbf{R}^T \mathbf{m} \mathbf{R} \tag{4.58}$$

Considering the coupling coordinates only, for the first order approximation, we have

$$\mathbf{u}^c = \mathbf{\Phi}_l^c \mathbf{p}_l + \mathbf{R}^c \mathbf{f}^c \tag{4.59}$$

and for the second order approximation

$$\mathbf{u}^c = \mathbf{\Phi}_l^c \mathbf{p}_l + \left(\mathbf{R}^c + \omega^2 \overline{\mathbf{R}}^c\right) \mathbf{f}^c \tag{4.60}$$

For the coupling analysis using the *first-order approximation*, the compatibility condition (4.36) becomes

$${}_A\mathbf{\Phi}_l^c \; {}_A\mathbf{p}_l + {}_A\mathbf{R}^c \; {}_A\mathbf{f}^c = {}_B\mathbf{\Phi}_l^c \; {}_B\mathbf{p}_l + {}_B\mathbf{R}^c \; {}_B\mathbf{f}^c \tag{4.61}$$

Applying the equilibrium condition (4.46) to (4.61), we have

$${}_A\mathbf{f}^c = \left({}_A\mathbf{R}^c + {}_B\mathbf{R}^c\right)^{-1} \left[-{}_A\mathbf{\Phi}_l^c \quad \vdots \quad {}_B\mathbf{\Phi}_l^c \right] \begin{Bmatrix} {}_A\mathbf{p}_l \\ \cdots \\ {}_B\mathbf{p}_l \end{Bmatrix} \tag{4.62}$$

$${}_B\mathbf{f}^c = \left({}_A\mathbf{R}^c + {}_B\mathbf{R}^c\right)^{-1} \left[{}_A\mathbf{\Phi}_l^c \quad \vdots \quad -{}_B\mathbf{\Phi}_l^c \right] \begin{Bmatrix} {}_A\mathbf{p}_l \\ \cdots \\ {}_B\mathbf{p}_l \end{Bmatrix} \tag{4.63}$$

Substituting (4.62) and (4.63) into (4.35), we form the coupled equation of motion

$$[\mathbf{I}]\begin{Bmatrix} {}_A\ddot{\mathbf{p}}_l \\ {}_B\ddot{\mathbf{p}}_l \end{Bmatrix}+\left(\begin{bmatrix} {}_A\boldsymbol{\omega}_l^2 & \mathbf{0} \\ \mathbf{0} & {}_B\boldsymbol{\omega}_l^2 \end{bmatrix}+\begin{bmatrix} {}_A\boldsymbol{\Phi}_l^{cT} & \mathbf{0} \\ \mathbf{0} & {}_B\boldsymbol{\Phi}_l^{cT} \end{bmatrix}\overline{\mathbf{K}}\begin{bmatrix} {}_A\boldsymbol{\Phi}_l^{c} & -{}_B\boldsymbol{\Phi}_l^{c} \\ -{}_A\boldsymbol{\Phi}_l^{c} & {}_B\boldsymbol{\Phi}_l^{c} \end{bmatrix}\right)\begin{Bmatrix} {}_A\mathbf{p}_l \\ {}_B\mathbf{p}_l \end{Bmatrix}=\begin{Bmatrix} \mathbf{0} \\ \mathbf{0} \end{Bmatrix} \quad (4.64)$$

where

$$\overline{\mathbf{K}}=\left({}_A\mathbf{R}^c+{}_B\mathbf{R}^c\right)^{-1} \quad (4.65)$$

The mode matrix from equation (4.64) can be transformed to physical space by

$$\boldsymbol{\Phi}_x^c=\mathbf{P}\mathbf{Q}\,\boldsymbol{\Phi}_p^c \quad (4.66)$$

where

$$\mathbf{P}=\begin{bmatrix} {}_A\boldsymbol{\Phi}_l^s & {}_A\mathbf{R}^{sc} & \mathbf{0} & \mathbf{0} \\ {}_A\boldsymbol{\Phi}_l^c & {}_A\mathbf{R}^{cc} & \mathbf{0} & \mathbf{0} \\ \mathbf{0} & \mathbf{0} & {}_B\boldsymbol{\Phi}_l^c & {}_B\mathbf{R}^{cc} \\ \mathbf{0} & \mathbf{0} & {}_B\boldsymbol{\Phi}_l^s & {}_B\mathbf{R}^{sc} \end{bmatrix} \quad (4.67)$$

$$\mathbf{Q}=\begin{bmatrix} \mathbf{I} & \mathbf{0} \\ -\overline{\mathbf{K}}\,{}_A\boldsymbol{\Phi}_l^c & \overline{\mathbf{K}}\,{}_B\boldsymbol{\Phi}_l^c \\ \mathbf{0} & \mathbf{I} \\ \overline{\mathbf{K}}\,{}_A\boldsymbol{\Phi}_l^c & -\overline{\mathbf{K}}\,{}_B\boldsymbol{\Phi}_l^c \end{bmatrix} \quad (4.68)$$

For the coupling analysis using the *second-order approximation*, the compatibility condition is then

$${}_A\boldsymbol{\Phi}_l^c\;{}_A\mathbf{p}_l+\left({}_A\mathbf{R}^c+\omega^2\,{}_A\overline{\mathbf{R}}^c\right){}_A\mathbf{f}^c={}_B\boldsymbol{\Phi}_l^c\;{}_B\mathbf{p}_l+\left({}_B\mathbf{R}^c+\omega^2\,{}_B\overline{\mathbf{R}}^c\right){}_B\mathbf{f}^c \quad (4.69)$$

Introducing the equilibrium equation, we have

$${}_A\boldsymbol{\Phi}_l^c\;{}_A\mathbf{p}_l-{}_B\boldsymbol{\Phi}_l^c\;{}_B\mathbf{p}_l=\left(\left({}_A\mathbf{R}^c+{}_B\mathbf{R}^c\right)+\omega^2\left({}_A\overline{\mathbf{R}}^c+{}_B\overline{\mathbf{R}}^c\right)\right){}_B\mathbf{f}^c \quad (4.70)$$

Pre-multiplying (4.70) by $\overline{\mathbf{K}}$, we have

$${}_B\mathbf{f}^c=\left(\mathbf{I}_B+\omega^2\overline{\mathbf{K}}\left({}_A\overline{\mathbf{R}}^c+{}_B\overline{\mathbf{R}}^c\right)\right)^{-1}\overline{\mathbf{K}}\left({}_A\boldsymbol{\Phi}_l^c\;{}_A\mathbf{p}_l-{}_B\boldsymbol{\Phi}_l^c\;{}_B\mathbf{p}_l\right) \quad (4.71)$$

The matrix inverse in (4.71) can be approximated by the first two terms of its MacLaurin series expansion as

$$\left(\mathbf{I}_B+\omega^2\overline{\mathbf{K}}\left({}_A\overline{\mathbf{R}}^c+{}_B\overline{\mathbf{R}}^c\right)\right)^{-1}\approx\mathbf{I}_B-\omega^2\overline{\mathbf{K}}\left({}_A\overline{\mathbf{R}}^c+{}_B\overline{\mathbf{R}}^c\right) \quad (4.72)$$

Let

$$\overline{\mathbf{M}} = \overline{\mathbf{K}}\left({}_A\overline{\mathbf{R}}^c + {}_B\overline{\mathbf{R}}^c\right)\overline{\mathbf{K}} \tag{4.73}$$

we have

$${}_B\mathbf{f}^c = \left(\overline{\mathbf{K}} + \omega^2\overline{\mathbf{M}}\right)\left({}_A\boldsymbol{\Phi}_l^c \;{}_A\mathbf{p}_l - {}_B\boldsymbol{\Phi}_l^c \;{}_B\mathbf{p}_l\right) \tag{4.74}$$

According to the condition of equilibrium, we have the expression of

$${}_A\mathbf{f}^c = \left(\overline{\mathbf{K}} + \omega^2\overline{\mathbf{M}}\right)\left(-{}_A\boldsymbol{\Phi}_l^c \;{}_A\mathbf{p}_l + {}_B\boldsymbol{\Phi}_l^c \;{}_B\mathbf{p}_l\right) \tag{4.75}$$

Substituting equation (4.74) and (4.75) into (4.35), we have

$$\left(\mathbf{I} + \mathbf{U}\overline{\mathbf{M}}\mathbf{V}\right)\begin{Bmatrix} {}_A\ddot{\mathbf{p}}_l \\ \cdots \\ {}_B\ddot{\mathbf{p}}_l \end{Bmatrix} + \left(\boldsymbol{\omega}_l^2 + \mathbf{U}\overline{\mathbf{K}}\mathbf{V}\right)\begin{Bmatrix} {}_A\mathbf{p}_l \\ \cdots \\ {}_B\mathbf{p}_l \end{Bmatrix} = \mathbf{0}_{n_c\times 1} \tag{4.76}$$

where

$$\mathbf{U} = \begin{bmatrix} {}_A\boldsymbol{\Phi}_l^{cT} & \mathbf{0} \\ \mathbf{0} & {}_B\boldsymbol{\Phi}_l^{cT} \end{bmatrix} \tag{4.77}$$

$$\mathbf{V} = \begin{bmatrix} {}_A\boldsymbol{\Phi}_l^{cT} & -{}_B\boldsymbol{\Phi}_l^{cT} \\ -{}_A\boldsymbol{\Phi}_l^{cT} & {}_B\boldsymbol{\Phi}_l^{cT} \end{bmatrix} \tag{4.78}$$

To convert the mode shape matrix obtained from (4.76) to physical coordinates, equations (4.66) can be used again, despite the second order approximation for the residual terms. $\|\overline{\mathbf{R}}\|$ is nomally very small relative to $\|\mathbf{R}\|$ and its influence in the mode shape matrix is virtually negligible.

4.3. CMS WITH JOINTS CONSIDERED METHOD (CMSJ)

The CMS methods reviewed in the last section do not include the contribution of joints between substructures. The connections of substructures are therefore supposed to be rigid. This assumption can be invalid in some engineering structures where their components are connected via bolted or some other joints. Urgueira´s method [Urgu89] takes the joint stiffness into account in the synthesis procedure but does not consider the effect of mode truncation. The method presented in this chapter overcomes these drawbacks by including both joints and compensation of mode truncation. Numerical simulation given in the

next section show that it can yield very good result even only a few modes from substructures are used.

4.3.1. Coupling Equations

The equations of motion of an assembled structure can be expressed as

$$\mathbf{M}\ddot{\mathbf{x}}(t) + \mathbf{C}\dot{\mathbf{x}}(t) + \mathbf{K}\mathbf{x}(t) = \mathbf{f}(t) \tag{4.79}$$

The stiffness matrix of the structure can be obtained from assembling the stiffness matrices of the substructures and the joints as

$$\mathbf{K} = \sum_{i=1}^{S} \boldsymbol{\alpha}_i^T \mathbf{k}_i \boldsymbol{\alpha}_i + \sum_{j=1}^{L} \boldsymbol{\beta}_j^T \mathbf{k}_j \boldsymbol{\beta}_j \tag{4.80}$$

where $\mathbf{k}_i$ is the stiffness matrix of the *i*-th free substructure, $\mathbf{k}_i \in \Re^{N_i \times N_i}$, $\mathbf{k}_j$ is the stiffness matrix of the *j*-th joint in its local physical coordinates, $\mathbf{k}_j \in \Re^{N_j \times N_j}$, $\boldsymbol{\alpha}_i \in \Re^{N_i \times N}$ and $\boldsymbol{\beta}_j \in \Re^{N_j \times N}$ are transformation assembly matrices. The total number of DOFs of the assembled structure is N and the number of substructures is S. N_i and N_j are the numbers of DOFs of the *i*-th free substructure and the *j*-th joint, respectively. The element of $\boldsymbol{\alpha}_i$ has the value of

$$\left(\alpha_{pq}\right)_i = \begin{cases} 1 & \text{if the } p^{\text{th}} \text{ local DOF is the } q^{\text{th}} \text{ global DOF} \\ 0 & \text{otherwise} \end{cases} \tag{4.81}$$

The matrix $\boldsymbol{\beta}_j$ has similar composition.

Similarly, the mass, damping and applied force matrices are formed as

$$\mathbf{M} = \sum_{i=1}^{S} \boldsymbol{\alpha}_i^T \mathbf{m}_i \boldsymbol{\alpha}_i + \sum_{j=1}^{L} \boldsymbol{\beta}_j^T \mathbf{m}_j \boldsymbol{\beta}_j \tag{4.82}$$

$$\mathbf{C} = \sum_{i=1}^{S} \boldsymbol{\alpha}_i^T \mathbf{c}_i \boldsymbol{\alpha}_i + \sum_{j=1}^{L} \boldsymbol{\beta}_j^T \mathbf{c}_j \boldsymbol{\beta}_j \tag{4.83}$$

$$\mathbf{f}(t) = \sum_{i=1}^{S} \boldsymbol{\alpha}_i^T \mathbf{f}_i(t) + \sum_{j=1}^{L} \boldsymbol{\beta}_j^T \mathbf{f}_j(t) \tag{4.84}$$

In the cases when there are no rigid-body modes in the substructures, the mode shapes for the *i*-th substructure are generated from the following eigenvalue equations:

$$\left(\mathbf{k}_i - \lambda_{ij}\mathbf{m}_i\right)\boldsymbol{\varphi}_{i,j} = \mathbf{0} \qquad \left(j = 1,2,...,N_i\right) \tag{4.85}$$

The displacement of the *i*-th substructure is therefore expressed in terms of the modal matrix as

$$\mathbf{x}_i = \boldsymbol{\Phi}_i \mathbf{q}_i \tag{4.86}$$

Because there are no internal DOFs in the joints, any DOF in the structure must belong to one and only one of the free substructures. Therefore, the displacement of a substructure can be independently expressed in terms of its mode shapes. The displacement vector of the whole structure is given by the simple equation:

$$\mathbf{x} = \begin{bmatrix} \boldsymbol{\Phi}_1 & \mathbf{0} & \cdots & \mathbf{0} \\ \mathbf{0} & \boldsymbol{\Phi}_2 & \cdots & \mathbf{0} \\ \cdots & \cdots & \cdots & \cdots \\ \mathbf{0} & \mathbf{0} & \cdots & \boldsymbol{\Phi}_S \end{bmatrix} \begin{Bmatrix} \mathbf{q}_1 \\ \mathbf{q}_2 \\ \vdots \\ \mathbf{q}_S \end{Bmatrix} = \mathbf{T}\mathbf{q} \tag{4.87}$$

where $\mathbf{T}$ is the transformation matrix of the structure from the physical coordinates to the normal coordinates.

Substituting (4.87) into (4.79) and pre-multiplying by $\mathbf{T}^T$, we have the governing dynamic equations for the assembled structure as

$$\mathbf{M}^*\ddot{\mathbf{q}}(t) + \mathbf{C}^*\dot{\mathbf{q}}(t) + \mathbf{K}^*\mathbf{q}(t) = \mathbf{f}^*(t) \tag{4.88}$$

where

$$\mathbf{M}^* = \mathbf{T}^T\mathbf{M}\mathbf{T},\ \mathbf{C}^* = \mathbf{T}^T\mathbf{C}\mathbf{T},\ \mathbf{K}^* = \mathbf{T}^T\mathbf{K}\mathbf{T} \text{ and } \mathbf{f}^*(t) = \mathbf{T}^T\mathbf{f}(t)$$

From equation (4.80), the generalised stiffness matrix $\mathbf{K}^*$ can be calculated for the substructures and the joints individually as

$$\mathbf{K}^* = \sum_{i=1}^{S} \mathbf{T}^T \boldsymbol{\alpha}_i^T \mathbf{k}_i \boldsymbol{\alpha}_i \mathbf{T} + \sum_{j=1}^{L} \mathbf{T}^T \boldsymbol{\beta}_j^T \mathbf{k}_j \boldsymbol{\beta}_j \mathbf{T} \tag{4.89}$$

According to the definition of the matrices $\boldsymbol{\alpha}_i$ and $\boldsymbol{\beta}_j$, the following relationships are evident:

$$\left.\begin{aligned}\boldsymbol{\alpha}_i\mathbf{T} &= \boldsymbol{\Phi}_i\boldsymbol{\alpha}_i^*\\ \boldsymbol{\beta}_j\mathbf{T} &= \boldsymbol{\Phi}_j\boldsymbol{\beta}_j^*\end{aligned}\right\} \tag{4.90}$$

where $\boldsymbol{\Phi}_i$ is the mode shape matrix of the *i*-th substructure; $\boldsymbol{\Phi}_j$ includes interface subvectors of the modal shapes of the free substructures which surround the *j*-th joint. $\boldsymbol{\alpha}_i^*$ and $\boldsymbol{\beta}_j^*$ have analogous form and function to $\boldsymbol{\alpha}_i$ and $\boldsymbol{\beta}_j$, which represent the relationship between the overall generalised coordinates and local generalised coordinates of the *i*-th substructure and the *j*-th joint. The relationship between the overall and the local physical coordinates is represented by $\boldsymbol{\alpha}_i$ and $\boldsymbol{\beta}_j$.

Substituting (4.90) into (4.89) leads to

$$\mathbf{K}^* = \sum_{i=1}^{S}\boldsymbol{\alpha}_i^{*T}\mathbf{k}_i^*\boldsymbol{\alpha}_i^* + \sum_{j=1}^{L}\boldsymbol{\beta}_j^{*T}\mathbf{k}_j^*\boldsymbol{\beta}_j^* \tag{4.91}$$

where

$$\mathbf{k}_i^* = \boldsymbol{\Phi}_i^T\mathbf{k}_i\boldsymbol{\Phi}_i \text{ and } \mathbf{k}_j^* = \boldsymbol{\Phi}_j^T\mathbf{k}_j\boldsymbol{\Phi}_j$$

A similar procedure is followed to obtain the corresponding expressions for the mass, damping and applied load. It is seen from (4.91) that the generalised stiffness matrix of the assembled structure can be expressed as the function of the stiffness matrices of substructures and the joints. The generalised mass and damping matrices of the assembled structure can be obtained in the same way.

4.3.2. Residual Attachment Modes

The number of modes of the substructures used in (4.91) is normally limited due to the expense in computation. To take into account the effect of the truncated higher modes, we introduce a concept of residual attachment modes.

Let $\mathbf{\Phi}_i$ be the complete modal shape matrix of the *n*-th substructure. This matrix can be partitioned to

$$\mathbf{\Phi}_i = \begin{bmatrix} \mathbf{\Phi}_i^l & \mathbf{\Phi}_i^h \end{bmatrix} \tag{4.92}$$

where $\mathbf{\Phi}_i^l$ contains the retained mode shapes with lower natural frequencies which are used to span the subspace and $\mathbf{\Phi}_i^h$ contains the truncated higher mode shapes.

The orthogonalisation of the mode shapes with respect to the stiffness matrix $\mathbf{k}_i$ and mass matrix $\mathbf{m}_i$ are written as:

$$\left.\begin{aligned} \mathbf{\Phi}_i^T \mathbf{k}_i \mathbf{\Phi}_i &= \mathbf{\Lambda}_i \\ \mathbf{\Phi}_i^T \mathbf{m}_i \mathbf{\Phi}_i &= \mathbf{I}_i \end{aligned}\right\} \tag{4.93}$$

Applying the inversion on both sides of the first equation in (4.93), we have

$$\mathbf{\Phi}_i^{-1} \mathbf{k}_i^{-1} \mathbf{\Phi}_i^{-T} = \mathbf{\Lambda}_i^{-1} \tag{4.94}$$

Pre-multiplying by $\mathbf{\Phi}_i$ and post-multiplying by $\mathbf{\Phi}_i^T$, equation (4.94) becomes

$$\mathbf{k}_i^{-1} = \mathbf{\Phi}_i \mathbf{\Lambda}_i^{-1} \mathbf{\Phi}_i^T = \begin{bmatrix} \mathbf{\Phi}_i^l & \mathbf{\Phi}_i^h \end{bmatrix} \begin{bmatrix} \left(\boldsymbol{\omega}_i^l\right)^{-2} & \mathbf{0} \\ \mathbf{0} & \left(\boldsymbol{\omega}_i^h\right)^{-2} \end{bmatrix} \begin{bmatrix} \left(\mathbf{\Phi}_i^l\right)^T \\ \left(\mathbf{\Phi}_i^h\right)^T \end{bmatrix} = \mathbf{\Phi}_i^l \left(\boldsymbol{\omega}_i^l\right)^{-2} \left(\mathbf{\Phi}_i^l\right)^T + \mathbf{\Phi}_i^h \left(\boldsymbol{\omega}_i^h\right)^{-2} \left(\mathbf{\Phi}_i^h\right)^T \tag{4.95}$$

If the higher modes are truncated, the residual flexibility matrix of the *i*-th substructure will be

$$\mathbf{R}_i = \mathbf{k}_i^{-1} - \mathbf{\Phi}_i^l \left(\boldsymbol{\omega}_i^l\right)^{-2} \left(\mathbf{\Phi}_i^l\right)^T \tag{4.96}$$

Neglecting the inertia effect intruduced by the truncated mode shapes, the compensatory displacement response of a substructure can be expressed in terms of the residual flexibility matrix $\mathbf{R}_i$ as

$$\Delta \mathbf{x}_i = \mathbf{R}_i \mathbf{f}_i \tag{4.97}$$

In the case of free vibration, there are only internal forces acting at the interfaces of the free substructure. Therefore,

$$\mathbf{f}_i = \begin{Bmatrix} \mathbf{f}_i^i \\ \mathbf{f}_i^c \end{Bmatrix} = \begin{Bmatrix} \mathbf{0} \\ \mathbf{f}_i^c \end{Bmatrix} \tag{4.98}$$

If $\mathbf{R}_i$ is written in partitioned form corresponding to the internal and interface DOFs, $\Delta\mathbf{x}_i$ can be written as

$$\Delta\mathbf{x}_i = \begin{bmatrix} \mathbf{R}_i^i & \mathbf{R}_i^c \end{bmatrix} \begin{Bmatrix} \mathbf{0} \\ \mathbf{f}_i^c \end{Bmatrix} = \mathbf{R}_i^c \mathbf{f}_i^c \tag{4.99}$$

The *residual attachment modes* of the free substructure are then defined on the interface boundary DOFs as

$$\mathbf{\Gamma}_i = \mathbf{R}_i^c \tag{4.100}$$

Therefore, the displacement of the substructure can be represented in terms of the mode shapes $\mathbf{\Phi}_i^l$ and the residual attachment modes $\mathbf{\Gamma}_i$ as

$$\mathbf{x}_i = \mathbf{\Phi}_i^l \mathbf{q}_i^l + \mathbf{\Gamma}_i \mathbf{f}_i^c \tag{4.101}$$

where $\mathbf{f}_i^c$ is the internal force acting at the interfaces of the *i*-th substructure.

Equation (4.101) can be partitioned with respect to the internal and coupling boundary DOFs:

$$\begin{Bmatrix} \mathbf{x}_i^i \\ \mathbf{x}_i^c \end{Bmatrix} = \begin{bmatrix} \mathbf{\Phi}_i^{li} & \mathbf{\Gamma}_i^i \\ \mathbf{\Phi}_i^{lc} & \mathbf{\Gamma}_i^c \end{bmatrix} \begin{Bmatrix} \mathbf{q}_i^l \\ \mathbf{f}_i^c \end{Bmatrix} \tag{4.102}$$

From the second row of (4.102), the interface force $\mathbf{f}_i^c$ can be written as

$$\mathbf{f}_i^c = \left(\mathbf{\Gamma}_i^c\right)^{-1} \left(\mathbf{x}_i^c - \mathbf{\Phi}_i^{lc} \mathbf{q}_i^l\right) = \mathbf{k}_i^a \mathbf{x}_i^c - \mathbf{k}_i^b \mathbf{q}_i^l \tag{4.103}$$

Substituting (4.103) back into (4.102), we have

$$\begin{Bmatrix} \mathbf{x}_i^i \\ \mathbf{x}_i^c \end{Bmatrix} = \begin{bmatrix} \mathbf{\Phi}_i^{li} - \mathbf{\Gamma}_i^i \mathbf{k}_i^b & \mathbf{\Gamma}_i^i \mathbf{k}_i^a \\ \mathbf{0} & \mathbf{I}_i \end{bmatrix} \begin{Bmatrix} \mathbf{q}_i^l \\ \mathbf{x}_i^c \end{Bmatrix} = \begin{bmatrix} \mathbf{A}_i & \mathbf{B}_i \\ \mathbf{0} & \mathbf{I}_i \end{bmatrix} \begin{Bmatrix} \mathbf{q}_i^l \\ \mathbf{x}_i^c \end{Bmatrix} \tag{4.104}$$

From equation (4.103), the total interface force vector of the substructures can be expressed as

$$\mathbf{f}^c = \begin{bmatrix} \mathbf{k}_1^a & \mathbf{0} & \cdots & \mathbf{0} \\ \mathbf{0} & \mathbf{k}_2^a & \cdots & \mathbf{0} \\ \cdots & \cdots & \cdots & \cdots \\ \mathbf{0} & \mathbf{0} & \cdots & \mathbf{k}_S^a \end{bmatrix} \begin{Bmatrix} \mathbf{x}_1^c \\ \mathbf{x}_2^c \\ \vdots \\ \mathbf{x}_S^c \end{Bmatrix} - \begin{bmatrix} \mathbf{k}_1^b & \mathbf{0} & \cdots & \mathbf{0} \\ \mathbf{0} & \mathbf{k}_2^b & \cdots & \mathbf{0} \\ \cdots & \cdots & \cdots & \cdots \\ \mathbf{0} & \mathbf{0} & \cdots & \mathbf{k}_S^b \end{bmatrix} \begin{Bmatrix} \mathbf{q}_1^l \\ \mathbf{q}_2^l \\ \vdots \\ \mathbf{q}_S^l \end{Bmatrix} = \mathbf{K}^a \mathbf{x}^c - \mathbf{K}^b \mathbf{q}^l \quad (4.105)$$

Using equation (4.104), the displacement vector of the collection of the substructures can be expressed as

$$\begin{Bmatrix} \mathbf{x}^i \\ \mathbf{x}^c \end{Bmatrix} = \begin{bmatrix} \mathbf{A} & \mathbf{B} \\ \mathbf{0} & \mathbf{I} \end{bmatrix} \begin{Bmatrix} \mathbf{q}^l \\ \mathbf{x}^c \end{Bmatrix} \quad (4.106)$$

Compatibility conditions at the coupling points are used to eliminate the DOFs at the interfaces. The compatibility conditions at the interfaces may be written as

$$\mathbf{x}^c = \mathbf{x}, \ \mathbf{f}^c + \mathbf{f} = \mathbf{0} \quad (4.107)$$

where the vectors $\mathbf{x}$ and $\mathbf{f}$ are the displacements and interface forces of the joints which are related by the following equation

$$\mathbf{f} = \mathbf{K}\mathbf{x} \quad (4.108)$$

Substituting equations (4.107) and (4.108) into (4.105), the interface displacement can be rewritten in terms of the generalised coordinates:

$$\mathbf{x}^c = \left(\mathbf{K} + \mathbf{K}^a\right)^{-1} \mathbf{K}^b \mathbf{q}^l = \mathbf{T}^c \mathbf{q}^l \quad (4.109)$$

Substituting equation (4.109) into (4.106), the final transformation matrix $\mathbf{T}$ of the structure, considering the static effect of the truncated higher modes of the substructures, is generated as follows:

$$\mathbf{T} = \begin{bmatrix} \mathbf{A} & \mathbf{B} \\ \mathbf{0} & \mathbf{I} \end{bmatrix} \begin{Bmatrix} \mathbf{I} \\ \mathbf{T}^c \end{Bmatrix} = \begin{bmatrix} \mathbf{A} + \mathbf{B}\mathbf{T}^c \\ \mathbf{T}^c \end{bmatrix} = \begin{bmatrix} \mathbf{T}^i \\ \mathbf{T}^c \end{bmatrix} \quad (4.110)$$

To implement this method, a linear transformation should be applied on $\mathbf{T}$, which is obtained from (4.110), in order to adjust its rows according to the spatial coordinates of the assembled structure.

$$\overline{\mathbf{T}} = \mathbf{S}\mathbf{T} \quad (4.111)$$

The matrix $\overline{\mathbf{T}}$ can then be substituted into equation (4.89) as $\mathbf{T}$.

The local transformation matrix for the *i*-th substructure and the *j*-th joint can be written as

$$\mathbf{T}_i = \begin{bmatrix} \mathbf{T}_i^i \\ \mathbf{T}_i^c \end{bmatrix}, \ \mathbf{T}_j = \mathbf{T}_j^c \tag{4.112}$$

where $\mathbf{T}_i^i$ is the submatrix of $\mathbf{T}^i$ in its rows, $\mathbf{T}_i^c$ and $\mathbf{T}_j^c$ are the submatrices of $\mathbf{T}^c$ in its rows.

The reduced stiffness, mass and damping matrices as well as the load vector for the *i*-th substructure are calculated by the following equations:

$$\left.\begin{aligned} \mathbf{k}_i^* &= \mathbf{T}_i^T \mathbf{k}_i \mathbf{T}_i \\ \mathbf{m}_i^* &= \mathbf{T}_i^T \mathbf{m}_i \mathbf{T}_i \\ \mathbf{c}_i^* &= \mathbf{T}_i^T \mathbf{c}_i \mathbf{T}_i \\ \mathbf{f}_i^*(t) &= \mathbf{T}_i^T \mathbf{f}_i(t) \end{aligned}\right\} \tag{4.113}$$

Similar calculations can be performed for the joints as well.

4.3.3. Treatment of Rigid-Body Modes

When a substructure is unrestrained, the definition of the residual attachment modes in equation (4.100) becomes obsolete since the stiffness matrix is singular. Using the concept of *inertia relief attachment modes* mentioned in section 4.1, the *elastic flexibility matrix* $\mathbf{G}^e$ can be determined as

$$\mathbf{G}^e = \mathbf{P}^T \mathbf{G} \mathbf{P} \tag{4.114}$$

Since the flexibility terms have been derived under inertia loading effects leading to the elastic flexibility matrix $\mathbf{G}^e$, this flexibility matrix serves as the inverse of the singular stiffness matrix. It should be noted that $\mathbf{G}^e$ is still singular.

4.4. CASE STUDIES

Two case studies are designed to validate the proposed method, CMS with joint considered and residual attachment mode compensation. The first case is two

simple beam structures coupled via a beam joint. It shows how well the method works with different scale substructures. The second case is a more practical structure, in which both substructures are in free-free boundary condition and the joints are more complicated.

4.4.1. Clamped-Clamped Beam

The modal properties of a clamped-clamped beam are predicted by synthesising modal properties of a pair of shorter cantilever beams with a joint in between. Fig. 4.1 shows six pairs of substructures. The ratio of DOF numbers included in substructures A and B is different in each pair. When the first three modes are considered from substructure A and substructure B in each pair, the first six natural frequency of the assembled structure are predicted successfully for pair one and error increases for the rest of pairs as shown in Table 4.1.

The natural frequency comparison between substructures A and B in different pairs is given in Fig. 4.3. With the increase of the difference in scale between substructure A and B, the difference of the first three natural frequencies increases dramatically. In the worst case, pair 6, first three natural frequencies can still be predicted accurately. The relative errors of the natural frequencies against index number of the pairs are shown in Fig. 4.2.

This example demonstrates that the method of CMS with joint considered and residual attachment mode compensation can at least predict the same number of modes of the assembled structure as the number of modes provided from by each substructure. It also suggests that the scale of substructures had better be similar in order to obtain accurate results.

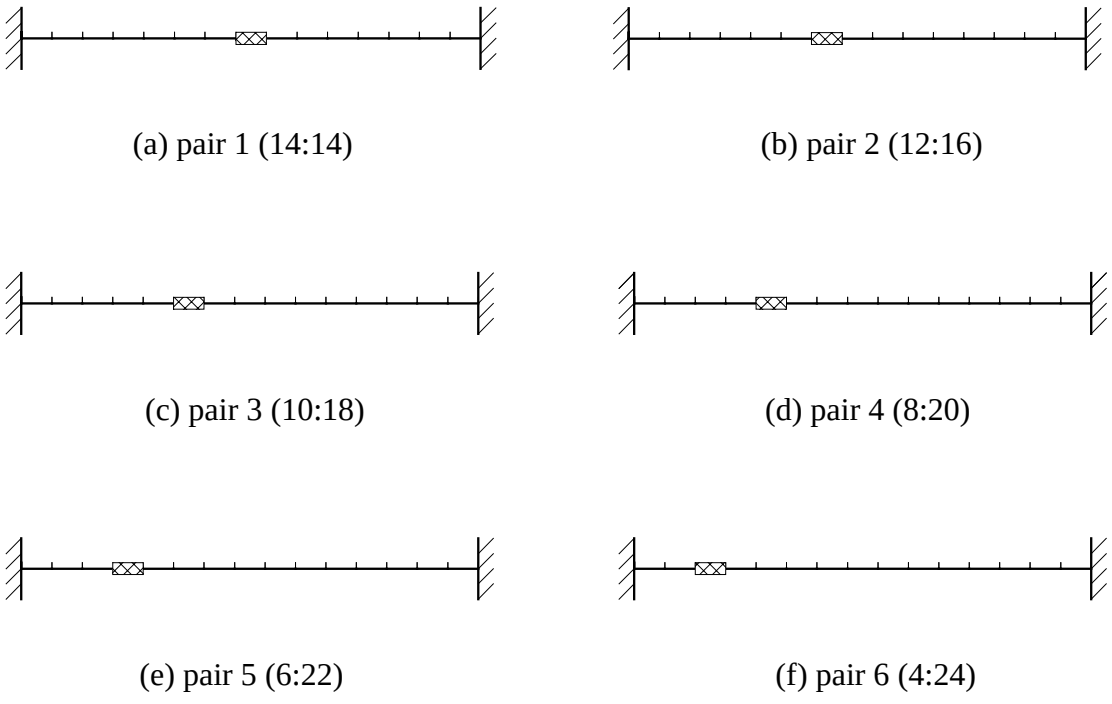

(a) pair 1 (14:14) (b) pair 2 (12:16)

(c) pair 3 (10:18) (d) pair 4 (8:20)

(e) pair 5 (6:22) (f) pair 6 (4:24)

Fig. 4.1 Six different pairs of substructures (The two numbers in parentheses are the numbers of DOFs of substructure A and B, respectively)

Table 4.1

	f_1	f_2	f_3	f_4	f_5	f_6
exact	***8.9601***	***24.7001***	***48.4291***	***80.0828***	***119.7072***	***167.3766***
pair 1	*8.9606*	*24.7001*	*48.4709*	*80.1001*	*120.1145*	*172.6389*
error (%)	*0.0056*	*0.0000*	*0.0863*	*0.0216*	*0.3402*	*3.1440*
pair 2	*8.9605*	*24.7019*	*48.4485*	*80.2146*	*120.6882*	*187.8944*
error (%)	*0.0045*	*0.0073*	*0.0401*	*0.1646*	*0.8195*	*12.2585*
pair 3	*8.9604*	*24.7050*	*48.4361*	*80.2214*	*128.8617*	*233.3507*
error (%)	*0.0033*	*0.0198*	*0.0145*	*0.1731*	*7.6476*	*39.4166*
pair 4	*8.9603*	*24.7052*	*48.4573*	*81.4308*	*152.9489*	*322.6363*
error (%)	*0.0022*	*0.0206*	*0.0582*	*1.6833*	*27.7692*	*92.7606*
pair 5	*8.9602*	*24.7032*	*48.4530*	*87.3631*	*205.8587*	*511.4926*
error (%)	*0.0011*	*0.0126*	*0.0494*	*9.0910*	*71.9685*	*205.5939*
pair 6	*8.9602*	*24.7028*	*48.6188*	*103.4081*	*330.8366*	*1048.428*
error (%)	*0.0011*	*0.0109*	*0.3917*	*29.1265*	*176.3715*	*526.3888*

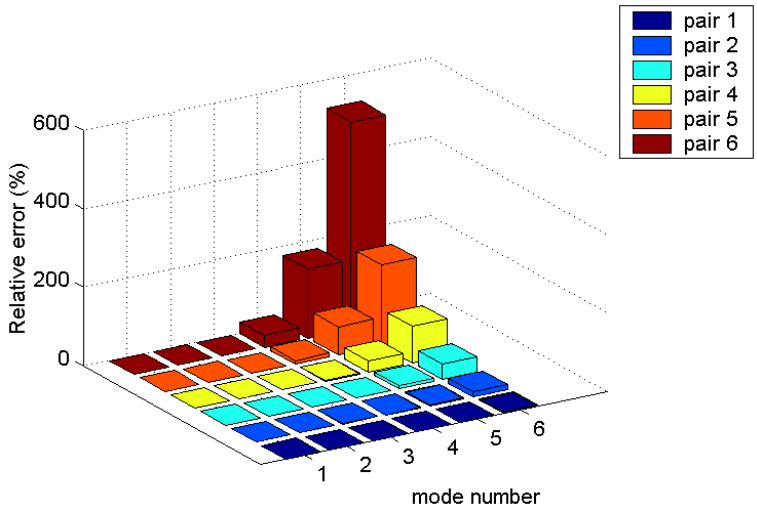

Fig. 4.2 Relative error of the natural frequencies vs. index number of the pairs for case study 1

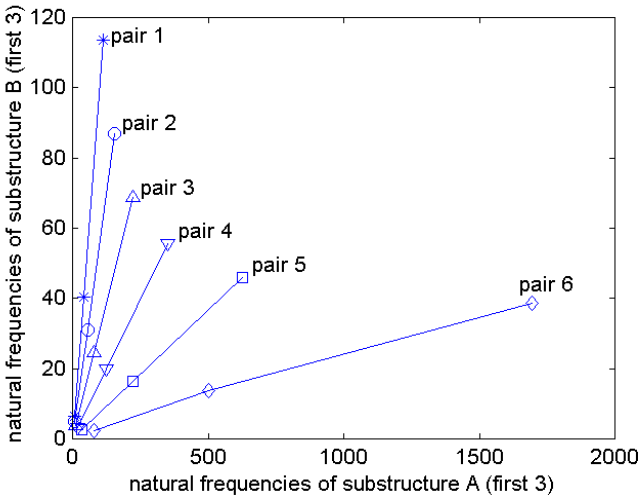

Fig. 4.3 Natural frequency comparison between substructures A and B in different pairs for case study 1

4.4.2. GARTEUR structure

The GARTEUR structure shown in Fig. 4.4 was built by ONERA in France for investigating modal test and analysis techniques. It consists of two main parts, the wing and the fuselage with tail. These two main parts are connected by four bolted joints. In this case study, the wing is taken as substructure A as shown in Fig. 4.5 and the fuselage with tail is taken as substructure B as shown in Fig. 4.6.

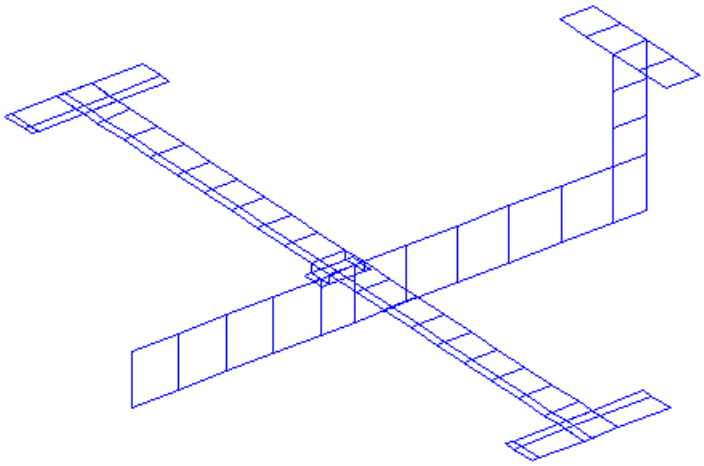

Fig. 4.4 The assembly of GARTEUR structure

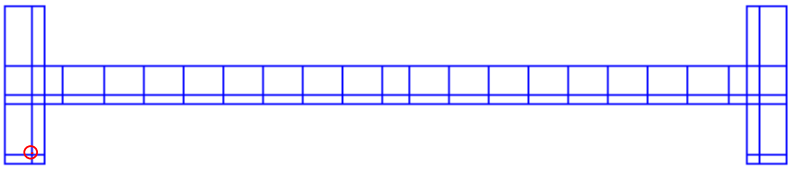

Fig. 4.5 Substructure A: the wing

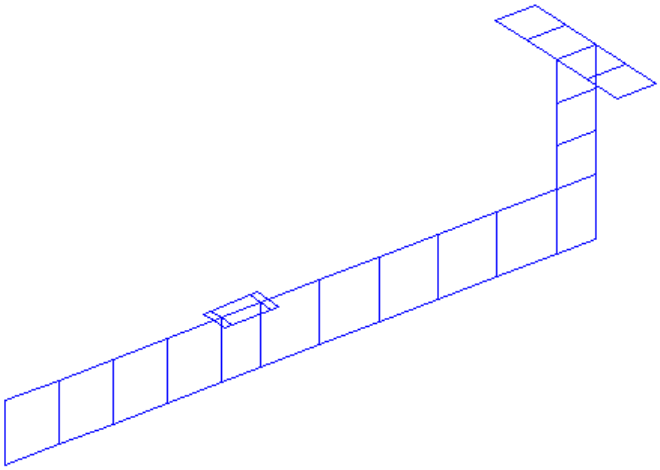

Fig. 4.6 Substructure B: the fuselage and tail

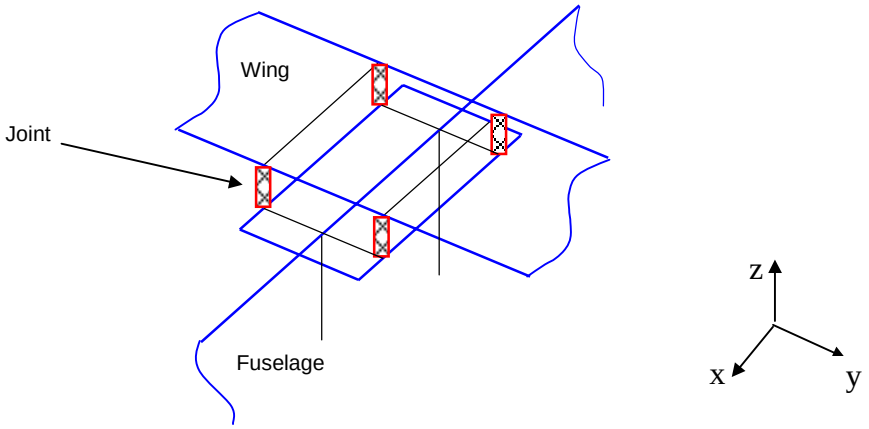

Fig. 4.7 Connections between substructures A and B

The joints between these two substructures are spring elements connecting 5 DOFs between substructure A and B, three translations and two rotations of θ_x and θ_y. They have an identical stiffness value, 1×10^{14} N/m.

Table 4.2 shows the parameters of FE models of substructure A and B. When 6 modes from substructure A and 4 modes from substructure B are used in the coupling analysis, the first 10 natural frequencies predicted using CMSJ are shown in table 4.3.

Table 4.2 Basic parameters of the FE model

	substructure A	substructure B
number of nodes	88	48
number of elements	60	24
number of DOFs	528	288

Table 4.3

mode	**exact**	Urgeria	error (%)	CMSJ	error (%)	reduced error (%)
1	***6.5152***	*7.8362*	*20.2747*	*6.5205*	*0.0801*	20.1946
2	***16.3131***	*18.1972*	*11.5497*	*16.3251*	*0.0731*	11.4766
3	***37.9458***	*38.4248*	*1.2623*	*37.9758*	*0.0790*	1.1833
4	***39.2928***	*41.6822*	*6.0810*	*39.3204*	*0.0703*	6.0107
5	***39.6716***	*41.7039*	*5.1228*	*39.6979*	*0.0661*	5.0567
6	***52.4577***	*63.2477*	*20.5690*	*52.5092*	*0.0983*	20.4707
7	***53.6223***	*65.4051*	*21.9739*	*53.7543*	*0.2462*	21.7277
8	***57.2831***	*66.0479*	*15.3008*	*56.6558*	*1.0950*	14.2058
9	***69.8696***	*70.9170*	*1.4990*	*69.9124*	*0.0612*	1.4378
10	***70.0156***	*87.0351*	*24.3081*	*70.1765*	*0.2297*	24.0784

The original method proposed by Urgeria [Urgu89] yields huge errors when such a few number of modes are used in coupling analysis. In fact, the results of

that method shown here were obtained using 60 modes of substructure A and 40 modes of substructure B, 10 times more than the number of modes used by CMSJ.

4.5. CONCLUSION

The CMS method with joints considered and residual attachment mode compensation (CMSJ) has been presented in this chapter and the numerical simulations show that the method works very well. The main advantages of the method are:

- Joints can be introduced in between the substructures. Since the joints are normally the most difficult part to model, this method provides a convenient way to modify the joints and predict the dynamic characters of the assembly without re-analysing the substructures.
- In the currently available CMS methods, the inter-substructure continuity of the displacement and rotation fields is enforced pointwise. However, substructures are often designed by different teams of engineers, and their respective finite element models often require different mesh resolutions. In this case, the finite element substructure models are typically non-conforming. The introduction of joints also makes the connection between such non-conforming interfaces possible.
- The joints, which are excluded from the modal analysis of the individual substructures, can be used to simulate local non-linearity such as micro-slip in construction joints in structures. According to the principle of CMSJ method, this simulation should be realised without many difficulties.

In general, the CMSJ method satisfies all the criteria proposed by Hintz [Hint75] and it is worth to apply this method to large-scale structures.

CHAPTER 5

VIBRATION ANALYSIS OF COUPLED STRUCTURES - FRF METHODS

5.1. INTRODUCTION

If CMS is mainly based on analytical models, *i.e.* the spatial type of model, referring to Ewins′ definition [Ewin84], the FRF coupling method is then basically built on experimental models or in the other word, response models. In fact, since all the models can be interrelated with each other [Urgu89], both coupling methods allow the use of a combination of analytical and experimental data. Compared with the CMS method, FRF coupling has the advantage of using the measured FRFs directly, which implies that the errors introduced by modal analysis, and the errors caused by high mode truncation, could be eliminated since the effects of the higher modes are inherent in the measured data.

The widely used expression of FRF coupling [JeBi88] connects two substructures rigidly at the coupling co-ordinates. Other coupling methods, either in the group

of impedance coupling (spatial coupling method) or modal coupling (free interface and fixed interface methods), follow the same compatibility condition of displacement as well.

To refine the general coupling analysis techniques, more researches on some specific aspects were carried out. Since the computed FRFs of the assembled structure may be contaminated by errors, Otte *et al* [OtLe91] proposed two data reduction methods to enhance the measured FRFs for coupling in the spatial and frequency domains respectively. These methods are based on singular value decomposition and resolve the problems of the ill-conditioned matrix inversion and the influence of noise. Two sources of error are normally encountered: (i) the inconsistencies of measured data (noise, frequency shifts), and the inability to measure correctly all DOFs of the connection; and (ii) ill conditioned matrix inversion for a large numbers of DOFs. Suatez [SuMa92] introduced a force derivative method to compensate for the effect of the truncated higher modes in the representation of the substructures' response. It was demonstrated that the method is capable of providing very accurate estimates of the natural frequencies of the combined structure as well as the associated modes of vibration and elastic forces.

It is worth pointing out that the essential principles in those methods mentioned above are the same as the FRF coupling method in the treatment of connections between substructures, *i.e.*, they suppose the same compatibility conditions of displacement at the interfaces of the connections. The substructures for numerical simulation were designed to meet the conditions and, therefore, the solutions of coupled structure analysis were satisfactory. Practically, however, the accurate analysis of coupled structures requires not only good substructure data estimation but also the reliable modelling of the joints, which connect the substructures. If the rigid connection assumption cannot describe the characteristics of realistic joints, it is clear that the FRFs obtained from the coupling analysis will certainly differ from the experimental results of the corresponding assembled structure, no matter how fine the algorithms are.

Basically, the theory of coupled structure analysis developed so far has not taken into account of the effect of practical joints. The effect of joints should be estimated carefully and the joint models should be established. Furthermore, the theory of substructure coupling analysis should be developed further to include the joint effects.

5.2. REVIEW OF THE ESSENTIAL PRINCIPLES

The currently used FRF coupling method was originally presented by Klosterman in 1971 according to [OtLe90]. The basic idea of the method can be chased up to 1960 by Bishop and Johnson [BiJo60].

5.2.1. FRF coupling without joint

The mathematical expression of FRF coupling method is well known as [JeBi88]

$$\mathbf{H}=\begin{bmatrix} {}_A\mathbf{H}_{ii} & {}_A\mathbf{H}_{ic} & \mathbf{0} \\ {}_A\mathbf{H}_{ci} & {}_A\mathbf{H}_{cc} & \mathbf{0} \\ \mathbf{0} & \mathbf{0} & {}_B\mathbf{H}_{ii} \end{bmatrix}-\begin{bmatrix} {}_A\mathbf{H}_{ic} \\ {}_A\mathbf{H}_{cc} \\ -{}_B\mathbf{H}_{ic} \end{bmatrix}\left[{}_A\mathbf{H}_{cc}+{}_B\mathbf{H}_{cc}\right]^{-1}\left[{}_A\mathbf{H}_{ci} \quad {}_A\mathbf{H}_{cc} \quad -{}_B\mathbf{H}_{ci}\right] \tag{5.1}$$

in which $\mathbf{H}$ is the FRF matrix of the assembled structure, ${}_A\mathbf{H}$, ${}_B\mathbf{H}$ is the FRF matrix of substructure A and B respectively. Subscript i represents internal DOFs and c is the coupling or interface DOFs.

If the FRF matrix of the coupled structure has the content as

$$\mathbf{H}=\begin{bmatrix} \mathbf{H}_{aa} & \mathbf{H}_{ac} & \mathbf{H}_{ab} \\ \mathbf{H}_{ca} & \mathbf{H}_{cc} & \mathbf{H}_{cb} \\ \mathbf{H}_{ba} & \mathbf{H}_{bc} & \mathbf{H}_{bb} \end{bmatrix} \tag{5.2}$$

then each submatrix can be expressed as

$$
\begin{aligned}
\mathbf{H}_{aa} &= {}_A\mathbf{H}_{ii} - {}_A\mathbf{H}_{ic}\left[{}_A\mathbf{H}_{cc} + {}_B\mathbf{H}_{cc}\right]^{-1}{}_A\mathbf{H}_{ci} \\
\mathbf{H}_{ac} &= {}_A\mathbf{H}_{ic} - {}_A\mathbf{H}_{ic}\left[{}_A\mathbf{H}_{cc} + {}_B\mathbf{H}_{cc}\right]^{-1}{}_A\mathbf{H}_{cc} \\
\mathbf{H}_{ab} &= {}_A\mathbf{H}_{ic}\left[{}_A\mathbf{H}_{cc} + {}_B\mathbf{H}_{cc}\right]^{-1}{}_B\mathbf{H}_{ci} \\
\mathbf{H}_{cc} &= {}_A\mathbf{H}_{cc} - {}_A\mathbf{H}_{cc}\left[{}_A\mathbf{H}_{cc} + {}_B\mathbf{H}_{cc}\right]^{-1}{}_A\mathbf{H}_{cc} \\
\mathbf{H}_{cb} &= {}_A\mathbf{H}_{cc}\left[{}_A\mathbf{H}_{cc} + {}_B\mathbf{H}_{cc}\right]^{-1}{}_B\mathbf{H}_{ci} \\
\mathbf{H}_{bb} &= {}_B\mathbf{H}_{ii} - {}_B\mathbf{H}_{ic}\left[{}_A\mathbf{H}_{cc} + {}_B\mathbf{H}_{cc}\right]^{-1}{}_B\mathbf{H}_{ci}
\end{aligned}
\tag{5.3}
$$

and by symmetry,

$$
\begin{aligned}
\mathbf{H}_{ca} &= \mathbf{H}_{ac}^{T} \\
\mathbf{H}_{ba} &= \mathbf{H}_{ab}^{T} \\
\mathbf{H}_{bc} &= \mathbf{H}_{cb}^{T}
\end{aligned}
\tag{5.4}
$$

5.2.2. FRF coupling with joint

The FRF coupling method presented in (5.1) does not include joints between substructures. A method of FRF coupling with joints was recently reported by Ferreira [Ferr98], in which the description of substructures and their assembly are the same as that mentioned in [Ren92]. The new development of the method in [Ferr98], in the aspect of substructure coupling analysis, is the joint description and synthesis with substructures. However, it can be noticed in the derivation process of the coupling method [Ferr98], that the expressions of the forces applied on the substructures, $\mathbf{f}_{\bar{c}}$ and $\mathbf{f}_{\tilde{c}}$, are not unique. It seems that the solution should be consistent only if the describing function $\mathbf{G}$ is infinite, or in the other words, of $\mathbf{G}^{-1} = 0$. Obviously, this condition conflicts with the purpose of the coupling analysis and, therefore, there must be an error in the derivation.

In fact, the joint model expressions given by Ferreira is

$$
-\begin{Bmatrix} \mathbf{f}_{\bar{c}} \\ \mathbf{f}_{\tilde{c}} \end{Bmatrix} = \begin{bmatrix} \mathbf{G} & -\mathbf{G} \\ -\mathbf{G} & \mathbf{G} \end{bmatrix} \begin{Bmatrix} \mathbf{x}_{\bar{c}} \\ \mathbf{x}_{\tilde{c}} \end{Bmatrix}
\tag{5.5}
$$

This joint model is based on two essential assumptions (which are not clearly mentioned in [Ferr98]): the first assumption is that the equilibrium condition and the compatibility condition are given in the form of

$$\begin{Bmatrix} \mathbf{f}_{\bar{c}} \\ \mathbf{f}_{\tilde{c}} \end{Bmatrix} = -\begin{Bmatrix} \bar{\mathbf{f}} \\ \tilde{\mathbf{f}} \end{Bmatrix} \text{ and } \begin{Bmatrix} \mathbf{x}_{\bar{c}} \\ \mathbf{x}_{\tilde{c}} \end{Bmatrix} = \begin{Bmatrix} \bar{\mathbf{x}} \\ \tilde{\mathbf{x}} \end{Bmatrix} \tag{5.6}$$

and the second assumption is that the stiffness matrix of the joint has to take the specific form of

$$\mathbf{K} = \begin{bmatrix} \mathbf{G} & -\mathbf{G} \\ -\mathbf{G} & \mathbf{G} \end{bmatrix} \tag{5.7}$$

The second assumption implies that the joints between the substructures can only be parallel scalar springs.

According to the proposed equilibrium conditions in [Ferr98], the forces applied at the interfaces of the assembled structure have to be always zeros:

$$\mathbf{F}_{\bar{C}} = \mathbf{F}_{\tilde{C}} = \mathbf{f}_{\bar{c}} + \mathbf{f}_{\tilde{c}} \equiv \mathbf{0} \tag{5.8}$$

Therefore, when these basic assumptions are used in the derivations, these two forces, $\mathbf{F}_{\bar{C}}$ and $\mathbf{F}_{\tilde{C}}$, appear in the expressions of $\mathbf{f}_{\bar{c}}$ and $\mathbf{f}_{\tilde{c}}$, can have arbitrary coefficients without affecting the values of $\mathbf{f}_{\bar{c}}$ and $\mathbf{f}_{\tilde{c}}$. That is why the solutions are not unique.

5.3. GENERAL JOINT DESCRIPTION METHOD - NEW DEVELOPMENT

5.3.1. Theory background

To correct the equilibrium condition used in [Ferr98], and to employ a general joint description matrix, a generalised substructure coupling method using FRF data is derived in this section.

JOINT DESCRIPTION

A joint can be analytically described as

$$\mathbf{f} = \mathbf{Z}\mathbf{x} \tag{5.9}$$

where $\mathbf{Z}$ is the impedance matrix of the joint. Since it is normally symmetric, such that

$$\mathbf{Z} = \begin{bmatrix} \mathbf{Z}_{\bar{c}\bar{c}} & \mathbf{Z}_{\bar{c}\tilde{c}} \\ \mathbf{Z}_{\tilde{c}\bar{c}} & \mathbf{Z}_{\tilde{c}\tilde{c}} \end{bmatrix} \tag{5.10}$$

with $\mathbf{Z}_{\bar{c}\bar{c}} = \mathbf{Z}_{\bar{c}\bar{c}}^T$, $\mathbf{Z}_{\bar{c}\tilde{c}} = \mathbf{Z}_{\tilde{c}\bar{c}}^T$ and $\mathbf{Z}_{\tilde{c}\tilde{c}} = \mathbf{Z}_{\tilde{c}\tilde{c}}^T$.

The joint has no internal degrees of freedom. All of its degrees of freedom are on its boundaries. If the number of degrees of freedom at the boundary of substructure A equals that of substructute B, $n_{\bar{c}} = n_{\tilde{c}}$, then $\mathbf{Z}_{\bar{c}\tilde{c}}$ is a square matrix. Otherwise, in more general cases, if $n_{\bar{c}} \neq n_{\tilde{c}}$, $\mathbf{Z}_{\bar{c}\tilde{c}}$ is rectangular.

CONDITIONS OF COMPATIBILITY AND EQUILIBRIUM

The displacement vector of joint, $\mathbf{x}$, satisfies the compatibility condition:

$$\mathbf{x} = \begin{Bmatrix} \mathbf{x}_{\bar{c}} \\ \mathbf{x}_{\tilde{c}} \end{Bmatrix} \tag{5.11}$$

The force vector, $\mathbf{f}$, satisfies the equilibrium condition at the coupling interfaces:

$$\begin{Bmatrix} \mathbf{f}_{\bar{c}} \\ \mathbf{f}_{\tilde{c}} \end{Bmatrix} = \begin{Bmatrix} \mathbf{F}_{\bar{C}} \\ \mathbf{F}_{\tilde{C}} \end{Bmatrix} - \begin{Bmatrix} \bar{\mathbf{f}} \\ \tilde{\mathbf{f}} \end{Bmatrix} \tag{5.12}$$

where $\mathbf{F}_{\bar{C}}$ and $\mathbf{F}_{\tilde{C}}$ are the external forces acting on the interface DOFs, and

$$\mathbf{f} = \begin{Bmatrix} \bar{\mathbf{f}} \\ \tilde{\mathbf{f}} \end{Bmatrix} \tag{5.13}$$

When there are no external forces applied on the interface DOFs, equation (5.9) becomes

$$\mathbf{f} = -\begin{Bmatrix} \mathbf{f}_{\bar{c}} \\ \mathbf{f}_{\tilde{c}} \end{Bmatrix} \tag{5.14}$$

DESCRIPTION OF SUBSTRUCTURES

To describe each of the uncoupled substructures, we have

$$\begin{Bmatrix} \mathbf{x}_i \\ \mathbf{x}_{\bar{c}} \\ \mathbf{x}_{\tilde{c}} \end{Bmatrix} = \begin{bmatrix} \mathbf{H}_{ii} & \mathbf{H}_{i\bar{c}} & \mathbf{H}_{i\tilde{c}} \\ \mathbf{H}_{\bar{c}i} & \mathbf{H}_{\bar{c}\bar{c}} & \mathbf{H}_{\bar{c}\tilde{c}} \\ \mathbf{H}_{\tilde{c}i} & \mathbf{H}_{\tilde{c}\bar{c}} & \mathbf{H}_{\tilde{c}\tilde{c}} \end{bmatrix} \begin{Bmatrix} \mathbf{f}_i \\ \mathbf{f}_{\bar{c}} \\ \mathbf{f}_{\tilde{c}} \end{Bmatrix} \tag{5.15}$$

DERIVATION OF THE RECEPTANCE MATRIX OF THE COUPLED STRUCTURE

Solving $\mathbf{x}_{\bar{c}}$ and $\mathbf{x}_{\tilde{c}}$ from (5.15) and substituting them into (5.9), we have

$$\mathbf{Z}_{\bar{c}\bar{c}}\left(\mathbf{H}_{\bar{c}i}\mathbf{f}_i + \mathbf{H}_{\bar{c}\bar{c}}\mathbf{f}_{\bar{c}} + \mathbf{H}_{\bar{c}\tilde{c}}\mathbf{f}_{\tilde{c}}\right) + \mathbf{Z}_{\bar{c}\tilde{c}}\left(\mathbf{H}_{\tilde{c}i}\mathbf{f}_i + \mathbf{H}_{\tilde{c}\bar{c}}\mathbf{f}_{\bar{c}} + \mathbf{H}_{\tilde{c}\tilde{c}}\mathbf{f}_{\tilde{c}}\right) - \bar{\mathbf{f}} = \mathbf{0} \tag{5.16}$$

$$\mathbf{Z}_{\tilde{c}\bar{c}}\left(\mathbf{H}_{\bar{c}i}\mathbf{f}_i + \mathbf{H}_{\bar{c}\bar{c}}\mathbf{f}_{\bar{c}} + \mathbf{H}_{\bar{c}\tilde{c}}\mathbf{f}_{\tilde{c}}\right) + \mathbf{Z}_{\tilde{c}\tilde{c}}\left(\mathbf{H}_{\tilde{c}i}\mathbf{f}_i + \mathbf{H}_{\tilde{c}\bar{c}}\mathbf{f}_{\bar{c}} + \mathbf{H}_{\tilde{c}\tilde{c}}\mathbf{f}_{\tilde{c}}\right) - \tilde{\mathbf{f}} = \mathbf{0} \tag{5.17}$$

Substituting (5.12) into (5.16) and (5.17), noticing that $\mathbf{f}_i = \mathbf{F}_I$, we have

$$\mathbf{Z}_{\bar{c}\bar{c}}\left(\mathbf{H}_{\bar{c}i}\mathbf{F}_I + \mathbf{H}_{\bar{c}\bar{c}}\mathbf{f}_{\bar{c}} + \mathbf{H}_{\bar{c}\tilde{c}}\mathbf{f}_{\tilde{c}}\right) + \mathbf{Z}_{\bar{c}\tilde{c}}\left(\mathbf{H}_{\tilde{c}i}\mathbf{F}_I + \mathbf{H}_{\tilde{c}\bar{c}}\mathbf{f}_{\bar{c}} + \mathbf{H}_{\tilde{c}\tilde{c}}\mathbf{f}_{\tilde{c}}\right) - \mathbf{F}_{\bar{C}} + \mathbf{f}_{\bar{c}} = \mathbf{0} \tag{5.18}$$

$$\mathbf{Z}_{\tilde{c}\bar{c}}\left(\mathbf{H}_{\bar{c}i}\mathbf{F}_I + \mathbf{H}_{\bar{c}\bar{c}}\mathbf{f}_{\bar{c}} + \mathbf{H}_{\bar{c}\tilde{c}}\mathbf{f}_{\tilde{c}}\right) + \mathbf{Z}_{\tilde{c}\tilde{c}}\left(\mathbf{H}_{\tilde{c}i}\mathbf{F}_I + \mathbf{H}_{\tilde{c}\bar{c}}\mathbf{f}_{\bar{c}} + \mathbf{H}_{\tilde{c}\tilde{c}}\mathbf{f}_{\tilde{c}}\right) - \mathbf{F}_{\tilde{C}} + \mathbf{f}_{\tilde{c}} = \mathbf{0} \tag{5.19}$$

Rearranging these two equations with respect to the force vectors, we have

$$\mathbf{a}_1\mathbf{f}_{\bar{c}} + \mathbf{a}_2\mathbf{f}_{\tilde{c}} = \mathbf{F}_{\bar{C}} - \mathbf{a}_3\mathbf{F}_I \tag{5.20}$$

$$\mathbf{b}_1\mathbf{f}_{\bar{c}} + \mathbf{b}_2\mathbf{f}_{\tilde{c}} = \mathbf{F}_{\tilde{C}} - \mathbf{b}_3\mathbf{F}_I \tag{5.21}$$

Solving equations (5.20) and (5.21), we have the force vectors for the uncoupled system uniquely expressed in terms of the external force vectors of the coupled system as

$$\mathbf{f}_{\bar{c}} = \bar{\mathbf{B}}^{-1}\left[\left(\mathbf{b}_3 - \mathbf{b}_2\mathbf{a}_2^{-1}\mathbf{a}_3\right)\mathbf{F}_I + \mathbf{b}_2\mathbf{a}_2^{-1}\mathbf{F}_{\bar{C}} - \mathbf{F}_{\tilde{C}}\right] \tag{5.22}$$

$$\mathbf{f}_{\tilde{c}} = \tilde{\mathbf{B}}^{-1}\left[\left(\mathbf{a}_3 - \mathbf{a}_1\mathbf{b}_1^{-1}\mathbf{b}_3\right)\mathbf{F}_I - \mathbf{F}_{\bar{C}} + \mathbf{a}_1\mathbf{b}_1^{-1}\mathbf{F}_{\tilde{C}}\right] \tag{5.23}$$

where

$$
\begin{aligned}
\mathbf{a}_1 &= \mathbf{Z}_{\bar{c}\bar{c}}\mathbf{H}_{\bar{c}\bar{c}} + \mathbf{Z}_{\bar{c}\tilde{c}}\mathbf{H}_{\tilde{c}\bar{c}} + \mathbf{I} \\
\mathbf{a}_2 &= \mathbf{Z}_{\bar{c}\bar{c}}\mathbf{H}_{\bar{c}\tilde{c}} + \mathbf{Z}_{\bar{c}\tilde{c}}\mathbf{H}_{\tilde{c}\tilde{c}} \\
\mathbf{a}_3 &= \mathbf{Z}_{\bar{c}\bar{c}}\mathbf{H}_{\bar{c}i} + \mathbf{Z}_{\bar{c}\tilde{c}}\mathbf{H}_{\tilde{c}i} \\
\mathbf{b}_1 &= \mathbf{Z}_{\tilde{c}\bar{c}}\mathbf{H}_{\bar{c}\bar{c}} + \mathbf{Z}_{\tilde{c}\tilde{c}}\mathbf{H}_{\tilde{c}\bar{c}} \\
\mathbf{b}_2 &= \mathbf{Z}_{\tilde{c}\bar{c}}\mathbf{H}_{\bar{c}\tilde{c}} + \mathbf{Z}_{\tilde{c}\tilde{c}}\mathbf{H}_{\tilde{c}\tilde{c}} + \mathbf{I} \\
\mathbf{b}_3 &= \mathbf{Z}_{\tilde{c}\bar{c}}\mathbf{H}_{\bar{c}i} + \mathbf{Z}_{\tilde{c}\tilde{c}}\mathbf{H}_{\tilde{c}i} \\
\overline{\mathbf{B}} &= \mathbf{b}_2\mathbf{a}_2^{-1}\mathbf{a}_1 - \mathbf{b}_1 \\
\tilde{\mathbf{B}} &= \mathbf{a}_1\mathbf{b}_1^{-1}\mathbf{b}_2 - \mathbf{a}_2
\end{aligned}
\tag{5.24}
$$

Substituting (5.22) and (5.23) into (5.15) and using the following compatibility conditions:

$$
\mathbf{X}_I = \mathbf{x}_i,\ \mathbf{X}_{\bar{C}} = \mathbf{x}_{\bar{c}} \text{ and } \mathbf{X}_{\tilde{C}} = \mathbf{x}_{\tilde{c}} \tag{5.25}
$$

the upper triangle part of the coupled structure′s FRF matrix is obtained as follows:

$$
\begin{aligned}
\mathbf{H}_{II} &= \mathbf{H}_{ii} + \mathbf{H}_{i\bar{c}}\overline{\mathbf{B}}^{-1}\left(\mathbf{b}_3 - \mathbf{b}_2\mathbf{a}_2^{-1}\mathbf{a}_3\right) + \mathbf{H}_{i\tilde{c}}\tilde{\mathbf{B}}^{-1}\left(\mathbf{a}_3 - \mathbf{a}_1\mathbf{b}_1^{-1}\mathbf{b}_3\right) \\
\mathbf{H}_{I\bar{C}} &= \mathbf{H}_{i\bar{c}}\overline{\mathbf{B}}^{-1}\mathbf{b}_2\mathbf{a}_2^{-1} - \mathbf{H}_{i\tilde{c}}\tilde{\mathbf{B}}^{-1} \\
\mathbf{H}_{I\tilde{C}} &= \mathbf{H}_{i\tilde{c}}\tilde{\mathbf{B}}^{-1}\mathbf{a}_1\mathbf{b}_1^{-1} - \mathbf{H}_{i\bar{c}}\overline{\mathbf{B}}^{-1} \\
\mathbf{H}_{\bar{C}\bar{C}} &= \mathbf{H}_{\bar{c}\bar{c}}\overline{\mathbf{B}}^{-1}\mathbf{b}_2\mathbf{a}_2^{-1} - \mathbf{H}_{\bar{c}\tilde{c}}\tilde{\mathbf{B}}^{-1} \\
\mathbf{H}_{\bar{C}\tilde{C}} &= \mathbf{H}_{\bar{c}\tilde{c}}\tilde{\mathbf{B}}^{-1}\mathbf{a}_1\mathbf{b}_1^{-1} - \mathbf{H}_{\bar{c}\bar{c}}\overline{\mathbf{B}}^{-1} \\
\mathbf{H}_{\tilde{C}\tilde{C}} &= \mathbf{H}_{\tilde{c}\tilde{c}}\tilde{\mathbf{B}}^{-1}\mathbf{a}_1\mathbf{b}_1^{-1} - \mathbf{H}_{\tilde{c}\bar{c}}\overline{\mathbf{B}}^{-1}
\end{aligned}
\tag{5.26}
$$

Those FRFs compose the receptance matrix of the coupled structure:

$$
\begin{Bmatrix} \mathbf{X}_I \\ \mathbf{X}_{\bar{C}} \\ \mathbf{X}_{\tilde{C}} \end{Bmatrix} = \begin{bmatrix} \mathbf{H}_{II} & \mathbf{H}_{I\bar{C}} & \mathbf{H}_{I\tilde{C}} \\ \mathbf{H}_{\bar{C}I} & \mathbf{H}_{\bar{C}\bar{C}} & \mathbf{H}_{\bar{C}\tilde{C}} \\ \mathbf{H}_{\tilde{C}I} & \mathbf{H}_{\tilde{C}\bar{C}} & \mathbf{H}_{\tilde{C}\tilde{C}} \end{bmatrix} \begin{Bmatrix} \mathbf{F}_I \\ \mathbf{F}_{\bar{C}} \\ \mathbf{F}_{\tilde{C}} \end{Bmatrix} \tag{5.27}
$$

where

$$
\begin{aligned}
\mathbf{H}_{\bar{C}I} &= \mathbf{H}_{I\bar{C}}^T \\
\mathbf{H}_{\tilde{C}I} &= \mathbf{H}_{I\tilde{C}}^T \\
\mathbf{H}_{\tilde{C}\bar{C}} &= \mathbf{H}_{\bar{C}\tilde{C}}^T
\end{aligned}
\tag{5.28}
$$

5.3.2. Algorithm

The expressions in (5.24) can be simplified according to the fact that

$$\mathbf{H}_{\bar{c}\tilde{c}} = \mathbf{H}_{\tilde{c}\bar{c}} = \mathbf{0} \tag{5.29}$$

Substituting (5.29) into (5.24), we have

$$\begin{aligned}
\mathbf{a}_1 &= \mathbf{Z}_{\bar{c}\bar{c}}\mathbf{H}_{\bar{c}\bar{c}} + \mathbf{I} \\
\mathbf{a}_2 &= \mathbf{Z}_{\bar{c}\tilde{c}}\mathbf{H}_{\tilde{c}\tilde{c}} \\
\mathbf{a}_3 &= \mathbf{Z}_{\bar{c}\bar{c}}\mathbf{H}_{\bar{c}i} + \mathbf{Z}_{\bar{c}\tilde{c}}\mathbf{H}_{\tilde{c}i} \\
\mathbf{b}_1 &= \mathbf{Z}_{\tilde{c}\bar{c}}\mathbf{H}_{\bar{c}\bar{c}} \\
\mathbf{b}_2 &= \mathbf{Z}_{\tilde{c}\tilde{c}}\mathbf{H}_{\tilde{c}\tilde{c}} + \mathbf{I} \\
\mathbf{b}_3 &= \mathbf{Z}_{\tilde{c}\bar{c}}\mathbf{H}_{\bar{c}i} + \mathbf{Z}_{\tilde{c}\tilde{c}}\mathbf{H}_{\tilde{c}i}
\end{aligned} \tag{5.30}$$

and

$$\begin{aligned}
\overline{\mathbf{B}} &= \mathbf{H}_{\tilde{c}\tilde{c}}^{-1}\left\{\mathbf{H}_{\tilde{c}\bar{c}}\left(\mathbf{Z}_{\tilde{c}\bar{c}}\mathbf{Z}_{\bar{c}\tilde{c}}^{+}\mathbf{Z}_{\bar{c}\bar{c}} - \mathbf{Z}_{\tilde{c}\bar{c}}\right)\mathbf{H}_{\bar{c}\bar{c}} + \left(\mathbf{H}_{\tilde{c}\tilde{c}}\mathbf{Z}_{\tilde{c}\tilde{c}}\mathbf{Z}_{\bar{c}\tilde{c}}^{+} + \mathbf{Z}_{\tilde{c}\tilde{c}}^{+}\mathbf{Z}_{\bar{c}\bar{c}}\mathbf{H}_{\bar{c}\bar{c}}\right) + \mathbf{Z}_{\bar{c}\tilde{c}}^{+}\right\} \\
\widetilde{\mathbf{B}} &= \mathbf{H}_{\bar{c}\bar{c}}^{-1}\left\{\mathbf{H}_{\bar{c}\bar{c}}\left(\mathbf{Z}_{\bar{c}\bar{c}}\mathbf{Z}_{\tilde{c}\bar{c}}^{+}\mathbf{Z}_{\tilde{c}\tilde{c}} - \mathbf{Z}_{\bar{c}\tilde{c}}\right)\mathbf{H}_{\tilde{c}\tilde{c}} + \left(\mathbf{H}_{\bar{c}\bar{c}}\mathbf{Z}_{\bar{c}\bar{c}}\mathbf{Z}_{\tilde{c}\bar{c}}^{+} + \mathbf{Z}_{\tilde{c}\bar{c}}^{+}\mathbf{Z}_{\tilde{c}\tilde{c}}\mathbf{H}_{\tilde{c}\tilde{c}}\right) + \mathbf{Z}_{\tilde{c}\bar{c}}^{+}\right\}
\end{aligned} \tag{5.31}$$

$$\begin{aligned}
\overline{\mathbf{B}}^{+} &= \left\{\mathbf{H}_{\tilde{c}\tilde{c}}\left(\mathbf{Z}_{\tilde{c}\tilde{c}}\mathbf{Z}_{\bar{c}\tilde{c}}^{+}\mathbf{Z}_{\bar{c}\bar{c}} - \mathbf{Z}_{\tilde{c}\bar{c}}\right)\mathbf{H}_{\bar{c}\bar{c}} + \left(\mathbf{H}_{\tilde{c}\tilde{c}}\mathbf{Z}_{\tilde{c}\tilde{c}}\mathbf{Z}_{\bar{c}\tilde{c}}^{+} + \mathbf{Z}_{\bar{c}\tilde{c}}^{+}\mathbf{Z}_{\bar{c}\bar{c}}\mathbf{H}_{\bar{c}\bar{c}}\right) + \mathbf{Z}_{\tilde{c}\bar{c}}^{+}\right\}^{+}\mathbf{H}_{\tilde{c}\tilde{c}} \\
\widetilde{\mathbf{B}}^{+} &= \left\{\mathbf{H}_{\bar{c}\bar{c}}\left(\mathbf{Z}_{\bar{c}\bar{c}}\mathbf{Z}_{\tilde{c}\bar{c}}^{+}\mathbf{Z}_{\tilde{c}\tilde{c}} - \mathbf{Z}_{\bar{c}\tilde{c}}\right)\mathbf{H}_{\tilde{c}\tilde{c}} + \left(\mathbf{H}_{\bar{c}\bar{c}}\mathbf{Z}_{\bar{c}\bar{c}}\mathbf{Z}_{\tilde{c}\bar{c}}^{+} + \mathbf{Z}_{\tilde{c}\bar{c}}^{+}\mathbf{Z}_{\tilde{c}\tilde{c}}\mathbf{H}_{\tilde{c}\tilde{c}}\right) + \mathbf{Z}_{\tilde{c}\bar{c}}^{+}\right\}^{+}\mathbf{H}_{\bar{c}\bar{c}}
\end{aligned} \tag{5.32}$$

Rewriting (5.32) in a short form and comparing the expressions in the flower brackets, we noticed that if denote

$$\overline{\mathbf{B}}^{+} = \mathbf{D}^{+}\mathbf{H}_{\tilde{c}\tilde{c}} \tag{5.33}$$

then

$$\widetilde{\mathbf{B}}^{+} = \left(\mathbf{D}^{T}\right)^{+}\mathbf{H}_{\bar{c}\bar{c}} = \mathbf{D}^{+T}\mathbf{H}_{\bar{c}\bar{c}} \tag{5.34}$$

Therefore, the FRFs of the coupled structure in (5.26) becomes

$$\begin{aligned}
\mathbf{H}_{II} &= \mathbf{H}_{ii} + \mathbf{H}_{i\bar{c}}\mathbf{D}^{+}\mathbf{H}_{\tilde{c}\tilde{c}}\left(\mathbf{b}_3 - \mathbf{b}_2\mathbf{a}_2^{-1}\mathbf{a}_3\right) + \mathbf{H}_{i\tilde{c}}\mathbf{D}^{+T}\mathbf{H}_{\bar{c}\bar{c}}\left(\mathbf{a}_3 - \mathbf{a}_1\mathbf{b}_1^{-1}\mathbf{b}_3\right) \\
\mathbf{H}_{I\bar{C}} &= \mathbf{H}_{i\bar{c}}\mathbf{D}^{+}\mathbf{H}_{\tilde{c}\tilde{c}}\mathbf{b}_2\mathbf{a}_2^{-1} - \mathbf{H}_{i\tilde{c}}\mathbf{D}^{+T}\mathbf{H}_{\bar{c}\bar{c}} \\
\mathbf{H}_{I\tilde{C}} &= \mathbf{H}_{i\tilde{c}}\mathbf{D}^{+T}\mathbf{H}_{\bar{c}\bar{c}}\mathbf{a}_1\mathbf{b}_1^{-1} - \mathbf{H}_{i\bar{c}}\mathbf{D}^{+}\mathbf{H}_{\tilde{c}\tilde{c}} \\
\mathbf{H}_{\bar{C}\bar{C}} &= \mathbf{H}_{\bar{c}\bar{c}}\mathbf{D}^{+}\mathbf{H}_{\tilde{c}\tilde{c}}\mathbf{b}_2\mathbf{a}_2^{-1} \\
\mathbf{H}_{\bar{C}\tilde{C}} &= -\mathbf{H}_{\bar{c}\bar{c}}\mathbf{D}^{+}\mathbf{H}_{\tilde{c}\tilde{c}} \\
\mathbf{H}_{\tilde{C}\tilde{C}} &= \mathbf{H}_{\tilde{c}\tilde{c}}\mathbf{D}^{+T}\mathbf{H}_{\bar{c}\bar{c}}\mathbf{a}_1\mathbf{b}_1^{-1}
\end{aligned} \tag{5.35}$$

From (5.30), we have

$$\begin{aligned}
\mathbf{b}_3 - \mathbf{b}_2\mathbf{a}_2^{-1}\mathbf{a}_3 &= \mathbf{H}_{\tilde{c}\tilde{c}}^{-1}\left\{\left(\mathbf{H}_{\tilde{c}\tilde{c}}\mathbf{Z}_{\tilde{c}\bar{c}} - \mathbf{H}_{\tilde{c}\tilde{c}}\mathbf{Z}_{\tilde{c}\tilde{c}}\mathbf{Z}_{\bar{c}\tilde{c}}^{+}\mathbf{Z}_{\bar{c}\bar{c}} - \mathbf{Z}_{\tilde{c}\tilde{c}}^{+}\mathbf{Z}_{\bar{c}\bar{c}}\right)\mathbf{H}_{\bar{c}i} - \mathbf{H}_{\tilde{c}i}\right\} \\
\mathbf{a}_3 - \mathbf{a}_1\mathbf{b}_1^{-1}\mathbf{b}_3 &= \mathbf{H}_{\bar{c}\bar{c}}^{-1}\left\{\left(\mathbf{H}_{\bar{c}\bar{c}}\mathbf{Z}_{\bar{c}\tilde{c}} - \mathbf{H}_{\bar{c}\bar{c}}\mathbf{Z}_{\bar{c}\bar{c}}\mathbf{Z}_{\tilde{c}\bar{c}}^{+}\mathbf{Z}_{\tilde{c}\tilde{c}} - \mathbf{Z}_{\bar{c}\tilde{c}}^{+}\mathbf{Z}_{\tilde{c}\tilde{c}}\right)\mathbf{H}_{\tilde{c}i} - \mathbf{H}_{\bar{c}i}\right\}
\end{aligned} \tag{5.36}$$

and

$$\begin{aligned}\mathbf{b}_2\mathbf{a}_2^{-1} &= \mathbf{H}_{\tilde{c}\tilde{c}}^{-1}\left(\mathbf{H}_{\tilde{c}\tilde{c}}\mathbf{Z}_{\tilde{c}\tilde{c}}+\mathbf{I}\right)\mathbf{Z}_{\tilde{c}\tilde{c}}^{+}\\ \mathbf{a}_1\mathbf{b}_1^{-1} &= \mathbf{H}_{\bar{c}\bar{c}}^{-1}\left(\mathbf{H}_{\bar{c}\bar{c}}\mathbf{Z}_{\bar{c}\bar{c}}+\mathbf{I}\right)\mathbf{Z}_{\tilde{c}\bar{c}}^{+}\end{aligned} \tag{5.37}$$

Substitute (5.36) and (5.37) into (5.35), we have

$$\begin{aligned}\mathbf{H}_{II} &= \mathbf{H}_{ii}+\mathbf{H}_{i\bar{c}}\mathbf{D}^{+}\mathbf{H}_a+\mathbf{H}_{i\tilde{c}}\mathbf{D}^{+T}\mathbf{H}_b\\ \mathbf{H}_{I\bar{C}} &= \mathbf{H}_{i\bar{c}}\mathbf{D}^{+}\mathbf{H}_c-\mathbf{H}_{i\tilde{c}}\mathbf{D}^{+T}\mathbf{H}_{\bar{c}\bar{c}}\\ \mathbf{H}_{I\tilde{C}} &= \mathbf{H}_{i\tilde{c}}\mathbf{D}^{+T}\mathbf{H}_d-\mathbf{H}_{i\bar{c}}\mathbf{D}^{+}\mathbf{H}_{\tilde{c}\tilde{c}}\\ \mathbf{H}_{\bar{C}\bar{C}} &= \mathbf{H}_{\bar{c}\bar{c}}\mathbf{D}^{+}\mathbf{H}_c\\ \mathbf{H}_{\bar{C}\tilde{C}} &= -\mathbf{H}_{\bar{c}\bar{c}}\mathbf{D}^{+}\mathbf{H}_{\tilde{c}\tilde{c}}\\ \mathbf{H}_{\tilde{C}\tilde{C}} &= \mathbf{H}_{\tilde{c}\tilde{c}}\mathbf{D}^{+T}\mathbf{H}_d\end{aligned} \tag{5.38}$$

where

$$\begin{aligned}\mathbf{H}_a &= \left(\mathbf{H}_{\tilde{c}\tilde{c}}\mathbf{Z}_{\tilde{c}\bar{c}}-\mathbf{H}_{\tilde{c}\tilde{c}}\mathbf{Z}_{\tilde{c}\tilde{c}}\mathbf{Z}_{\tilde{c}\tilde{c}}^{+}\mathbf{Z}_{\bar{c}\bar{c}}-\mathbf{Z}_{\tilde{c}\tilde{c}}^{+}\mathbf{Z}_{\bar{c}\bar{c}}\right)\mathbf{H}_{\bar{c}i}-\mathbf{H}_{\tilde{c}i}\\ \mathbf{H}_b &= \left(\mathbf{H}_{\bar{c}\bar{c}}\mathbf{Z}_{\bar{c}\tilde{c}}-\mathbf{H}_{\bar{c}\bar{c}}\mathbf{Z}_{\bar{c}\bar{c}}\mathbf{Z}_{\tilde{c}\tilde{c}}^{+}\mathbf{Z}_{\tilde{c}\tilde{c}}-\mathbf{Z}_{\tilde{c}\tilde{c}}^{+}\mathbf{Z}_{\tilde{c}\tilde{c}}\right)\mathbf{H}_{\tilde{c}i}-\mathbf{H}_{\bar{c}i}\\ \mathbf{H}_c &= \left(\mathbf{H}_{\tilde{c}\tilde{c}}\mathbf{Z}_{\tilde{c}\tilde{c}}+\mathbf{I}\right)\mathbf{Z}_{\tilde{c}\tilde{c}}^{+}\\ \mathbf{H}_d &= \left(\mathbf{H}_{\bar{c}\bar{c}}\mathbf{Z}_{\bar{c}\bar{c}}+\mathbf{I}\right)\mathbf{Z}_{\tilde{c}\bar{c}}^{+}\end{aligned} \tag{5.39}$$

There is only one inverse operation for frequency response functions in equation (5.38), which is $\mathbf{D}^{+}$. This is the same as the Klosterman-Jetmundsen method (K-J method) as shown in equation (5.3). Therefore, the computation time and the sensitivity to noise in the FRF data are basically the same for both coupling methods. The calculation of $\mathbf{Z}_{\tilde{c}\tilde{c}}^{+}$ should not have a problem since matrix $\mathbf{Z}_{\tilde{c}\tilde{c}}$ is given analytically and its size is relatively small.

The pseudo-inverse $\mathbf{D}^{+}$ is calculated using singular value decomposition (SVD). Performing an SVD on matrix $\mathbf{D}$, which has dimension $n_{\bar{c}}\times n_{\tilde{c}}$, we have

$$\mathbf{D}=\mathbf{U}\mathbf{S}\mathbf{V}^{h} \tag{5.40}$$

If matrix $\mathbf{D}$ is ill conditioned or even singular, the singular value truncation technique will be applied by setting a certain threshold value *tol* and truncate the singular values which are smaller than *tol*. If the remained number of singular values is r, then we have

$$\mathbf{D}^{+} = \mathbf{V}_r \mathbf{S}_r \mathbf{U}_r^h \tag{5.41}$$

The dimensions of $\mathbf{V}_r$, $\mathbf{S}_r$ and $\mathbf{U}_r^h$ are $n_{\tilde{c}} \times r$, $r \times r$ and $r \times n_{\bar{c}}$ respectively.

5.4. CASE STUDIES

Two case studies are presented in this section. The advantages of the newly-developed generalised joint description method (GJDM) for coupling analysis are demonstrated by these examples.

The first case is designed to show how the properties of joint parameters, mainly stiffness and damping, affect the coupling results. The second case is more practical - a larger finite element model is used to investigate the high-order mode truncation effect and tolerance to noisy data. The results are compared with those obtained from the standard K-J method.

5.4.1. Cross beam structure

DESCRIPTION OF THE STRUCTURE

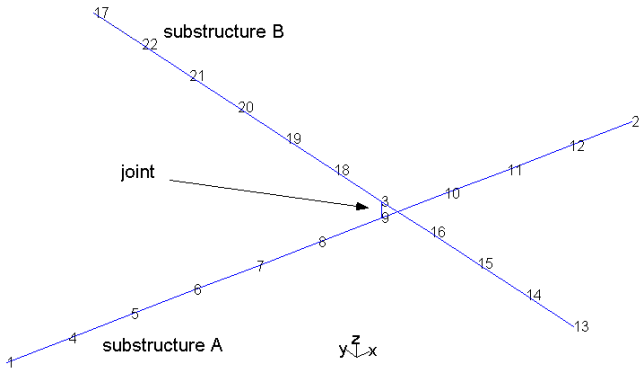

Fig. 5.1 Cross beam structure

Two identical beams are placed horizontally in a right angle and are connected vertically via another very short beam which plays the role of the joint. The lower beam is named substructure A and the higher beam is substructure B. The length of each of the substructures is $419mm$ and the length of the joint is $3mm$. The

cross section of the substructures is rectangular, $30mm \times 5mm$. The cross section of the joint beam is circular with diameter $\phi = 8mm$.

Each substructure is divided evenly into 10 Timoshenko beam elements. The joint is described by a single beam element which has 6 degrees of freedom at each end. Its mass and stiffness matrices are formed by standard finite element method. The proportional damping is introduced to generate frequency response functions for both substructures and the joint. The proportional viscous damping model is

$$\mathbf{c} = \beta \mathbf{k} \tag{5.42}$$

If the mass of the joint is neglected then the describing matrix of the joint becomes

$$\mathbf{Z}(\omega) = \mathbf{k} + i\omega\mathbf{c} = \mathbf{k}(1 + i\omega\beta) \tag{5.43}$$

GJDM COUPLING ANALYSIS

To validate the generalised joint describing method for coupling analysis, its theory and algorithm, the coupling analysis result is compared with the result of the complete assembled finite element model. In this comparison, the joint parameters prepared for coupling analysis are set to be the same as those used in the assembled finite element model. Based on noise-free input FRFs, all the frequency response functions of the assembled structure are predicted accurately using GJDM. An example is given in Fig. 5.2.

One of the advantages of GJDM is that the joint parameters can be modified independently. This advantage makes it possible that the dynamic characteristics of a structure can be tuned to some extend by varying the joint parameters only. In other words, the joints, which are normally the most difficult parts in finite element modelling, can be completely separated from the substructures and treated independently. After the joint parameters are properly adjusted, they can be used together with frequency response functions of the individual substructures to implement the GJDM coupling analysis. In the case shown in Fig. 5.1, for instance, if we increase the damping of the joint by setting a larger

β value in equation (5.42), $\beta = 1\times10^{-5}$, the coupling result will then show the effect of this perturbation, as shown in Fig. 5.3 in which the proportional damping factor for the assembled structure is 5×10^{-7}.

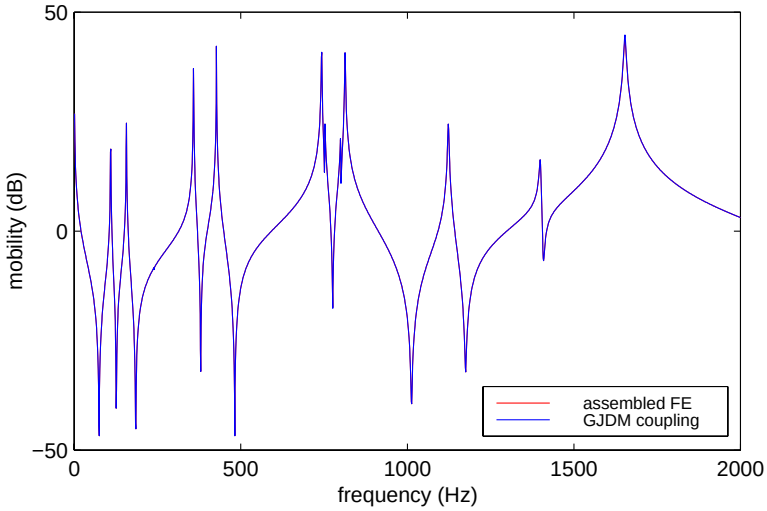

Fig. 5.2 Validation of GJDM

The flexibility of changing joint parameters cannot be so easily achieved in the assembled finite element model. This means that GJDM coupling analysis not only saves computation cost by breaking down a large structure into smaller substructures, but it also solves problems which cannot be worked out efficiently using the assembled finite element model.

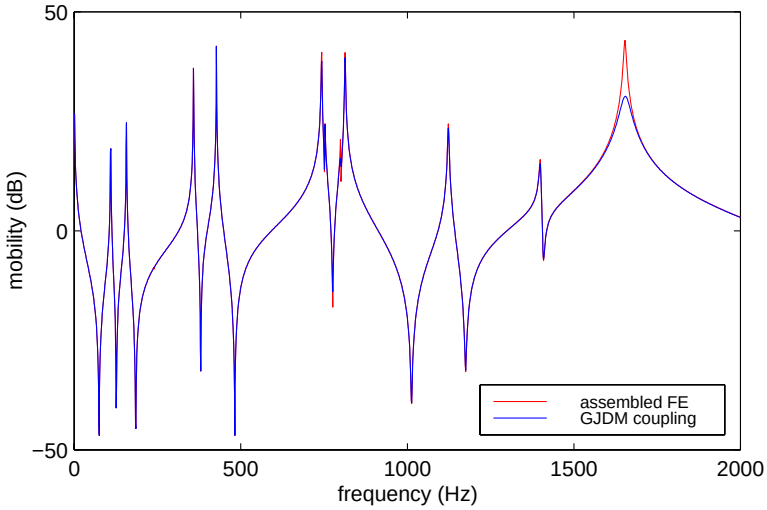

Fig. 5.3 Coupling result of increasing the joint damping

APPLICATION OF K-J COUPLING METHOD

If this same coupling problem is dealt with using Klostarman-Jetmunden coupling method, the joint has to be assigned belonging to one of the substructures. This will generally bring two problems: the first is that the modification of joint parameters will no longer be achieved so flexibly. Any small change of joint parameters will result in the need for a re-analysis of the substructure to which the joint is attached. This is time-consuming if the number of degrees of freedom of the substructure is large, or if the modification needs to be done a number of times; the second problem is that the introduction of a joint may cause the stiffness matrix of the joint attached substructure to be ill-conditioning because, in general, the stiffness of the joint is much greater than the stiffness of the substructure elements. The ill-conditioned stiffness martrix will further cause difficulties in the eigen-solution.

In this simple case, the coupling result of K-J method is as accurate as that of GJDM as shown in Fig. 5.2. The tolerance to noisy input data is more or less the same as GJDM, according to the analysis in section 5.3. More detail comparisons between these two FRF coupling methods will be given and discussed in the next section for a more complicated case study, a plate couples with a beam.

5.4.2. Plate couples with beam

DESCRIPTION OF THE STRUCTURE

A brass plate shown in Fig. 5.4 and a brass beam shown in Fig. 5.5 are to be coupled together using a steel bolt. The alignment of the coupled system is shown in Fig. 5.6. The detail of the connection joint is shown in Fig. 5.7 where the size of the steel bolt is M4. The material properties of the structure are listed in Table 5.1.

Table 5.1

material	Young's modulus	Poisson's ratio	density
brass	$1.10\times10^{11}\,N/m^2$	0.29	$8.54\times10^{3}\,kg/m^3$
steel	$2.10\times10^{11}\,N/m^2$	0.30	$7.80\times10^{3}\,kg/m^3$

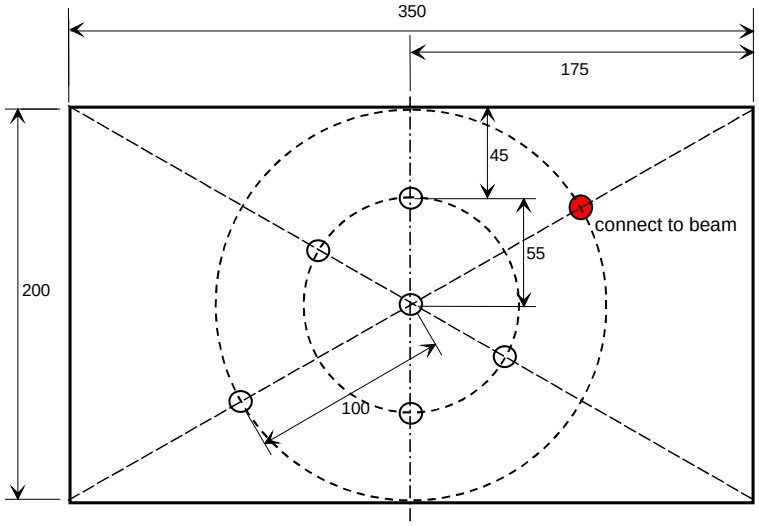

Fig. 5.4 Brass plate, thickness 3mm

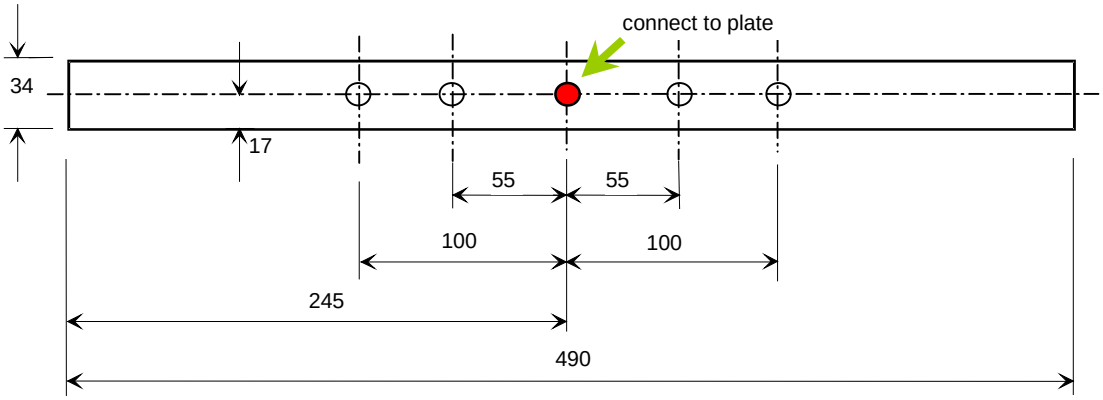

Fig. 5.5 Brass beam, thickness 3mm

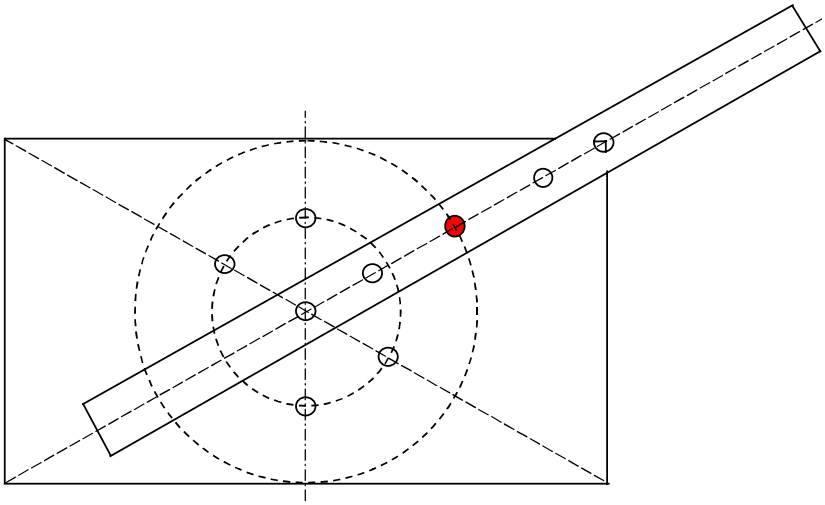

Fig. 5.6 The assembled structure

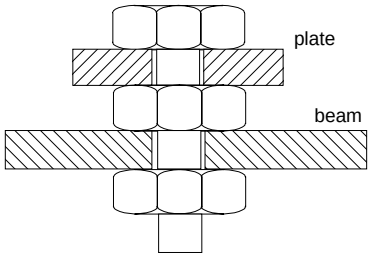

Fig. 5.7 Bolt connection

COUPLING ANALYSIS I: KLOSTERMAN- JETMUNDSEN METHOD

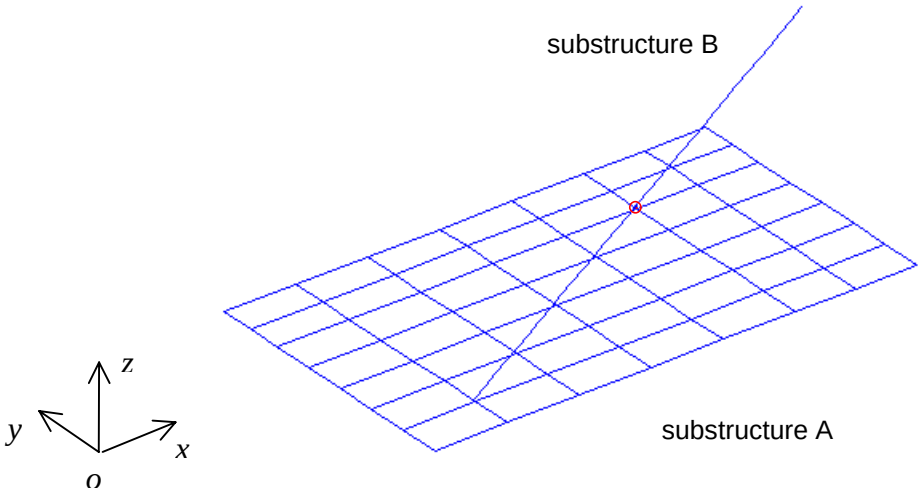

Fig. 5.8 FE mesh for coupling analysis

Substructure definition

The plate is taken as substructure A and the beam together with the bolt are taken as substructure B. The FRFs of the two substructures, A and B, are generated from the modal analysis of their finite element models. The 4-node 20-DOF plate elements are used to model the plate, and Timoshenko beam elements are used to analyse the beam, substructure B. FRFs were generated using the mode superposition method: the numbers of modes used were: $m_A = 300$, $m_B = 50$.

Coupling result

FRFs of the coupled structure were obtained by implementing the analysis based on the Klosterman-Jetmundsen method. Input data were the FRFs of the substructures. The result is compared with the "exact" FRFs which were

produced by analysing the finite element model of the whole assembled structure. One FRF of the coupling analysis results, the point FRF H_{5z5z}, *i.e.* the translation point FRF in the *z* direction of node 5, which is the coupling node on the plate, is shown in Fig. 5.9 overlaid with its corresponding "exact" FRF. It is seen that the K-J method works well in general except the frequency shift the frequency range of 800Hz to 1200Hz.

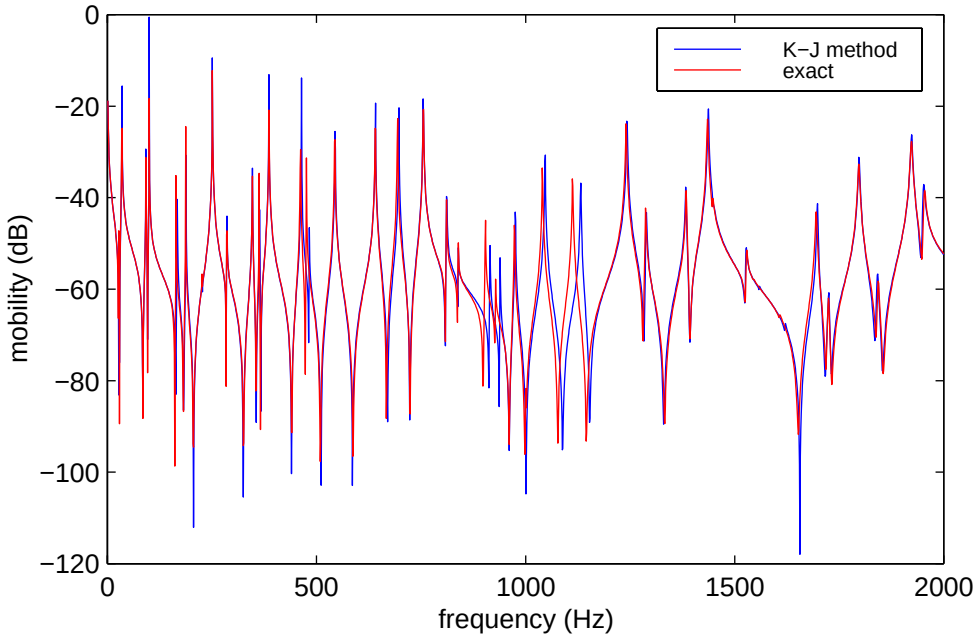

Fig. 5.9 Point FRF H_{5z5z} obtained from the K-J coupling analysis

COUPLING ANALYSIS II: GENERAL JOINT DESCRIPTION METHOD

Substructure definition

In this analysis, the plate is still taken as substructure A but the beam is taken as substructure B which excludes the bolted joint. FRFs of the two substructures, A and B, are also generated from the modal analysis of their finite element models using mode superposition method.

Joint definition

The bolt which connects plate and beam is defined as a beam element. Since the mass of the bolt is very small compared with any of the substructures, either the plate or the beam, only the bolt stiffness is taken into account to construct the joint description impedance matrix, $\mathbf{Z}$. The compatibility of degrees of freedom

is considered in forming the matrix, $\mathbf{Z}$. The beam element has 6-DOFs at the boundary connecting it to the beam $(n_{\tilde{c}} = 6)$ and 5-DOFs at the boundary connecting to the plate $(n_{\bar{c}} = 5)$. Therefore, the dimension of matrix $\mathbf{Z}$ is 11×11.

Coupling result

FRFs of the coupled structure were obtained by implementing the programme of the general joint description method. Input data were the FRFs of the substructures as well as joint description matrix, $\mathbf{Z}$. The result is validated by the "exact" FRFs which were produced by analysing the finite element model of the whole assembled structure. One FRF of the coupling analysis results, the point FRF of 5*z*, *i.e.* the translation DOF in *z* direction of node 5, which is the coupling node on the plate, is shown in Fig. 5.10 overlaid with its corresponding "exact" FRF. It is clear in Fig. 5.10 that the coupling analysis yields a very good result. There are no significant frequency shifts as shown in Fig. 5.9.

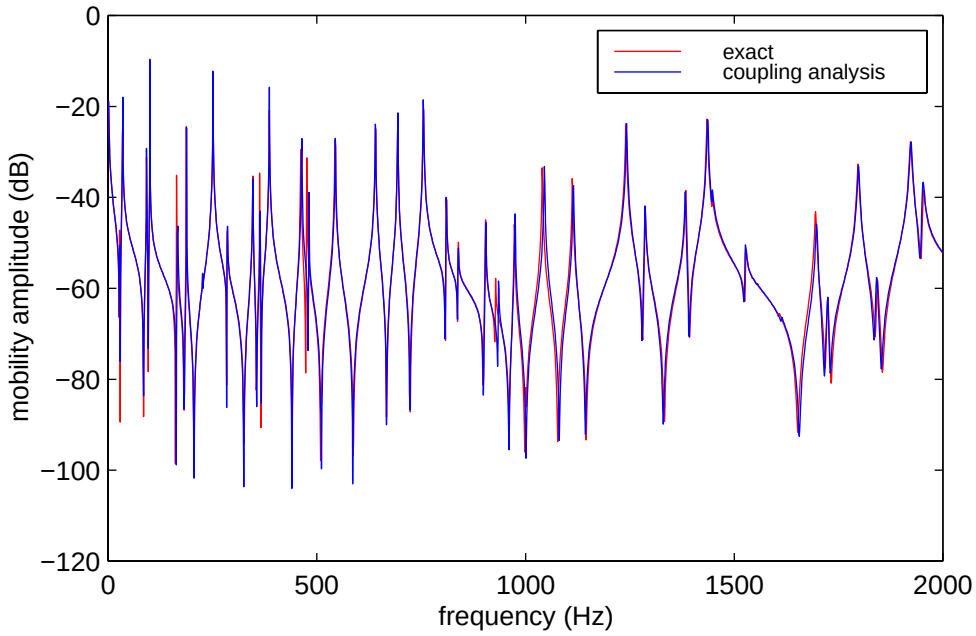

Fig. 5.10 Point FRF H_{5z5z} obtained from the GJDM coupling analysis

Substructure residual effect

It should be pointed out that the total numbers of modes used for substructures A and B were 320 and 186 respectively, while the coupling result shown in Fig.

5.10 was achieved by using only the first 300 modes from substructure A and the first 50 modes from substructure B.

To investigate the substructure residual effect, the number of modes used in generating the FRFs is set as a variable. Table 5.2 shows the numbers of modes of substructure A (plate) which were used in the study, together with the corresponding highest natural frequencies. In all cases, the FRFs of substructure B (beam) were generated using 30 modes in which the highest natural frequency was 7049 Hz.

Table 5.2

	$m_A = 130$	$m_A = 150$	$m_A = 200$	$m_A = 250$	$m_A = 300$
f_{m_A} (Hz)	12875	16545	28872	52693	95703

The coupling analysis results obtained by different numbers of high-order mode truncations are shown in Fig. 5.11. This is the same FRF as shown in Fig. 5.10, the point FRF at 5*z*. According to the modal analysis of the assembled system finite element model, there are 43 elastic modes in the frequency range of 0 to 2,000Hz, but not all of them are included in this point FRF plot. It is noticed in Fig. 5.11 that only three modes, numbered as 23, 24 and 28, which have the frequency values of 903.7Hz, 927.8Hz and 1112.3Hz respectively, are significantly affected by the high-order mode truncations. The rest modes are almost consistent with respect to different numbers of mode truncation.

It is found that mode 28 in Fig. 5.11 (at 1112.3Hz) is dominated by residuals. Its frequency shifts to a higher value and its amplitude becomes smaller with regard to the decrease of m_A, the number of modes included for generating FRFs of substructure A, the plate. Further calculations show that if m_A is chosen such that $m_A < 120$, this mode will disappear from this FRF plot.

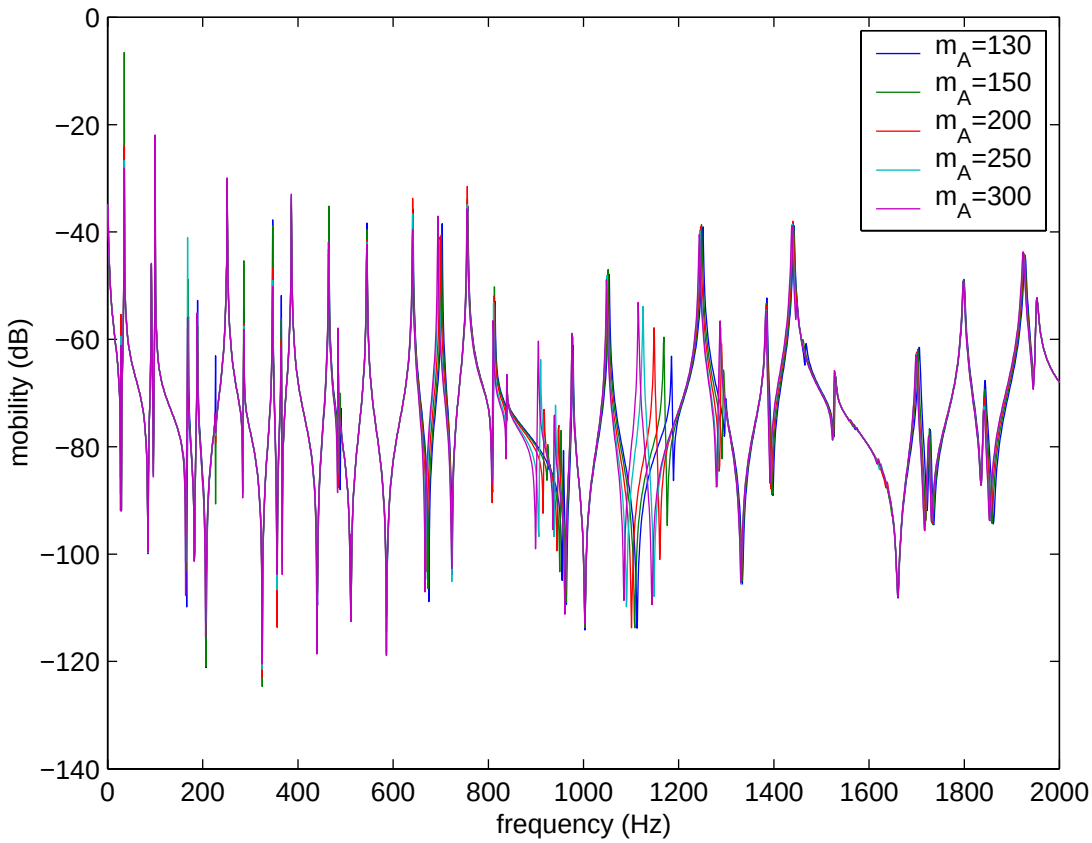

Fig. 5.11 Investigation of residual effect ($m_B = 30$)

It is obvious that the number of modes included in generating the FRFs for substructure A plays a very important role in the accuracy of the coupling result. The residual FRFs in the frequency range 0 to 2,000Hz were then generated including the truncated modes, from mode 131 to 300, and are shown in Fig. 5.12. These FRFs are, from top to bottom: $H_{5\theta_x 5\theta_x}$, $H_{5\theta_y 5\theta_y}$, $H_{5\theta_x 5\theta_y}$, $H_{5z5\theta_x}$, $H_{5z5\theta_y}$, H_{5z5z}, H_{5x5x}, H_{5y5y} and H_{5x5y}.

Comparing the amplitudes of these residual FRFs with those of the FRFs used for coupling analysis, which are shown in Fig. 5.13, we can see that these residual FRFs are not negligible even though the truncation frequency has already been 6 times of the highest interested frequency.

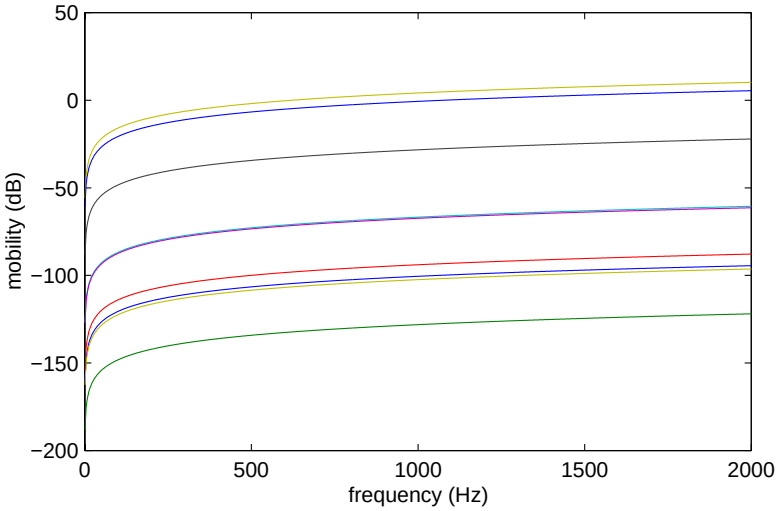

Fig. 5.12 Residual FRFs of substructure A

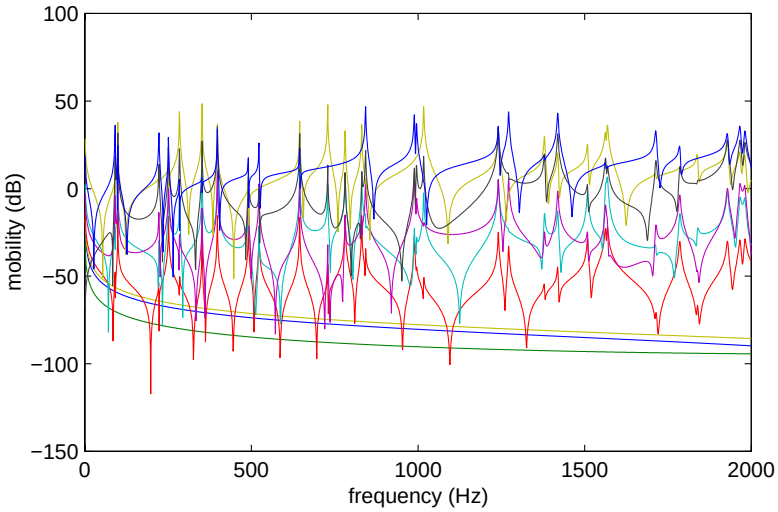

Fig. 5.13 FRFs of plate at coupling DOFs

Therefore, in principle, the GJDM method is recommended when measured FRFs are available because they do not have mode truncation error. For analytical coupling analysis, the improved CMS method, CMSJ, should be the first choice. In the cases where FRF coupling method has to be applied, a large number of modes need to be calculated in order to generate the substructures′ FRFs.

Tolerance to noisy data

The motivation to develop the K-J method and the GJDM is to permit direct use of measured frequency response functions. Therefore, It is important to verify that these methods can work properly when they are supplied with noise-contaminated data.

If 10% random noise is added to the FRF matrices for both substructures A and B, the coupled result obtained from GJDM previously shown in Fig. 5.10 is shown here in Fig. 5.14.

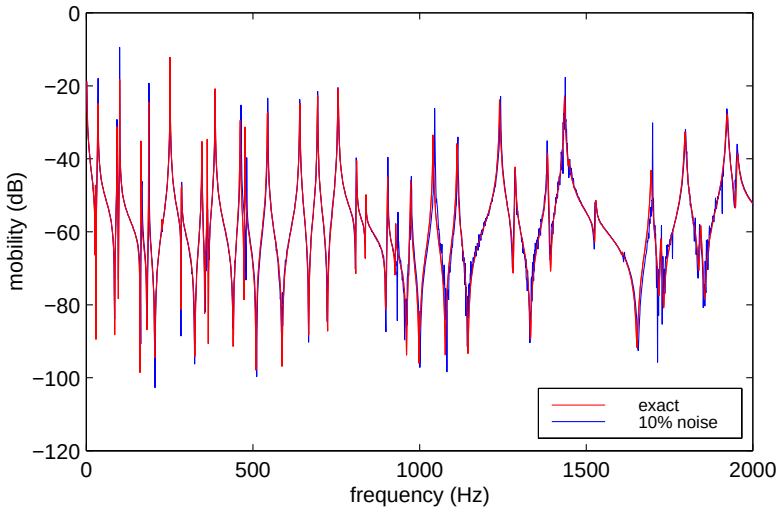

Fig. 5.14 Coupling result (GJDM) when 10% noise in input FRFs

Following the same procedure, Fig. 5.15 shows the coupling result when the FRF matrices of the substructures are contaminated by 20% noise.

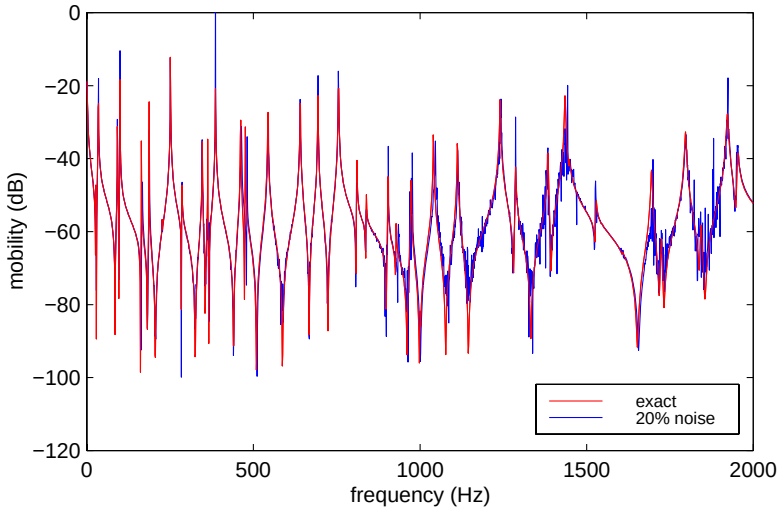

Fig. 5.15 Coupling result (GJDM) when 20% noise in input FRFs

By applying singular-value truncation to the 20% noise case in which the threshold was set as $\varepsilon = 10^{-6}$, the result is improved. To justify the quality of the predicted FRFs which are obtained using noisy FRFs from the substructures, the correlation (FRAC, defined in Appendix F) between the predicted FRF matrices and the exact FRF matrix is calculated. The FRAC values shown in Fig. 5.16 are the correlations of the upper triangle FRF matrices, in which there are 15 FRFs. The corresponding full FRF matrix is shown in equation (5.44).

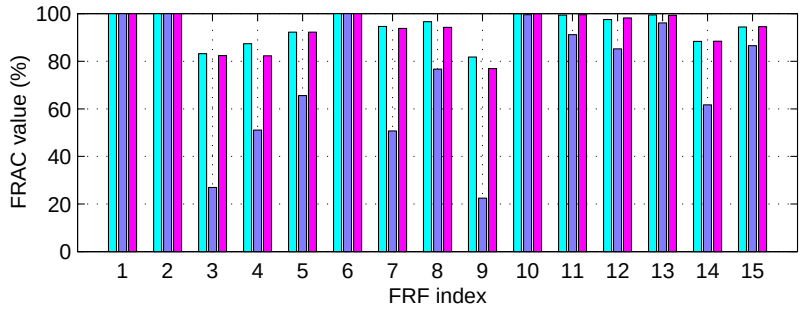

Fig. 5.16 FRACs: 10% noise, 20% noise, 20% with σ-value truncation

$$\mathbf{H}_{\bar{C}} = \begin{bmatrix} H_{5x5x} & H_{5x5y} & H_{5x5z} & H_{5x5\theta_x} & H_{5x5\theta_y} \\ H_{5y5x} & H_{5y5y} & H_{5y5z} & H_{5y5\theta_x} & H_{5y5\theta_y} \\ H_{5z5x} & H_{5z5y} & H_{5z5z} & H_{5z5\theta_x} & H_{5z5\theta_y} \\ H_{5\theta_x5x} & H_{5\theta_x5y} & H_{5\theta_x5z} & H_{5\theta_x5\theta_x} & H_{5\theta_x5\theta_y} \\ H_{5\theta_y5x} & H_{5\theta_y5y} & H_{5\theta_y5z} & H_{5\theta_y5\theta_x} & H_{5\theta_y5\theta_y} \end{bmatrix} \tag{5.44}$$

It is shown that GJDM is generally not sensitive to noise. All point FRFs, those are number 1, 6, 10, 13 and 15, are very well predicted, even in the 20% noise case. The results which have low FRAC values are basically those FRFs which have low response levels. The FRAC values increase significantly when singular value truncation is applied to the 20% noise case. They are almost the same as 10% noise case without the singular value truncation.

Comparison between K-J method and GJDM

The coupling results produced by K-J method and GJDM are compared under the same conditions: the same numbers of modes are used to generate the FRFs of the substructures and these FRFs are free of noise. The FRAC – correlation between the coupling analysis results and the assembled finite element analysis result – is calculated and displayed in Fig. 5.17.

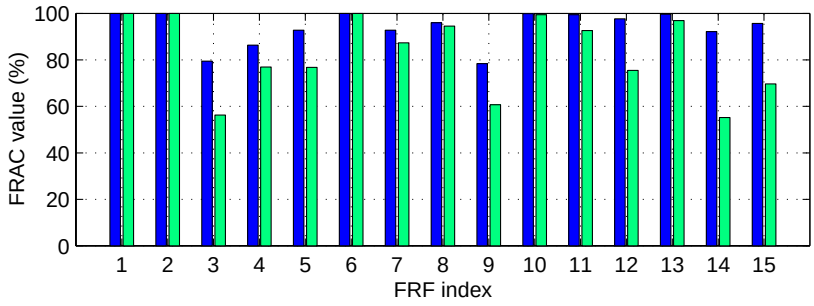

Fig. 5.17 FRAC of the two coupling methods: GJDM, K-J method

It is seen that the GJDM is universally superior to the K-J method in this example.

5.5. CONCLUSION

The development of a new FRF coupling analysis method, the generalised joint describing method (GJDM) has been reported and it has the following advantages compared with the conventional Klosterman-Jetmunden (K-J) method:

- the joint is completely separated from the main substrutures, and joint parameters are modified independently. The substructures do not need to be re-analysed with respect to the variation of joint parameters;
- separating the joint from the substructures will help to avoid generating an ill-conditioned stiffness matrix and therefore to reduce the difficulties in solving the eigen-problem of substructuresand the method is not sensible to the noise in the input FRF data;
- the number of coupling degrees of freedom in one substructure can be different from another to accommodate the DOF non-conforming interfaces[FaGe92];
- the joint describing impedance matrix is very flexible. Its stiffness and damping can be adjusted to fulfil the requirment of the system response. This is not only an advantage for substructure coupling analysis but also provide a technique for damper design in vibration control.

CHAPTER 6

NON-LINEARITY CONSIDERATIONS IN JOINT MODELLING AND SUBSTRUCTURE COUPLING

6.1. MOTIVATIONS

Linear modelling of structural joints has been introduced and applied in the four preceding chapters, chapter 2, 3, 4 and 5. A linear joint model is an idealised description of joint properties in the sense that it has constant-valued mass, stiffness and damping matrices. This idealisation is normally accurate enough to represent most structural joints which are designed for firmly-fastened connections such as welded, glued, bolted and riveted joints. The physical explanation of this kind of joint is that there should be no relative movement between interfaces; in other words, the interfaces are ***stuck*** together. In contrast, joints which are designed for utilising friction damping to control vibration response levels belong to a different regime. These connections are designed to have relative movement between interfaces, *i.e.*, ***macro-slip*** occurs between the

interfaces. The friction introduced by macro-slip dissipates vibration energy and generally causes a non-linear behaviour of the system.

The classification of joints into two categories – stuck and macro-slip – is based on the lumped parameter model and Coulomb friction theory [Caug60]. When a continuous model is considered as developed by Meng [MeBG86], another phenomenon, ***micro-slip***, can be revealed. This is a transition status between stuck and macro-slip and is, of course, non-linear. Since it is possible for micro-slip to occur in fastened joints, a comprehensive research on joint modelling should not only include linear cases as the status of stuck joints, but should also include non-linear cases, such as micro- and macro-slip. Macro-slip, however, involving the entire relative motion of the contact surfaces in tangential direction, can be defined as a failure to a fastened joint and is not mainly concerned here.

In this chapter, the current status of research on friction in joint modelling is reviewed including the related theoretical background and the applicability in practice. The purpose of this chapter is to help users of linear joint models to understand the possible errors caused by non-linearities and also to indicate a direction for future work in the area of non-linear joint modelling.

To clarify the terminology, the three status of the contact surfaces are named as stuck, micro-slip and macro-slip. Some other names appear in the relevant publications are listed here:

stuck = locked, stop
micro-slip = partial slip, slip
macro-slip = gross slip, global slip, sliding

6.2. STATE OF THE ART

Research which specifically focuses on modelling non-linearity of fastened joints is very limited compared with that on linear joint modelling methods,

while a large number of publications can be found on general non-linear topics, and on contact and friction. Since contact and friction constitute the physical essence of some commonly-used joints, such as bolted and riveted ones, we will briefly look back at the milestones of their development and then pay more attention in the analysis of micro-slip, its theory and applicability aspects.

The main references of this chapter which cover 70 years are categorised here as shown in Fig.6.1.

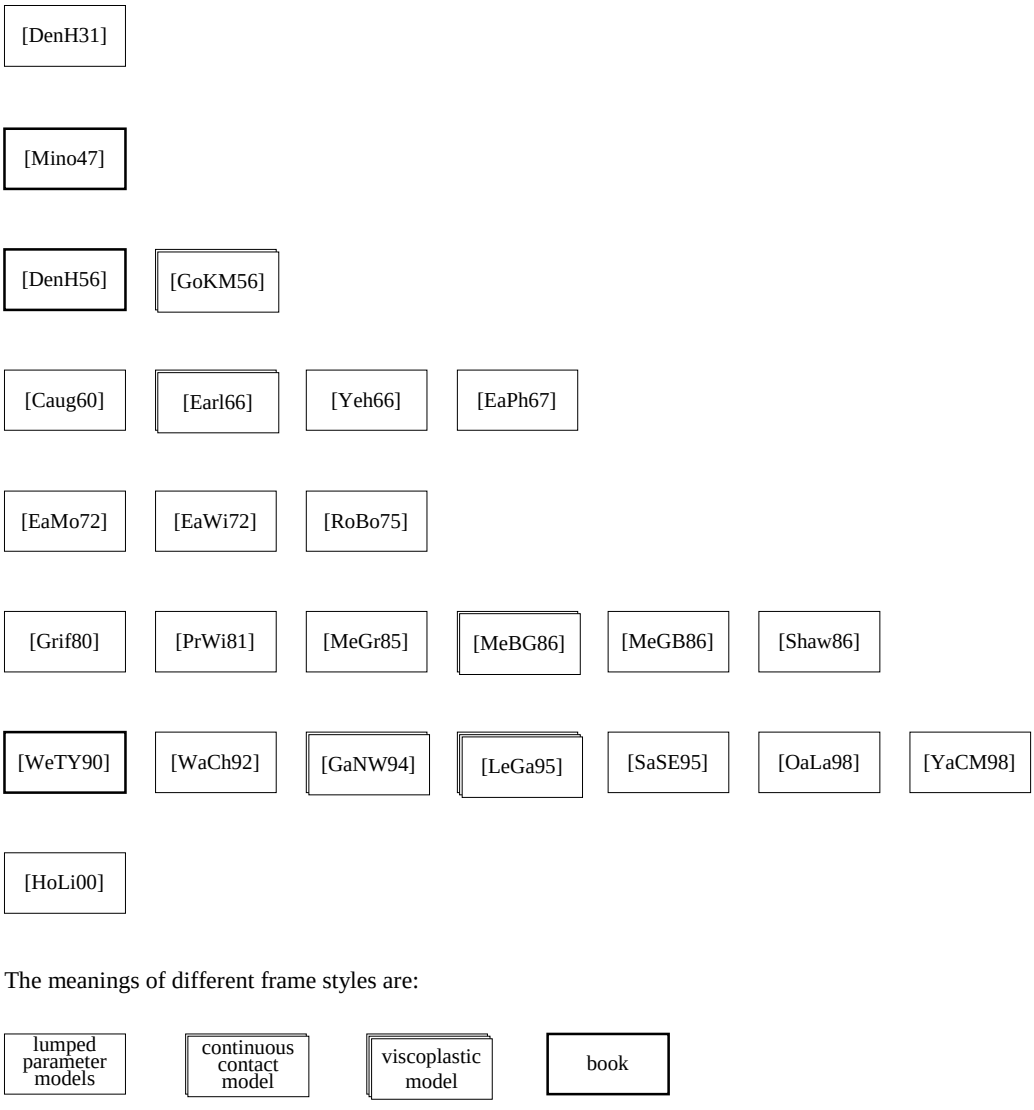

Fig.6.1 Categorised references

6.2.1. Friction Modelling Based on Coulomb Theory: Lumped Parameter Models

In analysing the dynamic response of structures it is common practice to represent the friction that occurs at contact surfaces by means of single point contact models. By using these Coulomb theory based models it is effectively assumed that the bodies in contact are rigid and that the friction force at the interface is proportional to the corresponding normal force. Basically, the use of single point contact models can only represent accurately a fully-slipping or a fully-stuck situation.

Since Den Hartog published his pioneering work in 1931 [DenH31], many followers have been involved in the research area of friction damping. Most of them studied the non-linear behaviour of a single-degree-of-freedom (SDOF) system with a Coulomb friction element. These SDOF models have lumped parameters and can describe either stuck or macro-slip status. The physical model used by Den Hartog (without viscous damping) is shown in Fig.6.2 in which the friction model is described by equation (6.1) and Fig.6.3.

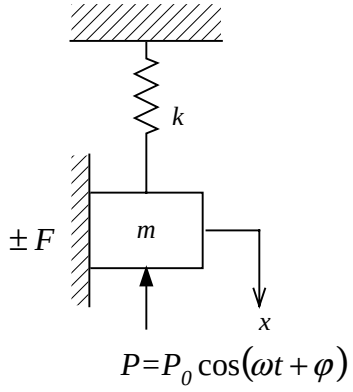

Fig.6.2 The frictional vibration system [DenH31]

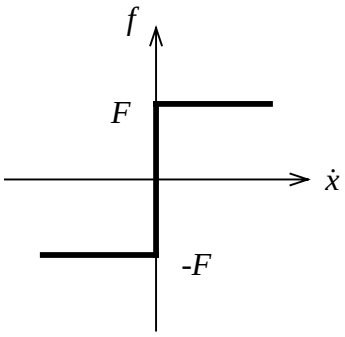

Fig.6.3 Friction model

$$f\begin{cases} = F & \text{if } \dot{x} > 0 \\ \in [-F, F] & \text{if } \dot{x} = 0 \\ = -F & \text{if } \dot{x} < 0 \end{cases} \tag{6.1}$$

An exact solution is given in Den Hartog's paper [DenH31] for the motion of the SDOF system with a sinusoidal excitation force and Coulomb friction damping. He showed that for a resonant system, friction alone controls the response amplitude only over a very narrow range of amplitude of the exciting force. If the exciting force is less than the friction force, the mass will not move at all (stuck) and if it is greater than $4/\pi$ times the friction force, the amplitude of an otherwise linear system is not limited at resonance. His results shown in Fig.6.4 are widely accepted and collected in his later textbook [DenH56] and Timoshenko's book [WeTY90].

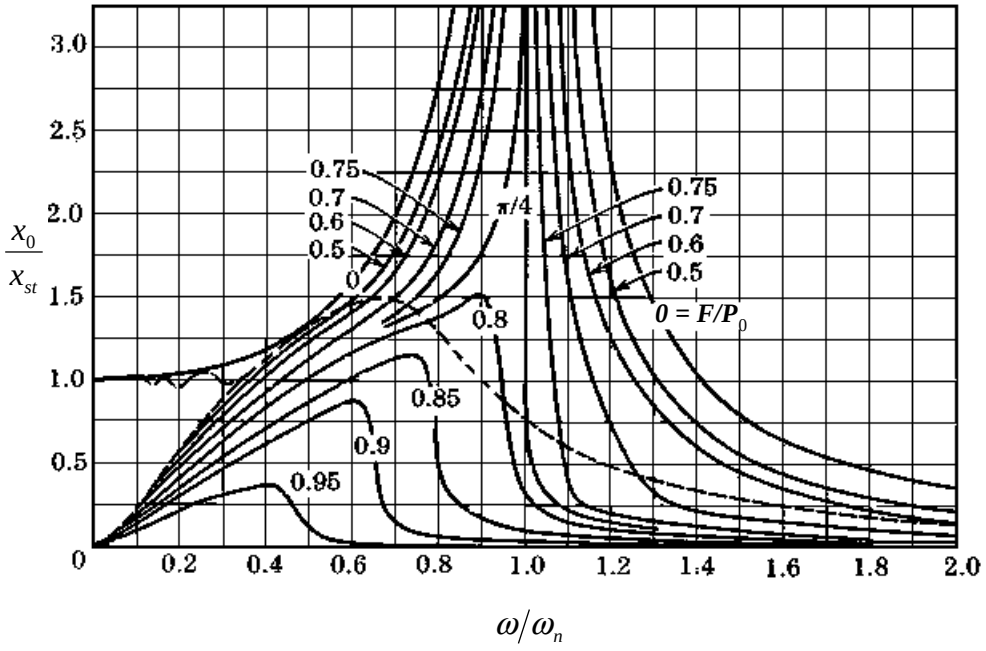

Fig.6.4 Amplitude diagram with Coulomb damping only

The results shown in Fig.6.4 were obtained from two possible types of motion. One is that the mass never comes to rest. This motion is depicted in Fig.6.5 and corresponds to the part of Fig.6.4 above the broken line. The other type of motion is that during each half-cycle the mass will stick for a while, and, while

sticking, the value of the friction is within $[-F, F]$, as shown in Fig.6.6 with the result shown in the curves below the broken line of Fig.6.4.

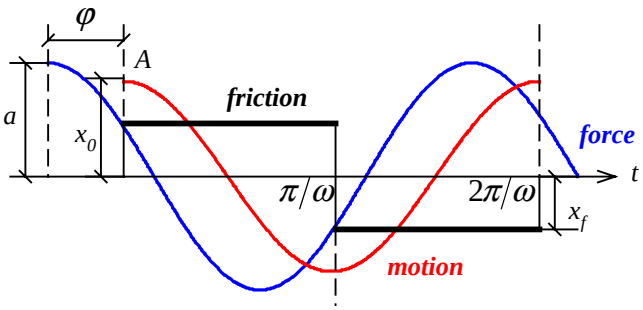

Fig.6.5 Motion without stuck

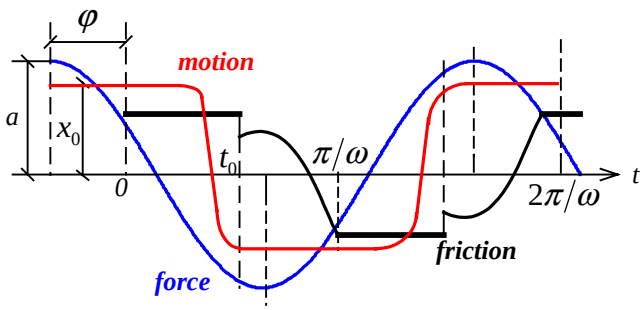

Fig.6.6 Motion with one stuck ($0 < t < t_0$ macro-slip, $t_0 < t < \pi/\omega$ stuck)

The once-stuck motion had also been verified by experiment of Den Hartog. The hysteresis loop obtained from his test shows the phenomenon of stuck and macro-slip as in Fig.6.7, where the straight lines construct an approximated bilinear hysteresis.

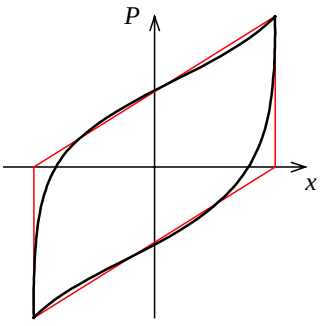

Fig.6.7 Record of motion with one stuck per half-cycle

To simplify the analysis of friction damping, Den Hartog proposed a concept of equivalent viscous damping constant [DenH56], which works in such a manner

that with sinusoidal motion the friction damping force does the same work per cycle as is done by the equivalent viscous damping force. The equivalent viscous damping constant c_e thus obtained is a function of frequency, ω, and displacement amplitude, x_0, as

$$c_e = \frac{4F}{\pi\omega x_0} \tag{6.2}$$

The amplitude diagram for viscous damping is shown in Fig.6.8 and the corresponding diagram for equivalent viscous damping is shown in Fig.6.9. Considering the cases where the damping is reasonably small, we notice that the results of Fig.6.9 are approximately the same as the corresponding curves in Fig.6.4.

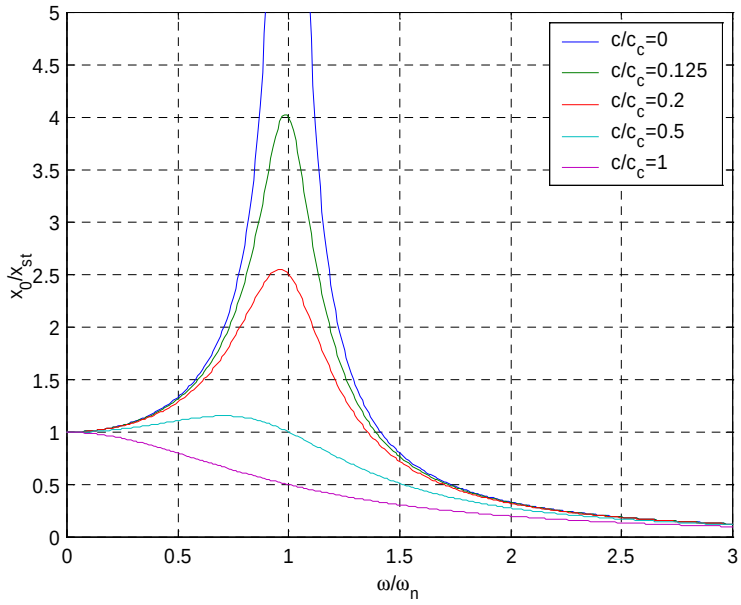

Fig.6.8 Amplitude diagram for viscous damping

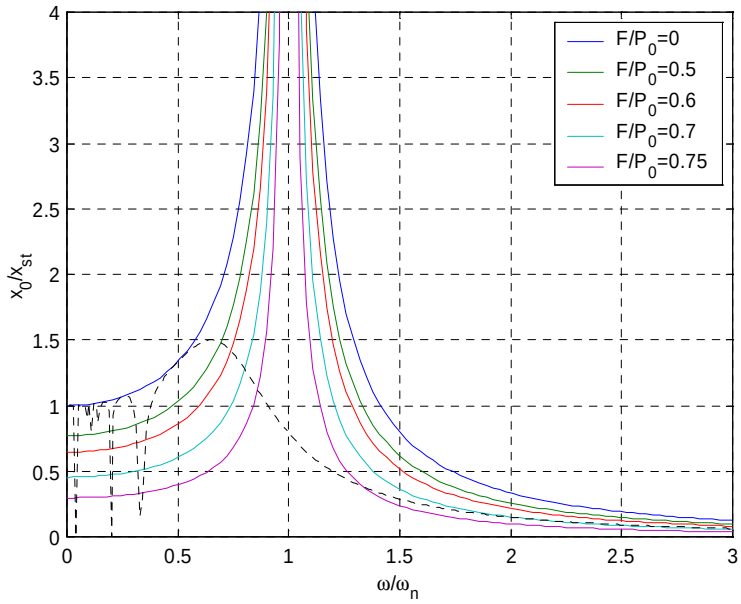

Fig.6.9 Amplitude diagram for equivalent viscous damping

A SDOF system, shown in Fig.6.10, which exhibits more general bilinear hysteresis as shown in Fig.6.11 and undergoes sinusoidal excitation, was analysed by Caughey [Caug60]. The method of solution is called the *method of slowly varying parameters*. It supposes that the system response takes the form of

$$x(t) = X\cos(\omega t + \phi) \tag{6.3}$$

where X and ϕ are slowly varying functions of t. These slowly varying parameters can be replaced by their mean values over one cycle of θ, where $\theta = \omega t + \phi$.

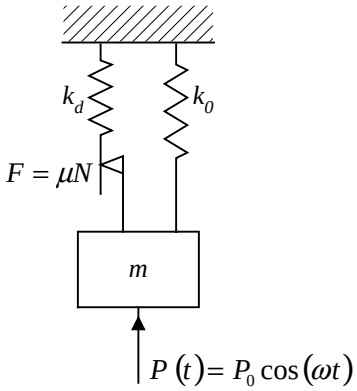

Fig.6.10 A 3-parameter SDOF system

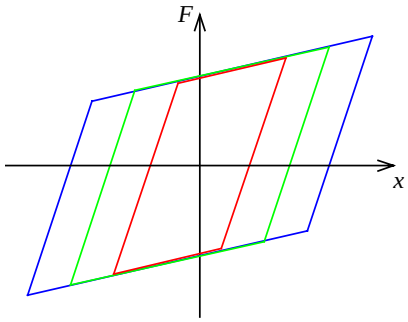

Fig.6.11 Bilinear hysteresis

The following conclusions were drawn from Caughey's results (refer to Fig.6.12):

- the system exhibits a "soft" type of resonance; *i.e.*, the resonance peak moves to a lower frequency as the amplitude of the driving force is increased;
- the response curves are single-valued and stable, and show very steep slopes on the low-frequency side of the resonance;
- phase resonance and amplitude resonance occur at the same frequency in this system;
- for large enough excitation, the system exhibits an undamped resonance.

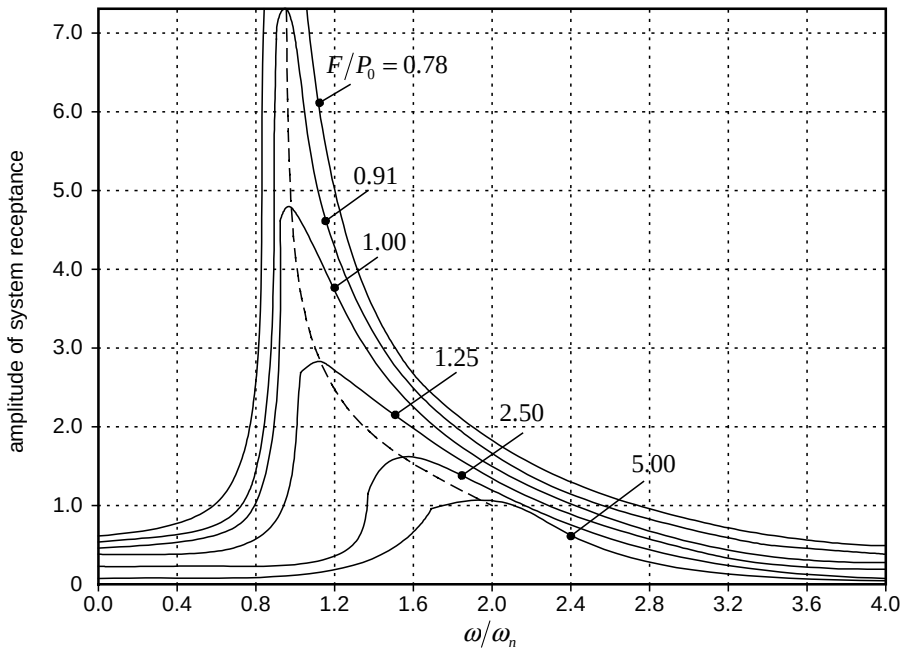

Fig.6.12 System receptance obtained by Caughey

The exact method for solving this non-linear problem is normally lengthy in computation time and this factor may make it unacceptable in a practical application to system with many DOFs. By comparison, methods whereby the frictional force is replaced by an equivalent sinusoidal force are rapid, yielding analytical solutions for the response of the system. A general, linear, MDOF structure excited by m sinusoidally varying forces P_j, $j=1,2,\ldots,m$, and having a single frictional damper linking two co-ordinates was analysed by Earles and Williams [EaWi72]. A linearised analysis of the frictionally-damped system was proposed based on two basic assumptions about the form of the frictional force: (i) at any frequency the frictional force may be written as $F(t)=F_L\sin(\omega t+\phi)$, where ϕ is the phase angle between the frictional and applied forces and is not a function of time; (ii) if macro-slip occurs at the damper, the frictional force is 180° out-of-phase with the relative slip velocity. Depending on the limiting value of friction at the joint, the applied forces and the frequency, macro-slip may or may not occur. These two states give rise to two distinct response regimes for the analysis, stuck and macro-slip. In the stuck regime, there is no slip at the damper interface, the relative slip amplitude is zero at all times, and $\theta=0$. The stuck condition is

$$|F_L| < \mu_s N \tag{6.4}$$

where μ_s is the coefficient of static friction and N is the normal load across the friction interface. The amplitudes of linearised friction force and response have the forms

$$F_L=\sum_j a_j P_j \text{ and } X_i=\sum_j b_{ij}P_j \tag{6.5}$$

where a_j and b_{ij} are constants determined by the receptance coefficients of the structure.

In the macro-slip regime, experiments showed that the measured amplitude of the frictional force was not constant as described in Fig.6.3. The frictional force

increased with increasing slip amplitude. It would appear reasonable, therefore, to examine, as a possible alternative for F_L, the expression

$$F_L = \mu_s N + \delta U \tag{6.6}$$

or

$$F_L = \mu_e N \tag{6.7}$$

where $\mu_e = \mu_s + (\delta/N)U$ and δ is assumed to be a constant for any given system. Its magnitude basically depends on the material and configuration of the interacting surfaces. For the rig used by Earles, and for the range of normal loads and displacements tested, the term δ/N should be constant $(\approx 29 mm^{-1})$. This conclusion is consistent with the assertion that the term $(\delta/N)U$ results from the work required to deform the contacting asperities during slipping. By substituting for the slip amplitude, U, an expression of linearised frictional force is then available explicitly as a function of μ_s, δ, N, P *etc.*

The curves of system receptance obtained from the linearised friction force analysis gave a good prediction of the pattern – not the exact amplitude – of the measured response of the system. Earles′ linearised analysis, as well as experiments, verified the "soft" type resonance behaviour, which was concluded from Caughey's study. In addition, the use of (6.7) for the linearised frictional force produces a significant improvement over Den Hartog′s expression where $\delta = 0$ only.

Since the early 1980s, Meng and his colleagues have published a series of papers on the subject of friction damping. These papers developed the methods used for stick-slip analysis and also made contributions to the analysis of micro-slip phenomenon which is a transition between stick and macro-slip. Using the same model as that used by Caughey, Fig.6.10, Meng assumed that the reaction force from the damper can be approximated as a sinusoid by expanding it in a Fourier series and keeping only the lowest terms [MeGr85]. The results obtained in this way are identical to the steady-state solutions of Caughey. An extensive application of this method to a beam structure with flexible damper

system yielded a response diagram, shown here as Fig.6.13, which verified and also completed Caughey's results.

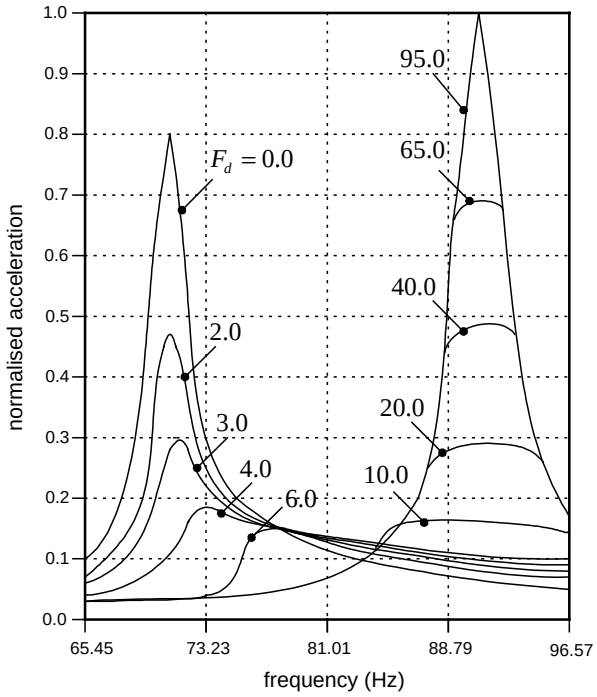

Fig.6.13 Responses of stuck and slip states

Fig.6.13 illustrates the procedure that the damper is from fully-slipping to fully-stuck with the change of the damper slip load, F_d. The curves obtained for $F_d \leq 6.0$ show typical non-linear features, the same "soft" character as Caughey's results in Fig.6.12, while the curves corresponding to $F_d \geq 10.0$ describe the sticking condition. The system is linear under these two extreme conditions – when the damper slip load F_d is zero or when it is completely stuck.

6.2.2. Friction Modelling Based on Coulomb Theory: Continuous Contact Models

Laboratory experiments have shown that idealisation of the friction problem to single point contact models, *i.e.*, lumped parameter models, may be acceptable if macro-slip occurs at the interface, usually as a consequence of the normal load being small. For high normal loads, however, only micro-slip may be expected. It has been recognised since the early 1950s when Mindlin showed

that there is micro-slip at the interface between two elastic bodies in contact [Dere74]. As a result, the energy dissipation increases as the third power of the displacement and Coulomb friction can control resonant vibration amplitude for excitation levels less than that necessary to cause macro-slip.

Mindlin tackled the problem from the viewpoint of contact mechanics [Dere74] and used a 2-sphere contact model. In general, when non-conforming faces of two elastic bodies are pressed together, the geometry of the contact area is a non-linear function of the normal pressure. In many cases the normal stress drops to zero at the contact boundary so that even small tangential loads cause some slip. The micro-slip at the interface between two elastic spheres with contact normal force and oscillatory tangential force was first analysed and this analysis led to further work on damping and stiffness of particulates under oscillatory loading [Dere74]. Except for some relatively minor effects, the energy dissipation at the interface increases with the cube of the displacement and has some effect even at vanishingly small loads. This makes it quite different from Den Hartog's solution in which there is no effect at small loads and where the energy dissipation increases linearly with the displacement. It is also true in this case that there is a critical vibration amplitude above which the frictional dissipation can no longer limit the vibration amplitude without help from other dissipation mechanisms, *e.g.*, viscous damping. Both the level of damping and the critical amplitude depend on the normal force. The results obtained from the analysis of spheres are applicable to beams and some of the validated analyses were summarised by Goodman [Good88].

The research on friction damping has been pushed forwards since 1950s in part due to the development of gas turbine engines. It has been known that slip in blade roots can yield useful damping for turbine and compressor blades. Goodman in the 1950s, Earls in the 1970s and Meng in the 1980s are some of the representatives.

The micro-slip concept was clearly described by Goodman and Klumpp [GoKl56]. Mainly working on the purpose of reducing resonant stresses by means of slip damping, Goodman and Klumpp gave an explicit formula for the

energy dissipated per cycle of vibration. They also concluded that joints must be designed so as to maintain a particular value of clamping pressure at the interface in order to achieve a maximum energy loss as shown in Fig.6.14. This result is consistent with that of Meng′s shown in Fig.6.13. The stress analysis of a plane interface under uniform pressure, but with variable slip, was carried out. The predictions of the theory were then confirmed by experiment. However, Goodman and Klumpp did not give a frequency response function.

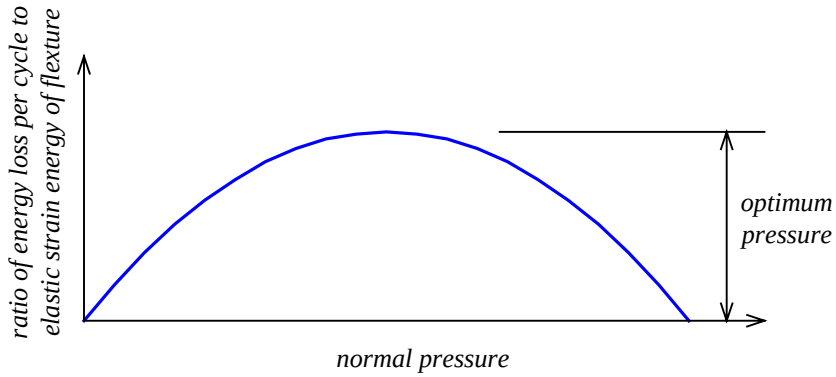

Fig.6.14 Variation of energy loss per cycle with joint normal pressure

A more systematic study of the micro-slip condition was reported by Meng *et al* [MeBG86] and a micro-slip model was proposed based on a continuous friction contact physical model. In its general form, the model consists of two elastic bars joined by an elastoplastic shear layer. One feature of this model is that the deformation paths for cyclic or irregular loading and unloading are determined automatically since the element has the inherent capacity to “memorise” the relevant portions of the past loading history. Another feature is that the relationship between the displacement and the force within the non-linear range was given in parametric form in terms of a parameter that measures the amount of slip in the element. Thus, it does not require *a priori* that the force be expressed in terms of the displacement or, conversely, the displacements in terms of the force. Instead, either choice is allowed.

The development of Meng′s partial-slip friction model is summarised as follows.

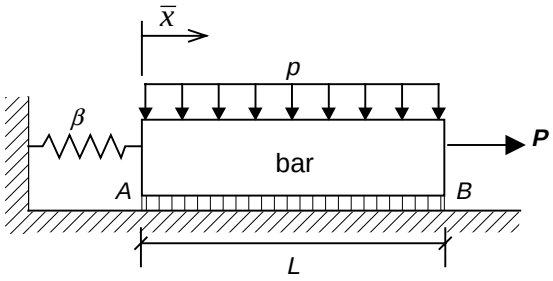

Fig.6.15 The continuous friction contact physical model

In the continuous model shown in Fig.6.15, it is assumed that the bar deforms elastically. If it is further assumed that friction at each contact point is governed by Coulomb's law, then the bar will start to slip at point *B* immediately after the application of the load. The region of slip will gradually extend leftwards with increasing load until *P* reaches the value μpL, for which case macro-slip will occur. In order to model the actual physical behaviour, an idealised elastoplastic shear layer of negligible thickness is placed between the elastic bar and the rigid support. To allow for the possibility of strain hardening in the element after the entire shear layer has yielded, it is convenient to add a discrete spring, of stiffness β, at the free end of the bar.

The elastic bar has a constant cross-sectional area, A, and a uniform Young's modulus, E. The friction force in the shear layer per unit length, τ, is given by

$$\tau = \begin{cases} ku & |u| \le \tau_m / k \\ \tau_m & \text{otherwise} \end{cases} \tag{6.8}$$

where k is the stiffness per unit length of the shear layer for small deformations, τ_m is the yield level (usually $\tau_m = \mu p$) and $u(\bar{x})$ is the displacement at a point a distance $\bar{x}$ from the left end of the bar.

The deformation, u, and friction force, τ, in the bar must satisfy the following equilibrium equation:

$$EAu'' - \tau = 0 \qquad 0 \le \bar{x} \le L \tag{6.9}$$

together with the boundary conditions,

$$EAu'(0) - \beta u(0) = 0 \qquad EAu'(L) = P \tag{6.10}$$

For solving the above equations three separate cases must be considered, depending on the deformed state of the shear layer: (i) purely elastic, (ii) micro-slip and (iii) macro-slip. In the case of elastic deformation, the system will respond elastically as long as the displacement at the right end of the bar remains below the value τ_m/k. By solving equation (6.9) with the substitution of $\tau = ku$, force *P* can be expressed in terms of displacement. *P* will, in general, be non-zero and should vanish if only the relative stiffness of the shear layer to the bar is infinite large. That means that the bar will start to slip for an arbitrarily small value of the tangential force in the absence of a flexible shear layer. As *P* increases beyond the value for which the shear layer starts yielding, micro-slip occurs. The parameter a $(0 \le a \le 1)$ denotes the fraction of the contact length that has slipped for a given value of *P*. The governing equations of the micro-slip situation are

$$\begin{aligned} EAu'' - ku &= 0 \ \text{ for } \ 0 < \bar{x} < (1-a)L \\ EAu'' - \tau_m &= 0 \ \text{ for } \ (1-a)L < \bar{x} < L \end{aligned} \tag{6.11}$$

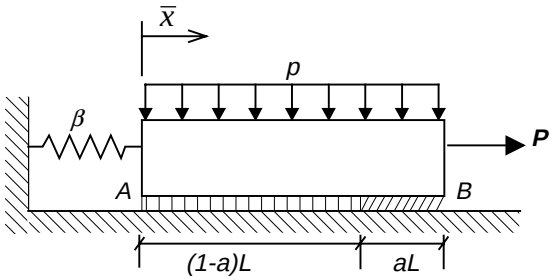

Fig.6.16 Micro-slip model

Equation (6.11) is linear and can be solved explicitly. A set of two parametric equations that define the portion of the skeleton curve corresponding to micro-slip in terms of the plasticity index, a, are then obtained. The derivations were given step by step in [MeBG86]. Macro-slip occurs when the entire contact surface becomes plastic with increases of the tangential force *P*. This plastic state will remain unchanged until unloading begins. The shape of the skeleton curve is as shown in Fig.6.17 in which Δ is the displacement at point B as shown in Fig.6.16 and subscript g stands for the start of macro-slip. Due to the presence of the lumped spring at A, the skeleton curve does not become

horizontal but exhibits linear strain hardening. The slope of the skeleton curve becomes discontinuous as the shear layer becomes fully plastic.

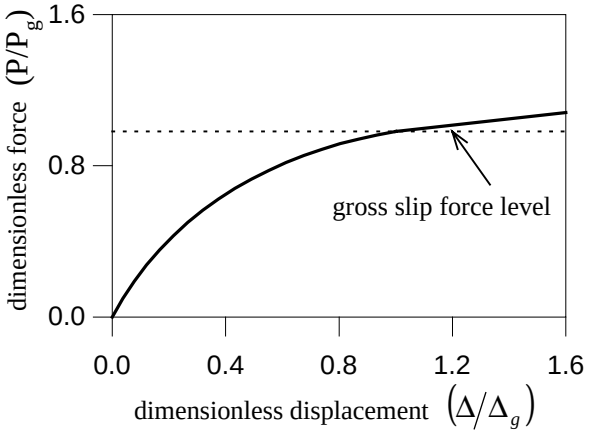

Fig.6.17 Skeleton curve of a single bar contact model

The behaviour of a lap joint shown in Fig.6.18 is similar to that of the single bar studied previously and exhibits three distinct types of behaviour. In contrast to the single bar behaviour, however, slip in the lap joint does not progress monotonically from one end of the joint to the other. Slip, instead, is initiated at one end, progresses inwards with increasing load until the shear force at the other end reaches the yield level and begins to slip. Thereafter, the slipped regions move inward from both ends until macro-slip occurs. The theoretical formulation for the lap joint is similar to that for the single bar.

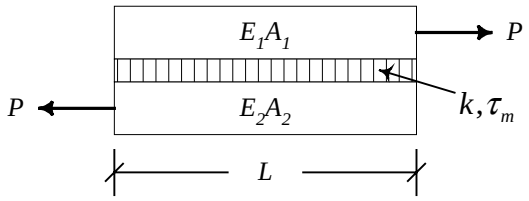

Fig.6.18 A lap joint model

A skeleton curve describing the relative displacement between the two points of application of the loads versus the applied loads is sketched in Fig.6.19. The similarity between this curve and that corresponding to the single bar element is apparent.

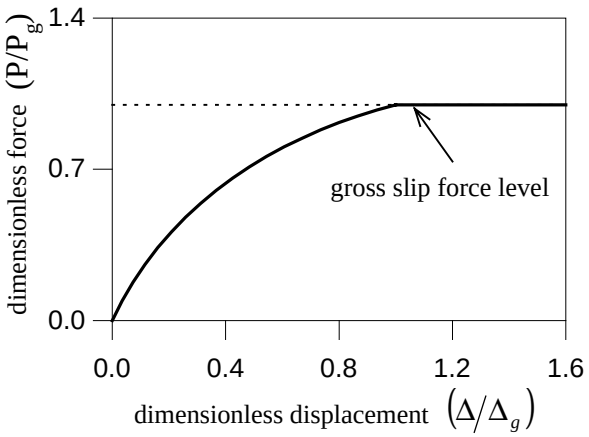

Fig.6.19 Skeleton curve of a lap joint model

The hysteresis loop obtained by Masing rules [Herr65] for describing cyclic unloading and reloading is shown in Fig.6.20.

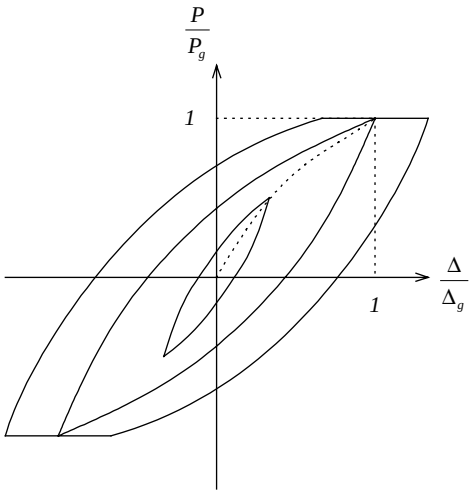

Fig.6.20 Hysteresis loop

To demonstrate the characteristics of steady-state response, two separate cases with different values of λ, the relative stiffness between the shear layer and the bar, were analysed by an approximate method. The results are shown in Fig.6.21 for increasing values of the dimensionless normal load ε ($\varepsilon = \mu pL/f_0$, where f_0 is the maximum amplitude of the sinusoidal excitation force). There is no difference between the two cases for small values of the normal load. For a softer shear layer $(\lambda = 1)$, the load is transmitted almost uniformly through the layer. Thus, depending on the values of the normal load and the excitation frequency, the joint either remains completely locked or it undergoes macro-slip

as shown in Fig.6.21 (a), since yielding occurs simultaneously at every point of the shear layer. For the stiffer layer, however, yielding develops gradually, giving rise to micro-slip of the joint as shown in Fig.6.21 (b).

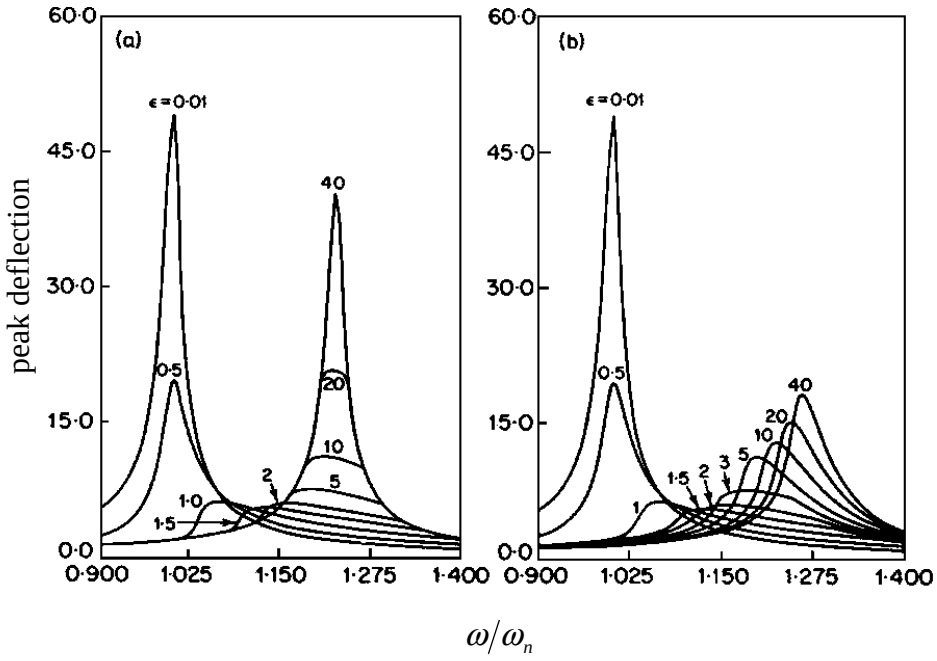

Fig.6.21 Frequency response functions: (a) $\lambda = 1$ (b) $\lambda = 5$

Three conclusions can be drawn from the frequency response curves shown above:

- the presence of micro-slip affects the dynamic responses in such a way that for a given value of the normal load the peak response of the system with stiff layer is considerably smaller than that of the system with a soft layer;
- the resonant frequency of the system with a soft layer is not sensitive to changes of the normal load, while normal load reduction results in a softening of the system with the stiff layer; and
- for very high normal loads the system with a stiff layer exhibits a higher resonant frequency due to the large stiffness of the shear layer as compared to the case with a soft layer.

The frequency response characteristics obtained from simulations mentioned above were validated by experiments and reported in [MeGB86a]. One of the experiments was that an idealised turbine blade was excited at various

frequencies and with different friction loads imposed by a rubbing block acting on the blade's platform. The parameters used in the prediction model for describing the shear layer property were $k = 1.5 \times 10^4 (N/m/m)$ and $\mu = 0.3$. The predictions agreed well with the measured data and exhibited both softened and shifted response as shown in Fig.6.21 (b).

6.2.3. Friction Modelling Based on Other Principles

The mechanism of influence of joints on structural behaviour was investigated more recently by Gaul *et al* [GNWL94]. Both response function measurements and detailed finite element calculations were carried out based on a bolted joint test rig, a resonator shown in Fig.6.22. The FE analyses helped to interpret the measured results, thereby leading to a deeper insight into the dissipation mechanism in bolted connections including the transition from micro-slip to macro-slip and the associated stress distributions.

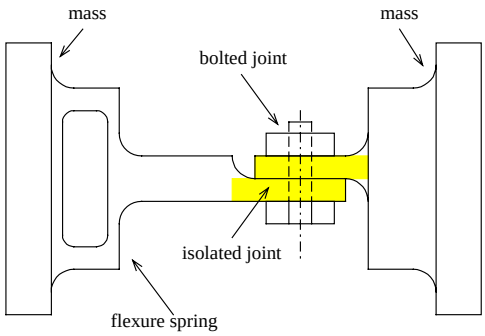

Fig.6.22 A resonator with lap joint

Similar to the work reported earlier, such as [Caug60] [MeBG86] *etc.*, the response functions were measured with different excitation force levels. Their characteristics can be summed up as: (i) the resonance frequency drops with increasing excitation force. This is caused by softening of the system with increasing slip areas. At higher excitation forces the slip portion of a cycle increases, which results in a decrease of the equivalent stiffness. (ii) The inertia decreases with increasing excitation force due to an increase of frictional damping. (iii) The run up flank is steeper than the run down flank, the same effect as shown in Fig.6.12 and 6.21.

Finite element analysis of the lap joint was carried out in two steps. In the first step only an isolated joint (the shadowed part in Fig.6.22) was modelled, discretising the lap joint using 450 four-node plain stress elements. In this model, 40 gap friction elements with Coulomb-type constitutive equations represented the friction interface. After the normal force was applied as a static pre-load to simulate the bolt compression, the model was subjected to tangential forces, both statically and dynamically. With this model, the theoretically expected bilinear hysteresis was reproduced and no influence of inertia and stiffness effects was observed. The transmitted force was limited to a finite value after macro-slip had occurred. Thus the 3-parameter model seemed to be an inadequate description of the isolated joint. The typical form of a measured hysteresis did not show up. In the second step, the whole resonator was discretised. As a simplification, the large resonator masses were lumped to point masses and the flexure spring was discretised by simple spring elements. An eigen-value analysis validated the finite element model by comparing measured and calculated natural frequencies. The bending effects led to varying normal pressure distributions in the contact interface and so did the shear stress distributions. At the limit points, the slip limit was reached over almost the whole contact length. Only a small portion in the middle remained stuck. This indicated micro-slip, progressing from the edges to the middle without reaching a macro-slip state.

Gaul′s finite element simulations revealed that a joint model not only has to account for micro-slip but also for the interaction with the dynamics of the structure. The structural interaction of the test rig can influence the hysteresis. In fact, both the isolated joint properties and the properties of the whole resonator with a lap joint were included in the measured response function, which could not be represented only by an isolated joint model.

The discrete parameter models of frictional systems have the advantages of being mathematically simple and physically meaningful. As shown in Fig.6.11, the bilinear hysteresis loop, which describes the relationship between transmitted force and displacement and exists in systems with Coulomb friction

and systems with elastoplastic material, is obtained from the discrete parameter models. A drawback of this type of models is, however, their incompleteness – they can only describe the regimes of stuck and macro-slip but not the regime of micro-slip. Since the joint in a lumped parameter model is normally modelled by three parameters, k_0, k_d and F, as shown in Fig.6.10, it can also be described as a "3-parameter model".

The equation of motion for the 3-parameter model shown in Fig.6.10 is

$$m\ddot{x} = P_0 \cos(\omega t) - \overline{F}(x, \dot{x}) \tag{6.12}$$

The transmitted longitudinal force in the joint is

$$\overline{F}(x, \dot{x}) = F_a + F_b \tag{6.13}$$

where

$$F_a = k_0 x \tag{6.14}$$

$$F_b = \begin{cases} k_d (x - x_d) + F \operatorname{sgn} \dot{x} & \text{if } |F_b| < F \\ F \operatorname{sgn} \dot{x} & \text{if } |F_b| \geq F \end{cases} \tag{6.15}$$

One modified lumped parameter model was proposed by Lenz *et al* [LeGa95]. The purpose is to adapt the bilinear hysteresis loop, Fig.6.11, to the measured one, as shown in Fig.6.7, where the round corners show the transition between stuck and macro-slip, *i.e.* the micro-slip.

To capture the behaviour of all three regimes with one model, the Valanis model known from plasticity [Vala71] was adapted. Without slip-stick parameters, and by assuming velocity independence, the model is governed by the first order differential equation

$$\frac{d\overline{F}(z)}{dz} + \lambda \overline{F}(z) = E_0 \frac{dq(z)}{dz} + \lambda E_t q(z) \tag{6.16}$$

The relation between the generalised variable $\dot{z}(t)$ and physical time t was given by

$$\frac{dz(t)}{dt} = \left| \frac{dq(z)}{dt} - \frac{\kappa}{E_0} \frac{d\overline{F}(t)}{dt} \right| \tag{6.17}$$

where q is a generalised co-ordinate, λ, E_0 and E_t are material parameters, F is a generalised force and κ is a dimensionless parameter, $0 \le \kappa \le 1$. Starting from these two equations, a different equation for the joint hysteresis was worked out as

$$\dot{\overline{F}} = \frac{E_0 \dot{q} \left[1 + \frac{\lambda}{E_0} \frac{\dot{q}}{|\dot{q}|} \left(E_t q - \overline{F} \right) \right]}{1 + \kappa \frac{\lambda}{E_0} \frac{\dot{q}}{|\dot{q}|} \left(E_t q - \overline{F} \right)} \tag{6.18}$$

If interpreting that $q = x$ and $\overline{F}$ has the same meaning as in (6.13), and combing the joint model (6.18) with (6.12), the following differential equation of motion in terms of the displacement x is then achieved:

$$m\ddot{x} = \frac{E_0 \dot{x} \left[1 + \frac{\lambda}{E_0} \frac{\dot{x}}{|\dot{x}|} \left(E_t x - \overline{F} \right) \right]}{1 + \kappa \frac{\lambda}{E_0} \frac{\dot{x}}{|\dot{x}|} \left(E_t x - \overline{F} \right)} + \overline{F}_0 \omega \sin(\omega t) \tag{6.19}$$

The numerical solution of equation (6.19) can describe the transition between stuck and macro-slip, *i.e.* it can determine the load under which the transition happens. The physical interpretation of the parameters in the description of the joint model (6.18) is given in Fig.6.23. The stiffness moduli of stick condition and slip condition are denoted by E_0 and E_t respectively. The parameter, κ, can be used to control the portion of micro-slip. The parameter $\kappa = 0.99$ approximates the 3-parameter joint model with slightly rounded corners. The corner radius increases with the decrease of κ value. The parameter σ_0 denotes a stick limit equivalent to the yield stress and was defined by

$$\lambda = \frac{E_0}{\sigma_0 \left(1 - \kappa \frac{E_t}{E_0} \right)} \tag{6.20}$$

We notice that the Valanis model has 4 independent parameters: E_t, E_0, σ_0 and κ. Parameter λ was derived from these four as shown in (6.20). Comparing the Valanis model with the 3-parameter model, we find the following relationships between their parameters:

$$E_t = k_0,\ E_0 = k_0 + k_d \text{ and } \sigma_0 = F = \mu N \tag{6.21}$$

There is no counterpart in the 3-parameter model for parameter κ in the Valanis model, which describes the transition from stick state to macro-slip. The parameters of the Valanis joint model can be identified from measured hysteresis and by iterative fitting of κ.

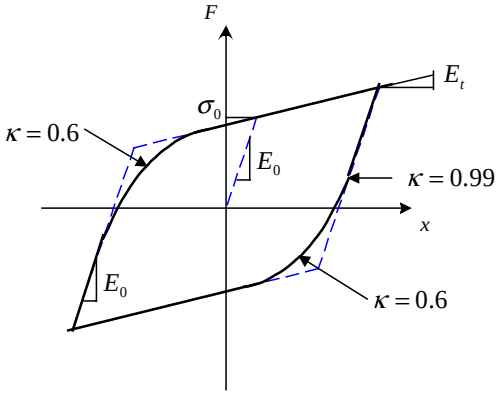

Fig.6.23 parameters of the Valanis model

Another modification to the 3-parameter model was done by Sanliturk *et al.* [SaEw95]. They developed a hybrid model for the study of friction dampers used for turbine blade vibration control, which is a non-linear combination of macro-slip and micro-slip models:

$$F_{hyb}(x) = e^{-\beta x/x_{cr}} F_{mic}(x) + (1 - e^{-\beta x/x_{cr}}) F_{mac}(x) \tag{6.22}$$

where the micro-slip model was given by Rogers and Boothroyd [RoBo75] as

$$F_{mic}(x) = \mu N (1 - e^{-\kappa x}) \tag{6.23}$$

and the macro-slip model is

$$F_{mac}(x) = \begin{cases} k_d x & x < x_{cr} \\ \mu N & x \geq x_{cr} \end{cases} \tag{6.24}$$

Four independent parameters in this model are:

k_d	contact stiffness
F	friction force, $F = \mu N$
β	empirical factor
κ	micro-slip parameter

The empirical parameter, β, plays the role of controlling the portion of slip in the contact area. $F_{hyb}(x) = F_{mic}(x)$ when $\beta = 0$ and $F_{hyb}(x) \to F_{mac}(x)$ when $\beta \to \infty$, while parameter κ has the similar function working inside the micro-slip model. The shape of hysteresis loop described by the hybrid model with different κ-values is shown in Fig.6.24.

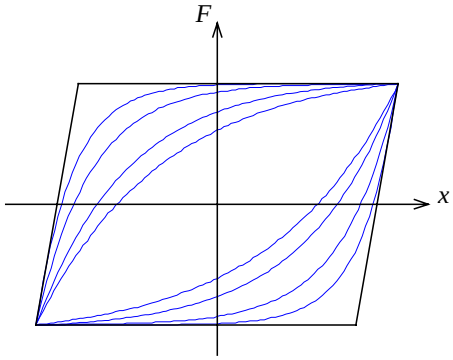

Fig.6.24 Hysteresis loop described by the hybrid model

It is noticed from studies of the dynamic behaviour of systems with frictional mechanisms that in the present situation we can predict the behaviour of very simple systems under laboratory conditions. We are far from being able either to predict or to control the damping produced by micro-slip between surfaces in complex, fabricated structures. More advanced research work is demanded since several studies have shown that joints and connection damping are the most important mechanisms for energy dissipation in most real structures [Unga73] [Bear79].

6.3. IMPORTANCE OF NON-LINEAR JOINT MODELLING

Many structures with mechanical joints possess slip interfaces. Lap joints, for instance, are often used in practical structures to connect components. In one such joint, two components are held together at their interfaces by the action of

a pre-stressed bolt, which creates a clamping pressure on the components. The axial force is transferred by the joint through the frictional force along the interface, caused by the clamping pressure. As loading is transferred through the joint, macro-slip along the interface will not be allowed if the joints are designed for the purpose of tightening or fastening. However, micro-slip in the friction interface is possible, *i.e.*, the slip along the interface is localised in a certain slip region while the rest of the interface is in the stuck region.

As has been reported in the last section, macro-slip and micro-slip cause energy dissipation and provide the dominant damping mechanism in many structures. The dissipated work per cycle is the area traced out by the hysteresis loop as shown in Fig.6.7. Lenz showed that the work vanishes in the stuck zone and is a linear function of relative displacement in the macro-slip zone [LeGa95]. In his experiments, the dissipated work per cycle from the measured hysteresis versus the amplitude of the relative displacement is the same linear curve in the range of macro-slip as described by the 3-parameter model. This was also shown in [GoKM56]. While in the range of smaller excitation forces, however, the curve of dissipated work shows an increasing slope with increasing relative displacement, and this regime is associated with micro-slip as shown in Fig.6.25. The same characteristics were also observed by Rogers and Boothroyd [RoBo75]. It is recognised from Fig.6.25 that the 3-parameter model is a simplified one which ignores the transition process from stick to macro-slip, the micro-slip.

To simplify the models for joint non-linearity analysis, currently available results on micro-slip studies are mostly obtained from isolated joints and do not include much of the influence from the components. However, the structural interaction of the components affects the hysteresis, and the significance of joint non-linear effect to the dynamic behaviour of structures changes from case to case, even with the same type of joint. In normal working conditions, fastened or tightened joints are in the stuck state and the systems are dominated by linear performance.

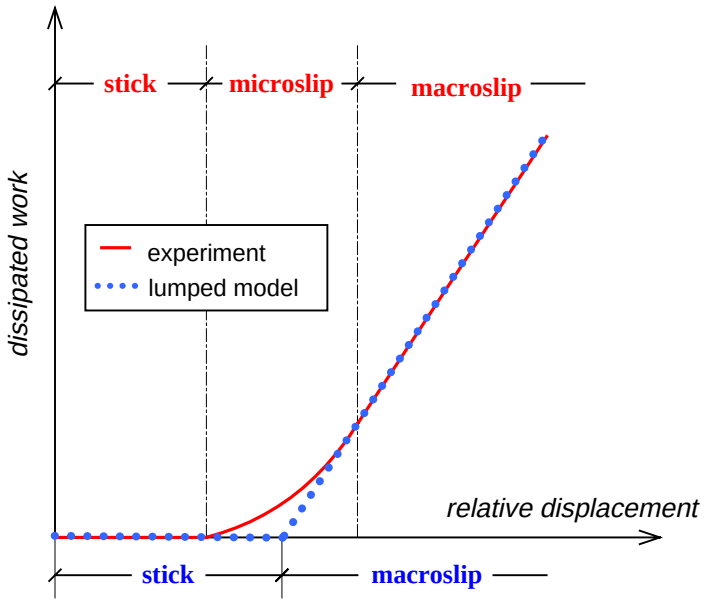

Fig.6.25 Dissipated work

An experiment was carried out to investigate the significance of non-linearity in a practical assembled structure, the “breadboard structure” shown in Fig.6.26. A beam is connected to a plate via two bolted joints. The details of the components and joint have been shown earlier in Figs.5.4, 5.5 and 5.7. The torque applied to fasten the bolts was 4N-m.

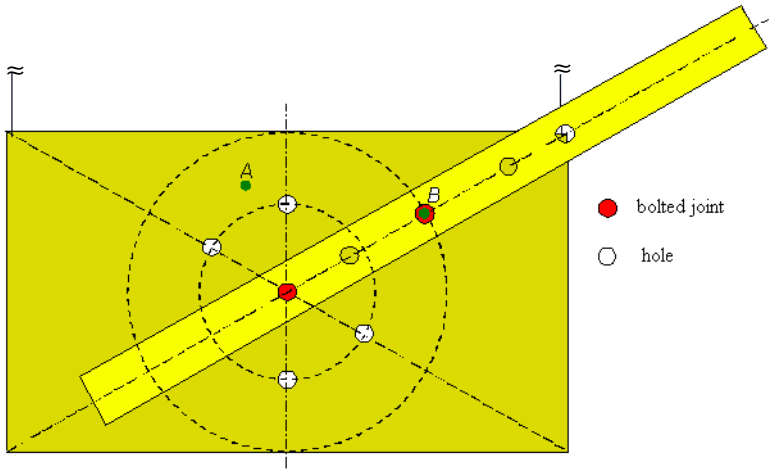

Fig.6.26 A plate-beam structure

In this experiment, the structure was suspended vertically by two strings at the top corners of the plate. A shaker was used as an exciter connected to point A on the plate via a push rod, exactly normal to the plane of the plate. The system response was picked up at point B by a Laser Doppler Vibrometer (LDV). The

excitation was given on one side of the plate where the beam was assembled and the responses were measured on the other side. The excitation signal was stepped-sine and the input force level was controlled by a computer program.

The non-linear behaviour of the breadboard structure was monitored first from the response time signal – the response signals were distorted sine waves at some excitation frequencies. In the frequency range between 20 and 2,000Hz, for the preliminary modal testing, four specific frequency zones were selected and measurements of mobility were carried out in these frequency zones by applying different levels of excitation force. Of all these four segments of FRFs, only one of them, in the frequency range of 250Hz to 300Hz, displayed a non-linear behaviour and the non-linearity affected less than a 10Hz frequency band. The measured FRFs with non-linear characteristics are shown in Fig.6.27.

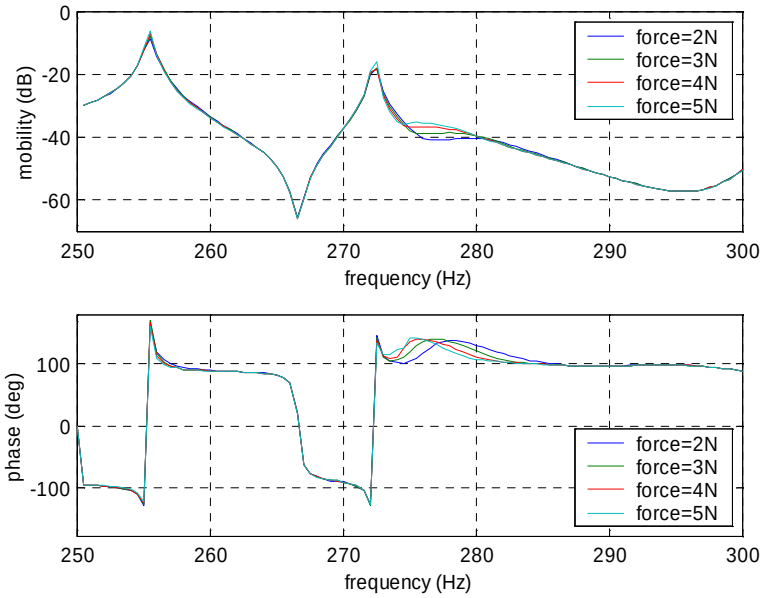

Fig.6.27 Measured FRFs

An finite element model was constituted for the test structure. It is a linear model, in which plate and beam were discretised by shell elements and the bolts were modelled by solid elements. No gap friction element was used in the contact interfaces. The linear finite element model shows good correlation with the experimental results. As shown in Table 6.1, the first 10 natural frequencies predicted by the finite element model have a maximum error less than 5% when compared with the test results. That means the linear finite element model

works well in describing the structure's dynamic properties. Two mode shapes, the 7th and the 8th, relating to the two modes in Fig.6.27, are shown in Fig.6.28 and 6.29. These two mode shapes show the modal displacements in *z* direction, which is perpendicular to the plate.

Table 6.1

No.	1	2	3	4	5	6	7	8	9	10
FE	35.70	74.20	96.90	107.60	183.20	227.50	257.60	276.70	316.40	353.80
Test	36.40	75.30	95.30	112.20	184.00	221.20	254.90	271.77	303.00	345.20
error%	1.92	1.46	-1.68	4.10	0.43	-2.85	-1.06	-1.81	-4.42	-2.49

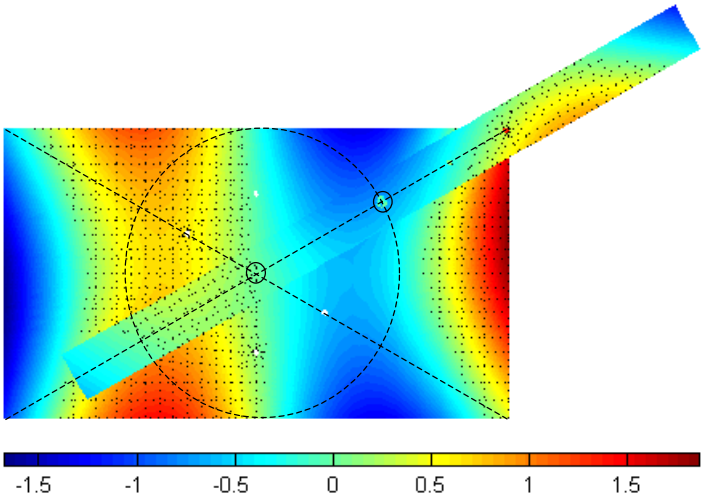

Fig.6.28 The 7th elastic mode at 257.60 Hz

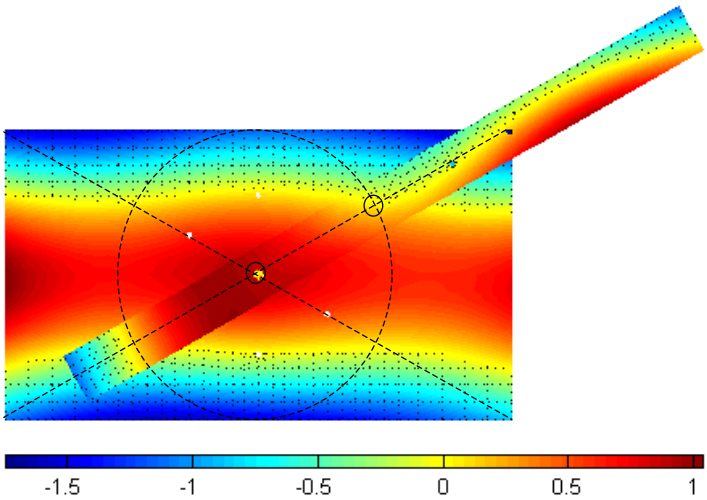

Fig.6.29 The 8th elastic mode at 276.70 Hz

Since the excitation force was applied in the *z* direction and the responses were mainly produced in the *z* direction as well, the tangential forces at the joints, either in the *x* or *y* directions, can only be induced by deformation of the plate and beam. In the circumstance of the experiment, these tangential forces were not large enough to give rise to micro-slip between the joint interfaces at most of the measurement frequencies. Therefore, the non-linear behaviour observed in the measurement is not significant.

The non-linear phenomenon around 277Hz in Fig.6.27 shows some of the features of friction damping. There exists a highly damped mode which exhibits softening characteristics, and since the normal pressure in the joints was constant (the tightening torque applied to the bolt was 4N-m), the amplitude of the mobility at this frequency increased with the increase of the excitation force.

It is concluded from this case study that no significant non-linear behaviour existed in the assembled breadboard structure, and so the effect of non-linearity in the estimation of the system FRFs can be neglected as it appears in a small frequency range.

6.4. STRATEGIES FOR DEALING WITH NON-LINEARITY IN FRF COUPLING

The substructure coupling methods discussed in Chapter 4 and 5 are based on the assumption that the relevant systems to be coupled are linear. This assumption is sometimes inadequate for the accurate description of some systems due to the inevitable existence of non-linearity in many structural joints. One of the outcomes of this problem is a method of solving the non-linear equations of motion by approximate procedures. These approximate procedures assume that the steady-state response is essentially harmonic. It is efficient and also sufficient to keep only the first term of the Fourier series expansion of the non-linear force and finally convert the non-linear differential equations of motion to a non-linear algebraic equation. One of the most popular procedures is known as principle of harmonic balance, which is heavily based on the Krylov-Bogoliubov approach [Mino47]. The describing function method,

which is regarded as an application of the principle of harmonic balance, and is widely used for the analysis of non-linear control systems [Silj69], can also be employed in structural non-linear coupling analysis.

6.4.1. The principle of harmonic balance

Considering a non-linear system which is subjected to harmonic excitation, the system differential equation can be written as

$$\mathbf{M}\ddot{\mathbf{x}} + \mathbf{C}\dot{\mathbf{x}} + \mathbf{K}\mathbf{x} + \mathbf{f}(\mathbf{x}, \dot{\mathbf{x}}) = \mathbf{P}e^{i\omega t} \tag{6.25}$$

where $\mathbf{f}(\mathbf{x}, \dot{\mathbf{x}})$ is a non-linear force. A steady-state solution for $\mathbf{x}(t)$ can be represented by a Fourier series as

$$\mathbf{x}(t) = \sum_{m=0}^{\infty} \mathbf{x}^m = \sum_{m=0}^{\infty} \mathbf{X}^m e^{im\omega t} \tag{6.26}$$

where superscript m indicates the mth order harmonic and $\mathbf{x}^m$ is the mth order component of displacement response. Then the complex displacement response amplitude $\mathbf{X}$ at the jth co-ordinate in the mth harmonic, X_j^m, can be written as

$$X_j^m = \overline{X}_j^m e^{i\phi_j^m} \tag{6.27}$$

where $\overline{X}_j^m$ is the magnitude and ϕ_j^m is the phase of the complex displacement X_j at the mth harmonic. If we consider the response to be dominated by the fundamental component of the Fourier series, we can assume that the response $\mathbf{x}(t)$ will be approximated by the fundamental component, $\mathbf{x}^1(t)$, written as

$$\mathbf{x}(t) \approx \mathbf{x}^1(t) = \mathbf{X}^1 e^{i\omega t} \tag{6.28}$$

The response $\mathbf{x}(t)$ at a general coordinate j can be written as

$$x_j(t) \approx x_j^1(t) = X_j^1 e^{i\omega t} \tag{6.29}$$

where the complex displacement response X_j^1 is

$$X_j^1 = \overline{X}_j^1 e^{i\phi_j^1} = C_j^1 + iD_j^1 \tag{6.30}$$

where

$$C_j^1 = X_j^1 \cos\phi_j^1$$
$$D_j^1 = X_j^1 \sin\phi_j^1$$

Similarly, the relative displacement response y between the inter-coordinates k and l $(k \neq l)$, y_{kl}, can be represented as

$$y_{kl} = x_k - x_l = \sum_{m=0}^{\infty} y_{kl}^m = \sum_{m=0}^{\infty} Y_{kl}^m e^{im\omega t} \tag{6.31}$$

where

$$Y_{kl}^m = X_k^m - X_l^m = \overline{Y}_{kl}^m e^{i\psi_{kl}^m} \tag{6.32}$$

If the variable, y_{kl}, in the non-linear function, $f_{kl}(y_{kl})$, has the form assumed in (6.31), the non-linear force, $f_{kl}(y_{kl})$, is complex and is also a periodic function of time. It then can be expressed by a Fourier series as

$$f_{kl}(y_{kl}) = \sum_{m=0}^{\infty} f_{kl}^m = \sum_{m=0}^{\infty} F_{kl}^m e^{im\omega t} \tag{6.33}$$

where

$$F_{kl}^m = \overline{F}_{kl}^m e^{i\theta_{kl}^m}$$
$$F_{kl}^0 = \frac{1}{2\pi}\int_0^{2\pi} f_{kl}(y_{kl})\, dt$$
$$F_{kl}^m = \frac{1}{\pi}\int_0^{2\pi} f_{kl}(y_{kl})\, e^{-im\omega t} dt \qquad (m \geq 1)$$

The Fourier series written in complex form (6.33) can also be expressed as

$$\sum_{m=0}^{\infty} F_{kl}^m e^{im\omega t} = A_{kl}^0 + \sum_{m=0}^{\infty} \left(A_{kl}^m \cos(m\omega t) + B_{kl}^m \sin(m\omega t)\right) \tag{6.34}$$

where

$$A_{kl}^0 = \frac{1}{2\pi}\int_0^{2\pi} f_{kl}(y_{kl}) dt$$
$$A_{kl}^m = \frac{1}{\pi}\int_0^{2\pi} f_{kl}(y_{kl}) \sin(m\omega t) dt \qquad m \geq 1$$
$$B_{kl}^m = \frac{1}{\pi}\int_0^{2\pi} f_{kl}(y_{kl}) \cos(m\omega t) dt \qquad m \geq 1$$

The non-linear force can be approximate by the fundamental component in its Fourier series written as

$$f_{kl}(y_{kl}) \approx f_{kl}(y_{kl}^1) = F_{kl}^1 e^{i\omega t} = A_{kl}^1 \cos(\omega t) + B_{kl}^1 \sin(\omega t) \tag{6.35}$$

where

$$A_{kl}^1 = \frac{1}{\pi}\int_0^{2\pi} f_{kl}(y_{kl}^1)\sin\omega t dt$$

$$B_{kl}^1 = \frac{1}{\pi}\int_0^{2\pi} f_{kl}(y_{kl}^1)\cos\omega t dt$$

Substituting the fundamental component of response given by equation (6.28) and the fundamental component of non-linear force given by equation (6.35) into the non-linear differential equation (6.25), yields

$$\left(\mathbf{K} - \omega^2\mathbf{M} + i\omega\mathbf{C}\right)\mathbf{X}^1 = \mathbf{P} - \mathbf{F}^1 \tag{6.36}$$

The solution of the response $\mathbf{X}^1$ is based on finding the fundamental linear coefficients C_j^1 and D_j^1 for the response and A_{kl}^1 and B_{kl}^1 for the non-linear force in which all the fundamental harmonic forces in equation (6.36) are balanced by each other. Different iterative methods are available to solve this kind of mathematical problem.

6.4.2. Describing function method

The describing function method linearises the non-linearity by defining the transfer function as the ratio of the fundamental harmonic components of the input and the output to the non-linearity. In order to present the concept of the describing function method, we consider an SDOF system with a non-linear restoring force driven by a sinusoidal excitation written as

$$m\ddot{x} + c\dot{x} + kx + f(x,\dot{x}) = A\sin\omega t \tag{6.37}$$

To solve the problem by the describing function method it is required to assume that the variable x appearing in the non-linear function, $f(x,\dot{x})$, is sufficiently close to a sinusoidal oscillation expressed as

$$x \approx X\sin(\omega t + \phi) = X\sin\theta \tag{6.38}$$

where X is a complex response amplitude, ω is the excitation frequency and ϕ is phase angle.

If the variable, x, in the non-linear function, $f(x,\dot{x})$, has the sinusoidal form assumed in (6.38), the non-linear function, $f(x,\dot{x})$, is complex and is also a periodic function of time. Defining now the describing function, υ, as the optimum equivalent linear complex stiffness representation of the non-linear force, $f(x,\dot{x})$, as

$$f(x,\dot{x}) \approx \upsilon(x,\dot{x})x \tag{6.39}$$

If the type of non-linearity in $f(x,\dot{x})$ is known, and assuming that the non-linear force $f(x,\dot{x})$ is also dominated by its fundamental term, then it can be simplified by the first harmonic component of its Fourier series, $f^1(x,\dot{x})$, and the describing function $\upsilon(x,\dot{x})$ can be obtained from it.

Substituting equation (6.38) and (6.39) into (6.37), the non-linear differential equation, we have

$$(-\omega^2 m + i\omega c + k + \upsilon)X = A \tag{6.40}$$

Equation (6.40) is an algebratic one.

6.5. CONCLUSIONS

A review on the research of friction in the joints of mechanical structures is made which aims at an understanding of friction phenomena and an awareness of currently available methods in dealing with friction in structural dynamics. The importance of the consideration of joint non-linearity has been examined and discussed via an experimental case study. The strategies in analysing coupled structure with non-linear joints are also provided.

The following conclusions are drawn from the study in this chapter:

- in most engineering structures, friction joints are often tightly fastened so that the non-linear problems caused by these joints can be avoided, and in the meantime, the damping levels at these joints are also reduced to a minimum;
- the load-deformation relationships of a friction joint, in both the normal and tangential directions, are not linear. However, the relationship in the normal direction becomes effectively linear after a pre-load is applied and can be considered as linear in most applications, while the relationship in the tangential direction is always non-linear and energy is dissipated when a cyclic load is applied;
- the transition process between stuck and macro-slip states usually exhibits the strongest degree of non-linearity. While in the status of either stuck or macro-slip the joint behaves almost linearly. This is concluded from both discrete parameter model and continuous contact model studies;
- the current study on joint dynamic non-linear behaviour is still far to the application for engineering structures. The investigations on simple models in laboratory conditions reveal the mechanics but the results cannot be quantitatively generalised due to the complexity of real joints, such as their material, dimension, roughness of the contact surface and lubrication condition *etc*;
- an experiment on a practical structure with bolted joints showed that no significant non-linear behaviour exists in that case. The non-linear effect in the estimation of the system FRFs can be neglected as it appears in a small frequency range;
- if the non-linearity description of a joint is available, the harmonic balance method and describing function method are ready to be used for the coupling analysis.

CHAPTER 7

IMPACT OF ROTATIONAL DOF INFORMATION

7.1. IMPACT OF RDOF DATA ON JOINT PARAMETER IDENTIFICATION

Rotational degrees of freedom (RDOFs) have to be taken into account in many branches of structural dynamic analysis as independent co-ordinates. However, the possibilities for measuring RDOFs are so limited that in some cases, the attempt has to be given up and confined to measure translational degrees of freedom (TDOFs) only. In the subjects described in this thesis, joint parameter identification and substructure coupling analysis, the information of RDOFs plays an important role. The full consequences and errors caused by excluding RDOF data in joint parameter identification and coupling analysis have not been clearly understood in the past. This Chapter systematically investigates this issue by theoretical analysis and numerical examples. At first, we discuss the impact of RDOF data on joint parameter identification.

7.1.1. Theoretical Analysis - DOF Incompatibility

From the view point of discretisation, the motion of any node on a spatial structure is generally described in a Cartesian co-ordinate system by six degrees of freedom, namely three translations x, y, z and three rotations θ_x, θ_y, θ_z. As to the nodes at the coupling interfaces which are involved, the number of DOFs of these nodes is critical to the identification results for the joint parameters. For a specific joint, the number of DOFs of the interface nodes has to be determined before the implementation of the identification procedure proposed in Chapter 2.

If the supposed DOFs of the interface nodes are the same as those that exist in practice; in other words, if the measurable DOFs on a joint are the same as the practically-existing DOFs, then, the joint is *DOF-compatible* and it is possible to identify the parameters. Otherwise, the joint is *DOF-incompatible* and it is not possible to identify its parameters using the proposed method in Chapter 2 – DOF-compatibility is a necessary condition for a correct identification.

The joint parameter identification method proposed earlier involves a basic assumption that all FRFs related to the pre-determined DOFs of joints are available, referring to (2.13) or (2.14). However, due to the difficulties in practical measurement, some FRFs related to rotational degrees of freedom (RDOF) cannot be measured even though they play significant roles in system responses. In principle, in those cases where angular displacements of joints cannot be neglected, if only translation degrees of freedom (TDOF) are pre-determined and measured, the implementation of identification procedure will yield an incorrect result. That is to say, it is the DOF-compatibility problem that results in a failure of the identification process. This statement is further explained as follows.

The joint parameter identification method proposed in Chapter 2 comes down to solving a set of linear equations:

$$\mathbf{Ax} = \mathbf{b} \tag{7.1}$$

where $\mathbf{x}$ is the vector of unknown joint parameters, and $\mathbf{A}$ and $\mathbf{b}$ are constructed using FRFs of both the substructures and the assembly, which are either related with or affected by the practical joint DOFs.

To explain the concepts of *DOF-compatibility* and *DOF-incompatibility*, we partition vector $\mathbf{x}$ to

$$\mathbf{x} = \begin{Bmatrix} \mathbf{x}_t \\ \mathbf{x}_r \end{Bmatrix} \tag{7.2}$$

where $\mathbf{x}_t$ is the sub-vector of parameters which relates to TDOFs only and $\mathbf{x}_r$ relates to the RDOFs. Substituting (7.2) into (7.1), we have

$$\begin{bmatrix} \mathbf{A}_{tt} & \mathbf{A}_{tr} \\ \mathbf{A}_{rt} & \mathbf{A}_{rr} \end{bmatrix} \begin{Bmatrix} \mathbf{x}_t \\ \mathbf{x}_r \end{Bmatrix} = \begin{Bmatrix} \mathbf{b}_t \\ \mathbf{b}_r \end{Bmatrix} \tag{7.3}$$

If the joint is DOF-compatible, all elements in matrix $\mathbf{A}$ and vector $\mathbf{b}$ are measurable and, therefore, the unknown vector $\mathbf{x}$ can be solved. If the joint is DOF-incompatible because FRFs relating to all or some of the RDOFs are not measurable, then we are not able to solve the equation. An attempt to solve $\mathbf{x}_t$ by providing only the measurement result $\mathbf{A}_{tt}$ cannot be realised, either. From (7.3), we know that

$$\mathbf{A}_{tt}\mathbf{x}_t = \mathbf{b}_t \tag{7.4}$$

holds if, and only if, $\mathbf{A}_{tr} = \mathbf{0}$. If equation (7.4) is used regardless of the fact of $\mathbf{A}_{tr} \neq \mathbf{0}$, we could only obtain a wrong result. The expression $\mathbf{A}_{tr} = 0$ implies that there is no RDOF active at any node of the joint.

7.1.2. Numerical Illustrations

Consider again the structure shown in Fig.2.4. The expected joint stiffness matrix is

$$\mathbf{k} = \begin{bmatrix} \frac{EA}{l} & 0 & -\frac{EA}{l} & 0 \\ 0 & \frac{4EI}{l} & 0 & 0 \\ -\frac{EA}{l} & 0 & \frac{EA}{l} & 0 \\ 0 & 0 & 0 & \frac{4EI}{l} \end{bmatrix} \tag{7.5}$$

The ideal case is simulated by assuming that all FRFs needed in the identification are available and the identified result is shown in Fig.7.1, in which all the 16 elements of matrix $\mathbf{k}$ are identified accurately.

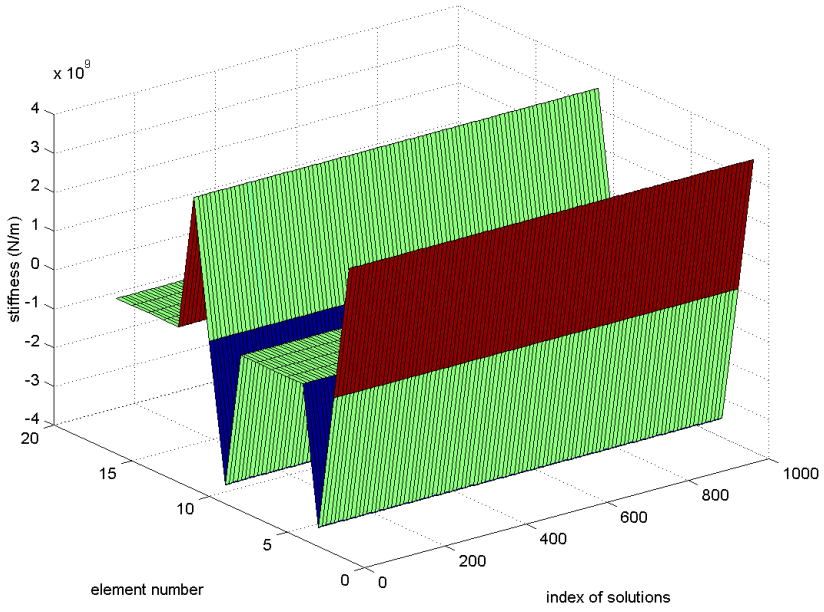

Fig.7.1 identification of the joint stiffness

One of the elements in the stiffness matrix, $\mathsf{k}_{11} = \frac{EA}{l}$, is 3.51858×10^9 N/m and the plot for all the solutions at different frequencies has been shown in Fig.2.5. It is seen that all the 1000 solutions obtained from PA in the frequency range between 0 and 2000Hz are accurate.

If the rotational DOFs at node 3 and 9 are not measurable, and only the translation FRFs are used to identify the axial stiffness of the joint, the joint stiffness matrix is then reduced to

$$\tilde{\mathbf{k}} = \begin{bmatrix} \frac{EA}{l} & -\frac{EA}{l} \\ -\frac{EA}{l} & \frac{EA}{l} \end{bmatrix}$$

The implementation of the partition algorithm (PA) yields the identified result as shown in Fig.7.2, in which only the first 10 solutions present a steady behaviour, and all the rest 990 solutions have very large errors. For instance, the first element, $\tilde{k}_{11} = 2.64454 \times 10^9 (\mathrm{N/m})$, is given by the first 10 solutions. Compared with the exact value, $k_{11} = 3.51858 \times 10^9 (\mathrm{N/m})$, its error is 24.84%. This case study shows that in the DOF-incompatible condition, the identified result can go wrong and the errors of the identified parameters can be unpredictably large.

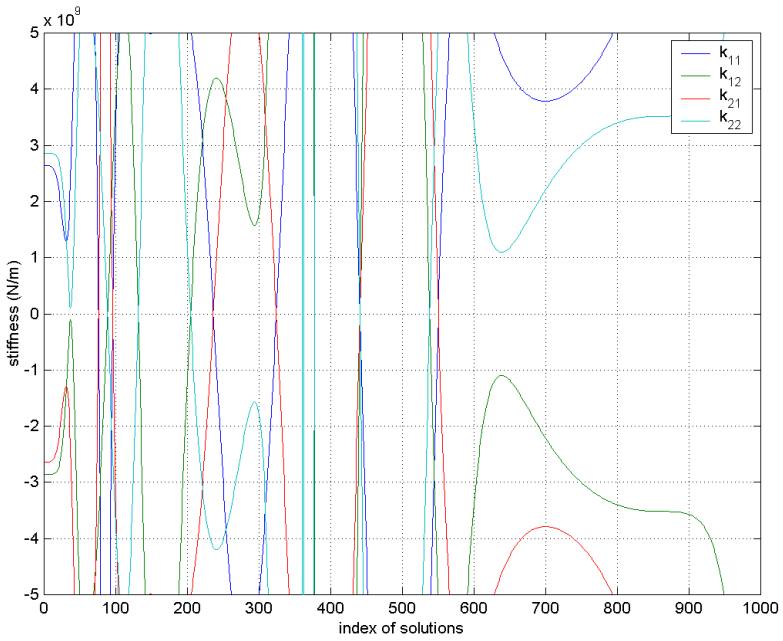

Fig.7.2 Stiffness identified using PA when no RDOF FRF included

7.2. IMPACT OF RDOF DATA ON FRF COUPLING ANALYSIS

In substructure coupling analysis, the information from the RDOFs also plays an important role and the extent of errors resulting in coupling analysis without using RDOF data needs to be clearly established. The investigation of the consequence of omitting RDOF-related FRFs form FRF coupling analysis is carried out here in a systematic study. The error analysis for FRF coupling without using RDOF related FRFs is based on the Klosterman-Jetmundsen method (K-J method) mentioned in Chapter 5. The importance of RDOF-related FRFs is quantitatively described by explicit error functions. These error functions reveal the composition of the error caused by the absence of RDOF-related FRFs. In the error function for general cases, the error is decomposed and the contributions of both TDOF and RDOF related FRFs to the error are thoroughly discussed. Two case studies are also presented to demonstrate the effectiveness of the analysis.

7.2.1. Theoretical Analysis

The K-J method for coupling analysis is given by the expression of

$$ {}_{\Sigma}\mathbf{H} = \begin{bmatrix} {}_{A}\mathbf{H}_{ii} & {}_{A}\mathbf{H}_{ic} & 0 \\ {}_{A}\mathbf{H}_{ci} & {}_{A}\mathbf{H}_{cc} & 0 \\ 0 & 0 & {}_{B}\mathbf{H}_{ii} \end{bmatrix} - \begin{bmatrix} {}_{A}\mathbf{H}_{ic} \\ {}_{A}\mathbf{H}_{cc} \\ -{}_{B}\mathbf{H}_{ic} \end{bmatrix} \left[{}_{A}\mathbf{H}_{cc} + {}_{B}\mathbf{H}_{cc} \right]^{-1} \left[{}_{A}\mathbf{H}_{ci} \quad {}_{A}\mathbf{H}_{cc} \quad -{}_{B}\mathbf{H}_{ci} \right] \quad (7.6) $$

If the size of matrix ${}_{A}\mathbf{H}_{ic}$ is $n_A^i \times n_A^c$ and matrix ${}_{B}\mathbf{H}_{ic}$ is $n_B^i \times n_B^c$, and notice that the number of coupling DOFs always has the relationship of $n_A^c = n_B^c = n^c$, the FRF matrix of the assembled structure, ${}_{\Sigma}\mathbf{H}$, will be a symmetric matrix with the dimension of $\left(n_A^i + n_B^i + n^c\right) \times \left(n_A^i + n_B^i + n^c\right)$.

If only coupling co-ordinates are concerned, the equation can be simplified to

$$ {}_{\Sigma}\mathbf{H} = {}_{A}\mathbf{H}_{cc} - {}_{A}\mathbf{H}_{cc} \left[{}_{A}\mathbf{H}_{cc} + {}_{B}\mathbf{H}_{cc} \right]^{-1} {}_{A}\mathbf{H}_{cc} \quad (7.7) $$

by setting

$$ {}_{A}\mathbf{H}_{ii} = {}_{A}\mathbf{H}_{ic} = {}_{A}\mathbf{H}_{ci} = \mathbf{0} $$

and

$$ {}_{B}\mathbf{H}_{ii} = {}_{B}\mathbf{H}_{ic} = {}_{B}\mathbf{H}_{ci} = \mathbf{0} $$

in equation (7.6).

An arbitrary element of ${}_{\Sigma}\mathbf{H}$ from (7.7) will be

$$ \left({}_{\Sigma}\mathbf{H}\right)_{jk} = \left({}_{A}\mathbf{H}_{cc}\right)_{jk} - \sum_{p=1}^{n^c}\sum_{q=1}^{n^c}\left({}_{A}\mathbf{H}_{cc}\right)_{jp}\left[{}_{A}\mathbf{H}_{cc} + {}_{B}\mathbf{H}_{cc}\right]^{-1}_{pq}\left({}_{A}\mathbf{H}_{cc}\right)_{qk} \quad \begin{cases} j = 1,2,...,n^c \\ k = 1,2,...,n^c \end{cases} \tag{7.8} $$

In general, the coupling DOFs consist of both translational DOFs and rotational DOFs. The number of coupling DOFs, n^c, can therefore be expressed as

$$ n^c = n_t^c + n_r^c \tag{7.9} $$

Denoting the coupling DOFs using the right-hand-side superscripts, we can re-write equation (7.7) as

$$ {}_{\Sigma}\mathbf{H} = {}_{A}\mathbf{H}^c - {}_{A}\mathbf{H}^c\left({}_{AB}\mathbf{H}^c\right)^{-1}{}_{A}\mathbf{H}^c \tag{7.10} $$

where

$$ {}_{AB}\mathbf{H}^c = {}_{A}\mathbf{H}^c + {}_{B}\mathbf{H}^c \tag{7.11} $$

Partitioning each matrix in equation (7.10) according to the number of translational DOFs, n_t^c, and the number of rotational FRFs, n_r^c, we have

$$ {}_{\Sigma}\mathbf{H} = \begin{bmatrix} {}_{\Sigma}\mathbf{H}_{tt}^c & \vdots & {}_{\Sigma}\mathbf{H}_{tr}^c \\ \cdots & \cdots & \cdots \\ {}_{\Sigma}\mathbf{H}_{rt}^c & \vdots & {}_{\Sigma}\mathbf{H}_{rr}^c \end{bmatrix} \tag{7.12} $$

$$ {}_{A}\mathbf{H}^c = \begin{bmatrix} {}_{A}\mathbf{H}_{tt}^c & \vdots & {}_{A}\mathbf{H}_{tr}^c \\ \cdots & \cdots & \cdots \\ {}_{A}\mathbf{H}_{rt}^c & \vdots & {}_{A}\mathbf{H}_{rr}^c \end{bmatrix} \tag{7.13} $$

$$ {}_{AB}\mathbf{H}^c = \begin{bmatrix} {}_{AB}\mathbf{H}_{tt}^c & \vdots & {}_{AB}\mathbf{H}_{tr}^c \\ \cdots & \cdots & \cdots \\ {}_{AB}\mathbf{H}_{rt}^c & \vdots & {}_{AB}\mathbf{H}_{rr}^c \end{bmatrix} \tag{7.14} $$

If the amplitudes of the FRFs in sub-matrix ${}_{AB}\mathbf{H}_{tr}^{c}$ in equation (7.14) are numerically much smaller than those in the sub-matrces ${}_{AB}\mathbf{H}_{tt}^{c}$ and ${}_{AB}\mathbf{H}_{rr}^{c}$, the system is a weakly-coupled TDOF-RDOF system.

For a weakly-coupled TDOF-RDOF system, the summation of the FRF matrices of substructure A and substructure B at the coupling DOFs can be expressed approximately in the form of block diagonal matrix as

$$ {}_{AB}\mathbf{H}^{c} \approx \begin{bmatrix} {}_{AB}\mathbf{H}_{tt}^{c} & \vdots & \mathbf{0} \\ \cdots & \cdots & \cdots \\ \mathbf{0} & \vdots & {}_{AB}\mathbf{H}_{rr}^{c} \end{bmatrix} \tag{7.15} $$

from which, we have

$$ \left({}_{AB}\mathbf{H}^{c}\right)^{-1} \approx \begin{bmatrix} \left({}_{AB}\mathbf{H}_{tt}^{c}\right)^{-1} & \vdots & \mathbf{0} \\ \cdots & \cdots & \cdots \\ \mathbf{0} & \vdots & \left({}_{AB}\mathbf{H}_{rr}^{c}\right)^{-1} \end{bmatrix} \tag{7.16} $$

Substituting equations (7.12), (7.13) and (7.16) into equation (7.10), the sub-matrix of ${}_{\Sigma}\mathbf{H}$ (which includes only the translational FRFs) can be obtained as

$$ {}_{\Sigma}\mathbf{H}_{tt}^{c} = {}_{A}\mathbf{H}_{tt}^{c} - {}_{A}\mathbf{H}_{tt}^{c}\left({}_{AB}\mathbf{H}_{tt}^{c}\right)^{-1}{}_{A}\mathbf{H}_{tt}^{c} - {}_{A}\mathbf{H}_{tr}^{c}\left({}_{AB}\mathbf{H}_{rr}^{c}\right)^{-1}{}_{A}\mathbf{H}_{rt}^{c} \tag{7.17} $$

If only the translational FRFs of the substructures are taken into account for predicting the FRFs of the assembled system, the predicted translational FRFs of the assembly will be

$$ {}_{\Sigma}\hat{\mathbf{H}}_{tt}^{c} = {}_{A}\mathbf{H}_{tt}^{c} - {}_{A}\mathbf{H}_{tt}^{c}\left({}_{AB}\mathbf{H}_{tt}^{c}\right)^{-1}{}_{A}\mathbf{H}_{tt}^{c} \tag{7.18} $$

Comparing equation (7.18) with (7.17), the error caused by ignoring rotational FRFs is

$$ \mathbf{E}_{tt} = {}_{\Sigma}\mathbf{H}_{tt}^{c} - {}_{\Sigma}\hat{\mathbf{H}}_{tt}^{c} = -{}_{A}\mathbf{H}_{tr}^{c}\left({}_{AB}\mathbf{H}_{rr}^{c}\right)^{-1}{}_{A}\mathbf{H}_{rt}^{c} \tag{7.19} $$

In the cases when the condition of equation (7.15) is not satisfied, the inverse of matrix ${}_{AB}\mathbf{H}^{c}$ can then be partitioned with regard to the size of the partitioned matrix of equation (7.14) and should hence have the form of

$$\left({}_{AB}\mathbf{H}^{c}\right)^{-1}=\begin{bmatrix} {}_{AB}\mathbf{H}_{tt}^{ci} & \vdots & {}_{AB}\mathbf{H}_{tr}^{ci} \\ \cdots & \cdots & \cdots \\ {}_{AB}\mathbf{H}_{rt}^{ci} & \vdots & {}_{AB}\mathbf{H}_{rr}^{ci} \end{bmatrix} \tag{7.20}$$

The submatrices in (7.20) can be expressed by the submatrices in (7.14) as

$${}_{AB}\mathbf{H}_{tt}^{ci}=\left({}_{AB}\mathbf{H}_{tt}^{c}\right)^{-1}+\left({}_{AB}\mathbf{H}_{tt}^{c}\right)^{-1}{}_{AB}\mathbf{H}_{tr}^{c}\cdot{}_{AB}\mathbf{H}_{rr}^{ci}\cdot{}_{AB}\mathbf{H}_{rt}^{c}\left({}_{AB}\mathbf{H}_{tt}^{c}\right)^{-1} \tag{7.21}$$

$${}_{AB}\mathbf{H}_{tr}^{ci}=-\left({}_{AB}\mathbf{H}_{tt}^{c}\right)^{-1}{}_{AB}\mathbf{H}_{tr}^{c}\cdot{}_{AB}\mathbf{H}_{rr}^{ci} \tag{7.22}$$

$${}_{AB}\mathbf{H}_{rt}^{ci}=\left({}_{AB}\mathbf{H}_{tr}^{ci}\right)^{T} \tag{7.23}$$

$${}_{AB}\mathbf{H}_{rr}^{ci}=\left({}_{AB}\mathbf{H}_{rr}^{c}-{}_{AB}\mathbf{H}_{rt}^{c}\left({}_{AB}\mathbf{H}_{tt}^{c}\right)^{-1}{}_{AB}\mathbf{H}_{tr}^{c}\right)^{-1} \tag{7.24}$$

The derivation of equations (7.21) to (7.24) is given in Appendix E. Notice that every partitioned sub-matrix of the matrix $\left({}_{AB}\mathbf{H}^{c}\right)^{-1}$ contains not only the information of TDOF FRFs, but also that of the RDOF FRFs. These two sorts of information cannot be split as was done in equation (7.16). The matrix is partitioned to be the same size as equation (7.14), *e.g.* ${}_{AB}\mathbf{H}_{tt}^{ci}$ has the same dimension as $\left({}_{AB}\mathbf{H}_{tt}^{c}\right)^{-1}$ and so on. ${}_{AB}\mathbf{H}_{tt}^{ci}$ can be equal to $\left({}_{AB}\mathbf{H}_{tt}^{c}\right)^{-1}$ only if the TDOF-RDOF weak coupling condition (7.15) is satisfied.

Substituting equations (7.12), (7.13) and (7.20) into (7.10), the sub-matrix of ${}_{\Sigma}\mathbf{H}$, which includes only the translational FRFs, can be obtained as:

$${}_{\Sigma}\mathbf{H}_{tt}^{c}={}_{A}\mathbf{H}_{tt}^{c}-{}_{A}\mathbf{H}_{tt}^{c}\cdot{}_{AB}\mathbf{H}_{tt}^{ci}\cdot{}_{A}\mathbf{H}_{tt}^{c}-{}_{A}\mathbf{H}_{tr}^{c}\cdot{}_{AB}\mathbf{H}_{rt}^{ci}\cdot{}_{A}\mathbf{H}_{tt}^{c}-{}_{A}\mathbf{H}_{tt}^{c}\cdot{}_{AB}\mathbf{H}_{tr}^{ci}\cdot{}_{A}\mathbf{H}_{rt}^{c}-{}_{A}\mathbf{H}_{tr}^{c}\cdot{}_{AB}\mathbf{H}_{rr}^{ci}\cdot{}_{A}\mathbf{H}_{rt}^{c} \tag{7.25}$$

Comparing equation (7.25) with equation (7.18), the error caused by ignoring rotational FRFs is

$$\begin{aligned}\mathbf{E}_{tt}={}_{\Sigma}\mathbf{H}_{tt}^{c}-{}_{\Sigma}\hat{\mathbf{H}}_{tt}^{c}={}_{A}\mathbf{H}_{tt}^{c}\left({}_{AB}\mathbf{H}_{tt}^{c}\right)^{-1}{}_{A}\mathbf{H}_{tt}^{c}-{}_{A}\mathbf{H}_{tt}^{c}\cdot{}_{AB}\mathbf{H}_{tt}^{ci}\cdot{}_{A}\mathbf{H}_{tt}^{c}-{}_{A}\mathbf{H}_{tr}^{c}\cdot{}_{AB}\mathbf{H}_{rt}^{ci}\cdot{}_{A}\mathbf{H}_{tt}^{c}\\ -{}_{A}\mathbf{H}_{tt}^{c}\cdot{}_{AB}\mathbf{H}_{tr}^{ci}\cdot{}_{A}\mathbf{H}_{rt}^{c}-{}_{A}\mathbf{H}_{tr}^{c}\cdot{}_{AB}\mathbf{H}_{rr}^{ci}\cdot{}_{A}\mathbf{H}_{rt}^{c}\end{aligned} \tag{7.26}$$

Notice that

$$\left({}_{A}\mathbf{H}_{rt}^{c}\right)^{T}={}_{A}\mathbf{H}_{tr}^{c}$$

and

$$\left({}_{AB}\mathbf{H}_{tr}^{ci}\right)^{T} = {}_{AB}\mathbf{H}_{rt}^{ci}$$

so that, equation (7.26) becomes

$$\mathbf{E}_{tt} = \mathbf{E}_1 + \mathbf{E}_2 + \mathbf{E}_3 \tag{7.27}$$

Each individual term in (7.27) is

$$\mathbf{E}_1 = -\mathbf{P}^{T}\,{}_{AB}\mathbf{H}_{rr}^{ci}\mathbf{P} \tag{7.28}$$

$$\mathbf{E}_2 = -\,{}_{A}\mathbf{H}_{tr}^{c}\cdot{}_{AB}\mathbf{H}_{rr}^{ci}\cdot\mathbf{P} - \mathbf{P}^{T}\cdot{}_{AB}\mathbf{H}_{rr}^{ci}\cdot{}_{A}\mathbf{H}_{rt}^{c} \tag{7.29}$$

$$\mathbf{E}_3 = -\left({}_{A}\mathbf{H}_{rt}^{c}\right)^{T}\,{}_{AB}\mathbf{H}_{rr}^{ci}\cdot{}_{A}\mathbf{H}_{rt}^{c} \tag{7.30}$$

where

$$\mathbf{P} = {}_{AB}\mathbf{H}_{rt}^{c}\left({}_{AB}\mathbf{H}_{tt}^{c}\right)^{-1}\,{}_{A}\mathbf{H}_{tt}^{c} \tag{7.31}$$

Equations (7.27) to (7.31) provide the means to predict the errors in the TDOF-FRFs of the coupled structure which are obtained without using RDOF related FRFs. This tool is useful in the assessment of the importance of RDOF related FRFs in FRF coupling analysis before implementing the procedure of coupling analysis.

The contributions of the different components in (7.27), $\mathbf{E}_1$, $\mathbf{E}_2$ and $\mathbf{E}_3$, to the total error, $\mathbf{E}_{tt}$, differ from case to case. Here, we can see that the TDOF RDOF weakly coupled system is a special case of the general case with $E_1 \approx 0$, $E_2 \approx 0$ and therefore

$$\mathbf{E}_{tt} \approx \mathbf{E}_3$$

In the following numerical simulation, it will be demonstrated that the significance of each component in equation (7.27) changes in different cases.

7.2.2. Numerical Illustrations

WEAKLY-COUPLED SYSTEM

Two identical planar beams are coupled to form a longer beam as shown in Fig.7.3. The first beam, nodes 1 to 11, is taken as substructure A and the second beam, nodes 11 to 21, is taken as substructure B. Each node has three DOFs: x, z and θ_y. The two beams are fully coupled at node 11.

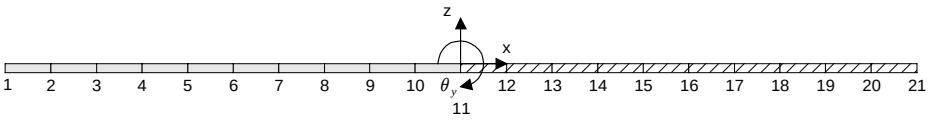

Fig.7.3 Two beams coupled adjacently

The FRF matrix of substructure A at the coupling co-ordinates is

$$ {}_A\mathbf{H}^c = \begin{bmatrix} H^c_{xx} & H^c_{xz} & H^c_{x\theta} \\ H^c_{zx} & H^c_{zz} & H^c_{z\theta} \\ H^c_{\theta x} & H^c_{\theta z} & H^c_{\theta\theta} \end{bmatrix} \tag{7.32} $$

It is symmetric and all the elements are drawn in Fig.7.4.

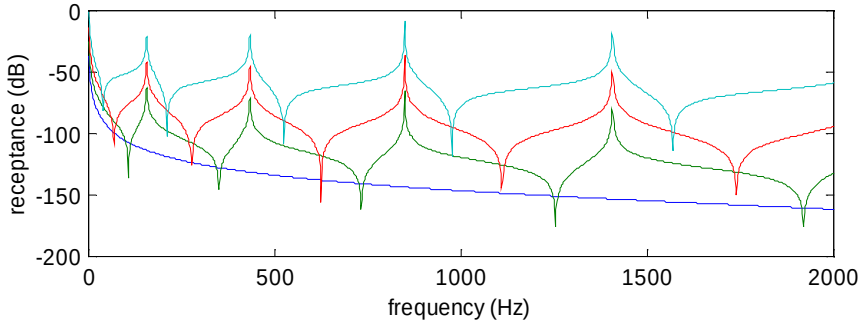

Fig.7.4 FRFs of substructure A at the coupling DOFs

These four FRFs shown in Fig.7.4 are, from bottom to top, H^c_{xx}, H^c_{zz}, $H^c_{z\theta}$ and $H^c_{\theta\theta}$. Elements H^c_{xz} and $H^c_{x\theta}$ in matrix (7.32) are zeros. The summation of two FRF matrices of the substructures, ${}_{AB}\mathbf{H}^c = {}_A\mathbf{H}^c + {}_B\mathbf{H}^c$, has its 4 elements shown in Fig.7.5.

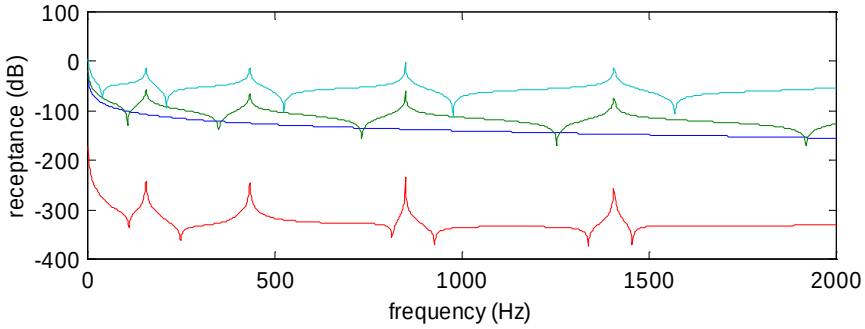

Fig.7.5 Summation of two FRF matrices from substructure A and B

The four FRFs shown in Fig.7.5 are, from bottom to top, ${}_{AB}H^{c}_{z\theta}$, ${}_{AB}H^{c}_{xx}$, ${}_{AB}H^{c}_{zz}$ and ${}_{AB}H^{c}_{\theta\theta}$. The cross FRF, ${}_{AB}H^{c}_{z\theta}$, is much smaller than the three point FRFs, and the system is therefore recognised as a TDOF-RDOF weakly-coupled system. The matrix ${}_{AB}\mathbf{H}^{c}$ is approximately diagonal.

The coupling analysis is carried out in two steps. First, we suppose that all FRFs are available for both substructures and use these accurate FRFs to predict the FRFs of the coupled structure. Second, we suppose only translation FRFs are measurable (even though the rotational degree of freedom θ_y is still kept in the substructures) and use these TDOF FRFs only to predict the FRFs of the coupled structures. These two results are then compared in Fig.7.6. The error function is calculated according to equation (7.19). The specific compared FRF shown in this figure is ${}_{\Sigma}H^{c}_{zz}$, which is a point FRF of translation z at the interface.

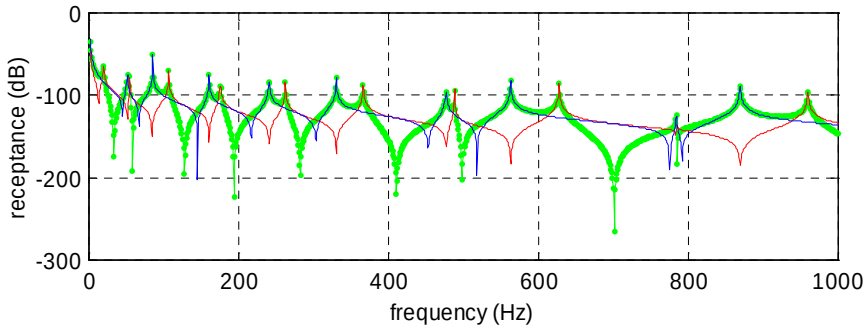

Fig.7.6 Comparison of coupling results: exact coupling error

A MORE GENERAL CASE

This is a more general case than the first one: two planar beams are coupled through a joint as shown in Fig.7.7. To simplify the analysis, the upper beam and the joint are taken as substructure A and the lower beam is substructure B. The DOFs at each node are *x*, *z* and θ_y.

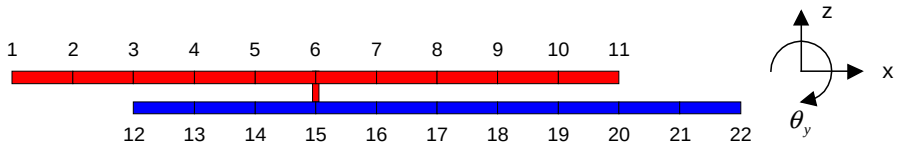

Fig.7.7. Two planar beams are coupled through a joint

Some elements of the FRF matrices of substructures A and B are shown in Fig.7.8, specifically, those FRFs related to the degrees of freedom at the interface, node 15. The elements of the summation of these two FRF matrices, ${}_{AB}\mathbf{H}^c = {}_A\mathbf{H}^c + {}_B\mathbf{H}^c$, as shown in equation (7.11) are presented in Fig.7.9, where the lowest curve is ${}_{AB}H^c_{xz}$.

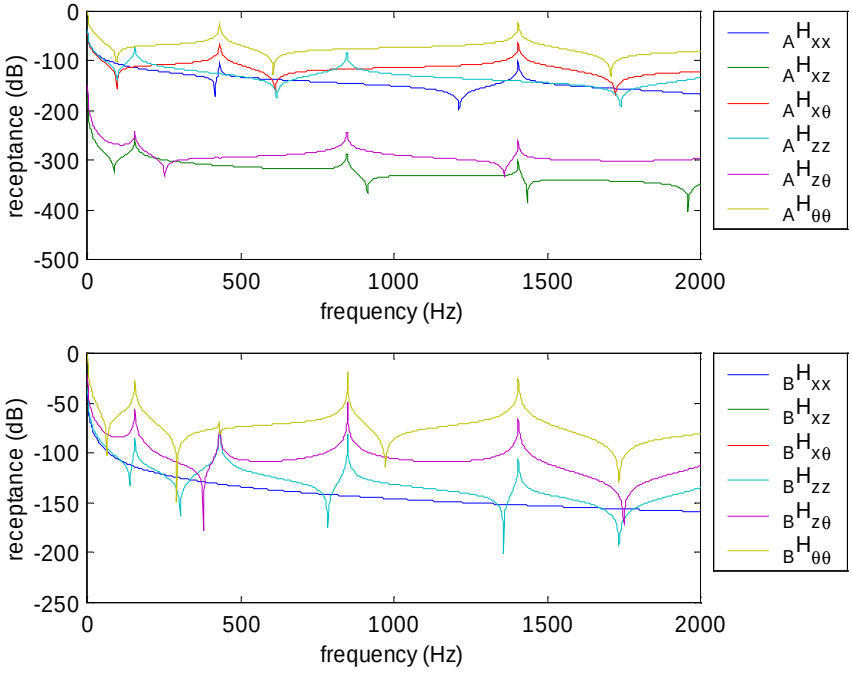

Fig.7.8 FRFs of substructure A and B

It is noticed that both of the translation-rotation cross FRFs, ${}_{AB}H^{c}_{x\theta}$ and ${}_{AB}H^{c}_{z\theta}$, are not small compared with the point FRFs. Therefore, they are not negligible and this situation exists in the general cases.

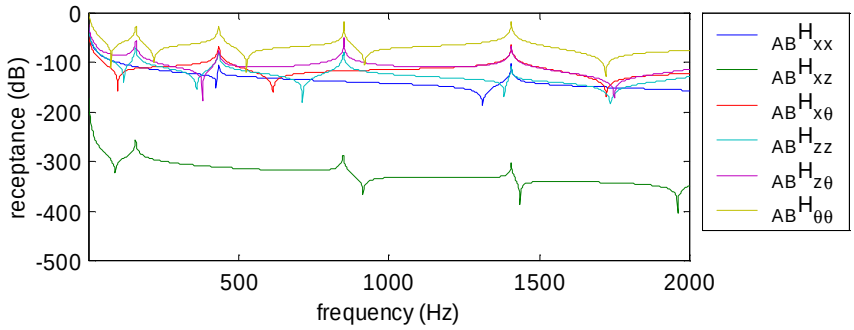

Fig.7.9 Summation of two FRF matrices from substructure A and B

The coupling analyses are carried out with and without RDOF-related FRFs and the results are shown in Fig.7.10, where ‘exact’ means the result obtained using both TDOF-FRFs and RDOF-FRFs and ‘coupling’ represents the result obtained using the TDOF-FRFs only. The discrepancy between these two curves is obvious. It should be pointed out that, in general, the coupling analysis without RDOF-related FRFs does not always underestimate the natural frequencies as was shown in Fig.7.6, which relates to the TDOF-RDOF weakly coupled system.

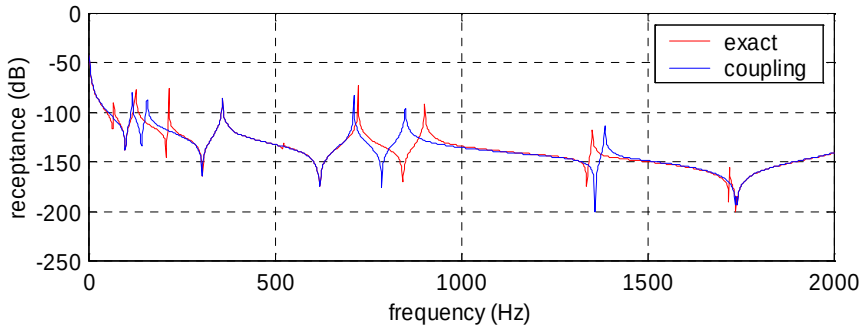

Fig.7.10 Comparison of coupling results

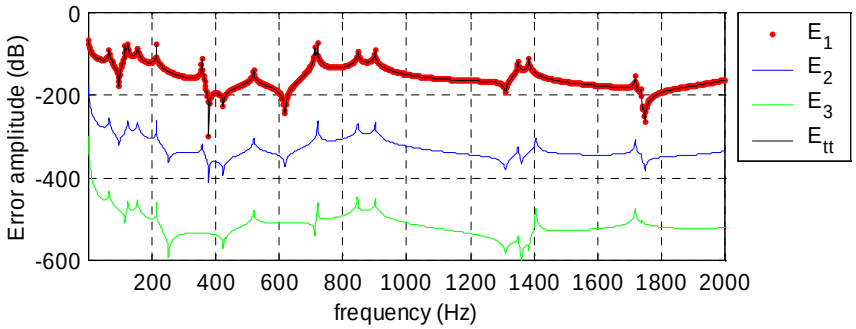

Fig.7.11 The composition of error

The errors in the FRFs of the coupled system for the general case have been given in equation (7.22). The three terms of the error of ${}_{\Sigma}H_{zz}^{c}$ are illustrated in Fig.7.11. The magnitudes of their values have the same order as their sequence numbers as

$$E_1 > E_2 > E_3$$

It is clear that, in this case, the total error is approximately equal to the first term:

$$E_{tt} \approx E_1$$

A PRACTICAL CASE

The plate and beam coupled structure introduced in Fig.5.6 (FE model in Fig.5.10) is examined here as a practical case. This case demonstrates the impact of RDOF information to the GJDM coupling analysis. The error matrix as equation (7.27) for the K-J FRF coupling analysis is not given for GJDM because of the mathematical complexity.

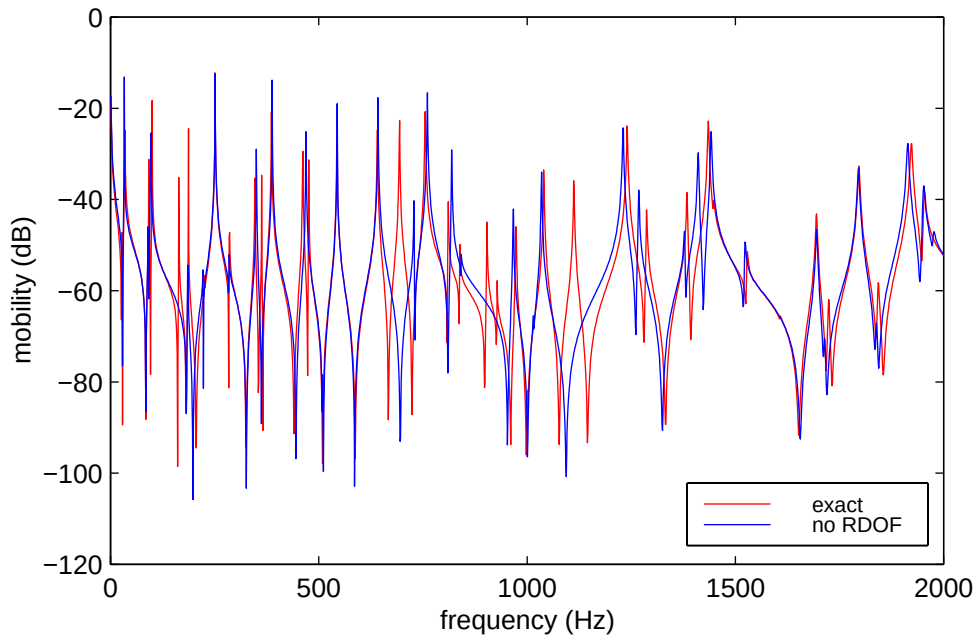

Fig.7.12 Comparison between the no-RDOF coupling and the exact solutions

In the coupling process of the plate and beam coupled structure using GJDM, a significant advantage is that the joint impedance matrix can be adjusted properly to match the number of DOFs on its interfaces to substructures. When all translation and rotation FRFs are measurable, as in the case shown in Chapter 5, and the joint impedance matrix contains all the elements corresponding to the measured DOFs, the result of the coupling analysis is accurate, as shown in Fig.5.12. If only the translation FRFs of the substructures are supplied, say, translations in *z*-direction only, the joint impedance matrix needs to be adjusted to include merely the elements of axial stiffness, which makes the dimension of $\mathbf{Z}$ become 2×2. The result of coupling without RDOF-related FRFs is given in Fig.7.12 where it is compared with the exact solution. It is seen from this comparison that the error caused by the lack of RDOF-related information is significant. In a certain frequency range, even though FRFs from the no-RDOF coupling analysis can match some of the modes of the exact solution, the number of modes in the TDOF-only coupling is generally less than that in the exact solution. This error may not be acceptable in application.

7.3. CONCLUSIONS

The impact of data from the rotation degrees of freedom (RDOFs) to the joint parameter identification using LSM, and to the FRF coupling analysis, has been studied. The following conclusions can be drawn from this study:

- DOF-compatibility of the identified model has to be considered before the implementation of the identification method. Since the input data to the LSM based joint parameter identification procedure are measured FRFs of the substructures and their assembly, the pre-determined DOFs of the joint model, whose parameters are to be determined by the identification process, have to be compatible with those of the joint in the measured practical structure. DOF-incompatible case can result in unacceptably large errors;
- the RDOF-related FRFs, which are ususally difficult to measure or to measure precisely compared with the translation FRFs, play a very important role in FRF coupling analysis. Coupling made without RDOF-related FRFs produces errornous results. The errors can be predicted quantitvely using the error functions provided here using information from substructures only;
- the development of an accurate experimental technique for the measurement of RDOF-related FRFs is then important for the application of both the LSM-based joint parameter identification method and the FRF coupling analysis. The expected accuracy is the same as that of the translation FRFs obtained by the currently available techniques.

CHAPTER 8

CONCLUSIONS AND FUTURE WORK

Substructure coupling analysis is an important subject in structural dynamics. Its task is to facilitate the prediction of the dynamic behaviour of an assembled structure from the dynamic properties of substructures. In practice, substructures are physically assembled together using various types of joint, and in many cases these joints significantly affect the dynamic response of the assembled structure. Recognising the importance of joints in coupling analysis, the author has made contributions in this thesis on joint modelling and on the involvement of joints in coupling analysis. The work reported in the thesis mainly comprises three parts: (i) method review and development for joint parameter identification; (ii) method review and development for substructure coupling analysis, and (iii) critical discussion of the relevant issues of non-linearity and rotational degrees of freedom. Concentrating all these aspects around the subject of substructure coupling analysis, this thesis is based on solid mathematical foundations and their validation by numerical studies. Overall conclusions and suggested further developments on each part are summarised in this chapter.

The main contributions of this thesis are:

- a new algorithm for LSM based joint parameter identification;

- a new method for joint parameter identification using neural networks;
- a new theorem on transmissibility;
- development and validation of a CMS approach including joint impedance;
- a new FRF coupling technique with joint impedance matrix included.

8.1. JOINT MODELLING

Methods for joint modelling in general are reviewed in this thesis. A least-squares method (LSM) based joint parameter identification method has been developed and presented here, including its basic equations, algorithm, numerical validation and robustness investigation. As a further development, neural networks are introduced into the area of joint parameter identification.

The LSM-based joint parameter identification method can identify mass, stiffness and damping parameters from a joint impedance matrix. This method, in principle, can identify parameters in all kinds of linear joint. The partitioning algorithm (PA) presented in this work for implementation of the LSM identification method, is superior to the non-partition direct algorithm (NPA) because it not only significantly decreases the number of equations involved in a solution but also improves the condition of the coefficient matrix in the linear equations. Therefore, the PA approach is an efficient and accurate algorithm.

The *transmissibility theorem*, a side-product in the algorithm study, reveals an important correlation between FRFs in chain-like structures and provides a guideline for selecting internal DOFs for the application of the joint parameter identification method.

Neural networks have a good reputation in mapping non-linear relationships between input and output data. A neural network can learn from available input-output pairs. In other words, it can be trained by a set of input-output data. A well-trained neural network will produce an accurate answer with an arbitrary input within the range of the training set. To apply neural networks to this particular subject, joint parameter identification, the main difficulty is in the

preparation of training sets. A technique based on parametric families of FE models has been used in this work to generate FRFs for an assembled structure with variety of joint parameters. These FRF data are then compressed by using principal component analysis (PCA) to form a much more compact input data set. The output data set is formed by uncertainty factors of joint parameters rather than the physical parameters themselves because these dimensionless factors have better numerical properties. Two types of feedforward network are used in the numerical simulations, MLP and RBF networks. Both of these successfully identified the joint parameters in numerical studies made to validate the method. This implies that the training sets obtained in the pre-processing procedure (applying PCA to the FRF matrix) reflect the features of the structures′ dynamic behaviour with the variation of joint parameters. The RBF networks are more accurate and more efficient compared with the MLPs. The neural network methods in general, either MLP or RBF, are robust and easy to implement in practice.

8.2. COUPLING ANALYSIS

Component mode synthesis (CMS) and FRF coupling analysis are two approaches for predicting the dynamic properties of an assembled structure using the modal data or FRFs from its substructures. Developments have been made in this thesis for both of these approaches by taking joints into account in the coupling process. These developments are more complete and practical as compared with the earlier attempts [Urgu89] [Ferr98] in the sense that the high mode-truncation error is compensated and a more general joint model is used.

The CMS method with joints included, and residual attachment mode compensation, (CMSJ), extends the conventional free-interface CMS method by introducing joints into the synthesis process. The joint appears in a general impedance matrix form and its parameters are easy to adjust. Since joints are normally the most difficult part to model, this method provides a convenient way to modify the representation of the joints and to predict the dynamic characteristics of the assembly without re-analysing the substructures. The

residual attachment mode feature greatly increases the accuracy of the synthesis analysis. In the second example of Chapter 4, when 6 and 4 modes were used from substructures A and B, respectively, the first 10 predicted natural frequencies of the assembled structure have a maximum error of only 1.1%. In addition, the introduction of joints also makes the connection between the DOFs of non-conforming interfaces possible.

A generalised joint describing method (GJDM) was derived and presented here in which the FRF submatrices of the assembled structure are explicitely expressed by the FRF submatrices of the substructures. The principle and algorithm for this method have been validated by numerical studies. It has been shown that the joint parameters can be tuned independently to change the dynamic properties of the assembly. That is to say, the substructures need not be re-analysed with respect to variations in the joint parameters. This is not only an advantage for substructure coupling analysis, but also provides a means for designing joints as dampers for vibration control. The numerical studies presented also demonstrated that this method is insensitive to random noise on the input FRFs. For higher noise levels, a singular-value truncation can be used to improve the quality of the predicted FRFs.

8.3. NON-LINEARITY CONSIDERATIONS AND IMPACT OF RDOFS

Almost all papers which mark the milestones of the research on non-linear joint modelling have been reviewed in this thesis and their connections in respect of analysis methods and conclusions are summarised. It is concluded that in most engineering structures, friction joints are often tightly fastened so that their potential non-linear behaviour is suppressed and so is not significant. This conclusion is validated by an experiment on a practical structure. Numerical studies on both discrete parameter models and a continuous contact model indicate that the transition process between stuck and macro-slip conditions usually coincide with the region of strongest non-linearity. While in the status of either stuck or macro-slip, the joint behaves almost as if it were linear. The load-deformation relationship in the normal direction becomes effectively linear

after a pre-load and can be considered as linear in most applications, while the relationship in the tangential direction is always non-linear and energy is dissipated when a cyclic load is applied. When the non-linearity description of a joint is available, the harmonic balance method and description function method are ready for use in the coupling analysis.

The importance of RDOF-related FRFs for joint parameter identification (LSM based method) and for FRF coupling analysis (K-J method) have been studied theoretically. The effect on the GJDM is also demonstrated via a practical case study. A DOF-compatibility concept is put forward in joint parameter identification using measured FRFs. The pre-determined DOFs of a joint model have to be compatible to those of the joint in the measured practical structure. DOF-incompatible case (*e.g.* absence of RDOF information in the measured FRFs) can result in unacceptably large errors.

In FRF coupling analysis, RDOF-related FRFs also play a very important role. Coupling analysis without RDOF-related FRFs produces erroneous results. The errors can be predicted quantitvely using the error functions provided here using information from the substructures only. The RDOF-related FRFs are ususally difficult to measure, or to measured precisely, compared with the translation (TDOF) FRFs. Therefore, the development of an accurate experimental technique for the measurement of RDOF-related FRFs is demanded by these two applications with expected accuracy that is the same as that of the translation FRFs obtained by the currently-available techniques.

8.4. SUGGESTED FUTURE WORK

All four methods presented in this thesis – LSM-based joint parameter identification, using neural networks to identify joint parameters, CMS with joint considered (CMSJ) and general joint description method (GJDM) for FRF coupling analysis – are expected to experience more applications to complicated and practical structures. Problems may be exposed in the application process and the algorithms may therefore need to be updated.

Further research on the methodology of this topic should include an uncertainty study of the proposed methods and the solution to non-linear problems. Uncertainty, or error propagation, study is critical to the FRF based methods since it is practically very difficult to measure the required FRFs on real engineering structures with very good consistency and very low noise level. The consistency and noise levels in FRFs need to be quantitatively justified and their propagation through the procedure of solution should be analysed. On the other hand, starting form the solid basis of linear analysis, it should not be much work to extend some of the methods developed in this thesis to deal with non-linear cases. For instance, applying neural network method to identify the non-linear properties in joints; introduce non-linear description of joints to CMSJ and GJDM.

APPENDIX A

TRANSMISSIBILITY PROPERTIES OF MDOF SYSTEMS

A.1. INTRODUCTION

In many aspects of structural dynamics analysis, FRFs - either measured or generated - are used directly to represent the characteristics of the structures in question. In system identification, model updating as well as substructure synthesis, various FRF matrices are used. Accordingly, it is important to understand the construction of FRF matrices and to be aware of the relationships between the individual FRFs.

The issue of transmissibility properties of MDOF systems is addressed here to clarify the concept and to provide a criterion for the existence of the properties in MDOF systems.

A.2. THE THEOREM OF TRANSMISSIBILITY

For a system which has a diagonal mass matrix and a banded stiffness matrix, such as

$$\mathbf{M}=\begin{bmatrix} m_1 & 0 & \cdots & \cdots & 0 \\ 0 & m_2 & 0 & \cdots & 0 \\ \vdots & 0 & \ddots & \ddots & \vdots \\ \vdots & \vdots & \ddots & \ddots & 0 \\ 0 & 0 & \cdots & 0 & m_n \end{bmatrix} \tag{A.1}$$

and

$$\mathbf{K}=\begin{bmatrix} k_{11} & k_{12} & 0 & \cdots & 0 \\ k_{21} & k_{22} & k_{23} & \ddots & \vdots \\ 0 & \ddots & \ddots & \ddots & 0 \\ \vdots & \ddots & \ddots & \ddots & k_{(n-1)n} \\ 0 & \cdots & 0 & k_{n(n-1)} & k_{nn} \end{bmatrix} \tag{A.2}$$

the following relationship between its FRFs holds:

$$\frac{{}_A H_{j_1 k_1}(\omega)}{{}_A H_{j_2 k_1}(\omega)} = \frac{{}_A H_{j_1 k_2}(\omega)}{{}_A H_{j_2 k_2}(\omega)} \tag{A.3}$$

at all frequencies when the following condition for the subscripts in (A.3) is fulfilled:

$$(k_1, k_2) < (j_1, j_2) \text{ or } (k_1, k_2) > (j_1, j_2) \tag{A.4}$$

Here (k_1, k_2) represents a pair of excitation co-ordination numbers, and (j_1, j_2) represents a pair of response co-ordination numbers. The sequence of k and j is the same as the co-ordinate index, *i.e.*, the mass index given in $\mathbf{M}$ matrix.

Proof A spatial model is employed to prove this theorem. Consider the nDOF system shown in

Fig. A.1, in which the excitation is applied at k and the responses are measured on one side of the excitation DOF, at positions numbered as j_1 and j_2.

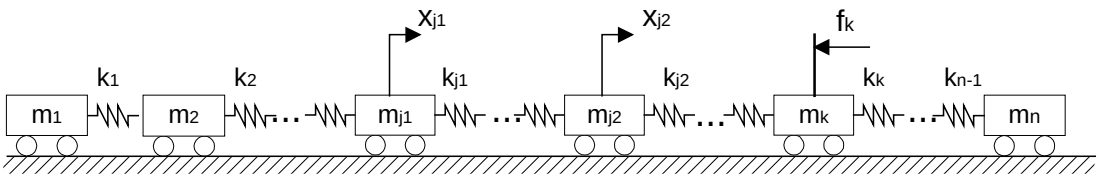

Fig. A.1 An n-DOF mass-spring system

The equation of motion has the form of

$$\mathbf{Zx} = \mathbf{f} \tag{A.5}$$

Its detailed form is

$$\begin{bmatrix} d_1 & -k_1 & & & & & & & \\ -k_1 & d_2 & -k_2 & & & & & & \\ & \cdots & \cdots & \cdots & & & & & \\ & & -k_{j-1} & d_j & -k_j & & & & \\ & & & \cdots & \cdots & \cdots & & & \\ & & & & \cdots & \cdots & \cdots & & \\ & & & & & -k_{k-1} & d_k & -k_k & \\ & & & & & & \cdots & \cdots & \cdots \\ & & 0 & & & & & \cdots & \cdots \\ & & & & & & & -k_{n-1} & d_n \end{bmatrix} \begin{Bmatrix} x_1 \\ x_2 \\ \vdots \\ x_j \\ \vdots \\ \vdots \\ x_k \\ \vdots \\ \vdots \\ x_n \end{Bmatrix} = \begin{Bmatrix} 0 \\ 0 \\ \vdots \\ 0 \\ \vdots \\ 0 \\ f_k \\ 0 \\ \vdots \\ 0 \end{Bmatrix} \tag{A.6}$$

where

$d_1 = k_1 - \omega^2 m_1$

$d_i = k_{i-1} + k_i - \omega^2 m_i \qquad i = 2, 3, ..., n\text{-}1$

$d_n = k_{n-1} - \omega^2 m_n$ and

j can be either j_1 or j_2

Big zeros in the matrices stand for “zeros elsewhere” hereinafter.

Define sub-matrices of $\mathbf{Z}$ as $\mathbf{Z}_l$, $l = 1, 2, 3, ..., n$, which are square matrices formed by taking the first l rows and columns from $\mathbf{Z}$ as

$\mathbf{Z}_1 = d_1$

$\mathbf{Z}_2 = \begin{bmatrix} d_1 & -k_1 \\ -k_1 & d_2 \end{bmatrix}$

:

$$\mathbf{Z}_j = \begin{bmatrix} d_1 & -k_1 & & 0 & \\ -k_1 & d_2 & -k_2 & & \\ & \cdots & \cdots & \cdots & \\ & & \cdots & \cdots & \cdots \\ & 0 & & -k_{j-1} & d_j \end{bmatrix} \text{ and}$$

$\mathbf{Z}_n = \mathbf{Z}$.

From the fact that $f_i = 0$ for $i = 1, 2, ..., k-1$, we can obtain the relationship between x_1, the displacement of m_1, and x_k:

$$\frac{x_1}{x_k} = \frac{\prod_{p=1}^{k-1} k_p}{\det(\mathbf{Z}_{k-1})} \tag{A.7}$$

Similarly, the relationship between x_j and x_k is

$$\frac{x_j}{x_k} = \frac{\det(\mathbf{Z}_{j-1})}{\det(\mathbf{Z}_{k-1})} \prod_{p=j}^{k-1} k_p \qquad (j < k) \tag{A.8}$$

These two equations are derived later from equation (A.18) through (A.24) and they can be validated by using the following recurrence formula

$$x_2 = \frac{d_1}{k_1} x_1 \tag{A.9}$$

$$x_{l+1} = \frac{d_l}{k_l} x_l - \frac{d_{l-1}}{k_l} x_{l-1} \qquad l = 2, 3, ..., k\text{-}1 \tag{A.10}$$

Similarly, x_{k+1} can be derived using the last $n-k$ equations from (A.6):

$$x_{k+1} = \frac{k_k \det\left(\mathbf{Z}_n^{k+2}\right)}{\det\left(\mathbf{Z}_n^{k+1}\right)} x_k \tag{A.11}$$

where $\mathbf{Z}_n^{k+2}$ is a sub-matrix of $\mathbf{Z}$, which is formed by the $(k+2)^{th}$ to *n*th rows and the $(k+2)^{th}$ to *n*th columns. The same rule also applies to $\mathbf{Z}_n^{k+1}$.

The *k*th equation in (A.6) is

$$-k_{k-1}x_{k-1} + d_k x_k - k_k x_{k+1} = f_k \tag{A.12}$$

Substituting (A.7) and (A.11) into (A.12), we have

$$H_{1k} = \frac{x_1}{f_k} = \frac{\det(\mathbf{Z}_n^{k+1})\prod_{p=1}^{k-1} k_p}{d_k \det(\mathbf{Z}_{k-1})\det(\mathbf{Z}_n^{k+1}) - k_k^2 \det(\mathbf{Z}_{k-1})\det(\mathbf{Z}_n^{k+2}) - k_{k-1}^2 \det(\mathbf{Z}_{k-2})\det(\mathbf{Z}_n^{k+1})} \tag{A.13}$$

Substituting (A.8) and (A.11) into (A.12), we have

$$H_{jk} = \frac{x_j}{f_k} = \frac{\det(\mathbf{Z}_n^{k+1})\det(\mathbf{Z}_{j-1})\prod_{p=j}^{k-1} k_p}{d_k \det(\mathbf{Z}_{k-1})\det(\mathbf{Z}_n^{k+1}) - k_k^2 \det(\mathbf{Z}_{k-1})\det(\mathbf{Z}_n^{k+2}) - k_{k-1}^2 \det(\mathbf{Z}_{k-1})\det(\mathbf{Z}_n^{k+1})} \tag{A.14}$$

Equation (A.13) and (A.14) are FRFs expressed in the form of rational fractions. The denominator is a *2n*-order polynomial in ω, and the highest order of ω for their numerator polynomials is *2n-2*. The poles and residues of the fraction correspond to the natural frequencies and modal constants of the system.

Let $j = j_1$ and $j = j_2$ separately in equation (A.14), we have expressions for H_{j1k} and H_{j2k}, respectively. The ratio of H_{j1k} and H_{j2k} is defined as *Transmissibility Function*:

$$T_{j1,j2}(\omega) = \frac{H_{j1k}}{H_{j2k}} = \frac{\det(\mathbf{Z}_{j1-1})\prod_{p=j1}^{k-1} k_p}{\det(\mathbf{Z}_{j2-1})\prod_{p=j2}^{k-1} k_p} = \frac{\det(\mathbf{Z}_{j1-1})}{\det(\mathbf{Z}_{j2-1})}\prod_{p=j1}^{j2-1} k_p \tag{A.15}$$

Specifically, when let $j_1 = 1$ and $j_2 = j$ then

$$T_{1,j}(\omega) = \frac{H_{1k}}{H_{jk}} = \frac{\prod_{p=1}^{k-1} k_p}{\det(\mathbf{Z}_{j1-1})\prod_{p=j}^{k-1} k_p} = \frac{\prod_{p=1}^{j-1} k_p}{\det(\mathbf{Z}_{j1-1})} \tag{A.16}$$

The expression of $T(\omega)$ in equation (A.15) is not a function of excitation co-ordinate *k*, which means that $T(\omega)$ is not dependent on the excitation position.

From the derivation process, we know the only requirement for the excitation position is $k > j$. It means that if we rename the co-ordinate *k*, which is used in the above derivation, to k_1, and give the system an excitation at k_2 $(k_2 > k_1)$, we will have the same function $T(\omega)$. That is, the following relationship holds

$$T(\omega) = \frac{H_{j1k1}(\omega)}{H_{j2k1}(\omega)} = \frac{H_{j1k2}(\omega)}{H_{j2k2}(\omega)} \tag{A.17}$$

Equation (A.17) can take the other form as

$$T(\omega) = \frac{H_{j1k1}(\omega)}{H_{j1k2}(\omega)} = \frac{H_{j2k1}(\omega)}{H_{j2k2}(\omega)} \tag{A.18}$$

So far, the theorem has been proved.

The derivation of equation (A.7) and (A.8) follows.

The first $(k-l)$ equations in (A.6) are shown as equation (A.19). Changing the $\mathbf{Z}$ matrix of (A.19) to a square matrix of $(k-l)\times(k-l)$, *i.e.*, $\mathbf{Z}_{k-1}$, by moving x_k to the right hand side, we have equation (A.20)

$$\begin{bmatrix} d_1 & -k_1 & & & & & \\ -k_1 & d_2 & -k_2 & & & & \\ & \cdots & \cdots & \cdots & & & \\ & & \cdots & \cdots & \cdots & & \\ & & & -k_{j-1} & d_j & -k_j & \\ & 0 & & & \cdots & \cdots & \cdots \\ & & & & & -k_{k-2} & d_{k-1} & -k_{k-1} \end{bmatrix} \begin{Bmatrix} x_1 \\ x_2 \\ \vdots \\ \vdots \\ x_j \\ \vdots \\ x_{k-1} \\ x_k \end{Bmatrix} = \begin{Bmatrix} 0 \\ 0 \\ \vdots \\ \vdots \\ 0 \\ \vdots \\ 0 \end{Bmatrix} \tag{A.19}$$

$$\begin{bmatrix} d_1 & -k_1 & & & & \\ -k_1 & d_2 & -k_2 & & & \\ & \cdots & \cdots & \cdots & & \\ & & -k_{j-1} & d_j & -k_j & \\ & & & \cdots & \cdots & \cdots \\ & 0 & & & -k_{k-3} & d_{k-2} & -k_{k-2} \\ & & & & & -k_{k-2} & d_{k-1} \end{bmatrix} \begin{Bmatrix} x_1 \\ x_2 \\ \vdots \\ x_j \\ \vdots \\ x_{k-2} \\ x_{k-1} \end{Bmatrix} = \begin{Bmatrix} 0 \\ 0 \\ \vdots \\ 0 \\ \vdots \\ 0 \\ k_{k-1}x_k \end{Bmatrix} \tag{A.20}$$

Solving for x_j from equation (A.20) using Cramer's rule, we have a unique solution when $\det(\mathbf{Z}_{k-1}) \neq 0$ as

$$x_j = \frac{k_{k-1}x_k}{\det(\mathbf{Z}_{k-1})} \cdot (\mathbf{Z}_{k-1})_{k-1,j} \tag{A.21}$$

where

$$(\mathbf{Z}_{k-1})_{k-1,j} = (-1)^{k-1+j} \det(\mathbf{Z}_{k-1}^{k-1,j}) \tag{A.22}$$

and

$$\mathbf{Z}_{k-1}^{k-1,j} = \begin{bmatrix} d_1 & -k_1 & & & & & & \\ -k_1 & d_2 & -k_2 & & & & 0 & \\ & \cdots & \cdots & \cdots & & & & \\ & & -k_{j-2} & d_{j-1} & & & & \\ & & & -k_{j-1} & -k_j & & & \\ & & & & d_{j+1} & -k_{j+1} & & \\ & 0 & & & \cdots & \cdots & \cdots & \\ & & & & & -k_{k-3} & d_{k-2} & -k_{k-2} \end{bmatrix} \tag{A.23}$$

is the remainder of $\mathbf{Z}_{k-1}$ when the $(k-l)$th row and the jth column are taken away.

It is clear now that

$$\det(\mathbf{Z}_{k-1}^{k-1,j}) = \det(\mathbf{Z}_{j-1})(-1)^{k-j-1}\prod_{p=j}^{k-2} k_p \tag{A.24}$$

Substituting (A.24) into (A.22), we have

$$(\mathbf{Z}_{k-1})_{k-1,j} = (-1)^{k-1+j}(-1)^{k-j-1}\det(\mathbf{Z}_{j-1})\prod_{p=j}^{k-2} k_p = \det(\mathbf{Z}_{j-1})\prod_{p=j}^{k-2} k_p \tag{A.25}$$

Substituting (A.25) into (A.21), we have

$$\frac{x_j}{x_k} = \frac{k_{k-1}}{\det(\mathbf{Z}_{k-1})} \cdot \det(\mathbf{Z}_{j-1})\prod_{p=j}^{k-2} k_p = \frac{\det(\mathbf{Z}_{j-1})}{\det(\mathbf{Z}_{k-1})}\prod_{p=j}^{k-1} k_p \tag{A.26}$$

This is equation (A.8), and in the special case when $j=1$, we obtain equation (A.7) from equation (A.26).

A.3. EXTENSION OF THE THEOREM

The theorem proved in section A.2 is applicable to relatively simple cases, such as the chain-like mass-spring systems. We will see in this section that this basic theorem can be extended to more complicated cases and later, in section A.4, the bounds of the correlation properties of FRFs is presented.

To extend this theorem, we consider two general positive-definite systems connected with a single spring or several springs, without losing generality. Combinations of more than two systems can always be treated as the two-system case without any difficulty.

A.3.1. Two systems connected with a single spring: " - " connection

The case of two systems connected with a single spring is shown as Fig.A.2. Equation (A.3) still holds in this case, regardless of the interior connections of system A or system B, when excitations are given in system B and responses are measured in system A. Of course, the *Transmissibility function,* $T(\omega)$, would not take exactly the same form as equation (A.15). However, it will be seen that a more general expression can be derived and equation (A.15) is simply a special case of this more general version.

When these two systems are coupled with a single spring, and an excitation acts at the *k*th DOF of system B, equation (A.5) has the form of (A.27).

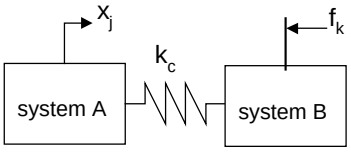

Fig.A.2 Two general systems connected with a spring: " - " connection

$$\begin{bmatrix} \mathbf{Z}_A & 0 \\ & -k_c \\ -k_c & \\ 0 & \mathbf{Z}_B \end{bmatrix} \begin{Bmatrix} {}_A x_1 \\ \vdots \\ {}_A x_j \\ \vdots \\ {}_A x_n \\ {}_B x_1 \\ \vdots \\ {}_B x_k \\ \vdots \\ {}_B x_{n'} \end{Bmatrix} = \begin{Bmatrix} 0 \\ \vdots \\ 0 \\ f_k \\ 0 \\ \vdots \\ 0 \end{Bmatrix} \tag{A.27}$$

Considering the first *n* equations of (A.27), we obtain

$${}_A x_j = \frac{k_c (\mathbf{Z}_A)_{n,j}}{\det(\mathbf{Z}_A)} \cdot {}_B x_1 \tag{A.28}$$

Considering all the equations of (A.27), we have

$${}_B x_j = \frac{(\mathbf{Z})_{k,B1}}{\det(\mathbf{Z})} \cdot f_k \tag{A.29}$$

Substituting equation (A.29) into (A.28) and re-arranging, we have an expression for the frequency response function, $H_{jk}(\omega)$:

$$H_{jk}(\omega) = \frac{{}_A x_j}{f_k} = k_c \cdot \frac{(\mathbf{Z})_{k,B1}}{\det(\mathbf{Z}_A) \cdot \det(\mathbf{Z})} \cdot (\mathbf{Z}_A)_{n,j} \tag{A.30}$$

When the response of system A is measured at two DOFs, j_1 and j_2, we have the ratio of two FRFs as a *Transmissibility function*:

$$T_{j1,j2}(\omega) = \frac{H_{j1k}(\omega)}{H_{j2k}(\omega)} = \frac{(\mathbf{Z}_A)_{n,j1}}{(\mathbf{Z}_A)_{n,j2}} \tag{A.31}$$

We can certainly have equation (A.3) from equation (A.31), which shows that $T_{j1,j2}(\omega)$ is independent of *k*, the excitation co-ordinate on structure B. That means the theorem has been successfully extended to the case of Fig.A.2.

It is not difficult to check that equation (A.31) and (A.15) are identical. When $\mathbf{Z}_A$ is a tri-diagonal matrix, the result of equation (A.31) is equation (A.15).

A.3.2. Systems connected with two springs I: " < " connection

The "<" connection is demonstrated in Fig. A.3. One DOF in system A, ${}_A x_n$, connects to two DOFs in system B, ${}_B x_1$ and ${}_B x_l$.

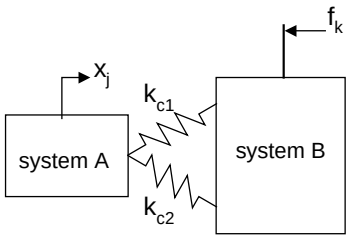

Fig. A.3 Two systems connected with two springs I: " < " connection

The $\mathbf{Z}$ matrix in equation (A.5), in this case, takes the form of

$$\mathbf{Z} = \begin{bmatrix} \mathbf{Z}_A & 0 \\ -k_{c1} & (-k_{c2})_{n,l} \\ -k_{c1} & \\ (-k_{c2})_{l,n} & \mathbf{Z}_B \\ 0 & \end{bmatrix} \tag{A.32}$$

From the first *n* equations, we can solve for ${}_A x_j$:

$${}_A x_j = \frac{(\mathbf{Z}_A)_{n,j}}{\det(\mathbf{Z}_A)} \cdot \left(k_{c1} \cdot {}_B x_1 + k_{c2} \cdot {}_B x_1\right) \tag{A.33}$$

Considering all the equations of (A.32), we have

$${}_B x_1 = \frac{(\mathbf{Z})_{k,B1}}{\det(\mathbf{Z})} \cdot f_k \text{ and } {}_B x_l = \frac{(\mathbf{Z})_{k,l}}{\det(\mathbf{Z})} \cdot f_k \tag{A.34}$$

Substituting equations (A.34) into (A.33) and re-arranging, we have an expression for the frequency response function, $H_{jk}(\omega)$:

$$H_{jk}(\omega) = \frac{{}_A x_j}{f_k} = \frac{k_{c1} \cdot (\mathbf{Z})_{k,B1} + k_{c2} \cdot (\mathbf{Z})_{k,j}}{\det(\mathbf{Z}_A) \cdot \det(\mathbf{Z})} \cdot (\mathbf{Z}_A)_{n,j} \tag{A.35}$$

When the response of system A is measured at two DOFs, j_1 and j_2, we have the same *Transmissibility function* as equation (A.31).

Obviously, if the number of connections increases, say, from ${}_A x_n$ to all the DOFs of system B, equation (A.31) still holds.

A.3.3. Two systems connected with two springs II: " > " connection

The " > " connection is demonstrated in Fig. A.4. Two DOFs in system A, ${}_A x_n$ and ${}_A x_m$, connect to one DOF in system B, ${}_B x_1$.

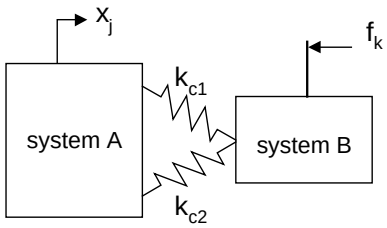

Fig. A.4 Two systems connected with two springs II: " > " connection

The $\mathbf{Z}$ matrix in equation (A.5), in this case, takes the form of

$$\mathbf{Z} = \begin{bmatrix} \mathbf{Z}_A & \begin{matrix} 0 \\ (-k_{c2})_{m,B1} \end{matrix} \\ \begin{matrix} -k_{c1} \\ (-k_{c2})_{B1,m} \end{matrix} & \begin{matrix} -k_{c1} \\ \mathbf{Z}_B \end{matrix} \\ 0 & \end{bmatrix} \tag{A.36}$$

From the first *n* equations, we have

$${}_A x_j = \frac{(\mathbf{Z}_A)_{n,j}}{\det(\mathbf{Z}_A)} \cdot k_{c1} \cdot {}_B x_1 + \frac{(\mathbf{Z}_A)_{m,j}}{\det(\mathbf{Z}_A)} \cdot k_{c2} \cdot {}_B x_1 \tag{A.37}$$

Considering all the equations of (A.36), we have ${}_B x_1$ the same as (A.33). Substituting equations (A.33) into (A.36) and re-arranging, we have the expression of frequency response function $H_{jk}(\omega)$:

$$H_{jk}(\omega) = \frac{{}_A x_j}{f_k} = \frac{(\mathbf{Z})_{k,B1}}{\det(\mathbf{Z}_A) \cdot \det(\mathbf{Z})} \cdot \left(k_{c1} \cdot (\mathbf{Z}_A)_{n,j} + k_{c2} \cdot (\mathbf{Z}_A)_{m,j} \right) \tag{A.38}$$

When the response of system A is measured at two DOFs, j_1 and j_2, we have the *Transmissibility function*:

$$T_{j1,j2}(\omega)=\frac{H_{j1k}(\omega)}{H_{j2k}(\omega)}=\frac{k_{c1}\cdot(\mathbf{Z}_A)_{n,j1}+k_{c2}\cdot(\mathbf{Z}_A)_{m,j1}}{k_{c1}\cdot(\mathbf{Z}_A)_{n,j2}+k_{c2}\cdot(\mathbf{Z}_A)_{m,j2}} \tag{A.39}$$

If the number of connections increases, say from all DOFs of system A to ${}_B x_1$, still exists and equation (A.39) becomes

$$T_{j1,j2}(\omega)=\frac{H_{j1k}(\omega)}{H_{j2k}(\omega)}=\frac{\sum_{p=1}^{n}k_{cp}\cdot(\mathbf{Z}_A)_{p,j1}}{\sum_{p=1}^{n}k_{cp}\cdot(\mathbf{Z}_A)_{p,j2}} \tag{A.40}$$

A.4. LIMITATION OF THE THEOREM

It has been proved that the proposed theorem is valid in all the cases mentioned above. Here we consider the case of two systems connected with two springs III: " = " connection, shown as Fig. A.5. Two DOFs in system A, ${}_A x_n$ and ${}_A x_m$, connect to two DOFs in system B, ${}_B x_1$ and ${}_B x_l$ respectively.

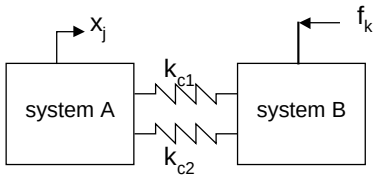

Fig. A.5 Two systems connected with two springs III: " = " connection

The $\mathbf{Z}$ matrix in equation (A.5), in this case, takes the form of

$$\mathbf{Z}=\begin{bmatrix} \mathbf{Z}_A & \begin{matrix}0\\(-k_{c2})_{m,l}\end{matrix} \\ \begin{matrix}-k_{c1}\\(-k_{c2})_{l,m}\end{matrix} & \begin{matrix}-k_{c1}\\0\end{matrix} \\ & \mathbf{Z}_B \end{bmatrix} \tag{A.41}$$

From the first *n* equations, we have

$$ {}_A x_j = \frac{(\mathbf{Z}_A)_{n,j}}{\det(\mathbf{Z}_A)} \cdot k_{c1} \cdot {}_B x_1 + \frac{(\mathbf{Z}_A)_{m,j}}{\det(\mathbf{Z}_A)} \cdot k_{c2} \cdot {}_B x_l \tag{A.42} $$

Considering all the equations in (A.41), we have ${}_B x_1$ and ${}_B x_l$, which are the same as (A.33). Substituting equations (A.8) into (A.42) and re-arranging, we have the expression of frequency response function $H_{jk}(\omega)$:

$$ H_{jk}(\omega) = \frac{{}_A x_j}{f_k} = \frac{k_{c1} \cdot (\mathbf{Z}_A)_{n,j} \cdot (\mathbf{Z})_{k,B1} + k_{c2} \cdot (\mathbf{Z}_A)_{m,j} (\mathbf{Z})_{k,j}}{\det(\mathbf{Z}_A) \cdot \det(\mathbf{Z})} \tag{A.43} $$

When the response of system A is measured at two DOFs, j_1 and j_2, the ratio of two FRFs, $H_{j1k}(\omega)/H_{j2k}(\omega)$, is not independent of the subscript, *k*. That means that the transmissibility function defined as equation (A.15) does not apply in this case. Moreover, any connection between system A and system B which is more complicated than this case, will make the whole assembly inapplicable to the proposed theorem. In other words, the three types of connection mentioned in section A.3 include not only the necessary conditions, but also the sufficient conditions for the theorem to apply.

A.5. NUMERICAL DEMONSTRATION

Three numerical cases are presented here to illustrate the validity of the theorem. These cases are formed by two basic systems connected in three different ways. The two basic systems are FE models of plates and the connections are rods. The parameters of the systems are:

plate: length 360 mm
width 200 mm
thickness 3 mm
Young's modulus 110×10^9 N/m^2
density 8.54 g/ cm^3

rod: Diameter 1.0 mm
distance between the two plates 120 mm
Young's modulus 110×10^9 N/m^2
density 8.54 g/ cm^3

Fig. A.6 shows the three assemblies of the two plates. They are (a) " = " connection, (b) " < " connection and (c) " > " connection. In all three cases, excitations are applied at 1*z* and 5*z*, and responses are measured at 21*z* and 40*z*. To make the rods used as springs, only translations in *z* direction are released at the nodes where plates and rods meet. Fig. A.7 presents overlaid FRFs in the left column and overlaid transmissibility functions in the right column.

In the cases of (b) and (c), the transmissibility functions are expressed as

$$T_{21,40}(\omega) = \frac{H_{21,1}(\omega)}{H_{40,1}(\omega)} = \frac{H_{21,5}(\omega)}{H_{40,5}(\omega)} \tag{A.44}$$

so, one can only see a single line.

In the general case, case (a), it is obvious that

$$\frac{H_{21,1}(\omega)}{H_{40,1}(\omega)} \neq \frac{H_{21,5}(\omega)}{H_{40,5}(\omega)} \tag{A.45}$$

These results illustrate the validity of the transmissibility theorem.

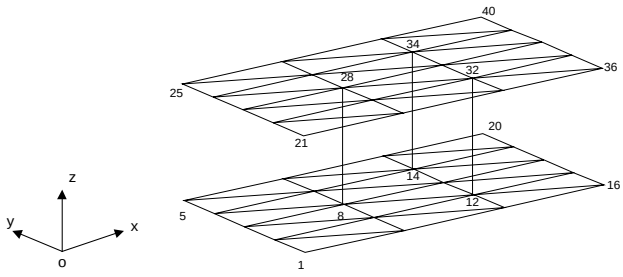

(a)

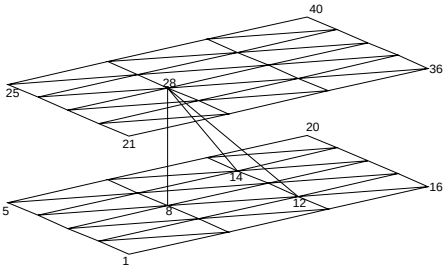

(b)

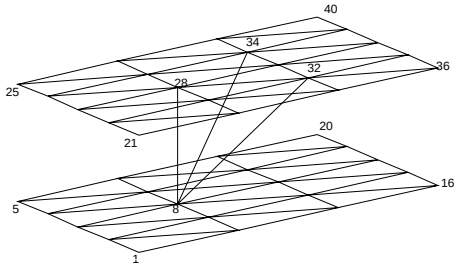

(c)

Fig. A.6 Two plates connected with rods. (a) " = " connection, the general case. (b) " < " connection. (c) " > " connection.

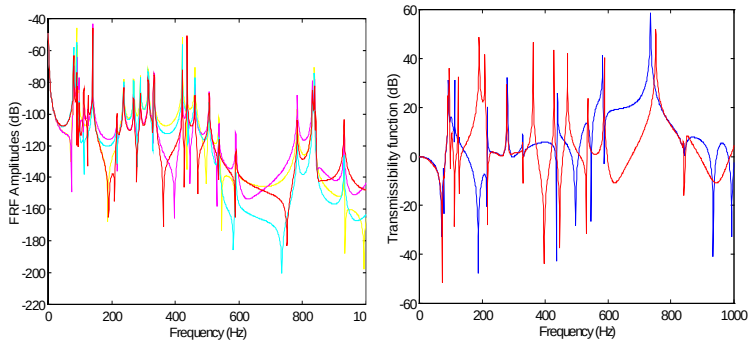

(a)

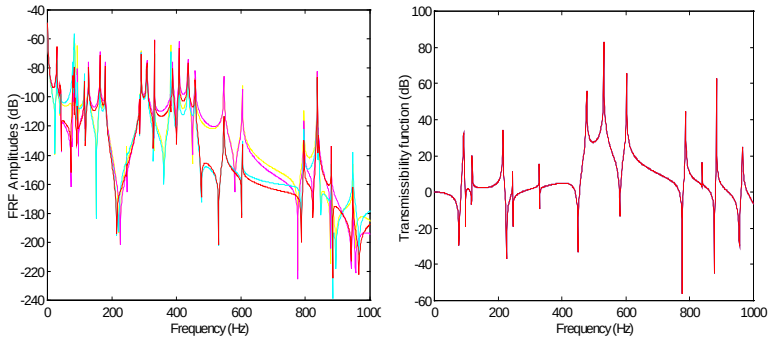

(b)

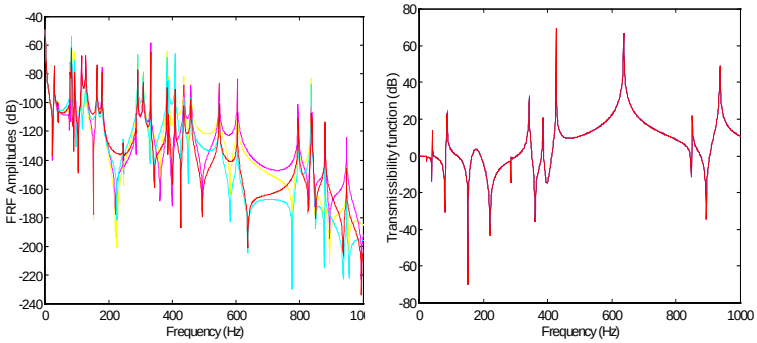

(c)

Fig. A.7 Overlaid FRFs and overlaid transmissibility functions

A.5. CONCLUSION

The transmissibility properties of MDOF systems have been thoroughly discussed here. A transmissibility function, defined as the ratio of FRFs, can always be found wherever the properties exist. The extension of the theorem, two systems connected in certain ways, shows that the transmissibility function can be analytically expressed as a function of only one system′s parameters. The particular feature which results in systems exhibiting this property is that the two response points must be separated from the excitation point by paths which pass through a common single connection. Numerical case studies have shown the validity of the theorem.

The discovery of the transmissibility properties of MDOF systems is valuable for understanding the construction of FRF matrices. As FRF matrices are so widely used in many aspects of structural dynamic and acoustic analysis, the proposed theorem and its extensions are expected to play an important role in these areas as essential knowledge.

APPENDIX B

THE ANALYSIS OF PERTURBATION

The objective here is to study the relationship of perturbation of the data of the LS problem to perturbation of its solution. In practice, the consideration of such perturbations can arise due to the uncertainties with which observable phenomena can be quantified. It is also possible to analyse the effects of round-off errors in the solution procedure as if their effects were due to perturbed data.

Results relating to perturbation of the pseudo-inverse or the solution of problem LS are described as follows.

Let $\mathbf{A}$ and $\mathbf{E}$ be $m \times n$ matrices and define the perturbed matrix, $\tilde{\mathbf{A}}$, as

$$\tilde{\mathbf{A}} = \mathbf{A} + \mathbf{E} \tag{B.1}$$

and the *residual matrix,* $\mathbf{R}$, as

$$\mathbf{R} = \tilde{\mathbf{A}}^{+} - \mathbf{A}^{+} \tag{B.2}$$

We wish to determine the dependence of $\mathbf{R}$ on $\mathbf{E}$ and, in particular, to obtain bounds for $\|\mathbf{R}\|$ in terms of $\|\mathbf{A}\|$ and $\|\mathbf{E}\|$.

It has been proved [LaHa95] that for the general case, the residual matrix $\mathbf{R}$ satisfies

$$\mathbf{R} = \mathbf{R}_1 + \mathbf{R}_2 + \mathbf{R}_3 \tag{B.3}$$

where

$$\mathbf{R}_1 = -\tilde{\mathbf{A}}^+ \mathbf{E} \mathbf{A}^+ \tag{B.4}$$

$$\mathbf{R}_2 = \tilde{\mathbf{A}}^+ (\mathbf{I} - \mathbf{Q}) = \tilde{\mathbf{A}}^+ \mathbf{A}^{T+} \mathbf{E}^T (\mathbf{I} - \mathbf{Q}) \tag{B.5}$$

$$\mathbf{R}_3 = -(\mathbf{I} - \tilde{\mathbf{P}}) \mathbf{A}^+ = (\mathbf{I} - \tilde{\mathbf{P}}) \mathbf{E}^T \mathbf{A}^{T+} \mathbf{A}^+ \tag{B.6}$$

$\mathbf{Q}$ and $\tilde{\mathbf{P}}$ are projection matrices:

$$\mathbf{Q} = \mathbf{A}\mathbf{A}^+ = \mathbf{A}^{T+}\mathbf{A}^T \text{ and } \tilde{\mathbf{P}} = \tilde{\mathbf{A}}^+ \tilde{\mathbf{A}} = \tilde{\mathbf{A}}^T \tilde{\mathbf{A}}^{T+} \tag{B.7}$$

These matrices are bounded as follows:

$$\left\|\mathbf{R}_1\right\| \le \left\|\mathbf{E}\right\| \cdot \left\|\mathbf{A}^+\right\| \cdot \left\|\tilde{\mathbf{A}}^+\right\| \tag{B.8}$$

$$\left\|\mathbf{R}_2\right\| \le \left\|\mathbf{E}\right\| \cdot \left\|\tilde{\mathbf{A}}^+\right\|^2 \tag{B.9}$$

$$\left\|\mathbf{R}_3\right\| \le \left\|\mathbf{E}\right\| \cdot \left\|\mathbf{A}^+\right\|^2 \tag{B.10}$$

More specifically, if we assume that $\left\|\mathbf{E}\right\| \cdot \left\|\mathbf{A}^+\right\| < 1$ and that $Rank(\tilde{\mathbf{A}}) \le Rank(\mathbf{A})$ then

$$Rank(\tilde{\mathbf{A}}) = Rank(\mathbf{A}) \tag{B.11}$$

and

$$\left\|\mathbf{R}_1\right\| \le \frac{\left\|\mathbf{E}\right\| \cdot \left\|\mathbf{A}^+\right\|^2}{1 - \left\|\mathbf{E}\right\| \cdot \left\|\mathbf{A}^+\right\|} \tag{B.12}$$

$$\left\|\mathbf{R}_2\right\| \le \frac{\left\|\mathbf{E}\right\| \cdot \left\|\mathbf{A}^+\right\|^2}{1 - \left\|\mathbf{E}\right\| \cdot \left\|\mathbf{A}^+\right\|} \tag{B.13}$$

$$\left\|\mathbf{R}_3\right\| \le \left\|\mathbf{E}\right\| \cdot \left\|\mathbf{A}^+\right\|^2 \tag{B.14}$$

$$\|\mathbf{R}\| \le \frac{c\|\mathbf{E}\| \cdot \|\mathbf{A}^{+}\|^{2}}{1-\|\mathbf{E}\| \cdot \|\mathbf{A}^{+}\|} \tag{B.15}$$

where

$c = \frac{1+\sqrt{5}}{2} \approx 1.618$ if $Rank(\mathbf{A}) < \min(m,n)$

$c = \sqrt{2} \approx 1.414$ if $Rank(\mathbf{A}) = \min(m,n) < \max(m,n)$

$c = 1$ if $Rank(\mathbf{A}) = m = n$

APPENDIX C

A NOTE ON ADDING DAMPING TO THE SIMULATIONS

In finite element simulations, the proportional viscous damping model is considered as

$$\mathbf{C} = \alpha \mathbf{M} + \beta \mathbf{K} \tag{C.1}$$

After the orthognality operation, one of the normal equations should be

$$\ddot{q} + 2\omega_r \xi_r \dot{q} + \omega_r^2 q = 0 \tag{C.2}$$

where q is the normal coordinate.

The process of orthogonalinisation is normally carried out as follows:

$$\mathbf{\Phi}^T \mathbf{M} \mathbf{\Phi} = \mathbf{I} \tag{C.3}$$

$$\mathbf{\Phi}^T \mathbf{K} \mathbf{\Phi} = diag(\omega_r^2) \tag{C.4}$$

$$\mathbf{\Phi}^T \mathbf{C} \mathbf{\Phi} = diag(\alpha + \beta\omega_r^2) = diag(2\omega_r \xi_r) \tag{C.5}$$

Therefore, when $\alpha = 0$, $\xi_r = \beta\omega_r / 2$, *i.e.* the modal damping ratios are proportinal to the natural frequencies.

In the process of simulation, the assembled system is constructed from the spatial models of substructures and joint. The dampling coefficient matrix of the coupled system, $\mathbf{C}$, is built in the same way to keep it proportional to the natural frequencies of the coupled system and so the dampings in substructures and their assembly are of consistance.

Suppose now that the damping coefficient matrices of substructures A and B are ${}_A\mathbf{c}$ and ${}_B\mathbf{c}$ respectively, which take the forms of

$$ {}_A\mathbf{c} = \begin{bmatrix} {}_A\mathbf{c}_{ii} & \vdots & {}_A\mathbf{c}_{ic} \\ \cdots & \cdots & \cdots \\ {}_A\mathbf{c}_{ci} & \vdots & {}_A\mathbf{c}_{cc} \end{bmatrix} \tag{C.6} $$

$$ {}_B\mathbf{c} = \begin{bmatrix} {}_B\mathbf{c}_{ii} & \vdots & {}_B\mathbf{c}_{ic} \\ \cdots & \cdots & \cdots \\ {}_B\mathbf{c}_{ci} & \vdots & {}_B\mathbf{c}_{cc} \end{bmatrix} \tag{C.7} $$

The damping coefficient matrix of joint is $\mathbf{c}$ and therefore, the damping coefficient matrix of the assembly, $\mathbf{C}$ is

$$ \mathbf{C} = \begin{bmatrix} {}_A\mathbf{c}_{ii} & {}_A\mathbf{c}_{ic} & \mathbf{0} \\ {}_A\mathbf{c}_{ci} & {}_A\mathbf{c}_{cc} + {}_B\mathbf{c}_{cc} + \mathbf{c} & {}_B\mathbf{c}_{ic} \\ \mathbf{0} & {}_B\mathbf{c}_{ci} & {}_B\mathbf{c}_{ii} \end{bmatrix} \tag{C.8} $$

The identifier will output the estimation of the elements of submatrix $\hat{\mathbf{c}}$. The accuracy of the estimation will be estimated by comparing $\hat{\mathbf{c}}$ with $\mathbf{c}$.

Since the stiffness matrices are known, we have

$$ {}_A\mathbf{c}_{cc} = \beta_A \mathbf{k}_{cc} \tag{C.9} $$

$$ {}_B\mathbf{c}_{cc} = \beta_B \mathbf{k}_{cc} \tag{C.10} $$

$$ \mathbf{C}_{CC} = \beta \mathbf{K}_{cc} \tag{C.11} $$

Therefore,

$$ \mathbf{c} = \mathbf{C}_{CC} - {}_A\mathbf{c}_{cc} - {}_B\mathbf{c}_{cc} \tag{C.12} $$

This damping model is used in the finite element simulations throughout this thesis, for joint parameter identificatin in Chapter 2 and coupling analysis in Chapter 4 and 5.

APPENDIX D

AN ANALYSIS ON NOISE SIMULATION

It is unavoidable that all test data will contain a finite amount of noise. The testing noises need to be considered in numerical simulations for examining the robustness of the algorithms.

D.1. NOISE MODELLING – TYPE AND LEVEL

In general the testing noises come from the transducers and the cable leads. All transducers have a signal level below which they cannot distinguish the signal from their inherent noise. This level will vary depending on the required amplitude and frequency ranges to be measured, and therefore depending on the type of transducer selected for the application. Further, transducers may also suffer from what is called transverse sensitivity. This is where part of the signal comes from a direction other than the primary measurement direction due to off axis vibration. Unfortunately, a certain amount of transverse sensitivity is an inherent by product of transducer design. The cable leads and connections may also add noise to the signal. The character of the noise depends on the quality of the cable (including the connectors), the length of the cable run and the nearby noise sources that may be picked up by the cable.

Noise simulation is classified into two categories: *amplitude-dependent* (sometimes referred to as "multiplicative") and *amplitude-independent* (sometimes referred to as "additive").

The amplitude dependent noise is described by [Duar96][Noba91]

$$\tilde{H}(\omega_i) = H(\omega_i) + \gamma \cdot n_i \cdot |H(\omega_i)| \tag{D.1}$$

where, γ is the noise level, n_i is the i^{th} element of a normally-distributed random sequence $\mathbf{n}$, and $|H(\omega_i)|$ is the absolute FRF amplitude. This type of noise is proportional to the amplitude of the FRF and it is not practical.

The amplitude-independent noise is described by

$$\tilde{H}(\omega_i) = H(\omega_i) + \gamma \cdot n(\omega_i) \tag{D.2}$$

This type of noise applies the same noise level to all amplitudes. It is most like a real transducer in that the large amplitudes are contaminated less than the small amplitudes. Therefore, the amplitude-independent noise is considered only in the simulations. This random sequence $\mathbf{n}$ has the statistical characteristics of

$E(\mathbf{n}) \approx 0$ (There is no DC component) and $\sigma(\mathbf{n}) \approx 1$

Its probability-density function is

$$f_n(m) = \frac{e^{-m^2/2}}{\sqrt{2\pi}}, \tag{D.3}$$

and the probability that the measured sample at time t_1, $n(t_1)$, will fall in the range m to $m + dm$ is given by $f_n(m)dm$ [Schw90].

The noise level (percentage γ) has different definitions, as presented in the following:

- Definition 1

$$\gamma = \frac{\sigma}{|H(\omega)|_{\max}} \times 100 \tag{D.4}$$

- Definition 2

$$\gamma = \frac{|n|_{\max}}{|H(\omega)|_{\max}} \times 100 \tag{D.5}$$

- Definition 3

$$\gamma = \frac{|n|_{\max}}{|h(t)|_{\max}} \times 100 \tag{D.6}$$

- Definition 4

$$\gamma = \frac{[dB(n)]_{\max}}{[dB(H(\omega))]_{\max} - [dB(H(\omega))]_{\min}} \times 100 \tag{D.7}$$

D.2. THE THEORY BACKGROUND OF NOISE LEVEL DEFINITION

Consider models where extraneous noise is measured at the input and output points to a linear system, $H(\omega)$. Let the true signals be $u(t)$ and $v(t)$ and the extraneous noise be $m(t)$ and $n(t)$, respectively. Assume that only $u(t)$ passes through the system to produce the true output $v(t)$, but that the measured input and output records are

$$x(t) = u(t) + m(t) \tag{D.8}$$

$$y(t) = v(t) + n(t) \tag{D.9}$$

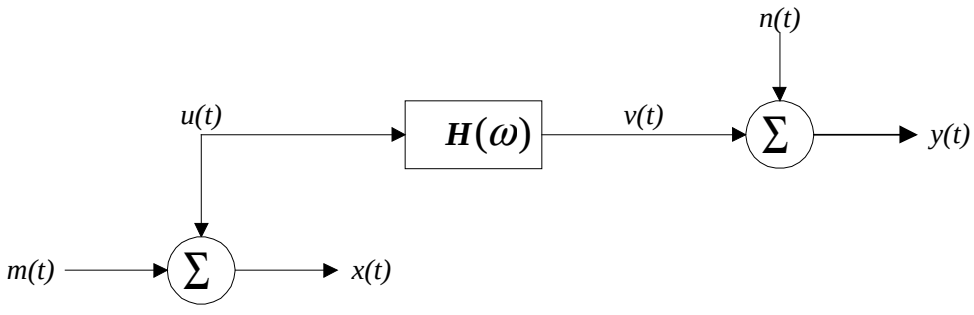

Fig. D.1 A system with noise contaminated input and output

For arbitrary correlation between the signal and noise terms, auto-spectral and cross-spectral density functions for $x(t)$ and $y(t)$ will be

$$\begin{aligned} G_{xx}(\omega) &= G_{uu}(\omega) + G_{mm}(\omega) + G_{um}(\omega) + G_{mu}(\omega) \\ G_{yy}(\omega) &= G_{vv}(\omega) + G_{nn}(\omega) + G_{vn}(\omega) + G_{nv}(\omega) \\ G_{xy}(\omega) &= G_{uv}(\omega) + G_{un}(\omega) + G_{mv}(\omega) + G_{mn}(\omega) \end{aligned} \tag{D.10}$$

where

$$\begin{aligned} G_{vv}(\omega) &= \left|H(\omega)\right|^2 G_{uu}(\omega) \\ G_{uv}(\omega) &= H(\omega)\, G_{uu}(\omega) \end{aligned} \tag{D.11}$$

Suppose that both sources of noise, $m(t)$ and $n(t)$, are uncorrelated with each other and with the signals, $u(t)$ and $v(t)$, we have

$$G_{um}(\omega) = G_{vn}(\omega) = 0 \text{ and } G_{mn}(\omega) = 0 \tag{D.12}$$

Therefore,

$$\begin{aligned} G_{xx}(\omega) &= G_{uu}(\omega) + G_{mm}(\omega) \\ G_{yy}(\omega) &= G_{vv}(\omega) + G_{nn}(\omega) \\ G_{xy}(\omega) &= G_{uv}(\omega) = H(\omega) G_{uu}(\omega) \\ G_{vv}(\omega) &= \left|H(\omega)\right|^2 G_{uu}(\omega) \end{aligned} \tag{D.13}$$

The frequency response function $H(\omega)$ cannot be determined from the measured $x(t)$ and $y(t)$ without a knowledge or measurement of the input noise.

$$H(\omega) = \frac{G_{xy}(\omega)}{G_{uu}(\omega)} = \frac{G_{xy}(\omega)}{G_{xx}(\omega) - G_{mm}(\omega)} \tag{D.14}$$

$$\left|H(\omega)\right|^2 = \frac{G_{vv}(\omega)}{G_{uu}(\omega)} = \frac{G_{yy}(\omega) - G_{nn}(\omega)}{G_{xx}(\omega) - G_{mm}(\omega)} \tag{D.15}$$

Express the directly measured frequency response function as $\hat{H}(\omega)$, $\hat{H}(\omega) = \dfrac{G_{xy}(\omega)}{G_{xx}(\omega)}$, the relative error of the measurement can be estimated by

$$\begin{aligned} e_H &= \frac{H(\omega) - \hat{H}(\omega)}{H(\omega)} = 1 - \frac{\hat{H}(\omega)}{H(\omega)} = 1 - \frac{G_{xy}(\omega)}{G_{xx}(\omega)} \cdot \frac{G_{xx}(\omega) - G_{mm}(\omega)}{G_{xy}(\omega)} \\ &= 1 - \frac{G_{xx}(\omega) - G_{mm}(\omega)}{G_{xx}(\omega)} = \frac{G_{mm}(\omega)}{G_{xx}(\omega)} \end{aligned} \tag{D.16}$$

It can also be expressed as a function of noise-to-signal ratio of the input signal, which is given by

$$\alpha(\omega) = G_{mm}(\omega) / G_{uu}(\omega) \tag{D.17}$$

as

$$e_H(\omega) = \frac{G_{mm}(\omega)}{G_{xx}(\omega)} = \frac{G_{mm}(\omega)}{G_{uu}(\omega) + G_{mm}(\omega)} = \frac{\alpha(\omega)}{1+\alpha(\omega)} \tag{D.18}$$

This last expression for $e_H(\omega)$ indicates that the relative error of the system's FRF can be estimated by the noise-to-signal ratio of the input signal. Suppose the relative error $e_H(\omega)$ is kept constant, then the noise level would change with the amplitude of the FRF. This implys that the noise is proportional to the FRF data as is was used in [Duar96]. Practically, however, the noise level should be independent of the measured data. The noise level here is defined at the frequency of the largest noise-signal-ratio, which corresponds to the smallest signal.

- Definition 5

$$\gamma = \frac{\sigma}{\left|H(\omega)\right|_{\min}} \times 100 \tag{D.19}$$

Here, σ is used instead of $\left|n\right|_{\max}$ to represent the statistic property of the noise, which will result a higher noise level. This noise level definition will be used here after in the FE simulations.

D.3. AN ILLUSTRATION OF NOISE SIMULATION

An example shows how heavily the FRFs are contaminated when 1% noise is added according to the five different noise level definitions given above.

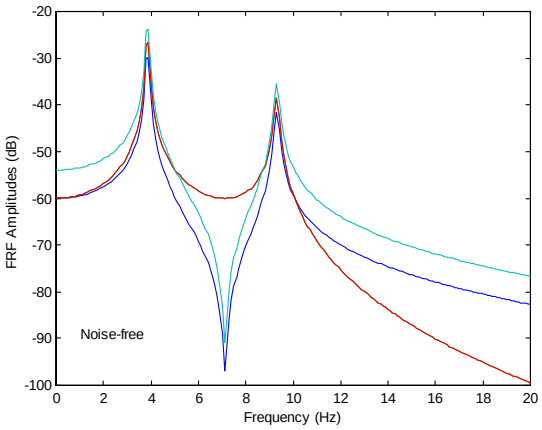

(i) Noise free FRFs

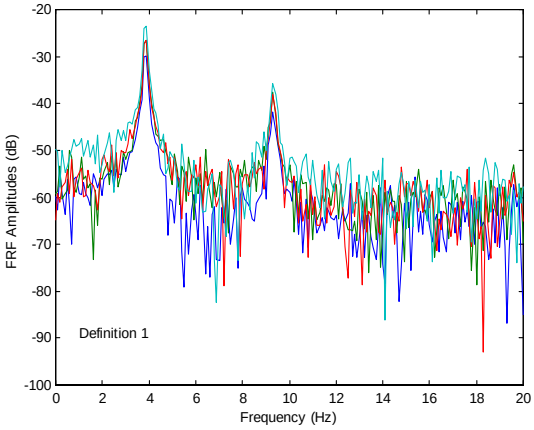

(ii) Noise added by definition 1

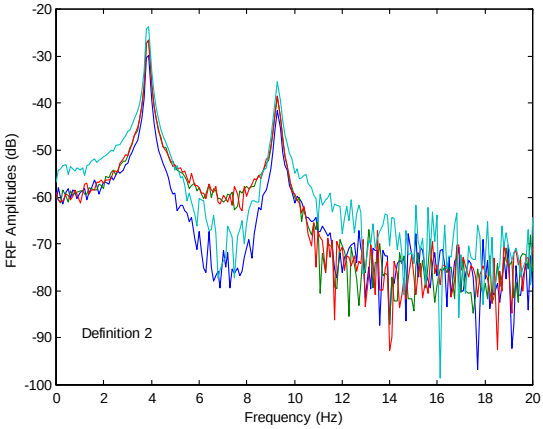

(iii) Noise added by definition 2

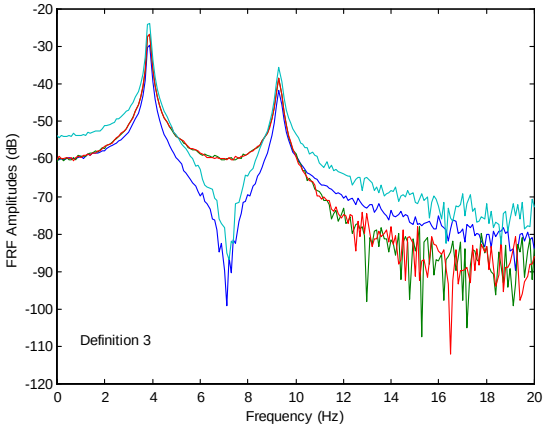

(iv) Noise added by definition 3

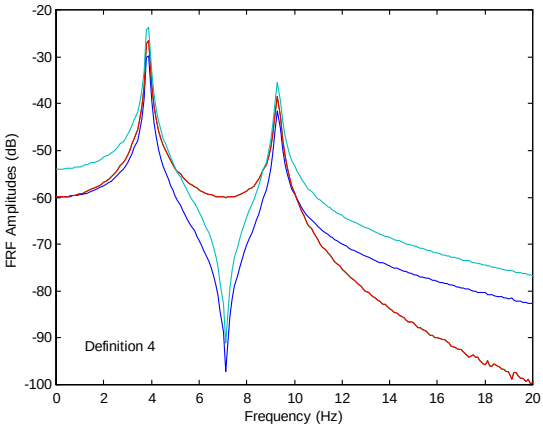

(v) Noise added by definition 4

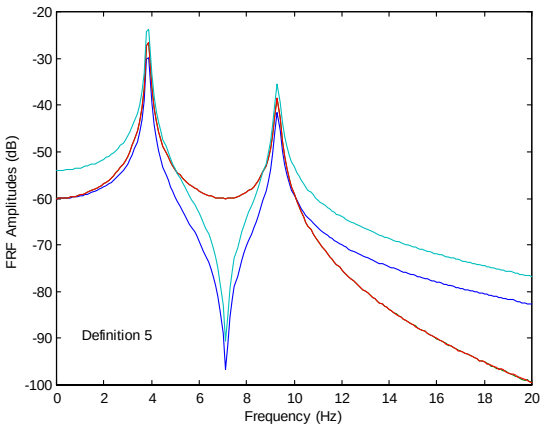

(vi) Noise added by definition 5

Fig. D.2 Noise affected FRFs from different noise models

APPENDIX E

DERIVATION OF EQUATIONS (7.21) TO (7.24)

From equation (7.9) and (7.15), we have

$$\begin{bmatrix} {}_{AB}\mathbf{H}^{c}_{tt} & \vdots & {}_{AB}\mathbf{H}^{c}_{tr} \\ \cdots & \cdots & \cdots \\ {}_{AB}\mathbf{H}^{c}_{rt} & \vdots & {}_{AB}\mathbf{H}^{c}_{rr} \end{bmatrix} \begin{bmatrix} {}_{AB}\mathbf{H}^{ci}_{tt} & \vdots & {}_{AB}\mathbf{H}^{ci}_{tr} \\ \cdots & \cdots & \cdots \\ {}_{AB}\mathbf{H}^{ci}_{rt} & \vdots & {}_{AB}\mathbf{H}^{ci}_{rr} \end{bmatrix} = \begin{bmatrix} \mathbf{I}_{tt} & \vdots & \mathbf{0} \\ \cdots & \cdots & \cdots \\ \mathbf{0} & \vdots & \mathbf{I}_{rr} \end{bmatrix} \tag{E.1}$$

The equivalent form of (E.1) is

$${}_{AB}\mathbf{H}^{c}_{tt}\,{}_{AB}\mathbf{H}^{ci}_{tt} + {}_{AB}\mathbf{H}^{c}_{tr}\,{}_{AB}\mathbf{H}^{ci}_{rt} = \mathbf{I}_{tt} \tag{E.2}$$

$${}_{AB}\mathbf{H}^{c}_{tt}\,{}_{AB}\mathbf{H}^{ci}_{tr} + {}_{AB}\mathbf{H}^{c}_{tr}\,{}_{AB}\mathbf{H}^{ci}_{rr} = 0 \tag{E.3}$$

$${}_{AB}\mathbf{H}^{c}_{rt}\,{}_{AB}\mathbf{H}^{ci}_{tt} + {}_{AB}\mathbf{H}^{c}_{rr}\,{}_{AB}\mathbf{H}^{ci}_{rt} = 0 \tag{E.4}$$

$${}_{AB}\mathbf{H}^{c}_{rt}\,{}_{AB}\mathbf{H}^{ci}_{tr} + {}_{AB}\mathbf{H}^{c}_{rr}\,{}_{AB}\mathbf{H}^{ci}_{rr} = \mathbf{I}_{rr} \tag{E.5}$$

From equation (E.3),

$${}_{AB}\mathbf{H}^{ci}_{tr} = -{}_{AB}\mathbf{H}^{c\,-1}_{tt}\,{}_{AB}\mathbf{H}^{c}_{tr}\,{}_{AB}\mathbf{H}^{ci}_{rr} \tag{E.6}$$

Substituting (E.6) into (E.5), we have

$${}_{AB}\mathbf{H}^{ci}_{rr} = \left({}_{AB}\mathbf{H}^{c}_{rr} - {}_{AB}\mathbf{H}^{c}_{rt}\,{}_{AB}\mathbf{H}^{c\,-1}_{tt}\,{}_{AB}\mathbf{H}^{c}_{tr}\right)^{-1} \tag{E.7}$$

E.1 DERIVATION OF SUBMATRIX ${}_{AB}\mathbf{H}_{tt}^{ci}$

From (E.4),

$$ {}_{AB}\mathbf{H}_{rt}^{ci} = -{}_{AB}\mathbf{H}_{rr}^{c\ -1}\ {}_{AB}\mathbf{H}_{rt}^{c}\ {}_{AB}\mathbf{H}_{tt}^{ci} \tag{E.8}$$

substituting (E.8) into (E.2), we have

$$ {}_{AB}\mathbf{H}_{tt}^{c}\left(\mathbf{I}_{tt} - {}_{AB}\mathbf{H}_{tt}^{c\ -1}\ {}_{AB}\mathbf{H}_{tr}^{c}\ {}_{AB}\mathbf{H}_{rr}^{c\ -1}\ {}_{AB}\mathbf{H}_{rt}^{c}\right){}_{AB}\mathbf{H}_{tt}^{ci} = \mathbf{I}_{tt} \tag{E.9}$$

Pre-multiply ${}_{AB}\mathbf{H}_{tt}^{c}$ in both sides of (E.9):

$$ \left(\mathbf{I}_{tt} - {}_{AB}\mathbf{H}_{tt}^{c\ -1}\ {}_{AB}\mathbf{H}_{tr}^{c}\ {}_{AB}\mathbf{H}_{rr}^{c\ -1}\ {}_{AB}\mathbf{H}_{rt}^{c}\right){}_{AB}\mathbf{H}_{tt}^{ci} = {}_{AB}\mathbf{H}_{tt}^{c\ -1} \tag{E.10}$$

and then

$$ {}_{AB}\mathbf{H}_{tt}^{ci} = \left(\mathbf{I}_{tt} - {}_{AB}\mathbf{H}_{tt}^{c\ -1}\ {}_{AB}\mathbf{H}_{tr}^{c}\ {}_{AB}\mathbf{H}_{rr}^{c\ -1}\ {}_{AB}\mathbf{H}_{rt}^{c}\right)^{-1}\ {}_{AB}\mathbf{H}_{tt}^{c\ -1} \tag{E.11}$$

Using the general inverse relationship

$$ \left(\mathbf{I} - \mathbf{AB}\right)^{-1} = \mathbf{I} + \mathbf{A}\left(\mathbf{I} - \mathbf{BA}\right)^{-1}\mathbf{B} \tag{E.12}$$

equation (E.11) becomes

$$ {}_{AB}\mathbf{H}_{tt}^{ci} = \left(\mathbf{I}_{tt} + {}_{AB}\mathbf{H}_{tt}^{c\ -1}\ {}_{AB}\mathbf{H}_{tr}^{c}\mathbf{D}^{-1}\ {}_{AB}\mathbf{H}_{rr}^{c\ -1}\ {}_{AB}\mathbf{H}_{rt}^{c}\right){}_{AB}\mathbf{H}_{tt}^{c\ -1} \tag{E.13}$$

where

$$ \mathbf{D} = \mathbf{I}_{rr} + {}_{AB}\mathbf{H}_{rr}^{c\ -1}\ {}_{AB}\mathbf{H}_{rt}^{c}\ {}_{AB}\mathbf{H}_{tt}^{c\ -1}\ {}_{AB}\mathbf{H}_{tr}^{c} \tag{E.14}$$

Since

$$ \left(\mathbf{AB}\right)^{-1} = \mathbf{B}^{-1}\mathbf{A}^{-1} \tag{E.15}$$

we have

$$ \mathbf{D}^{-1}\ {}_{AB}\mathbf{H}_{rr}^{c\ -1} = \left({}_{AB}\mathbf{H}_{rr}^{c}\mathbf{D}\right)^{-1} \tag{E.16}$$

Substituting (E.16) into (E.13)

$$ {}_{AB}\mathbf{H}_{tt}^{ci} = \left(\mathbf{I}_{tt} + {}_{AB}\mathbf{H}_{tt}^{c\ -1}\ {}_{AB}\mathbf{H}_{tr}^{c}\ {}_{AB}\mathbf{H}_{rr}^{ci}\ {}_{AB}\mathbf{H}_{rt}^{c}\right){}_{AB}\mathbf{H}_{tt}^{c\ -1} \tag{E.17}$$

therefore,

$$ {}_{AB}\mathbf{H}_{tt}^{ci} = {}_{AB}\mathbf{H}_{tt}^{c\ -1} + {}_{AB}\mathbf{H}_{tt}^{c\ -1}\ {}_{AB}\mathbf{H}_{tr}^{c}\ {}_{AB}\mathbf{H}_{rr}^{ci}\ {}_{AB}\mathbf{H}_{rt}^{c}\ {}_{AB}\mathbf{H}_{tt}^{c\ -1} \tag{E.18} $$

E.2 PROOF OF ${}_{AB}\mathbf{H}_{tr}^{ci\,T} = {}_{AB}\mathbf{H}_{rt}^{ci}$

Substituting (E.7) into (E.6), we have

$$ {}_{AB}\mathbf{H}_{tr}^{ci} = -{}_{AB}\mathbf{H}_{tt}^{c\ -1}\ {}_{AB}\mathbf{H}_{tr}^{c}\left({}_{AB}\mathbf{H}_{rr}^{c} - {}_{AB}\mathbf{H}_{rt}^{c}\ {}_{AB}\mathbf{H}_{tt}^{c\ -1}\ {}_{AB}\mathbf{H}_{tr}^{c}\right)^{-1} \tag{E.19} $$

Using equation (E.15), (E.19) becomes

$$ {}_{AB}\mathbf{H}_{tr}^{ci} = -\left({}_{AB}\mathbf{H}_{tr}^{c\ -1}\ {}_{AB}\mathbf{H}_{tt}^{c}\right)^{-1}\left({}_{AB}\mathbf{H}_{rr}^{c} - {}_{AB}\mathbf{H}_{rt}^{c}\right]_{AB}\mathbf{H}_{tt}^{c\ -1}\ {}_{AB}\mathbf{H}_{tr}^{c}\Big)^{-1} \tag{E.20} $$

and then

$$ {}_{AB}\mathbf{H}_{tr}^{ci} = -\left(\left({}_{AB}\mathbf{H}_{rr}^{c} - {}_{AB}\mathbf{H}_{rt}^{c}\ {}_{AB}\mathbf{H}_{tt}^{c\ -1}\ {}_{AB}\mathbf{H}_{tr}^{c}\right)\left({}_{AB}\mathbf{H}_{tr}^{c\ -1}\ {}_{AB}\mathbf{H}_{tt}^{c}\right)\right)^{-1} \tag{E.21} $$

therefore

$$ {}_{AB}\mathbf{H}_{tr}^{ci} = -\left({}_{AB}\mathbf{H}_{rr}^{c}\ {}_{AB}\mathbf{H}_{tr}^{c}\right]^{-1}\ {}_{AB}\mathbf{H}_{tt}^{c} - {}_{AB}\mathbf{H}_{rt}^{c}\Big)^{-1} \tag{E.22} $$

Similarly, from equations (E.2) and (E.4), we have

$$ {}_{AB}\mathbf{H}_{rt}^{ci} = -{}_{AB}\mathbf{H}_{rr}^{c\ -1}\ {}_{AB}\mathbf{H}_{rt}^{c}\left]\left({}_{AB}\mathbf{H}_{tt}^{c} - {}_{AB}\mathbf{H}_{tr}^{c}\ {}_{AB}\mathbf{H}_{rr}^{c\ -1}\ {}_{AB}\mathbf{H}_{rt}^{c}\right)^{-1}\right. \tag{E.23} $$

$$ {}_{AB}\mathbf{H}_{rt}^{ci} = -\left(\left({}_{AB}\mathbf{H}_{tt}^{c} - {}_{AB}\mathbf{H}_{tr}^{c}\ {}_{AB}\mathbf{H}_{rr}^{c\ -1}\ {}_{AB}\mathbf{H}_{rt}^{c}\right)\left({}_{AB}\mathbf{H}_{rt}^{c\ -1}\ {}_{AB}\mathbf{H}_{rr}^{c}\right)\right)^{-1} \tag{E.24} $$

$$ {}_{AB}\mathbf{H}_{rt}^{ci} = -\left({}_{AB}\mathbf{H}_{tt}^{c}\ {}_{AB}\mathbf{H}_{rt}^{c\ -1}\ {}_{AB}\mathbf{H}_{rr}^{c} - {}_{AB}\mathbf{H}_{tr}^{c}\right)^{-1} \tag{E.25} $$

The transpose of ${}_{AB}\mathbf{H}_{tr}^{ci}$ is

$$ \begin{aligned} {}_{AB}\mathbf{H}_{tr}^{ci\,T} &= -\left(\left({}_{AB}\mathbf{H}_{rr}^{c}\ {}_{AB}\mathbf{H}_{tr}^{c\ -1}\ {}_{AB}\mathbf{H}_{tt}^{c} - {}_{AB}\mathbf{H}_{rt}^{c}\right)^{T}\right)^{-1} \\ &= -\left({}_{AB}\mathbf{H}_{tt}^{c}\ {}_{AB}\mathbf{H}_{rt}^{c\ -1}\ {}_{AB}\mathbf{H}_{rr}^{c} - {}_{AB}\mathbf{H}_{rt}^{c}\right)^{-1} \end{aligned} \tag{E.26} $$

Comparing (E.26) with (E.25), we know that

$$ {}_{AB}\mathbf{H}_{tr}^{ci\,T} = {}_{AB}\mathbf{H}_{rt}^{ci} \tag{E.27} $$

APPENDIX F

FREQUENCY RESPONSE ASSURANCE CRITERIA (FRAC)

The Frequency Response Assurance Criteria [NeSu96] helps to identify the degree of similarity between a frequency response function that is measured, $\mathbf{H}(\omega)^x$, and one that is synthesised from the finite element model, $\mathbf{H}(\omega)^a$. In analogy to the MAC definition, the FRAC is defined as [HeAv98]

$$FRAC(j) = \frac{\left|\mathbf{H}(\omega_i)_j^a \cdot \mathbf{H}^h(\omega_i)_j^x\right|^2}{\left(\mathbf{H}(\omega_i)_j^a \cdot \mathbf{H}^h(\omega_i)_j^a\right)\left(\mathbf{H}(\omega_i)_j^x \cdot \mathbf{H}^h(\omega_i)_j^x\right)} \tag{F.1}$$

For identical frequency response functions for an analytical and experimental model, the FRAC will be 1.0 indicating good correlation; when the frequency response functions are significantly different, then the FRAC will approach zero indicating that there is little correlation between the two functions.

If a stiffness shifting factor, α, is included in the formulation, then the FRAC definition becomes

$$FRAC(j) = \max_{\beta}\left(\frac{\left|\mathbf{H}(\beta\omega_i)_j^a \cdot \mathbf{H}^h(\omega_i)_j^x\right|^2}{\left(\mathbf{H}(\beta\omega_i)_j^a \cdot \mathbf{H}^h(\beta\omega_i)_j^a\right)\left(\mathbf{H}(\omega_i)_j^x \cdot \mathbf{H}^h(\omega_i)_j^x\right)}\right) \tag{F.2}$$

where β is frequency shifting factor which has the relationship with α as

$$\alpha = (\beta_{\max})^2 \tag{F.3}$$

It also can be defined by absolute or logarithm values instead of the complex values in some cases where the differences in order of magnitude of the values of response functions are very large due to light damping or where the phase differences are significant. In these cases, FRAC values can be quite low while the analytical and experimental response functions visually show acceptable correlation.

References

[AhMF96] Ahmadian, H, Mottershead, J E and Friswell, M I
Joint Modelling for Finite Element Model Updating
Proceedings of 14th IMAC, 591-596, Dearborn, Michigan, 1996

[ArSa93] Arruda, J R F and Santos, J M C
Mechanical Joint Parameter Estimation Using Frequency Response Functions and Component Mode Synthesis
Mechanical Systems and signal Processing, **7**(6), 493-508, 1993

[AtIn96] Atalla, M J and Inman, D J
Model Updating Using Neural Networks
DTA/NAFEMS conference, July, 1996

[Balm95a] Balmes, E
Parametric Families of Reduced Finite Element Models. Theory and Applications
Mechanical System and Signal Processing, **10**(4), 381-394, 1996

[Balm95b] Balmes, E
Experimental and Analytical Structural Dynamics Toolbox: User's Guide
June 1995

[Balm96a] Balmes, E
Use of Generalized Interface Degrees of Freedom in Component Mode Synthesis
Proceedings of 14th IMAC, 204-210, Dearborn, Michigan, 1996

[Balm96b] Balmes, E
Optimal Ritz Vectors for Component Mode Synthesis Using the Singular Value Decomposition
AIAA Journal, Vol.34 No.6 1256-1260, June 1996

[BaGr81] Bathe, K J and Gracewski, S
On Non-linear Dynamic Analysis Using Substructuring and Mode Superposition
Computers and Structures, Vol.13 699-707, 1981

[Bear79] Beards, C F
Damping in Structural Joints
Shock and Vibration Digest, **11**(9), 35-41, 1979

[Bear86a] Beards, C F
Damping in Structural Joints
Shock and Vibration Digest, Nov 1986, Vol 17, No 11

[Bear86b] Beards, C F
The Damping of Structural Vibration by Controlled Interfacial Slip in Joints
ASME publication 81-DET-86, 1-5

[BePi86] Bendat, J S and Piesol, A G
Random Data Analysis and Measurement Procedure, 2nd Edition (Revised and Expanded)
John Wiley & Sons, 1986, 177 – 181

[BeWo85] Beards, C F and Woowat, A
The Control of Frame Vibration by Friction Damping in Joints
J of vibration, acoustics, stress and reliability in design, Jan. 1985, vol. 107

[BiJo60] Bishop, R E D and Johnson, D C
The Mechanics of Vibration
Cambridge, at the university press, 1960

[BrBo95] Brahmi, K., N. Bouhaddi and R. Fillod
Reduction of the junction degrees of freedom before assembly in dynamic substructuring
In 1995 Design Engineering Technical Conferences, ASME, Boston, USA

[BeWB99] Becker, P W, Wynn, R H and Berger, E J
Using Rigid-Body Dynamics to Measure Joint Stiffness
Mechanical Systems and Signal Processing, **13**(5), 789-801, 1999

[Caug60] Caughey, T K
Sinusoidal Excitation of a System with Bilinear Hysteresis
Trans. of ASME, J. of Applied Mechanics, vol. 27, 640-643, 1960

[Crai81] Craig Jr., R R
Structural Dynamics: An Introduction to Computer Methods
John Wiley & Sons, 1981

[Crai00] Craig Jr., R R
A Brief Tutorial on Substructure Analysis and Testing
Proceedings of 18th IMAC, 899-908, San Antonio, Texas, 2000

[Cran70] Crandall, S H
The Role of Damping in Vibration Theory
Journal of Sound and Vibration, **11**(1), 3-18, 1970

[CrBa68] Craig Jr., R R and Bampton, M C C
Coupling of Substructures for Dynamic Analysis
AIAA Journal, Vol.6 No.7 July 1968

[CrCh77] Craig, R and Chang, C
Substructure Coupling for Dynamic Analysis and Testing
NASA Contractor report, NASA CR-2781, 1977

[ChYM00] Chen, J J, Yang, B D and Meng, C H
Periodic Forced Response of Structures Having Three-dimensional Frictional Constraints
Journal of Sound and Vibration, **229**(4), 775-792, 2000

[Dank97] Dankowicz, H
Dynamic Friction Modelling
Contact Mechanics III : Third International Conference on Contact Mechanics
227-236, Spain, 1997

[DenH31] Den Hartog, J P
Forced Vibrations with Combined Coulomb and Viscous Friction
Transactions of the ASME, **53**, APM 107-115, 1931

[DenH56] Den Hartog, J P
Mechanical Vibrations
Dover Publications, Inc. New York, 1956

[Dere74] Deresiewitz, H
Bodies in Contact with Applications to Granular Media
In R D Mindlin and Applied Mechanics
edited by Herrmann, G, Pergamon Press, 1974

[DiKu96] Diamantaras, K I and Kung, S Y
Principal Component Neural Networks: Theory and Applications
John Wiley & Sons, Inc. 1996

[Duar96] Duart, M L M
Experimentally-derived Structural Models for Use in Further Dynamic Analysis
PhD Thesis, Dept of Mech. Eng. Imperial College, April, 1996

[DuEw95] Duart, M L M and Ewins, D J
Some Insights into the Importance of Rotational DOF and Residual Terms in Coupled Structure Analysis
Proceedings of 13th IMAC, 164-170, Tennessee,1995

[EaMo72] Earles, S W E and Mott, N
A Response Prediction and Optimisation of a Frictionally Damped Structure
13th International Machine Tool Design and Research Conference, Sept. 1972

[Earl66] Earles, S W E
Theoretical Estimation of the Frictional Energy Dissipation in a Simple Lap Joint
Journal of Mechanical Engineering, **8**, 207-214, 1966

[EaWi72] Earles, S W E and Williams, E J
A Linearised Analysis for Frictionally Damped System
Journal of Sound and Vibration, **24**(4), 445-0458, 1972

[Ewin84] Ewins, D J
Modal Testing: Theory and Practice
Research Studies Press, 1984

[FaGe92] Fahat, C and Geradin, M
A Hybrid Formulation of a Component Mode Synthesis Method
33rd SDM Conference, AIAA paper 92-2383-CP, 1783-1796, 1992

[FaSi95] Farstad, J E and Singh, R
Structurally Transmitted Dynamic Power Estimates in Discretely Jointed Damped Component Assemblies
J. Acoust. Soc. Am. **97**(5), 2855-2864, 1995

[FaSi96] Farstad, J E and Singh, R
Effective of Modal Truncation Errors on Transmitted Dynamic Power Estimates in Discretely Jointed Component Assemblies
J. Acoust. Soc. Am. **100**(5), 3144-3158, 1996

[Ferr98] Ferreira, J V
Dynamic Response Analysis of Structures with Nonlinear Components
PhD Thesis, Dept of Mech. Eng. Imperial College, May, 1998

[FlRo97] Fladung, W and Rost, R
Application and Correlation of the Exponential Window for Frequency Response Functions
Mechanical Systems and signal Processing, **11**(1), 23-36, 1997

[FrMo95] Friswell, M I and Mottershead, J E
Finite Element Model Updating in Structural Dynamics
Kluwer Academic 1995

[FrPe90] Freswell, M I and Penny, J E T
Updating Model Parameters from Frequency Domain Data via Reduced Order Models
Mechanical Systems and signal Processing, **4**(5), 377-391, 1990

[GaNW94] Gaul, L, Nackenhorst, U, Willner, K and Lenz, J
Nonlinear Vibration Damping of Structures with Bolted Joints
Proceedings of 13th IMAC, 875-881, Tennessee,1995

[Gaul83] Gaul, L
Wave Transmission And Energy Dissipation At Structural And Machine Joints
J of vibration, acoustics, stress and reliability in design, **105**, Oct. 489-496, 1983

[GéRi94] Géradin, M and Rixen, D
Mechanical Vibrations: Theory and Application to Structural Dynamics
John Wiley & Sons, 1994

[GéRi97] Géradin, M and Rixen, D
Mechanical Vibrations: Theory and Application to Structural Dynamics
2nd edition, John Wiley & Sons, 1997

[GiTs96] Gialamas, T, Tsahalis, D, Bregant, L, Otte, D and Auweraer, H
Substructuring by Means of FRFs: Some Investigations on the Significance of Rotational DOFs
Proceedings of 14th IMAC, 619-625, Dearborn, Michigan, 1996

[GoKl56] Goodman, L E, and Klumpp, J H
Analysis of Slip Damping with Reference to Turbine-Blade Vibration
Trans. Of ASME, J. of Applied Mechanics, **78**, 421-429, Sept.1956

[Good88] Goodman, L E
Material Damping and Slip Damping
In Shock and Vibration Handbook, C M Harris, McGraw-Hill, 3rd Ed., 1988

[Gord93] Gordis, J H
A Frequency Domain Theory for Structural Identification
Journal of the American Helicopter Society
25-33, April, 1993

[Griff80] Griffin, J H
Friction Damping of Resonant Stresses in Gas Turbine Engine Airfoils
Journal of Engineering for Power, Trans. ASME, **102**(4), 1980

[GuSH95] Gutzer, U, Seemann, W and Hagedorn, P
Nonlinear Structural Damping Described by the Masing Model and the Method of Slowly Varying Amplitude and Phase
ASME paper, DE-Vol. 84-1, 1995 Design Technical Conferences, Volume 3 – Part A

[Guya65] Guyan, R
Reduction of Stiffness and Mass Matrices
AIAA Journal, 3(2):380-, 1965

[Haya64] Hayashi, C
Nonlinear Oscillations in Physical Systems
New York : McGraw-Hill, 1964

[Hayk95] Haykin, S
Neural Networks, A Comprehensive Foundation
Macmillan College Publishing Company, 1995

[HaDB96] Hagan, M T, Demuth, H B and Beale, M
Neural network design
PWS Publishing Company, 1996

[HeAv98] Heylen, W and Avitabile, P
Correlation Considerations – Part 5 (Degree of Freedom Correlation Techniques)
Proceedings of 16th IMAC, 207-214, California, 1998

[Hint75] Hintz, R F
Analytical Methods in Component Mode Synthesis
AIAA Journal, 13 (8), 1007-1015, 1975

[Herr65] Herrera, I
Dynamic Models for Masing Type Material and Structures
Boletin Sociedat Mexicana De Ingenieria Sismica, Vol.3 1-8 (in Spanish)

[HoGu99] Horton, B, Gurgenci, H, Veidt, M and Friswell, M I
Finite Element Model Updating of the Welded Joints in a Tubular H-Frame
Proceedings of 17th IMAC, 1556-1562, Florida,1999

[HoLi00] Hong, H K and Liu, C S
Coulomb Friction Oscillator: Modelling and Responses to Harmonic Loads and Base Excitation
Journal of Sound and Vibration, **229**(5), 1171-1192, 2000

[JeBi88] Jetmundsen, B., Bielawa, R.L.and Flannelly, W.G.
Generalized Frequency Domain Substructure Synthesis
Journal of the American Helicopter Society, 55-64, 1988

[JeSe94a] Jezequel, L and Seito, H D
Component Modal Synthesis Methods Based on Hybrid Models, Part I: Theory of Hybrid Models and Modal Truncation Methods
J. of Applied Mechanics, Trans. of the ASME,vol.61, March 1994

[JeSe94b] Jezequel, L and Seito, H D
Component Modal Synthesis Methods Based on Hybrid Models, Part II: Numerical Tests and Experimental Identification of Hybrid Modes
J. of Applied Mechanics, Trans. of the ASME,vol.61, March 1994

[KiEh91] Kim, T R, Ehmann, K F and Wu, S M
Identification of Joint Structural Parameters Between Substructures
Trans. Of the ASME, Journal of Engineering for Industry, **113**, 419-424, Nov., 1991

[KiPa93] Kim, H K and Park, Y S
An Efficient Response Analysis Method for a Non-linear/parameter Changing System Using Sub-structure Modes
Proc. Instn Mech Engrs, Vol.207, IMechE 1993

[KiPa97] Kim, H B and Park, Y S
Sensor Placement Guide for Structural Joint Stiffness Model Improvement
Mechanical Systems and signal Processing, **11**(5), 651-672, 1997

[LaHa95] Lawson, C L and Hanson, R J
Solving Least Squares Problems
Society for Industrial and Applied Mathematics, Philadelphia, 1995

[LaOa97] Laursen, T A and Oancea, V G
On the Constitutive Modelling and Finite Element Computation of Rate-Dependent Frictional Sliding in Large Deformations
Computer Methods in Applied Mechanics and Engineering, **143**, 197-227, 1997

[LeGa95] Lenz, J and Gaul, L
The Influence of Microslip on the Dynamic Behaviour of Bolted Joints
Proceedings of 13th IMAC, 248 – 254, Tennessee, 1995

[Lesh93] Leshno, M, Lin, V, Pinkus, A and Schocken, S
Multilayer Feedforward Networks with a Nonpolynomial Activation Function Can Approximate Any Function
Neural Networks, Vol. 6, 1993, 861-867

[Levi98] Levin, R I
Dynamic Finite Element Model Updating Using Neural Networks
PhD Thesis, Faculty of Engineering, University of Bristol, UK, Nov. 1998

[Lin99] Lin, R M
Generalised Receptance-Based Method for Accurate and Efficient Modal Synthesis
Int. J Numer. Mech. Engng. **44**, 1749-1767, 1999

[LiEw95] Liu, W and Ewins, D J
Identification of Damping Non-linearities in Dynamic Structures Using Neural Networks
Internal Report, Dept of Mech Eng, Imperial College, 1995

[LiEw98] Liu, W and Ewins, D J
Transmissibility Properties in MDOF Systems
Proceedings of 16th IMAC, 847-854, California, 1998

[Liu96] Liu, W
Identification of Linear Joint Parameters in Structural Dynamic System
Interim report No. 2, Imperial College, June 1996

[Liu97a] Liu, W
Linear Joint Parameter Identification - A General Method
Interim Report No 5, 30 April 1997

[Liu97b] Liu, W
Joint Parameter Identification – Investigation on Application
Interim Report No 6, 6 October 1997

[LoGh93] Lou, M, Ghobarah, A and Aziz, T S
A Modal Synthesis Method for Dynamic Substructuring
European Journal of Mechanics, A/Solid, Vol.12 No.3, 1993

[MaCh93] Masri, S F, Chassiakos, A G and Caughey, T K
Identification of Nonlinear Dynamic System Using Neural Networks
J. of Applied Mechanics, ASME, (60) 1993

[MacN71] MacNeal, R H
A Hybrid Method of Component Mode Representation for Structural Dynamic Analysis
Computer and Structures, vol. 1, 581-601, 1971

[MaGh84] Martin, K F and Ghlaim, K H
On the Solution of Approximated Systems when Using Reduced Component Modes
Earthquake Engineering and Structural Dynamics, vol.12, 417-426, 1984

[MeBG86] Meng, C H, Bielak, J and Griffin, J H
The Influence of Microslip on Vibratory Response, Part I: A New Microslip Model
J of Sound and Vibration, **107**(2), 279-293, 1986

[MeGB86a] Meng, C H, Griffin, J H and Bielak, J
The Influence of Microslip on Vibratory Response, Part II: A Comparison with Experimental Results
J of Sound and Vibration, **107**(2), 295-307, 1986

[MeGB86b] Meng, C H, Griffin, J H and Bielak, J
The Influence of a Variable Normal Load on the Forced Vibration of a Frictionally Damped Structure
Trans. Of ASME, J. of Engineering for Gas Turbines and Power
vol. 108, 300-305, 1986

[MeGr85] Meng, C H and Griffin, J H
A Comparison of Transient and Steady State Finite Element Analyses of the Forced Response of a Frictional Damped Beam
Trans. Of ASME, J. of Vibration, Acoustics, Stress, and Reliability in Design
vol. 107, 19-25, 1985

[Mino47] Minorsky, N
Non-linear Mechanics
J. W. Edwards, Ann Arbor, Mich., 1947

[MoFr94] Mottershead, J E, Friswell, M I, Ng, G H T and Brandon, J A
Experience in Mechanical Joint Model Updating
19th International Seminar on Modal Analysis, Leuven, Belgium, Sept 1994

[MoJP99] Moon, Y M, Jee, T H and Park, Y P
Development of an Automotive Joint Model Using an Analytically Based Formulation
J. of Sound and Vibration, **220**(4), 625-640, 1999

[NaPa90] Narendra, K S and Pathasarathy, K
Identification and Control of Dynamical Systems Using Neural Networks
IEEE Trans. on Neural Networks, 1(1), 1990

[NaSe98] Narayanan, S and Sekar, P
A Frequency Domain Based Numeric-Analytical Method for Non-linear Dynamical System
J. of Sound and Vibration, **211**(3), 409-424, 1998

[NeSu96] Nefske, D and Sung, S H
Correlation of a Coarse-Mesh Finite Element Model Using Structural System Identification and a Frequency Response Assurance Criterion
Proceedings of 14th IMAC, 597-602, Dearborn, Michigan, 1996

[Noba91] Nobari A S
Identification of the Dynamic Characteristics of Structural Joints
Ph.D. Thesis, Imperial College, December, 1991

[OaLa98] Oancea, V G and Laursen, T A
Investigation of Low Frequency Stick-slip Motion: Experiments and Numerical Modelling
Journal of Sound and Vibration, 213(4), 577-600, 1998

[OcAv86] O'Callahan, J, Avitabile, P, Madden, R and Lieu, I
An Efficient Method of Determining Rotational Degrees of Freedom from Analytical and Experimental Modal Data
Proceedings of 4th IMAC, 50 - 58, Los Angeles, California, 1986

[OcAv89] O'Callahan, J, Avitabile, P and Riemer, R
System Equivalent Reduction Expansion Process
Proceedings of 7th IMAC, 29 - 37, Las Vegas, Nevada, 1989

[OtLe90] D. Otte, Leuridan, J, Grangier, H and Aquilina, R
Coupling of Structures Using Measured FRFs by Means of SVD-Based Data Reduction Techniques
Proceedings of 8th IMAC, 231-220, Florida, 1990

[OtLe91] D. Otte, Leuridan, J, Grangier, H and Aquilina, R
Prediction of the Dynamics of Structural Assemblies Using Measured FRF data: Some Improved Data Enhancement Techniques
Proceedings of 9th IMAC, 909-918, Florence, Italy, 1991

[PaKi95] Park, Y and Kim H B
Structural Joint Parameter Identification: Its theory and Application
ASIA-Pacific Vibration Conference'95, Kuala Lumpur, Nov. 1995

[Plun80] Plunkett, R
Friction Damping
Damping Applications for Vibration Control, AMD **38**
edited by Torvik, P J , ASME, New York, 1980

[PrWi81] Pratt, T K and Williams, R
Non-linear analysis of stick/slip motion
Journal of Sound and Vibration, **74**(4), 531-542, 1981

[QiYi97a] Qiu, J, Ying, Z and Williams, F W
Exact Modal Synthesis Techniques Using Residual Constraint Modes
Int. J Numer. Mech. Engng. **40**, 2475-2492, 1997

[QiYi97b] Qiu, J, Ying, Z and Yam, L H
New Modal Synthesis Technique Using Mixed Modes
AIAA Journal, vol.35, No.12 1997

[ReBe95] Ren, Y and Beards, C F
Identification of Joint Properties of a Structure Using FRF Data
J. of Sound and Vibration, **186**(4), 567-587, 1995

[Ren92] Ren, Y
The Analysis and Identification of Friction Joint Parameters in the Dynamic Response of Structures
PhD Thesis, Dept of Mech Eng, Imperial College London, 1992

[RoBo75] Rogers, P F and Boothroyd, G
Damping at Metallic Interfaces Subjected to Oscillating Tangential Loads
Trans. of the ASME, Journal of Engineering for Industry, August, 1995, 1087-1093

[RuMc66] Rumelhart, D E and McCleland, J L
Parallel Distributed Processing
MIT Press, 1966

[SaAs95] Sanliturk, K Y, Ashory, R and Immamovic, N
Investigation of Alternator Vibration via FRF Coupling
Interim Report No.1 Imperial College, 28 July 1995

[SaAs96] Sanliturk, K Y, Ashory, R and Immamovic, N
Investigation of Alternator Vibration via FRF Coupling
Interim Report No.2 Imperial College, 4 January 1996

[SaEw95] Sanliturk, K Y and Ewins, D J
Friction dampers: measurement, modelling and application to blade vibration control
ASME 1995 DE-vol 84-2, Vol 3-Part B

[SaEw96] Sanliturk, K Y and Ewins, D J
Modelling Two-Dimensional Friction Contact and Its Application Using Harmonic Balance Method
Journal of Sound and Vibration, 193(2), June 1996, p511-523

[SaSE95] Sanliturk, K Y, Stanbridge, A and Ewins, D J
Friction Dampers: Measurement, Modelling and Application to Blade Vibration Control
ASME paper, DE-Vol. 84-1, 1995 Design Technical Conferences, Volume 3 – Part A

[Sesh97] Seshu, P
Substructuring and Component Mode Synthesis
Shock and Vibration, Vol.4, No.3, 199-210, 1997

[Shaw86] Shaw, S W
On The Dynamic Response of a System with Dry Friction
Journal of Sound and Vibration **108**(2), 305-325, 1986

[Shwa90] Schwartz, M
Information transmission, modulation, and noise. 4th ed.
McGraw-Hill, 1990, 427

[Silj69] Šiljak, D D
Nonlinear Systems, The Parameter Analysis and Design
John Wiley & Sons, Inc. 1969

[StEw96] Stanbridge, A B and Ewins D J
Measurement of Translational and Angular Vibration Using a Scanning Laser Doppler Vibrometer
Shock and Vibration, 3(2), 141-152, 1996

[SuMa92] Suarez, L E, Matheu, E E
A Modal Synthesis Technique Based on the Force Derivative Method
J of Vibration and Acoustics, April 1992, Vol. 114

[ThLe72] Thornley, R H and Lees, K
Some Static and Dynamic Characteristics of Bounded, Machined Joint Faces
Proceedings of 13th Int. MTDR, 79-86, 1972

[TsCh88] Tsai, J S and Chou, Y F
The Identification of Dynamic Characteristics of a Single Bolt Joint
Journal of Sound and Vibration **125**(3), 487-502, 1988

[Unga73] Ungar, E E
The Status of Engineering Knowledge Concerning the Damping of Built-up Structures
Journal of Sound and Vibration, **26**(1), 141-154, 1973

[Urgu89] Urgueira A P V
Dynamic Analysis of Coupled Structures Using Experimental Data
PhD thesis, Dept of Mech Engng, Imperial College, 1989

[VaEw92] Vakakis, A F and Ewins, D J
Effect of Weak Nonlinearities on Modal Analysis
Proceedings of 10th IMAC, 72-78, San Diego, California, 1992

[Vala71] Valanis, K C
A Theory of Viscoplasticity without a Yield Surface
Archives of Mechanics, **23**(4), 517-533, Warsaw, 1971

[VaMc99] Varoto, P S and McConnell, K G
On the Identification of Interface Forces and Motions in Coupled Structures
Proceedings of 17th IMAC, 2031-2037, Florida,1999

[WaCh92] Wang, J H and Chen, W K
Investigation of the Vibration of a Blade with Friction Damper by HBM
ASME paper, 92-GT-8, The International Gas Turbine and Aeroengin Congress and Exhibition, Cologne, Germany, June 1-4, 1992

[WaLi90] Wang, J H and Liou, C M
Identification of Parameters of Structural Joints by Use of Noise-Contaminated FRFs
J of Sound and Vibration, **142**(2) , 261-277, 1990

[WaLi91] Wang, J H and Liou, C M
Experimental Identification of Mechanical Joint Parameters
J of Vibration and Acoustics, Jan. 1991, Vol. 113

[WaSa90] Wang, J and Sas, P
A Method for Identifying Paraneters of Mechanical Joints
Trans. of ASME, J of Applied Mechanics, vol. 57, 337-342, 1990

[WeTY90] Weaver, W Jr., Timoshenko, S P and Young, D H
Vibration Problems in Engineering (Fifth edition)
Jonh Wiley and Sons, 1990

[Wite97] Witek, A
Stiffness and Damping Identification of Vibroisolation Pads in Machine Elements Joints
Contact mechanics III : third International Conference on Contact Mechanics
editors: M.H. Aliabadi, A. Samartin, 1997

[WuGh92] Wu, X, Ghaboussi, J and Garrett, J H
Use of Neural networks in Detection of Structural Damage
Computers and Structures 42(4), 645-659, 1992

[YaPa93] Yang, K T and Park, Y S
Joint Structural Parameter Identification Using a Subset of Frequency Response Function Measurements
Mechanical Systems and signal Processing, **7**(6), 509-530, 1993

[YaCM98] Yang, B D, Chu, M L and Menq, C H
Stick–Slip–Separation Analysis and Non-Linear Stiffness and Damping Characterization of Friction Contacts Having Variable Normal Load
J of Sound and Vibration, **210**(4), 461 – 481, 1998

[Yeh64] YeH, Gordon C K
Forced Vibrations of a Two-degree-of-freedom System with Combined Coulomb and Viscous Damping
Journal of the Acoustical Society of America, **39**, 14-24, 1966

[Yosh77] Yoshimura, M
Measurement of Dynamic Rigidity and Damping Property for Simplified Joint Models and Simulation by Computer
Annals of the CIRP, vol. 25/1/1977, 193-198

[Yosh79] Yoshimura, M
Computer-Aided Design Improvement of Machine Tool Structure Incorporating Joint Dynamics Data
Annals of the CIRP, vol. 28/1/1979, 241-246

[YuWu85] Yuan, J X and Wu, X M
Identification of the Joint Structural Parameters of Machine Tool by DDS and FEM
ASME J of Engineering for Industry, vol. 107, Feb. 1985